

2  
MIT

DRA

**AMERICAN  
SCIENCE**   
AND ENGINEERING

12 OCTOBER 1972

ASE-3096

955 MASSACHUSETTS AVENUE, CAMBRIDGE,  
MASSACHUSETTS 02139 (617) (868-1600)

FINAL REPORT:

**LOXT MIRROR  
DESIGN STUDY**

(NASA-CR-124001) LOXT MIRROR DESIGN  
STUDY Final Report (American Science  
and Engineering, Inc.) 262 p HC \$15.25  
CSCL 17H G3/14 UNCLAS 16783  
ON73-19424

CONTRACT NO. NAS8-27795  
PERIOD COVERED:  
1 SEPTEMBER 1971 - 15 JUNE 1972



PREPARED FOR:  
**NATIONAL AERONAUTICS  
AND SPACE ADMINISTRATION  
GEORGE C. MARSHALL  
SPACE FLIGHT CENTER  
MARSHALL SPACE FLIGHT CENTER, ALABAMA 35812**

FINAL REPORT

LOXT MIRROR DESIGN STUDY

Contract No. NAS8-27795

Prepared by:

American Science and Engineering, Inc.  
955 Massachusetts Avenue  
Cambridge, Massachusetts 02139

Dr. Leon VanSpeybroeck  
William Antrim  
Dave Boyd

Dr. Riccardo Giacconi  
Gerald Sinnamon  
Frank Stille

Prepared for:

National Aeronautics and Space Administration  
George C. Marshall Space Flight Center  
Marshall Space Flight Center, Alabama 35812

12 October 1972

Approved:



Dr. Leon VanSpeybroeck  
Project Scientist



Dr. Riccardo Giacconi  
Principal Investigator

## CONTENTS

	<u>Page</u>
INTRODUCTION	vii
1.0 PROGRAM DEVELOPMENT	1-1
1.1 Design Approach	1-1
1.2 Design Parameters	1-1
1.3 Sample Test Program	1-3
2.0 TELESCOPE OPTICAL DESIGN	2-1
2.1 Principles of X-ray Imaging Systems	2-1
2.1.1 Theory of Total External Reflection	2-2
2.1.2 Calculation of $\beta$ and $\delta$ at X-ray Wave- lengths	2-3
2.1.3 Imaging Systems	2-7
2.1.4 Diffraction Effects	2-9
2.2 Parametric Studies	2-9
2.3 High Resolution Mirror Optical Tolerances	2-12
2.3.1 Mirror Assembly	2-16
2.3.2 Paraboloid-Hyperboloid Section Alignment Tolerances	2-17
2.3.3 Mirror Segment Tolerances	2-18
2.3.4 Micro-surface Requirements	2-22
3.0 MECHANICAL DESIGN CONSIDERATIONS	3-1
3.1 Fused Silica Mirrors	3-1
3.2 Launch Environment	3-2
3.3 Thermal Environment	3-3
3.4 Structural Materials	3-3
3.5 Ground Rules for the High Resolution Mirror Design Study	3-5
3.5.1 General	3-5
3.5.2 Mirror Assembly	3-6
4.0 SCATTERING TEST SAMPLE PROGRAM	4-1
4.1 Technique	4-1
4.1.1 Incident Beam Width Effects	4-4
4.1.2 Geometrical Effects of Optical Flat Misorientation	4-5
4.1.3 Geometrical Effects of Cylindrical Test Surface Misalignment	4-5
4.1.4 Summary	4-6
4.2 Results	4-6

## CONTENTS (cont'd)

	<u>Page</u>
4.2.1 Fused Silica, Submerged Process	4-9
4.2.2 Fused Silica, Barnsite Polishing	4-9
4.2.3 Fused Silica, Ion Polishing	4-10
4.2.4 Evaporated Nickel Surfaces	4-10
4.2.5 Electrodeless Nickel on Be, Con- ventional Polish	4-11
4.2.6 Electrodeless Nickel on Be, Speedring Process	4-11
4.2.7 Ion Polished Electrodeless Nickel on Be	4-12
4.2.8 Evaporated Glass on Be - Conventional or Ion Polished	4-12
4.2.9 Selective Dielectric Deposition on Be	4-13
4.3 Conclusion	4-14
5.0 REFERENCE DESIGN	5-1
5.1 Configuration	5-1
5.2 Fused Silica Mirror/Support Flange Thermal Stress Analysis	5-1
5.3 Mirror Distortion Under Gravity Load	5-4
5.4 High Resolution Mirror Dynamic Analysis	5-6
5.5 Mirror Support Structural Analysis	5-8
5.5.1 Static Analysis	5-8
5.5.2 Dynamic Analysis	5-9
5.6 Thermal Analysis	5-12
5.6.1 Thermal Configuration of Reference Design	5-12
5.6.2 Axial and Radial Gradients	5-13
5.6.3 Circumferential Gradients	5-15
5.6.4 Temperature Control	5-16
5.7 Fabrication Techniques	5-16
5.7.1 Fused Silica Mirror Blanks	5-17
5.7.2 Mirror Fabrication	5-18
5.7.3 Machining Tolerances	5-19
5.7.4 Invar Support Structure	5-20
5.7.5 Graphite Epoxy Composite Support Structure	5-20
5.8 Mirror End Flange Design	5-21
5.9 Flange/Mirror Bonding	5-22
5.10 Alignment Procedure	5-23
5.11 Weight and Volume	5-25
5.12 Advantages/Disadvantages of the Reference Design	5-25

## CONTENTS (cont'd)

	<u>Page</u>
6.0 ALTERNATE DESIGN	6-1
6.1 Configuration	6-1
6.2 Stress Analysis	6-1
6.2.1 Gravity Load Distortion	6-1
6.2.2 Static Loads Analysis	6-3
6.2.3 Dynamic Analysis	6-3
6.2.4 Support Structure Analysis	6-4
6.3 Thermal Analysis	6-4
6.3.1 Thermal Configuration of Alternate Design	6-4
6.3.2 Axial and Radial Temperature Gradients	6-5
6.3.3 Circumferential Gradients	6-5
6.3.4 Temperature Control	6-5
6.4 Alignment Procedure	6-6
6.5 Weight and Volume	6-6
7.0 SPECIFICATION FOR TEST MIRRORS	7-1
APPENDIX A Design Parameters of Parabaloid- Hyperboloid Telescopes for X-ray Astronomy	A-1
APPENDIX B Computer Solution: LOXT High Resolution Mirror Distortion Under Gravity Load	B-1
APPENDIX C LOXT High Resolution Mirror Dynamic Analysis	C-1
APPENDIX D Optical Bench Analysis	D-1
APPENDIX E Heat Flow To Space	E-1
APPENDIX F Temperature Gradient Patterns In The High Resolution Mirror Assembly	F-1
APPENDIX G Ambient Temperature Range of the High Resolution Mirror	G-1
APPENDIX H Relationship Between Mirror Assembly Focal Length and the Optical Bench	H-1

CONTENTS (concluded)

		<u>Page</u>
APPENDIX I	LOXT High Resolution Mirror Alternate Design Dynamic Analysis	I-1
APPENDIX J	Technical Specification for the Inner Parabaloid of the LOXT High Resolu- tion X-ray Telescope Assembly	J-1

## ILLUSTRATIONS

<u>Figure No.</u>		<u>Page</u>
2-1	Plot of Reflectance vs. Normalized Grazing Angle $\theta / \theta_c$ for Various Values of $\theta / \delta$ .	2-4
2-2	Theoretical Reflection Efficiency vs. Wavelength for Various Grazing Angles and Reflection Materials.	2-6
2-3	Three Possible Configurations for Image-Forming X-ray Telescopes.	2-8
2-4	Geometric Area and Angular Resolution as a Function of the Length and Number of Mirror Elements.	2-11
2-5	Mirror Surface Separation.	2-13
2-6	Effective Area of the High Resolution Mirror as a Function of Wavelength for Various Incident Angles.	2-14
2-7	R. M. S. Radius of Image Distribution as a Function of Incident Angle for a Flat Focal Plane and an Optimally Curved Focal Plane.	2-15
4-1	Schematic Diagram of the Experimental Set Up to Measure the Scattered Intensity Distribution	4-3
5-1	Fused Silica Mirror Assembly	5-2
5-2	High Resolution Mirror/Mirror Support Flange Model	5-3
5-3	Mirror Wall Thermal Distortion $\theta$ vs. Mirror Length for $T = +10^\circ\text{F}$	5-5
5-4	Thermal Gradient Patterns In Reference Design- Isotherms In Degrees Farenheit Below Space- craft Ambient	5-14
6-1	Beryllium Mirror Assembly	6-2

## INTRODUCTION

This document is the Final Report for the Large Orbiting X-Ray Telescope (LOXT) High Resolution Mirror Design Study performed by American Science and Engineering, Cambridge, Massachusetts under NASA, Marshall Spaceflight Center, Contract NAS8-27795.

Under this contract, American Science and Engineering performed the following tasks:

1. Generation of a reference and alternate preliminary design for the LOXT High Resolution Mirror Assembly, which will meet the LOXT scientific requirements, and are within the present state of the art of materials and fabrication techniques.
2. Measurement, in X-rays, of the scattering properties of a variety of optical flats, embodying materials, coatings, and polishing techniques which might be applicable to the flight configuration LOXT High Resolution Mirror.
3. Preparation of a procurement specification for a paraboloid test mirror of the size of the innermost paraboloid of the High Resolution Mirror Assembly, including the design requirements for the reference design evolved from this preliminary design study.

The results of the engineering and scientific analysis and the conclusions drawn therefrom are presented in this final report. The procurement specification for the test mirror is included as an Appendix.

The LOXT will be aboard the HEAO-C spacecraft which is presently scheduled to be launched during the fourth quarter of 1978. The LOXT assembly will be approximately eight feet in diameter and

30 feet long, and will contain 2 X-ray telescopes. One telescope will be optimized for high resolution (about one arc second) and will have a focal length of 20 feet. The other telescope will be optimized for high efficiency and will have a larger collecting area, a focal length of 26 feet, and a modest resolution (about 30 arc seconds). Located at the focal plane of each telescope will be a variety of scientific experiments mounted on an interchange assembly which will permit any combination of one high resolution telescope experiment and one high efficiency telescope to be operated simultaneously. The HEAO-C spacecraft will have a long duration pointing capability of the experiments with an accuracy of one arc minute, which is well within the field of view of either telescope. Aspect sensing equipment coaligned with the telescopes will provide, after ground data processing, aspect determination to one arc second accuracy.

The preliminary design study presented in this report was addressed to the preliminary design of the high resolution mirror assembly for the LOXT system. This effort was initiated early because the X-ray mirrors to be used in this assembly require a greater extension of present techniques and a longer fabrication time than any other LOXT element.

## 1.0 PROGRAM DEVELOPMENT

### 1.1 Design Approach

The reference preliminary design for the High Resolution Mirror Assembly was based upon the use of mirrors fabricated from fused silica with a thin deposition on the optical surface of a metal suitable for X-ray reflection. Fused silica mirrors were specified for the reference design in order to obtain the smoothest available surface, resulting in very low scattering in the X-ray region. The use of this material obviously had considerable influence on the reference design.

The alternate design was specified to be a back-up in the event that serious problems developed during the fabrication and testing of the reference design; therefore, a conservative approach, well within the state of the art, was indicated. An all beryllium mirror assembly was adopted at the outset of the alternate design study, since there was considerable experience at AS&E and elsewhere in the design and fabrication of beryllium mirrors for X-ray telescopes. A suitable High Resolution Mirror for the LOXT mission would thus be assured, although the fact that the alternate design would most likely exhibit a somewhat inferior performance to that of the reference design was recognized.

### 1.2 Design Parameters

An X-ray telescope design essentially is determined by specifying the focal length and the number of optical surfaces, their diameters, separations, and segment lengths. The LOXT High Resolution Mirror focal length was set at 20 feet in these studies because of the length of the HEAO spacecraft, and because of earlier preliminary studies of the distance behind the focal plane that will be required for telescope instruments. The outside diameter of the mirror,

which determines the X-ray reflection angle, was then fixed to obtain an effective cutoff energy of about 4 keV with a nickel reflecting surface. This cutoff is higher than the absorption cutoff of any presently observed sources, and yet is consistent with the desired effective area of about  $1,000 \text{ cm}^2$  that is required to perform many of the observations in a reasonable time. The remaining parameters are the number of surfaces, the length of the individual elements, and the separation of the optical surfaces required for mechanical integrity. A study was then made of the area and resolution of the X-ray mirrors as a function of these remaining three parameters in which the number of surfaces was varied from one to ten, the segment lengths from one to four feet, and the surface separations from  $1/2$  to 2 inches. The studies showed that the desired one arc second resolution over a reasonable field required surfaces of about 2 feet; this fact determined the segment length, since any further reduction would also reduce the effective area. The mechanical requirements for mirrors of this size then resulted in a mirror separation of about 0.75 inch, which was selected as the design separation, since once again any increase in the separation results in additional losses of effective area. Finally, the minimum number of surfaces required to obtain the desired effective area within these constraints was 5, and this number was chosen for the design. This number is near the point of diminishing returns, since each additional mirror must be smaller than the previous members, but it contributes almost equally to the cost of the mirror and the complications of properly supporting the mirror elements.

The final design does not differ significantly from the original experiment proposal, but is now known to be an approximately optimum design because of the parametric studies of neighboring designs that have been performed.

The performance of an X-ray mirror depends upon its optical design, mechanical tolerances upon a large and small scale, the quality of the reflecting surfaces, and the mechanical integrity of the mirror assembly. All these areas were studied during the mirror development program and more complete discussions are given in later sections of this report.

### 1.3 Sample Test Program

The largest area of uncertainty in the performance of the X-ray mirrors was the possibility of obtaining surfaces sufficiently smooth for efficient X-ray reflection with acceptably low scattering properties. Fused silica generally is believed to result in the smoothest available surfaces, but fused silica does not reflect efficiently throughout the desired X-ray wavelength interval, and it was not known if the smooth surfaces of fused silica could be maintained after coating with a suitable metal for X-ray reflection. (Aluminum and silver were known to result in smooth surfaces, but are not stable in the normal laboratory environment.) A program of measuring the scattering properties of different materials polished in various manners was conducted. These tests, which were performed at  $8.3 \text{ \AA}$ , showed that fused silica with a properly evaporated nickel surface coating essentially reproduced the incident beam distribution, thus indicating very low scattering. It was also found that properly polished nickel coated Be resulted in much less surface scattering than expected at the time of the LOXT proposal. The conclusion was thus reached that no fundamental problem exists in the physics of the reflecting surfaces, although care will be required in order to obtain this surface quality over a large area telescope.

The polishing process resulting in the best X-ray reflection properties was the so-called submerged process in which the polishing material is constantly reused so that the polishing particles are

broken down into finer and finer pieces. This process has been specified for the fabrication of the LOXT mirrors. None of the more recently introduced techniques, such as ion polishing or the Speed Ring proprietary process, resulted in equivalent performance. These results are discussed in greater detail in Section 4. This work will be extended to other wavelengths and surfaces during the LOXT Phase B study program.

## 2.0 TELESCOPE OPTICAL DESIGN

The objectives of the High Resolution Mirror design were to obtain about  $1,000 \text{ cm}^2$  effective area with one arc second resolution over a limited field of view and an energy range extending to about 4Kev. The  $1,000 \text{ cm}^2$  goal was required to perform certain observations, such as the study of typical X-ray sources in nearby galaxies and the study of nearby ordinary stars, in a reasonable time on the order of one day. This area also approaches the limit set by the length of the spacecraft and the small grazing angles necessary for the desired energy response of a few Kev. The energy response limits were determined by the need to observe beyond the 2-3 Kev absorption cutoffs which are typical of many galactic sources, and also possibly compact extragalactic objects. The high energy cutoff also extends the observations to energies typical of the electron temperatures of many sources, and consequently includes the most informative part of the spectrum of these objects. Finally, this range includes all important X-ray emission lines, except for the iron group, which are at an impractically high energy for telescope observations. The arc second resolution requirement will allow direct comparison with visible observations, which are limited to this resolution by seeing conditions; the arc second resolution also is consistent with the available imaging instruments. This resolution is only required over a small field (about 3 arc minutes) because of the pointing capabilities of the HEAO spacecraft.

### 2.1 Principles of X-ray Imaging Systems

The design of imaging systems for use at X-ray wavelengths is limited by two severe constraints. The first is that X-rays are readily absorbed by matter; the second is that the index of refraction at X-ray wavelengths is very nearly unity. For a refractive

system, these constraints imply an extremely thin lens and a very long focal length; no practical X-ray refractive imaging system has yet been devised. The fact that the index of refraction is slightly less than unity, however, means that at sufficiently shallow angles of incidence total external reflection will occur. It is this principle which is the basis for the realization of the grazing incidence X-ray imaging systems.

### 2.1.1 Theory of Total External Reflection

The transmission and reflection of X-rays at the boundary between two substances are described by Fresnel's equations. The index of refraction at X-ray wavelengths is conventionally written:

$$n = 1 - \delta - i \beta$$

where  $\beta$  and  $\delta$  are small quantities related to the absorption and phase velocity of the radiation respectively. If  $\beta$  is negligible and  $\delta$  positive, then radiation incident on a surface in a vacuum will be totally reflected at grazing angles of incidence less than the critical angle  $\theta_c$  given by Snell's law:

$$\cos \theta_c = \sqrt{2\delta}$$

or,

For radiation at a grazing angle  $\theta$  and polarized so that the electric field is perpendicular to the plane of incidence, the ratio of reflected to incident power is given by an expression derived from Fresnel's equations:

$$\frac{I_R}{I_O} = \frac{(\theta - a)^2 + b^2}{(\theta + a)^2 + b^2} \quad (1)$$

$$a = \frac{1}{\sqrt{2}} \left[ \sqrt{(\theta^2 - \theta_c^2)^2 + 4\beta^2} + (\theta^2 - \theta_c^2) \right]^{1/2}$$

$$b = \frac{1}{\sqrt{2}} \left[ \sqrt{(\theta^2 - \theta_c^2)^2 + 4\beta^2} - (\theta^2 - \theta_c^2) \right]^{1/2}$$

The reflection efficiency for the other polarization differs negligibly from that given by Equation 1; therefore, Equation 1 also describes the reflection of unpolarized X-rays. Figure 2-1 shows the variation of  $I_R/I_O$  as a function of  $\theta/\theta_c$  for various values of  $\beta/\delta$ . For  $\beta/\delta = 0$ , the reflectivity is total for angles less than  $\theta_c$  and falls off sharply at larger angles. For large values of  $\beta/\delta$  the reflectivity is lower for  $\theta < \theta_c$ , but does not fall off as rapidly at larger angles.

The thickness of material which contributes to grazing incidence reflection is small except for the case when  $\theta \approx \theta_c$ . Parratt (1954) has shown that for grazing incidence at X-ray wavelengths where  $\sin\theta_c \approx \theta_c$  and  $\delta$  and  $\beta$  are small quantities, the intensity of the electric field in the reflecting medium is reduced by a factor of  $1/e$  in a thickness  $z_o$  given by

$$z_o = \lambda/4\pi b \quad (2)$$

$$\text{where } b = \frac{1}{\sqrt{2}} \left[ \left( \left[ \theta^2 - \theta_c^2 \right]^2 + 4\beta^2 \right)^{1/2} - \left( \theta^2 - \theta_c^2 \right) \right]^{1/2}$$

$z_o$  has a maximum value when  $\beta = 0$ . In that case, for  $\theta < \theta_c$ :

$$\begin{aligned} (z_o)_{\max} &= \frac{\lambda}{4\pi (\theta^2 - \theta_c^2)^{1/2}} \\ &\approx \frac{\lambda}{4\pi \theta_c} \quad (\text{if } \theta \text{ is not very close to } \theta_c) \end{aligned}$$

For the nickel telescopes discussed here,  $\theta$  will be between 1 and 2 degrees in the wavelength region from 4 to 8 $\text{\AA}$ . Therefore,  $(z_o)_{\max}$  will be on the order of 20 $\text{\AA}$ , and evaporated metal surfaces need not be thicker than a few hundred angstroms.

### 2.1.2 Calculation of $\beta$ and $\delta$ at X-ray Wavelengths

The quantity  $\beta$  describes the absorption and is related to the linear absorption coefficient  $\mu$  e by expression:

$$\beta = \frac{\lambda}{4\pi} \mu = \frac{\lambda \rho}{4\pi} \left[ \frac{\mu}{\rho} \right] \quad (3)$$

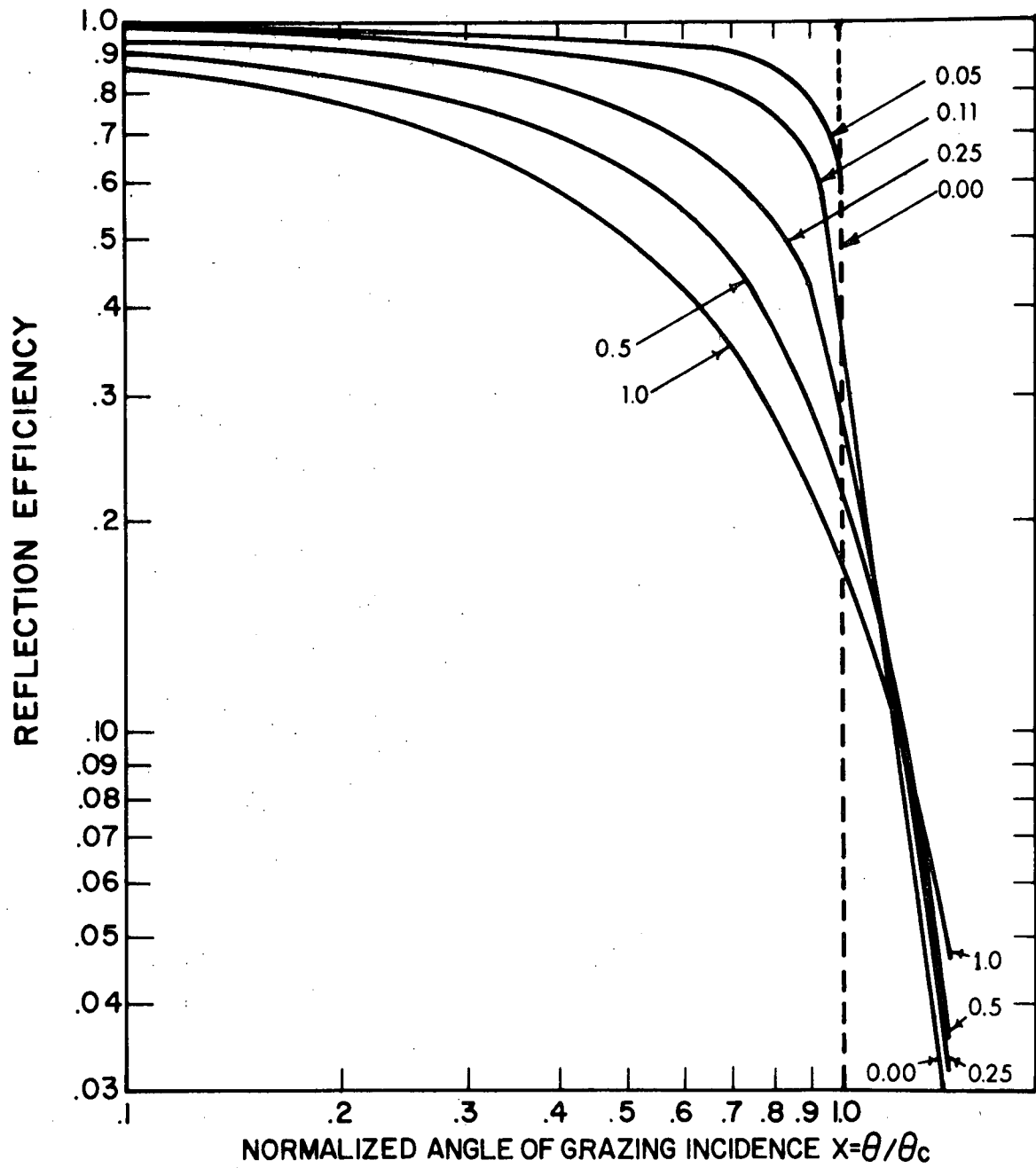


Figure 2-1. Plot of reflectance versus normalized grazing angle  $\theta/\theta_c$  for various values of  $\beta/\delta$ . (After Hendrick 1957).

where  $\lambda$  is the wavelength,  $\rho$  is the density, and  $(\mu/\rho)$  is the mass absorption coefficient. Thus,  $\beta$  can be calculated from experimentally measured data.

$\delta$  can be determined from experimental measurements of the reflectivity at grazing incidence (Hendrick, 1957; Lukirskii et al., 1964; Stewardson and Underwood, 1964) or it can be calculated from dispersion theory (Parratt and Hempstead, 1954; Henke, 1960). The reflection efficiency can be calculated with sufficient accuracy using the following simplified expression for

$$\delta = \frac{r_0 \lambda^2}{2\pi} \left[ N + \sum_H N_H \left( \frac{\lambda}{\lambda_H} \right)^2 \ln \left| \frac{\lambda_H^2}{\lambda^2} - 1 \right| \right] \quad (4)$$

where  $r_0$  is the classical electron radius,  $\lambda$  is the wavelength of the radiation,  $N$  is the electron density,  $N_H$  is the electron density associated with  $\lambda_H$ , and  $\lambda_H$  is the wavelength associated with the absorption edge  $H$ .

For frequencies far from an absorption edge, Equation 4 reduces to

$$\delta = N_A \left[ \frac{r_0 \lambda^2}{2\pi} \right]$$

where  $N_A$  is the density of electrons associated with resonance frequencies less than  $c/\lambda$ .

The reflection efficiency for beryllium, aluminum, nickel, and gold surfaces was calculated using this method, and the results are shown in Figure 2-2.

In general, experimental measurements of the X-ray reflectivity at grazing angles of incidence have been in good agreement with theory. Discrepancies may be attributed to surface properties such as oxidation, contamination, porosity, or annealing wavelength.

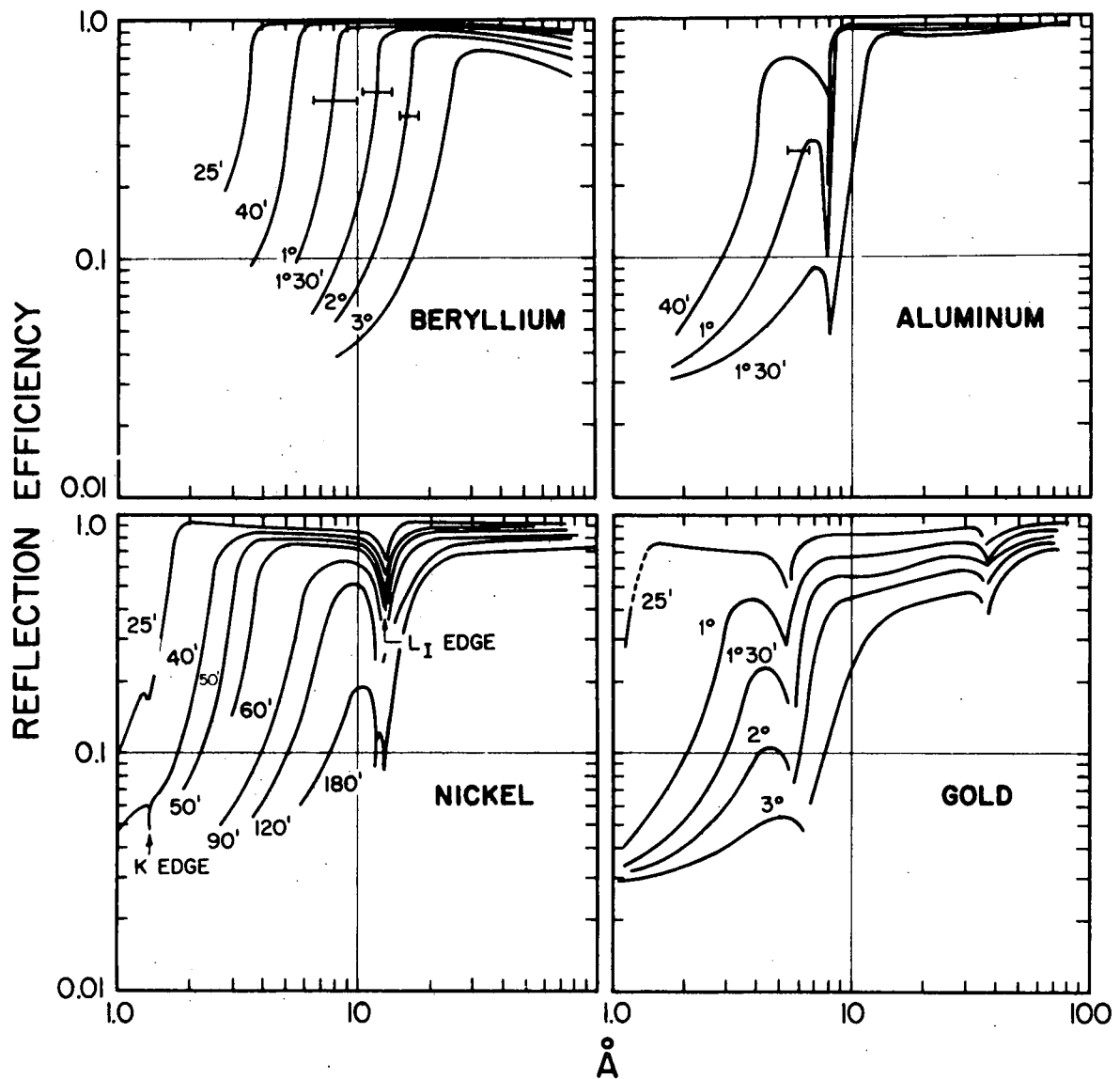


Figure 2-2. Theoretical reflection efficiency versus wavelength for various grazing angles and reflection materials.

### 2.1.3 Imaging Systems

The use of paraboloidal mirrors at grazing incidence in X-ray astronomy was first proposed by Giacconi and Rossi (1960). The paraboloid has the geometric property that paraxial rays will be imaged to a point at the focus of the paraboloid. The condition of grazing incidence, however, implies that the far zone of the paraboloid must be used as a reflecting element. It is not possible to satisfy the Abbe' sine condition for such a system (or for any other single reflection system at grazing incidence) and, thus, the image will be subject to severe comatic aberration. Wolter has shown that this aberration can be removed by the addition of a second reflecting surface; he considers three general systems of conic sections which are shown in Figure 2-3. In these designs the effective area can be increased by nesting one surface inside another. The individual mirrors must then be co-aligned to obtain the same optical axis and focal plane scale.

The LOXT High Resolution mirror is a paraboloid-hyperboloid type device, as shown in Figure 2. 3a, in which X-rays are first focused at the common paraboloid-hyperboloid focal plane, but with severe comatic distortion. The X-rays are then focused from the common focal plane to the near focal plane of the hyperboloid, and most of the distortion is compensated. This design type has a number of practical advantages, the principal ones being that both reflections occur in the same direction so that the focal length for a given aperture is less, and the physical surfaces actually intersect so that the necessary mechanical stability between the mirror elements is more easily achieved. Several such systems with about one arc second resolution have been built.

The equations of the individual surfaces are determined by the paraboloid-hyperboloid geometry, focal length, diameter at surface

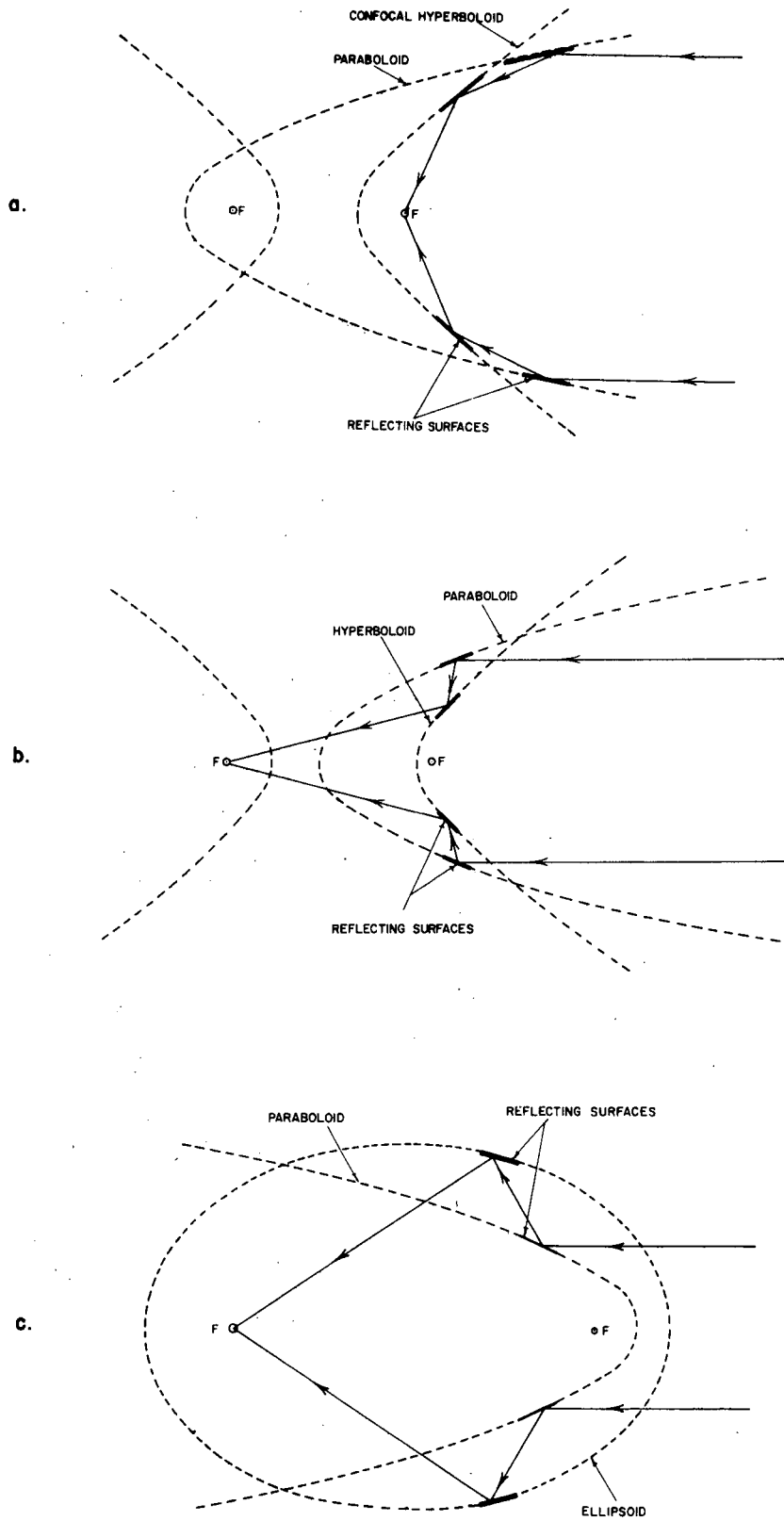


Figure 2-3. Three possible configurations for image-forming X-ray telescopes suggested by Wolter (1952a, b).

intersection, and the subsidiary requirement that the grazing angles at both surfaces be the same. The last requirement results in a maximum reflection efficiency at short wavelengths for a given aperture and focal length. The diameters of successive surfaces are chosen to avoid vignetting of axial rays and to allow the necessary mirror wall material. The wall material should be no thicker than required for polishing and to maintain tolerances so that the effective area may be maximized.

#### 2.1.4 Diffraction Effects

The diffraction pattern from a thin annular aperture is a series of concentric rings. The angular distance  $\theta_m \frac{0.38\lambda}{y_0}$  where  $\lambda$  is the wavelength and  $y_0$  the radius of the annulus. For the LOXT telescope  $\theta_m$  is on the order of 0.1 arc seconds at  $\lambda = 5000\text{\AA}$  and  $1.7 \times 10^{-4}$  arc seconds at  $\lambda = 10\text{\AA}$ . The X-ray diffraction effects clearly are negligible compared to the degradations which result from fabrication tolerances and surface scattering which has the important consequence that X-ray telescopes may be evaluated by means of geometrical optics.

#### 2.2 Parametric Studies

We have evaluated a large number of X-ray telescope designs, and have found simple empirical expressions for the principal optical properties of these telescopes. These results, which are given in detail in a paper reproduced here as Appendix A, allow one to approximately optimize a telescope design, although of course the actual final design was evaluated by ray tracing procedures.

The principal result is that the resolution of any X-ray telescope varies approximately as:

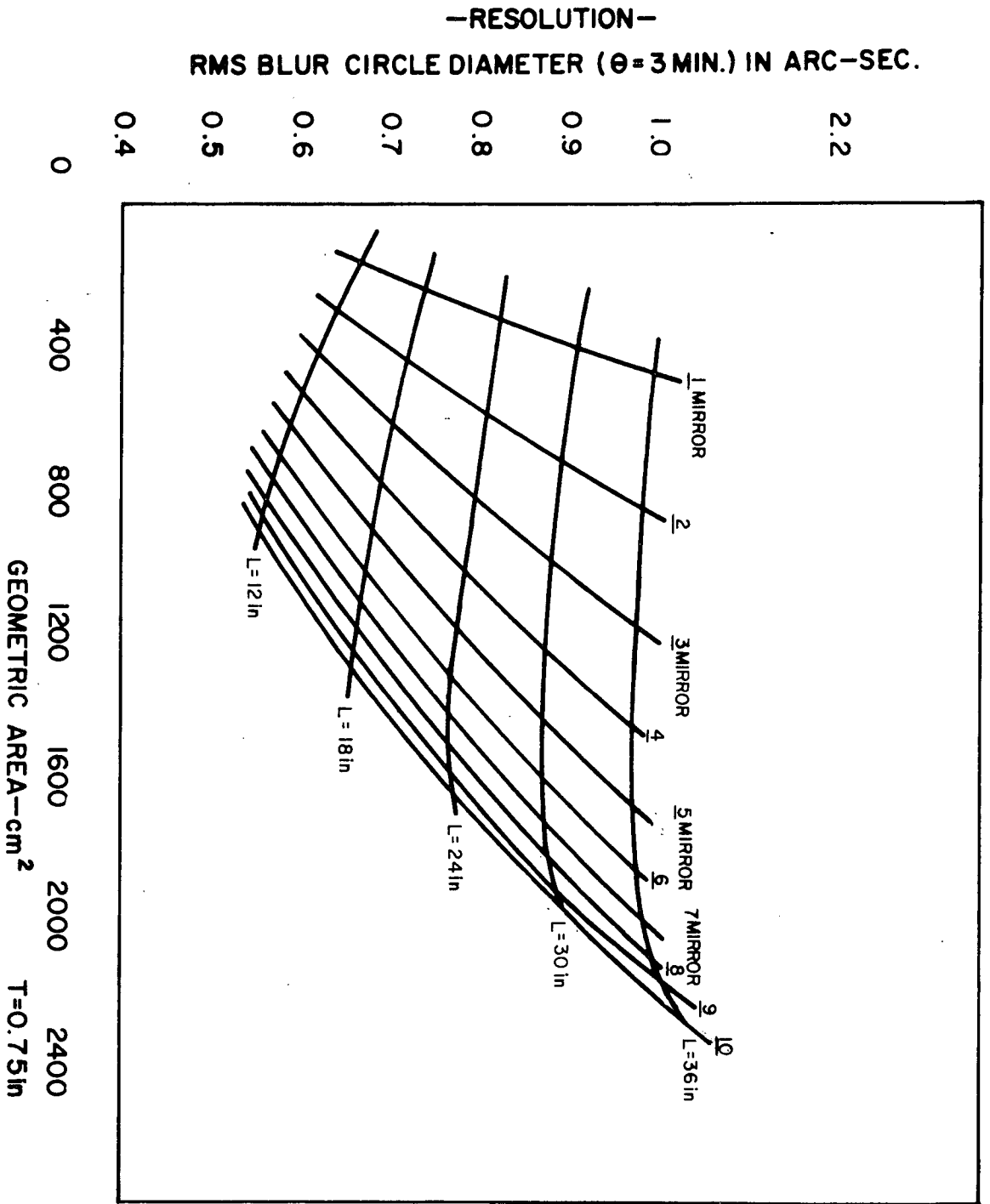
$$\left(\frac{K_1}{\alpha}\right) \left(\frac{L}{F}\right) \theta^2 + K_2 \alpha^2 \theta \quad (2.4.1)$$

where  $K_1, K_2$  are constants,  $\alpha$  is the grazing angle,  $L$  is the length of the Paraboloid,  $F$  is the focal length,  $\theta$  is the angle off axis, and we have assumed equal grazing angles at the Paraboloid and Hyperboloid in order to maximize the effective area for a given focal length and polished area. In most practical cases, the first term dominates over most of the field of view, and therefore, a single surface mirror requires a compromise between large area, which requires a large segment length, and good resolution, which requires a small segment length. This problem can be solved by nesting surfaces and thus achieving additional area without increasing the segment length. The geometric area and resolution at one angle for telescopes having one to ten surfaces are shown in Figure 2-4. The advantages of the many surface approach taken in the LOXT design are obvious.

The second feature of Formula 2.4.1 is that an optimum  $\alpha$  exists for a given area which is a slowly varying function of  $\theta$ . This optimum value is given in Figure 5 of Appendix A. The final LOXT mirror design is consistent with this optimum value and includes five surfaces to obtain additional area without an unacceptable segment length.

An examination of Figure 2-4 shows that the effective area for an additional surface decreases as the number of surfaces is increased, and that the gain per surface becomes negligible for more than about 7 mirror surfaces in systems of this approximate size. Our objective was to obtain an effective area of about  $1,000\text{cm}^2$  together with one arc second resolution, which requires a somewhat larger geometric area because of surface reflection losses. The resolution requirement sets an upper limit of about two feet for the mirror segment length, which is also consistent with mechanical support requirements. A mirror wall separation of .75 inches, which

**FIGURE 2-4 GEOMETRIC AREA AND ANGULAR RESOLUTION AS A FUNCTION OF THE LENGTH AND NUMBER OF MIRROR ELEMENTS**



is also consistent with mechanical requirements, then led to the choice of a 5 element mirror, as was originally proposed based upon experience with these designs but with insufficient study to assure a near-optical design.

The properties of mirror designs based upon different wall thickness were also studied. These effects are summarized in Figure 2-5, which shows the effective area as a function of mirror surface separation for mirror assemblies of 2 to 7 surfaces and the maximum allowable length of about two feet. These curves show that a 5 element mirror assembly of the LOXT size will lose about  $150 \text{ cm}^2$  of effective area for every 1/2 inch added to the wall thickness, which illustrates the importance of thin walls for these designs, but of course it is necessary to remain within the constraints imposed by mechanical tolerances.

The effective areas wavelength and resolution of the final mirror design are shown in Figure 2-6 and 2-7 respectively. The effective areas are based upon a nickel reflecting surface, which has been shown to be adequately smooth. The properties of other surface materials will be measured during the LOXT study program, and the final selection of surface material will affect these effective areas.

### 2.3 High Resolution Mirror Optical Tolerances

The tolerances for the mirror assembly can be divided into:

- a) Alignment tolerances between the individual mirrors of the nested set.
- b) Alignment tolerances between the elements of a single mirror; and
- c) Tolerances within an individual element (single hyperboloid or paraboloid).

We have developed programs for calculating the effects of any

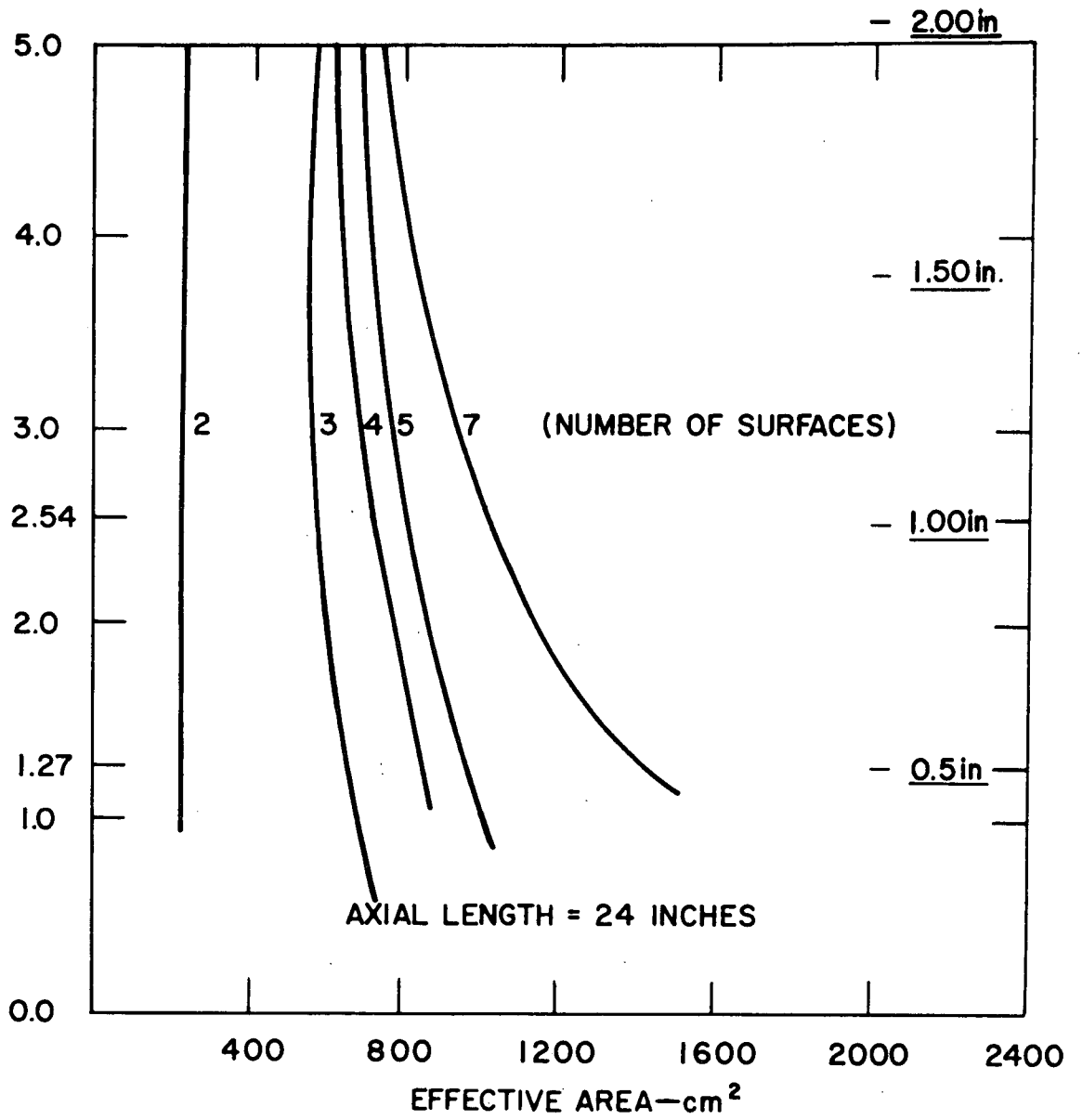


**FIG. 2-5 MIRROR SURFACE SEPARATION**

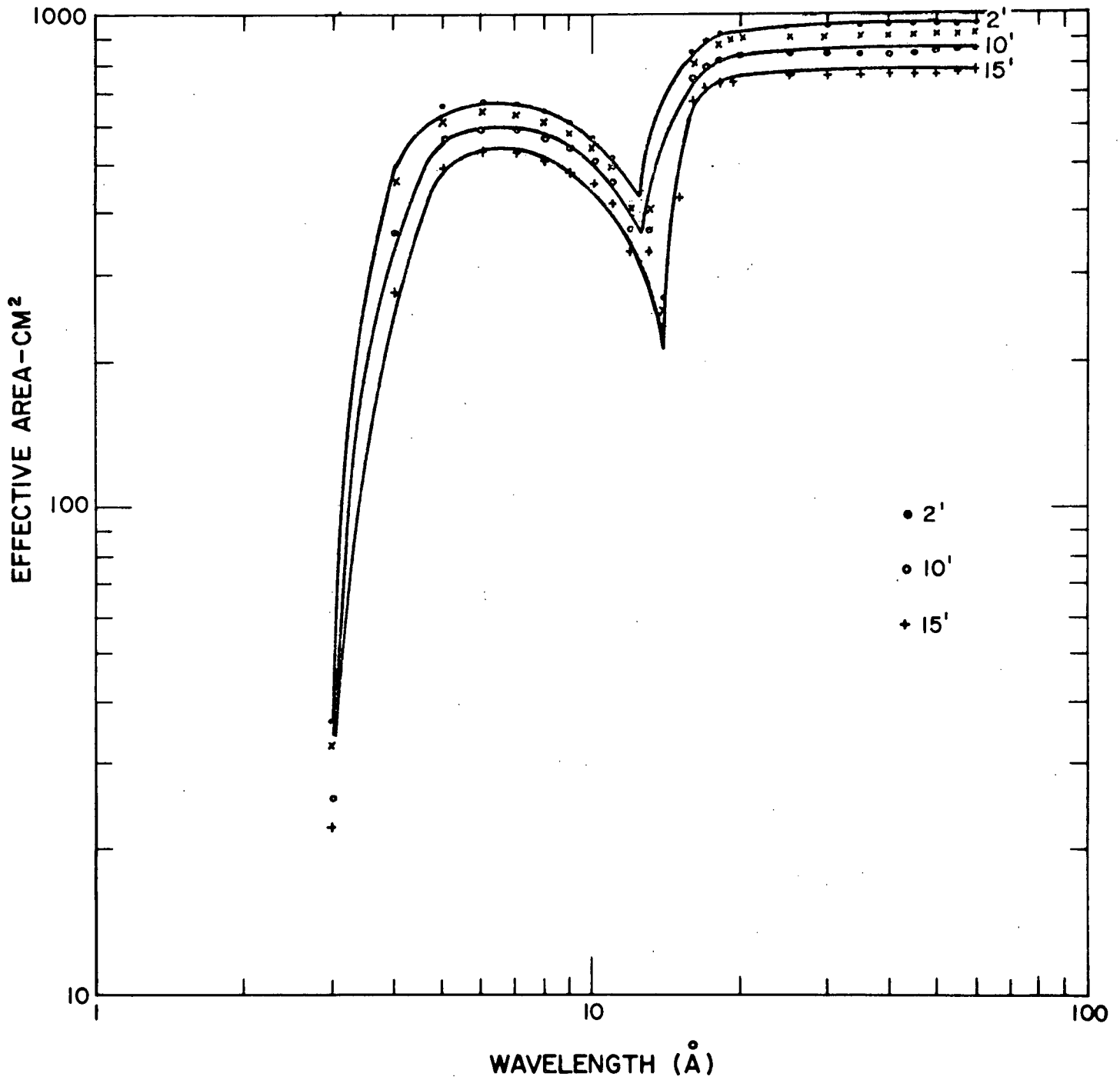


FIGURE 2-6 EFFECTIVE AREA OF THE HIGH RESOLUTION MIRROR AS A FUNCTION OF WAVELENGTH FOR VARIOUS INCIDENT ANGLES.

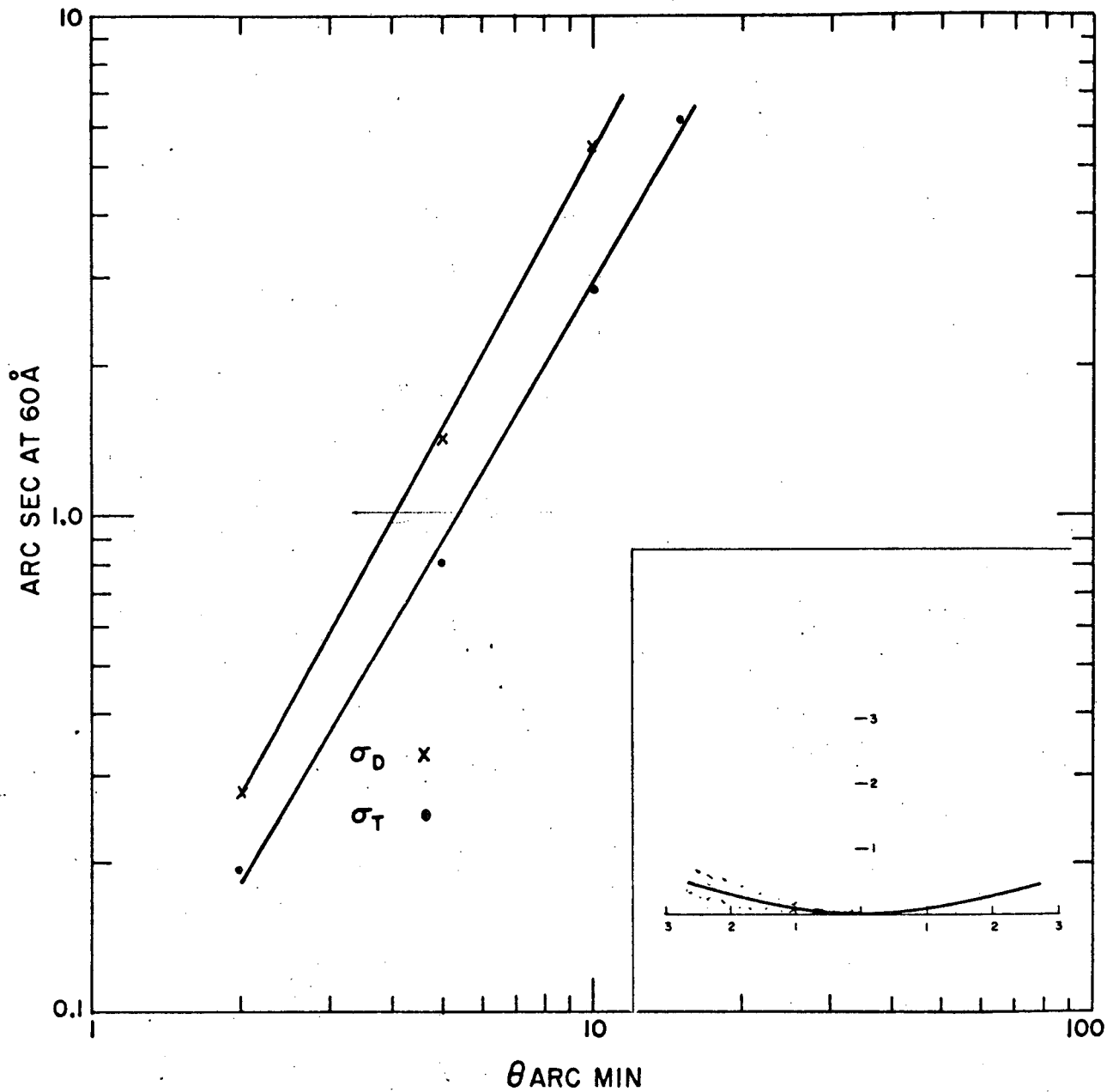


Figure 2-7. R.M.S. radius of image distribution as a function of incident angle for a flat focal plane and an optimally curved focal plane. The necessary curvature is shown in the insert of the illustration.

large scale deformations which result in locally smooth surfaces with, at most, a finite number of discontinuities. Although there are an infinite number of such possibilities, the results can be summarized by a few statements.

The alignment tolerances between different mirror segments or different mirrors in a nested set are comparable to the desired resolution in the focal plane. The principal, more difficult tolerances reduce to local slope tolerances; in this case, the axial slopes must be controlled to about one-half the desired resolution, while the transverse slope tolerances can be less stringent by a factor of the inverse of the grazing angle, or about fifty in the LOXT design. All of these tolerance statements can be applied to a best fit paraboloid or hyperboloid, since sufficient adjustment freedom has been left in the design of the mounting support. These requirements are discussed below in general terms. These statements, however, have been verified by extensive ray tracing calculations on a variety of mirrors and mirror deformations.

### 2.3.1 Mirror Assembly

These tolerances are determined by the requirement that the foci of the different mirrors coincide. The translation tolerances perpendicular to the axis, therefore, are just the desired resolution in the focal plane, or about 0.0005 inch for 1/2 arc-second resolution. The translational tolerance along the axis is the depth of field of the telescopes, or about  $\pm 0.004$  inches total, including optical bench and thermal expansion, as well as assembly tolerances for these mirrors. The angular alignment tolerances are not critical because of the focusing properties of the telescope. Errors of 10 arc-seconds correspond to mechanical tolerances of about 0.001 inch, whereas arc-minute errors would be acceptable in this parameter. All of the above tolerances correspond to good

mechanical precision, and are fairly routine in the optical industry.

### 2.3.2 Paraboloid-Hyperboloid Section Alignment Tolerances

These tolerances can be derived by considering displacements of the paraboloid only; displacements of the paraboloid and hyperboloid together have already been considered. We can consider a displacement error to modify the equations for the paraboloid by a quantity  $E(X, Y, Z)$  so that the equation for the paraboloid becomes:

$$Y^2 + Z^2 = d [2(x + F + 2ae) + d] + E(X, Y, Z)$$

where  $X$  is the symmetry axis. If we now trace a ray through this system we find that the approximate effect of the error term is to introduce an angular change of magnitude:

$$\Delta \theta \approx \frac{1}{2} \left[ \frac{rdE}{dx} + \tan \alpha \left( E + Y \frac{dE}{dY} + \frac{ZdE}{dZ} \right) \right]$$

where  $\alpha$  is the grazing angle. That portion of the change in angle which is common to all rays does not contribute to the loss of resolution since it can be compensated by realignment. Note that the effects of azimuthal errors are less than the axial errors by a factor of  $\tan \alpha$ . The effects of various misalignment errors can now be considered.

A relative axial translation by  $\delta$  is equivalent to the substitution

$$X \rightarrow X + \delta, \text{ or } E = 2 \delta d;$$

$$\text{and } \Delta \theta \approx \frac{2 \delta}{r} \left( \frac{d}{r} \right) \tan \alpha \approx \frac{2 \delta}{r} \tan^2 \alpha$$

Therefore, for a blur circle diameter of  $1/2$  arc-second we obtain  $\delta \approx 0.1$  inch, which is not difficult.

A relative translation perpendicular to the axis in the  $Y$  direction equivalent to

$$Y \rightarrow Y + \delta; E = 2 \delta Y + \delta^2;$$

and  $\Delta \theta \approx 4 \left( \frac{\delta}{r} \right) \tan \alpha$ ; for a blur circle diameter of  $1/2$  arc-second

we obtain  $\delta \approx 0.0005$  inch, which requires careful machining, but is fairly routine by optical standards.

A rotation of the paraboloid with respect to the hyperboloid is equivalent to rotating the paraboloid about its focus, which essentially only changes the definition of the axial ray, and then translating by the rotation angle times the distance to the paraboloid focus. Thus in practice, a rotation error can be compensated by a translation since this freedom of adjustment exists in the design. The tolerances necessary to adequately align the two segments of an individual telescope, therefore, are those of ordinary optical practice, which is largely the result of the grazing incidence optics.

### 2.3.3 Mirror Segment Tolerances

The above formula for the effects of error terms on the rays reflected from a paraboloid can be used to estimate the necessary large scale tolerances for its fabrication. The tolerances on the hyperboloid are similar to those on the paraboloid.

It is not necessary to apply the above tolerance conditions as a strict comparison between original design and the final product in some instances. For example, the final surface may be very nearly a paraboloid of slightly different focal length than the desired surface, and in this case, the deviation in its manufacture may be offset by a translation of the actual surface along the telescope axis. The tolerance criteria here are thus to be applied to a "best fit" surface, provided that the eventual "best fit" surface is adequate within the adjustment range of the support system, and does not result in an unacceptable change in the reflection angles.

Once a "best fit" surface is determined, the above formula may be used to determine the actual tolerances; in practice these tolerances

must be stated in terms of the measurement technique. The principal error term is seen to be errors in slope along the telescope axis, and these errors result in a displacement of the reflected ray by twice the value of the slope error. The azimuthal slope errors have smaller effects by a factor of the tangent of the grazing angle. All difficult large scale tolerances can be restated in terms of controlling the axial slope to less than the desired resolution, and the transverse slope to  $\cot \alpha$  times axial tolerance. The allowed tolerances on the displacement of a surface without slope errors are essentially the alignment tolerances, which are quite large by normal optical standard as a consequence of the grazing incidence configuration.

The mechanical tolerances are written in a way which reflects the methods of measurement and the necessary accuracy in the different dimensions. The following dimensions are specified:

- a. Average radius at each end =  $\overline{R}_a, \overline{R}_b, \Delta R = \overline{R}_a - \overline{R}_b$
- b. Maximum out of roundness =  $\max \left| R(\phi) - \overline{R} \right|$
- c. Maximum variation in  $\Delta R(\phi) = \max \left| \Delta R(\phi) - \overline{\Delta R} \right| = \max \left| R_a(\phi) - R_b(\phi) - \overline{\Delta R} \right|$
- d. Sagittal depth =  $\Delta S(x, \phi) =$  the deviation from a nominal curve running through the end points at which  $R_a(\phi)$  and  $R_b(\phi)$  are measured. In practice  $S(x)$  is measured by interferometric comparison of the mirror surface and a test plate, and the tolerances on this quantity are much smaller than the tolerance on the first three items above. Therefore, it is possible to measure the first three items only at the ends of the mirror segment, and then infer that the tolerances are met at other axial positions because of the tight tolerance in sagittal depth.

e. Axial and transverse slope errors.

We will discuss the effects of these tolerances on the performance of the paraboloid; the tolerances on the hyperboloid are similar.

1. The principal effect of changing the radius of each end by the same amount ( $\delta$ ) is to change the effective focal length of the parabola by  $(\delta / 2 \alpha)$  where  $\alpha$  is the grazing angle. An error of 0.001 inch in  $\delta$  would necessitate a translation of about 0.035 inch for the smallest parabola being considered here, which would also introduce a negligible addition to the blur circle ( $\phi \sim 0.01$  arc-second). The mechanical support structure design allows these translations.

- 1a. The principal effect of changing the radius at each end by opposite amounts

$$(r_a \rightarrow r_a - \frac{\delta}{2}; r_b \rightarrow r_b + \frac{\delta}{2})$$

is also to change the focal length of the parabola by approximately  $\frac{F \delta}{L \tan \alpha}$ .

The surface can then be fit with a parabola that differs from the actual surface by less than  $(\frac{L \tan \alpha}{4r}) \delta = 0.004 \delta$  in this case. The slope error between the actual and best-fit surface is less than  $(\frac{\delta}{r}) \tan \alpha$ .

2. The effects of a roundness error depend upon the errors introduced in the azimuthal slope. For the simplest case of elliptical deformation the effect is to introduce the substitution  $Y^2 \rightarrow Y^2 (1 + \epsilon)$ ;  $Z^2 \rightarrow Z^2 (1 - \epsilon)$  in the equations for the parabola, which results in a maximum angular change of about  $3 \epsilon$  than  $\alpha$ . Thus, for the mirrors considered here, the total out of roundness must be less than 0.0005 inch to obtain a blur circle diameter contribution of less than one-half arc-second.

3. The variation in  $\Delta R(\phi)$  results in a direct contribution to the blur circle by an angle equal to  $2\Delta R(\phi)/L$ , where  $L$  is the length of the telescope. In the present mirrors, a one arc-second diameter blur circle thus corresponds to  $\Delta R \approx 25 \cdot 10^{-6}$  inches, or about one wavelength of visible light. This tolerance, then, requires careful measurement by reasonably conventional optical techniques. It should be noted that this tolerance is applied to the "best-fit" surface rather than to the nominal design surface.
4. The maximum variation in  $\Delta S(X, \phi)$  has been overstated in an attempt to control slope errors. The tolerance is 5 micro inches, or about  $1/4$  wavelength of visible light, which corresponds to a slope error of  $1/2$  arc-second over a length of about 2 inches. This essentially determines the minimum allowable axial length in a polishing procedure to avoid introducing slope errors which are unacceptably large and yet do not violate the surface contour requirements.
5. Axial slope requirement. An axial slope error of  $\theta$  causes a ray error of  $2\theta$ . The tolerances for the LOXT parabolas thus must be of order  $\frac{1}{3}$  arc second over most of the surface in order to expect 1 arc second resolution after two reflections (assuming errors adding in quadrature).
- 5a. The transverse slope errors can be larger than the axial slope errors by a factor of about 5.0, and in fact, the actual tolerances consistent with normal fabrication techniques are only larger by a factor of about 15, and this tolerance was imposed to avoid an unnecessary loss of resolution in this tolerance.

#### 2.3.4 Micro-surface Requirements

The remaining effects which determine resolution are the micro-surface effects. These can be divided into the truly microscopic domain which refers to surface finish, and the intermediate scale range which is defined by our measurement capability. For example, if the optical measurement technique can detect contour changes of only  $500\text{\AA}$  or greater, and if a slope tolerance of  $2 \times 10^{-6}$  has been imposed, then the polishing procedure axial length times  $2 \times 10^{-6}$  must exceed  $500\text{\AA}$  (or be greater than about 2.5 cm) in order to be certain of not introducing local and unmeasurable slope errors. This concept has been used in specifying the acceptable LOXT mirror polishing procedures. The truly microscopic surface requirements can be measured by multiple pass interferometry and can be achieved, at least in small test samples; these results are discussed in Section 4.

### 3.0 MECHANICAL DESIGN CONSIDERATIONS

In addition to the High Resolution Mirror design parameters presented in previous sections of this report, there are a number of additional considerations that influenced the design of the mirror assembly. In summary these are the launch and orbital environments to be encountered and the use of fused silica mirrors in the reference design. The fused silica mirrors influenced the design in several ways: (a) tensile stresses in the glass had to be kept low, (b) the method of mounting the glass to the supporting structure had to avoid stress risers in the glass, and (c) structural materials had to be selected for thermal expansion compatibility with the mirrors.

#### 3.1 Fused Silica Mirrors

The use of fused silica for the mirrors in the reference design required the consideration of several important factors. First, this material has a thermal expansion coefficient near  $0.31 \times 10^{-6}$  in/in-<sup>o</sup>F, and analyses quickly showed that for the mirrors to retain one arc-second alignment and be distortion free in the thermal environment, either the structural materials used in the assembly required a close thermal expansion match to the fused silica, or a high degree of thermal control was required. The design approach was to match the thermal expansion coefficients as close as practical, thereby relaxing the thermal control requirements which considerably limited the selection of structural material. The second consideration is that fused silica is a fragile material as compared to metals. It is relatively weak in tension, thus the generally accepted 1000 psi design allowable tensile stress was used as a limiting parameter in this design study. In addition, fused silica is very susceptible to cracking around any form of stress riser, which required careful consideration as to the method of mounting the mirrors to their supporting structure. As discussed

in detail later in this report, the selected approach was to bond circumferentially, end-flanges on the outside surface of the mirrors near their ends. This approach avoided point loads within the mirrors and also allows a useful freedom in the final assembly of the mirrors.

### 3.2 Launch Environment

It is essential that this mirror assembly retain alignment after exposure to the launch environment. This factor required careful consideration of the loads imposed on the various parts of the mirror assembly by the launch environment, and also required that all parts have positive retention in order for them to hold their aligned position. The launch environment used in this design study was taken from the HEAO Experiment Developer's Handbook. Since the LOXT Optical Bench has not been designed, no specific information was available regarding its dynamic characteristics, which was a cause for concern at the outset of the design study.

It was evident from work performed early in the study that a very rigid mirror assembly was required in order to retain mirror distortions within the one arc second resolution requirement under the gravity load present during optical testing on the ground. Thus, it was projected that the resonant frequencies within the mirror assembly would not fall in the predominant regions of the spacecraft vibration spectrum. This projection offered the possibility that the mirror assembly and the optical bench could be hardmounted to the spacecraft, at least at the mirror end. If this proved to be the case, it would eliminate the troublesome requirement of providing softmounts, at least as far as the high resolution mirror was concerned, although it was recognized that the optical bench would require a provision in its mounting to allow for "hot-

dogging" flexure of the spacecraft. Thus, the design approach was to analyze the feasibility of a hardmounted system using typical transmissibility factors and in parallel perform a limited amount of analysis of a typical soft-mounted optical bench in order to estimate the dynamic environment to be seen by the mirror assembly in a soft-mounted system. The analysis, discussed in detail in later sections of this report, showed the hard-mounted approach to be feasible. The mirror assembly was then analyzed with respect to the soft-mounted environment (which showed that it was structurally adequate for use in a soft-mounted system) in case that at a later time it was determined that another LOXT component, such as the high efficiency mirror, required a soft-mounted optical bench.

### 3.3 Thermal Environment

The requirement that the mirror assembly hold alignment and that the mirror remain distortion free in orbit was also a high order consideration in this design study. The thermal behavior of the spacecraft was an important factor, since the mirror assembly could not reasonably be thermally analyzed as an isolated system. Radiative heat transfer, with respect to the spacecraft, heat loss to space, and the means of structural attachment from a thermal viewpoint, all required study in order to achieve a thermally adequate mirror assembly design.

### 3.4 Structural Materials

Since the mirror assembly is comprised of 5 concentric paraboloids and 5 concentric hyperboloids, a structure must hold these confocally aligned mirror elements in alignment after exposure to the launch environment, after transition from the one g ground environment to the zero g orbital condition, and it must also hold the mirrors distortion free in the thermal environment to be seen in orbit. The primary driver in the selection of structural materials

was obtaining the close thermal expansion match to fused silica in order to obtain distortion free mirrors in the orbital environment. One obvious approach was to make the entire mirror assembly of one material, which was the approach adopted for the alternate design. An all fused silica reference design was briefly examined, but there were indications that this approach required a considerable extension in the state of the art in producing an X-ray telescope of the size required, with high attendant risk, and therefore this approach was not pursued. The remaining structural materials having a thermal expansion coefficient near that of fused silica are Invar and graphite epoxy composite which are discussed below.

Invar is an alloy of iron, nickel, and minor percentages of other elements. Its modulus of elasticity is approximately  $21 \times 10^{-6}$  psi, about midway between aluminum and steel, and its ultimate strength (68000 psi) is comparable to steel. The thermal properties of Invar are variable with the percentage of alloying elements and our investigation indicated that Unispan LR-35, a trade name of Universal Cyclops, was best suited for this application. It is a stable alloy (with proper heat treatment) and has a thermal expansion coefficient between 0.25 and 0.35 in/in-<sup>o</sup>F. The thermal expansion properties of the material are a function of the heat treatment and, as discussed later, Universal Cyclops is performing tests to determine if a heat treatment can be specified which will provide a thermal expansion coefficient closer to that of fused silica than the outer limits of the range given above. In summary, Unispan LR-35 was found to be well suited to this application.

Graphite epoxy composite material has been under development for several years, and although it has not come into common usage as rapidly as predicted, it is now appearing as structural material in specialized applications. Two features of this material were at-

tractive as a structural material for the high resolution mirror reference design; first, its high strength to weight ratio, and second, it offers the possibility of tailoring its thermal expansion coefficient. This second feature arises from the fact that the graphite fibers have a negative expansion coefficient and the epoxy has a high positive expansion coefficient, thus a composite of the two has a compromising effect which can be tailored by varying the amounts of the two constituents. Nearly all the strength is provided by the graphite fibers; thus, various layups are used with layers of fibers running in prescribed directions depending upon how the material is to be used. The layup obviously affects the thermal expansion properties of the material, but there is considerable test data which indicates that a high strength composite having a thermal expansion coefficient near that of fused silica can be made. This material, in structural shapes, is not available off the shelf and fabrication costs are high.

In summary, Invar and graphite epoxy were considered to be suitable structural materials for the high resolution mirror reference design. The approach taken was to use graphite epoxy composite only if it afforded some distinct advantage over Invar.

### 3.5 Ground Rules for the High Resolution Mirror Design Study

The following presents the baseline and ground rules for conducting the preliminary design of the LOXT High Resolution Mirror in order to provide direction to the design study as to design requirements, materials to be considered, analyses to be performed, and the approach to be taken in assuring that this mirror design is compatible with the LOXT/HEAO-C.

#### 3.5.1 General

The HEAO A/B spacecraft will be used as the baseline for the spacecraft induced environment seen by the LOXT and for the spacecraft configuration into which the LOXT must fit.

Mechanical environment criteria for the mirror assembly will be developed from analysis of the dynamics of the overall LOXT configuration and its mounting to the spacecraft.

Compatibility between the deformation and stress limitations of the mirrors and a practical overall LOXT assembly will be analytically verified.

Thermal design criteria for the mirror assembly will be derived from analysis of the overall LOXT thermal system, including a thermal collimator on the front of the LOXT. Compatibility between the thermal limitations imposed by the mirror assembly and a practical overall LOXT thermal design will be analytically verified. The scaling of these effects with temperature and temperature gradients must be determined either analytically or numerically

### 3.5.2 Mirror Assembly

3.5.2.1 Material Considerations - The table presented below lists the mirror materials and the structural materials that will be considered during the study. Asterisks (\*) indicate those to be considered for the reference design. Further study and sample

TABLE

Mirror	Flanges and Attaching Provisions	Housing	Optical Bench
Fused Silica* Graphite Epoxy Composites with Fused Silica Substrate	Fused Silica* Invar* Composites	Invar* Composites*	Invar* Composites*
Beryllium	Beryllium	Beryllium	Beryllium Titanium

scattering tests may show that Beryllium is not a viable candidate for this application, in which case Invar and graphite epoxy composites become the candidates for the reference and the alternate design structural materials for the housing and optical bench.

3.5.2.2 Temperature Considerations -

- a. The mirror assembly design must be satisfactory with respect to the temperature regime, rates of change of temperature, and the resulting axial and radial temperature gradients. The scaling laws of these effects must be determined so that the allowable environment can be stated.
- b. Fused silica/flange mismatch.
- c. Non-isotropic thermal characteristics of composites, if used.
- d. Fused silica substrate/mirror backing material mismatch as applicable to the alternate mirror configuration.
- e. Thermal deformations and resultant stresses of the mirrors must be analyzed and satisfactory levels achieved with respect to both stress levels and defocusing. Thermal deformations must be expressed in a manner amenable to interpretation for ray tracing studies.

3.5.2.3 Mechanical Considerations -

- a. Must be able to optically test mirror elements separately and horizontally in a lg environment.
- b. Mirror mounting arrangements must allow for:
  1. Axial translation of up to 1/2" for all (or all but one) mirror elements.

2. Transverse translation of each mirror element (to a few tenths of a mil) or use of wedge-type shims.
- c. Must be able to take the mirror assembly apart and re-assemble it in a practical manner. No requirement for realignment testing shall be a design goal.
- d. Mirrors shall be decoupled from external distortions and loads within practical design approaches.
- e. Non-isotropic strength characteristics of composites, if used.
- f. Satisfactory limits of deformation and stress levels must be achieved for:
  1. Polishing loads
  2. 1g environment during ground operations
  3. Launch
  4. From spacecraft loads in orbit.
- g. Survivability during the launch environment will be analytically verified.
- h. Mirror assembly must not be self-contaminating.
- i. A means shall be provided to easily cap off the mirror assembly when not in use to minimize external contamination and accidental damage.

#### 4.0 SCATTERING TEST SAMPLE PROGRAM

The modification of the X-ray intensity distribution introduced by a reflection was measured for a number of test surfaces. These were either flats or segments of cylinders having radii typical of the LOXT mirrors and included variations upon conventional polishing procedures, as well as some of the more recently developed techniques. The best results were obtained with fused silica and metalized fused silica polished with the submerged process. These samples essentially reproduced the incident beam which had an effective full width of about 5 arc seconds. The conventionally polished electrodeless nickel on a Be substrate approached this performance:

The technique of the measurements is described in Section 4.1, and the actual results are discussed in Section 4.2. The X-ray scattering results correlate well with other indicators of surface roughness, such as visible light scattering or the appearance of multiple pass interferograms, but the effects are much more pronounced.

##### 4.1 Technique

The X-rays are produced by electron bombardment of an aluminum target, which generated a spectrum consisting of the characteristic aluminum  $K\alpha$  line at  $8.3 \text{ \AA}$  superimposed on a continuous bremsstrahlung spectrum of reduced intensity with a low energy cut-off at approximately  $4 \text{ \AA}$ . These X-rays were collected and focused by a grazing incidence telescope having a focal length of 76 in. which was situated 720 in. from the source. A mask was placed over the telescope which allowed radiation to reach the focus only if it had been reflected from either one of two small regions on either side of the horizontal diameter of the telescope.

A schematic diagram of the experimental set up is shown in Figure 4-1. If the telescope were perfect, the resulting image in the focal plane would be a horizontal line slightly broadened (vertically) by diffraction from the finite slit.

The telescope is not perfect, but the imperfections are such that a given part of its surface results primarily in radial rather than azimuthal errors, and, since the telescope is apertured by a horizontal slit, the primary effect of the telescope imperfection is to increase the horizontal extent of the line image with very little effect upon its vertical width. The image distribution can then be determined by scanning with a counter and slit in the focal plane. The resulting vertical beam width was measured to be about 5 arc seconds, full width, half maximum (FWHM), which is consistent with that expected to result from the sum of a number of sources discussed below.

The incident X-ray beam, which has a narrow vertical height, was then reflected in the vertical direction by a test sample surface which was oriented at a small angle to the horizontal. The scattering introduced by the test samples primarily increased the vertical width of the X-ray beam in the focal plane; this reflected image distribution was also measured by scanning with a horizontal slit apertured counter in the (slightly different) focal plane. The scattering due to the sample can thus be determined.

Two scattering sample geometries were used in the study, flats and segments of cylinders with 15 inch radii. The beam reflected from a perfect flat should have substantially the same vertical structure as the incident beam, whereas additional aberrations of the cylinder geometry result in an increase in the effective beam width to about 7 arc seconds. These additional terms are discussed below.

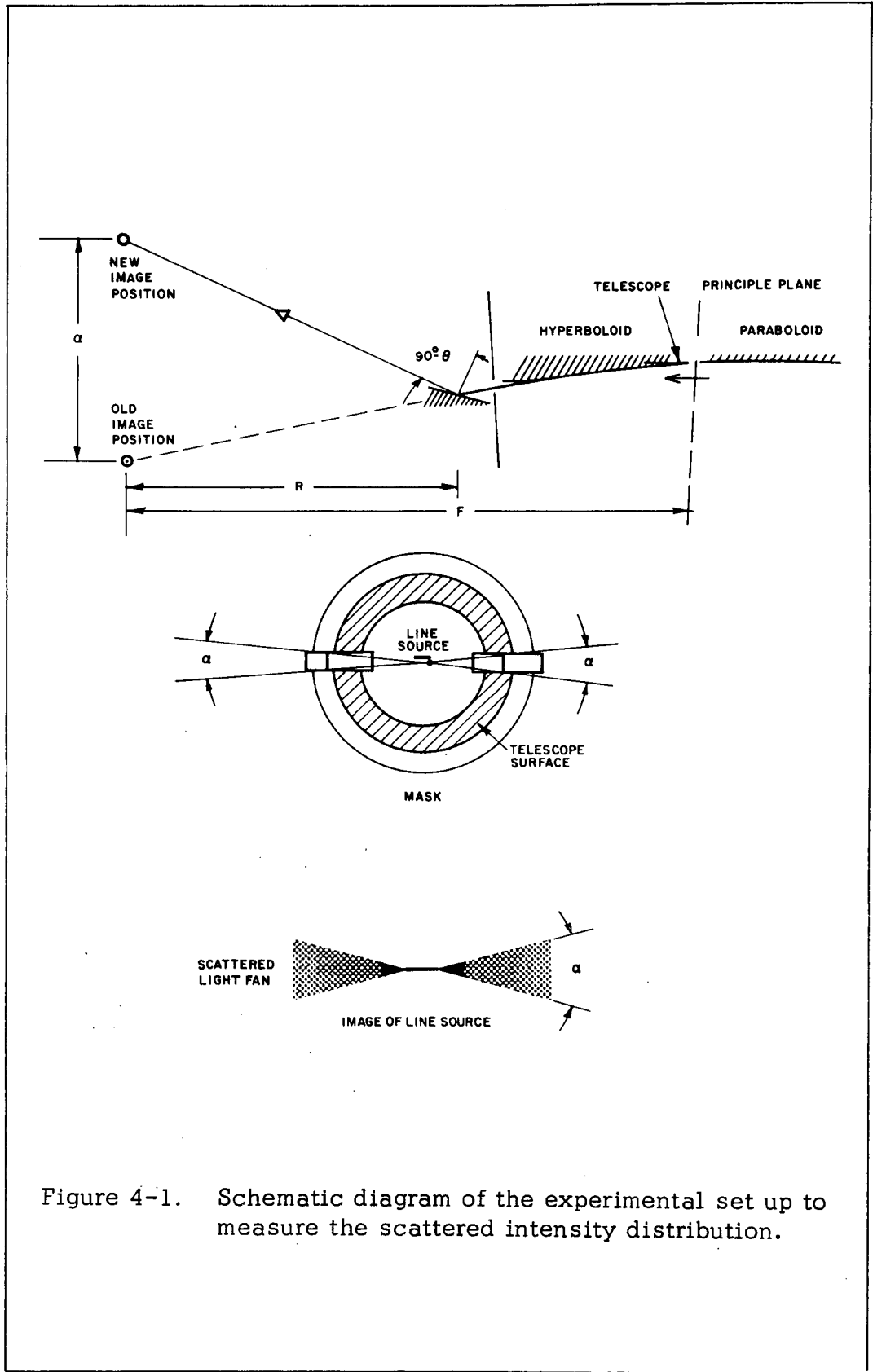


Figure 4-1. Schematic diagram of the experimental set up to measure the scattered intensity distribution.

Certain precautions were taken during the observation to achieve consistency. These included constant monitoring of the source by a counter which was placed behind another part of the telescope and which had a similar window and spectral acceptance (pulse height window) as the counter used to scan the focal plane. The source was operated at a constant voltage and current throughout the tests and the source anode was cleaned frequently so that stable source intensity and spectra were obtained. The mounting enabled interchange of samples without realignment so that geometrical effects are essentially constant for all tests at a given angle. The results obtained for certain samples are equivalent to those obtained from the same samples a year ago with a somewhat different apparatus. In a few cases, samples were removed from the chamber and then re-measured; these results were also consistent to within the expected measurement accuracy.

The consequence of any misalignment is to increase the apparent width of the scattered beam, and consequently, the measurements represent a conservative estimate of the performance of the telescope. Some of these effects are considered here.

#### 4. 1. 1 Incident Beam Width Effects

4. 1. 1. 1 Source Height - The effective source height is about 10 mils at a distance of 60 feet, or about three arc seconds.

4. 1. 1. 2 Telescope Imperfections - The telescope results in a beam spread of order 5 - 8 arc minutes in the radial direction. The spread in the direction of measurement, however, is much less than this, because of the narrow aperture which is aligned with the source and detector slit. If the alignment were perfect, the effective beam width from this source would be one arc second.

4. 1. 1. 3 Detector Slit Width - The slit width used in these measurements was one mil, or 2.5 arc seconds.

4. 1. 1. 4 Source/Detector Slit Misalignment - The source length is approximately 1 arc minute. A misalignment of  $1^{\circ}$ , which is comparable to the accuracy of determining the source orientation, thus results in a one arc second beam width.

4. 1. 1. 5 Telescope Aperture Misalignment - This effect broadens the beam by about 1 arc second for every 6 mils vertical error in slit position. The actual error is estimated to be less than 15 mils, or about 2.5 arc seconds.

4. 1. 1. 6 Diffraction Effects - The characteristic angle ( $\lambda/W$ ) for  $8.34 \text{ \AA}$  radiation and a 10 mil slit is 0.7 arc seconds.

The result of adding these sources of beam width as gaussian errors is about 5 arc seconds, which was actually observed in the measurements of the straight-through beam.

#### 4. 1. 2 Geometrical Effects of Optical Flat Misorientation

In this case the only effect is to change the reflection angle by an insignificant amount.

#### 4. 1. 3 Geometrical Effects of Cylindrical Test Surface Misalignment

4. 1. 3. 1 Effects of Slit Length and Transverse Displacements - The test sample curvature introduces an error due to the slit width and transverse displacement. The slit width is 0.15 inches, which is large compared to the displacement error of less than 0.01 inches. The slit width results in a focal plane spread of 0.5 arc seconds (distance =  $\frac{1}{2} (L/2)^2 / R$ ) where L is the length of the slip and R is the radius of the sample.

4. 1. 3. 2 Effect of Transverse Slope on Beam Width - If the reflection angle is  $\theta$ , the slit length is L, and the radius of the sample is R, then the effect of the transverse slope on the displacement perpendicular to the slit in the focal plane is approximately

$$2[(L/2R)^2 \sin \theta - (\frac{L}{2F})(\frac{L}{2R})] \approx 4 \text{ arc seconds.}$$

4. 1. 3. 3 Effect of Sample Rotation - If the rotation angle is  $\phi$ , a displacement perpendicular to the slit in the focal plane of  $\frac{L}{R} \sin \phi$  is produced. The exact value of  $\sin \phi$  is not known, but it is less than  $2 \times 10^{-3}$ , and a spread of 4 arc seconds would result from this effect. The expected value is less than one-third of this amount.

#### 4. 1. 4 Summary

The curvature effects, when added as gaussian errors, correspond to a source broadening between 4 and 6 arc seconds, depending upon the exact value of the sample rotation error. This results in an effective incident beam width of about 7 arc seconds when folded with the beam width factors discussed in Section 4. 1. 1.

## 4. 2 Results

The results of these measurements are summarized in Table 4. 1. This table includes a line number for identification purposes, a description of the reflecting surface, a code (C or F) which describes the sample geometry (cylinder or flat), the reflection angle in arc minutes, the total reflection efficiency measured with a wide slit, the measured width (FWHM) of the reflection radiation, and the width (FWHM) corrected for the incident beam width. The width measurements are accurate to about one arc second, and smaller differences are not significant. Some of the reflection curves have a narrow center peak, but wide low-level wings. In this case the FWHM does not describe the reflected distribution adequately, so the fractions of incident radiations which fall in a slit width of 5, 10 and 20 arc seconds have also been included. These values are not corrected for the incident beam distribution which is given in Line 1. Also included are some less complete

Line	Surface	Cylinder/Flat	Reflects Angle (Arc Minutes)	Total Efficiency	FWHM (Arc Seconds)	FWHM, Corrected Arc Seconds	Relative Efficiency			Absolute Efficiency		
							5	10	20	5	10	20
1	None (Incident Beam)	-	-	-	5	-	.45	.64	.84	.45	.64	.84
2	Fused Silica - Sub- merged Process (#3)	F	22	.70	6	3.3	.42	.57	.75	.29	.40	.59
3			55		6	3.3						
4	Evaporated Ni on Fused Si Submerged Process (#1, 2)	F	22	.93	7.5	5.6	.46	.59	.72	.43	.55	.67
5			72		7.0	4.9						
6	Fused Silica Barnsite Polished	F	23		6.0	3.3						
7			55		8.5	6.9						
8	Evaporated Ni on Fused Silica, Barnsite Polished	F	21	.60	10	8.7	.31	.47	.61	.19	.28	.37
9	Cervit, Submerged Process	F	55		12	10.9						
10	Cervit, Barnsite Polished	F	55		9	7.5						
11	Electrodeless Ni on Be (Speedring)	F	55		10	8.7						
12	Be., MgO Polished	F	23		13.5	12.5						
13			55		16							
14	Ni Coated Be Conventional Polish	C	22	.91	10.5	7.8	.36	.51	.66	.33	.46	.60
15			72		.44	11						
16	Ion Polished Fused Silica	C	22	.73	12	9.7	.10	.39	.64	.07	.28	.47
17			66		.16	15						
18	Ion Polished Evap. Glass on Be	C	22	.63	12.5	10.3	.29	.42	.53	.18	.26	.33
19	Conventionally Polished Evap. Glass on Be	C	22	.49	10	7.1	.31	.51	.61	.15	.25	.30
20	Ion Polished Electro- less Nickel on Be	C	22	.54	10	7.1	.24	.36	.60	.13	.19	.32
21	Selective Deposition of Dielectric on Polished Be	C	22	.57	13	10.9	.24	.30	.46	.14	.17	.26

Table 4-1 - Test Sample Results

TABLE 4. 1 NOTES

1. 
$$\text{FWHM (Corrected)} = \sqrt{\text{FWHM (Measured)}^2 - (\text{FWHM})^2 \text{ Incident}}$$

FWHM (incident) = 5 arc seconds (Flat)  
= 7 arc seconds (Cylinders)
  
2. Relative Efficiency (5, 10, and 20)  
Fraction of transmitted energy contained in a slit of width  
5, 10, or 20 arc seconds respectively.
  
3. Absolute Efficiency  
Fraction of incident energy contained in a slit of width  
5, 10, or 20 arc seconds respectively.

data from earlier tests (lines 3, 6, 7, 9, 10, 11, 12 and 13), which are related either to these measurements or to materials not included in the current program.

The measurements were made at about  $1/3^\circ$  and  $1^\circ$ ; the smaller angle was chosen to obtain reasonable reflection efficiency from the glass substrates, whereas the larger angle is typical of the actual LOXT mirrors.

The theoretical reflection efficiencies for  $8.3 \text{ \AA}$  X-rays and fused silica at  $22'$ , and nickel at  $22'$  and  $72'$  are approximately 0.85, 0.9, and 0.6 respectively. The results obtained for individual surfaces are discussed below.

#### 4.2.1 Fused Silica, Submerged Process

This technique of polishing fused silica consists of recirculating the polishing compound so that finer abrasive particles are obtained, and then completing the polishing procedure without abrasives. This technique is generally believed to result in the smoothest possible surface, and we have obtained the narrowest X-ray reflection curves with this type of surface. The reflected beam at small angles (lines 2 and 3 of Table 4-1) essentially reproduces the incident beam. The calculated contribution of the sample to the measured reflected efficiency of fused silica, however, does not extend to sufficiently high energies, and a fused silica mirror must be coated to be suitable for the LOXT program.

#### 4.2.2 Fused Silica, Barnsite Polishing

This polishing technique is more conventional and results in a slightly rougher surface than the submerged process as measured by visible light scatter and multiple pass interferometry techniques. The observed width of the reflected X-ray beam was the same as for the submerged process at  $22'$ , but was somewhat wider at  $55'$  (lines 6 and 7 compared to lines 2 and 3). The evaporated nickel

on the substrate, however, performed substantially poorer than the surface evaporated onto a submerged process substrate.

#### 4.2.3 Fused Silica, Ion Polishing

Two fused silica cylinders were optically polished, coated with aluminum, and measured for visible light scatter. The results (0.03 %) are comparable to results previously obtained with the best available flats (0.027%). This finding is extremely important, as it indicates that surface quality comparable to that of good quality flats can be obtained in the curved geometry of the LOXT high resolution telescope. The slight difference could easily be an instrumental effect of the different surface geometries. These surfaces were then stripped of aluminum, ion polished, re-coated and remeasured; the scattered light increased to 0.06% indicating some degradation of the surface. Multiple pass interferograms of the surfaces taken both before and after ion polishing are quite sharp, and show surface roughness less than about  $50 \text{ \AA}$ , the actual value being instrument limited. These surfaces, however, resulted in relatively poor X-ray performance (lines 16 and 17). In general, none of the ion polished surfaces performed as well in X-ray as more conventionally polished surfaces of the same material.

#### 4.2.4 Evaporated Nickel Surfaces

These surfaces were prepared by first evaporating  $200 \text{ \AA}$  of chromium and then  $800 \text{ \AA}$  of nickel; the substrates were heated to  $300^{\circ}\text{C}$  during this process. The evaporations onto the submerged and barnsite polished fused silica substrates were performed at the same time in the same apparatus, and should be equivalent. The importance of the substrate can be demonstrated by comparing lines 4 and 8; the submerged process resulted in a significantly higher (0.93 vs 0.6) total reflection efficiency and also in a narrower reflected intensity distribution. The efficiencies observed

for the nickel evaporated upon fused silica (lines 4 and 5) are approximately theoretical, and the reflected beam again essentially reproduces the incident beam. This fact proves that a properly evaporated coating of nickel on a properly polished substrate will achieve essentially theoretical X-ray mirror performance.

#### 4.2.5 Electrodeless Nickel on Be, Conventional Polish

These samples were prepared by Kanigen coating optically ground Be substrates and then carefully polishing the Kanigen by conventional techniques. The results (lines 14 and 15) are almost equivalent to those obtained with the evaporated nickel (lines 4 and 5) surfaces. The central peak width contribution is about 8 arc seconds width vs 5 for the evaporated nickel surfaces, and the measured total reflection efficiency at  $1^\circ$  is about 15% less than that obtained with the evaporated nickel surfaces. This apparent decrease in efficiency is partly, and perhaps entirely, due to wide angle scattering beyond the acceptance of the measurement apparatus. This view is supported partly by wider angle data not presented here, and partly by the fact that the total reflection efficiency for the directly polished nickel should actually be higher than for evaporated nickel, because evaporated coating densities typically are slightly lower than bulk density. A conventionally polished nickel telescope thus may have a slightly larger image flaring from bright objects or portions of an extended source than that obtained with an evaporated nickel surface. The surface obtained here, however, is clearly superior to that of the S-054 mirrors which were polished by a similar technique, and must at least be considered as a very suitable alternate design surface.

#### 4.2.6 Electrodeless Nickel on Be, Speedring Process

The Speedring Corporation proprietary process for polishing electrodeless nickel results in low visible light scattering, although some

evidence exists for residual structure with a horizontal scale of a few microns. The flat prepared by this process resulted in a sample scattering width of 8.7 arc seconds (Line 1), compared to 5 arc seconds for the evaporated nickel surface (Line 5) and 8.4 arc seconds for the conventionally polished electrodeless nickel (Line 15). The total reflection efficiency from this flat was not measured, but the AS&E solar rocket Kanigen coated X-ray telescope was repolished recently by this technique and achieved the theoretical reflection efficiency. The process is certainly an improvement over that used in the S-054 mirrors, but is not necessarily superior to other conventional techniques for polishing electrodeless nickel X-ray telescopes.

#### 4.2.7 Ion Polished Electrodeless Nickel on Be

This process (Line 20) resulted in a poorer total efficiency and somewhat poorer angular distribution than the conventionally polished electrodeless nickel (Line 14). The visible light scattering was a factor of about 5 greater than for the conventionally polished nickel samples. The visible light scattering from the samples varied from 0.04 to 0.15 after conventional polishing, and from 0.28 to 0.45% after ion polishing. These values must be increased by about 30% for comparisons with the aluminized fused silica results because of difference in reflectivity. The multipass interferograms of these surfaces have comparatively diffused fringes, indicating surface roughness values of order 100 Å.

#### 4.2.8 Evaporated Glass on Be - Conventional or Ion Polished

A number of samples essentially consist of a polished Be substrate which was then coated with a thin glass-like material and repolished by various techniques. This material was considered as a possible method of obtaining fused silica quality reflecting surfaces with

beryllium structural properties. The typical values of visible light scatter from the polished Be substrate are about 0.16%, but the range extends from 0.08 to 0.32%, thus indicating a large variation in the quality of the Be surfaces. These values should be doubled for comparison with the aluminized glass results because of the lower reflectivity of the Be surfaces. The multiple pass interferograms of the Be surfaces do not have sharp fringes; the widths are consistent with surface roughness of order 200 Å.

Four of the Be samples were coated with approximately 2 microns of Schott Glass #8329 by electron beam evaporation. Two of the glass surface samples were ion polished and two were conventionally polished (surface shine). The visible light scatter was about 0.25% for the ion polished and about 0.30% for the conventionally polished samples. Multipass interferograms of the ion polished samples are relatively sharp, although not as good as those obtained with the bulk fused silica surfaces. The interferogram of the nonconventionally polished glass coated Be samples indicate still somewhat lower surface quality.

#### 4.2.9 Selective Dielectric Deposition on Be

The evaporated glass, however, did not result in X-ray surfaces equivalent to those obtained with bulk fused silica. The conventionally polished evaporated glass (Line 19) had a lower efficiency than either the ion polished (Line 16) or submerged polished (Line 2) bulk fused silica. The ion polished evaporated glass (Line 18) had a slightly better efficiency, but a broader reflection distribution than the conventionally polished evaporated glass sample.

Two of the Be surfaces were coated with 0.32 micron of a low stress dielectric by means of a Perkin-Elmer proprietary process. These surfaces resulted in about 0.17% scatter of visible light,

and sharp multipass interferograms were consistent with a roughness of order  $50 \text{ \AA}$  or less, although not quite as sharp as the results obtained from bulk fused silica. This process does not require additional polishing after the deposition can be used to modify the mirror figure inexpensively, and obtains the structural advantages of beryllium. The results (Line 21), however, were a broader reflected image distribution and a lower total efficiency than obtained by a number of other techniques.

### 4.3 Conclusion

There are a number of important conclusions to be drawn from these studies. The first is that no mysterious or truly insurmountable problem exists in making X-ray telescopes. For example, a number of these surfaces perform better than the scattering estimates of the original proposal (0.17, 0.333, and 0.62 of reflected intensity in 5, 10, and 20 arc second spot diameters respectively), even without substantial corrections for the width of the incident X-ray beam. The fused silica polished by the submerged process essentially duplicates the incident beam profile. The evaporation of nickel onto these surfaces resulted in the theoretical reflection efficiency, but with no significant increase in the X-ray surface scattering. This result may also be true for the metals, such as platinum, which would extend the useful telescope energy range to shorter wavelengths. The process of polishing electrodeless nickel or beryllium also has been improved so that this process is almost equivalent to an evaporated nickel surface upon fused silica, and we conclude that this is certainly an acceptable alternate mirror design.

## 5.0 REFERENCE DESIGN

### 5.1 Configuration

The overall configuration of the High Resolution Mirror reference preliminary design is shown in Figure 5-1. The assembly consists of ten fused silica segments, five hyperboloids and five paraboloids mounted in confocal sets in a support structure. In addition to the mirrors, the assembly consists of an Invar center support ring which attaches the mirror assembly to the optical bench, a graphite epoxy composite inner support cylinder which provides the required stiffness and ties the ends of the assembly to the center support ring, and Invar end plates which tie the mirror together. The mirrors are attached to the support structure by means of Invar flanges bonded to the mirrors. The analyses and other engineering data which support the selection of this reference design are presented below.

### 5.2 Fused Silica Mirror/Support Flange Thermal Stress Analysis

The reference design H.R. Mirror Assembly (Figure 5-1) was analyzed for mirror wall thermal distortion in the mirror support flange region. A temperature change of  $+10^{\circ}\text{F}$  was applied to the 36 inch diameter outer mirror and its support flanges, assuming an isothermal temperature distribution. A model of the problem is shown in Figure 5-2. A coefficient of thermal expansion mismatch of  $0.10 \times 10^{-6} \text{ in/in-}^{\circ}\text{F}$  between Invar and fused silica was used (i. e., a mismatch somewhat greater than indicated by manufacturer's data).

The AVCO SAMS-1 (Shell Analysis Modular System) computer program was the analytical tool used in the analysis. The SAMS-1 program performs static thermoelastic stress analysis of multi-layered, isotropic, cylindrical shells and uses a Fourier Cosine

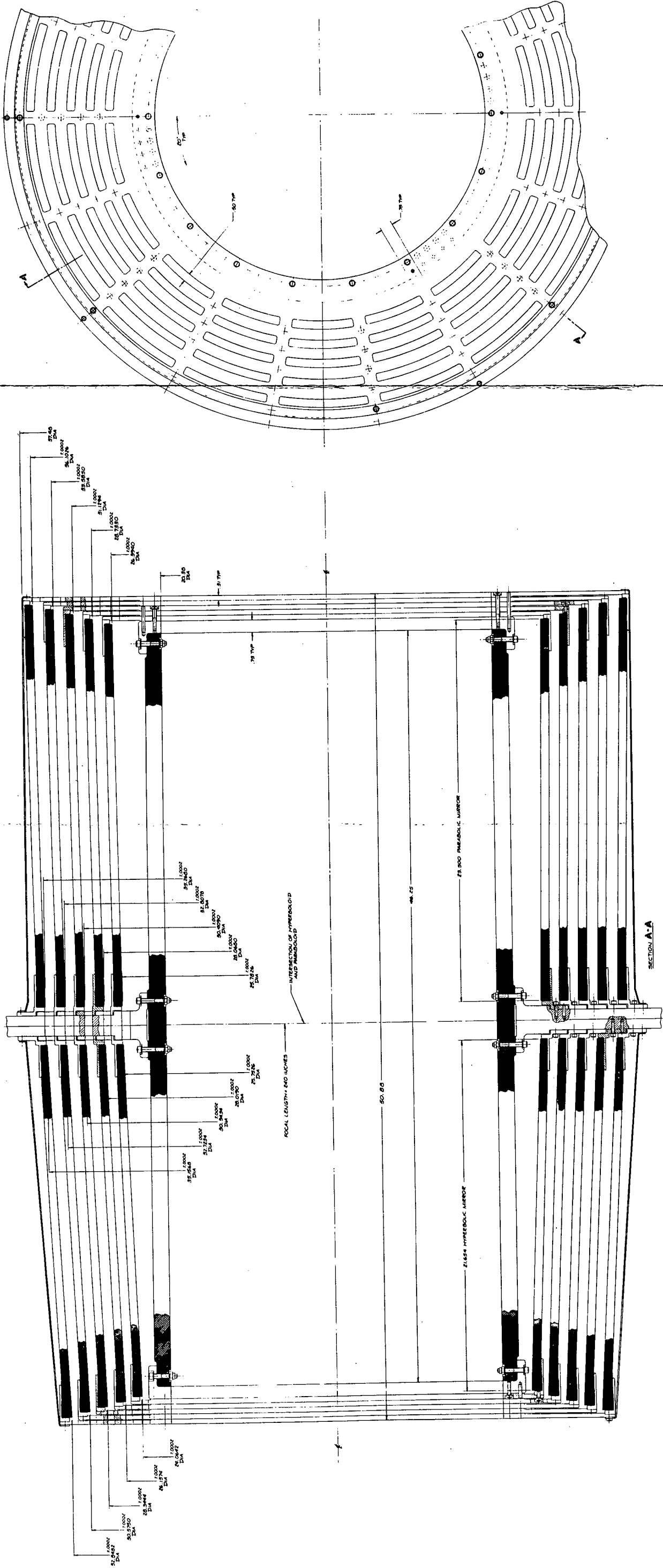
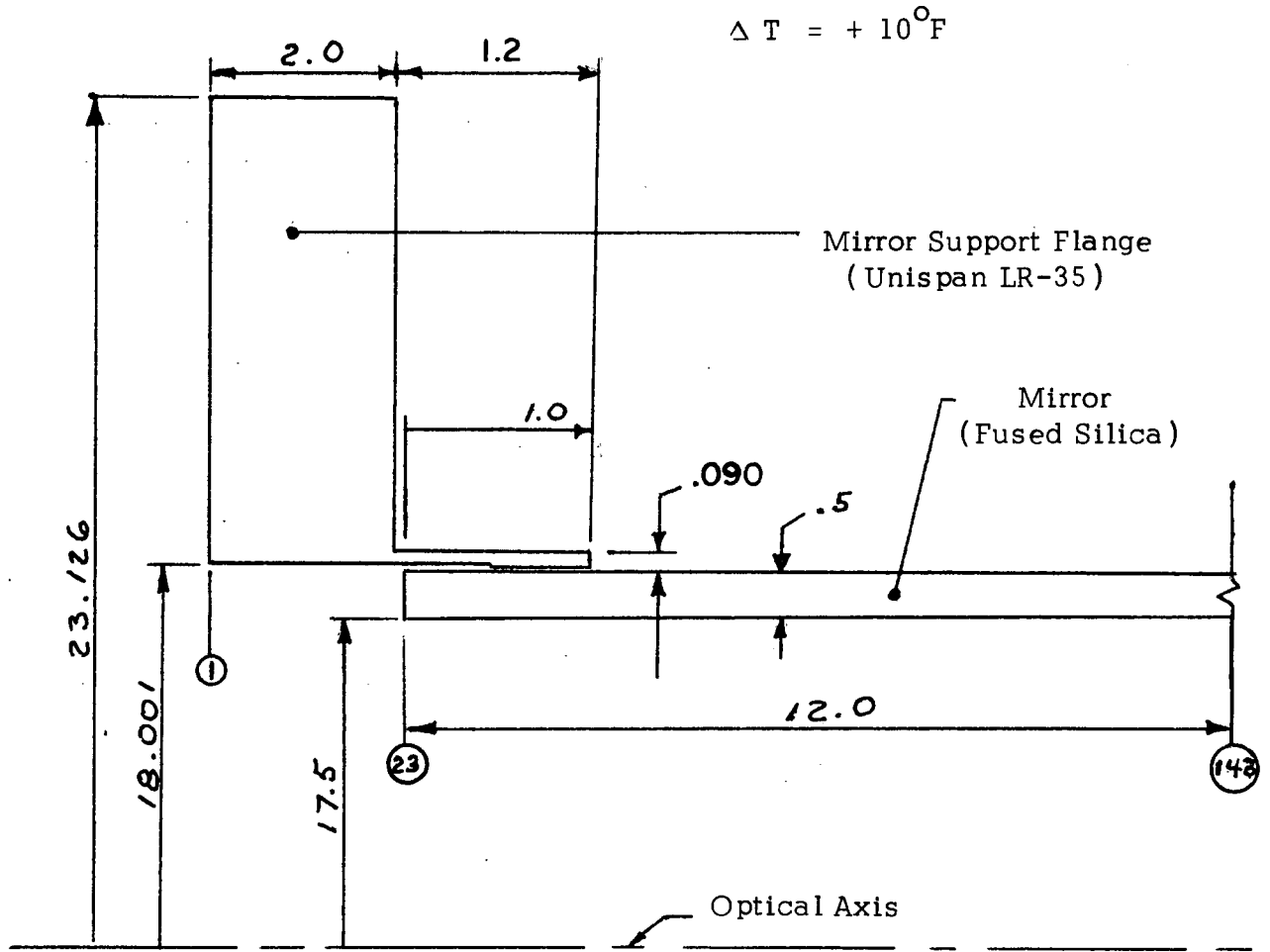


Figure 5-1. LOXT High Resolution Fused Silica Mirror Assembly

Figure 5-2

H. R. Mirror / Mirror Support Flange Model



Edge Conditions

Mirror Sta.	
1	143
$w \neq 0$	$w \neq 0$
$u \neq 0$	$u = 0$
$\phi = 0$	$\phi = 0$

Material Properties

Fused Silica	Unispan LR-35
$E = 10.5 \times 10^6$	$E = 21.4 \times 10^6$
$\nu = .2$	$\nu = .2$
$\alpha = .31 \times 10^{-6}$	$\alpha = .21 \times 10^{-6}$

Series for the circumferential coordinate and a finite difference scheme for the longitudinal coordinate.

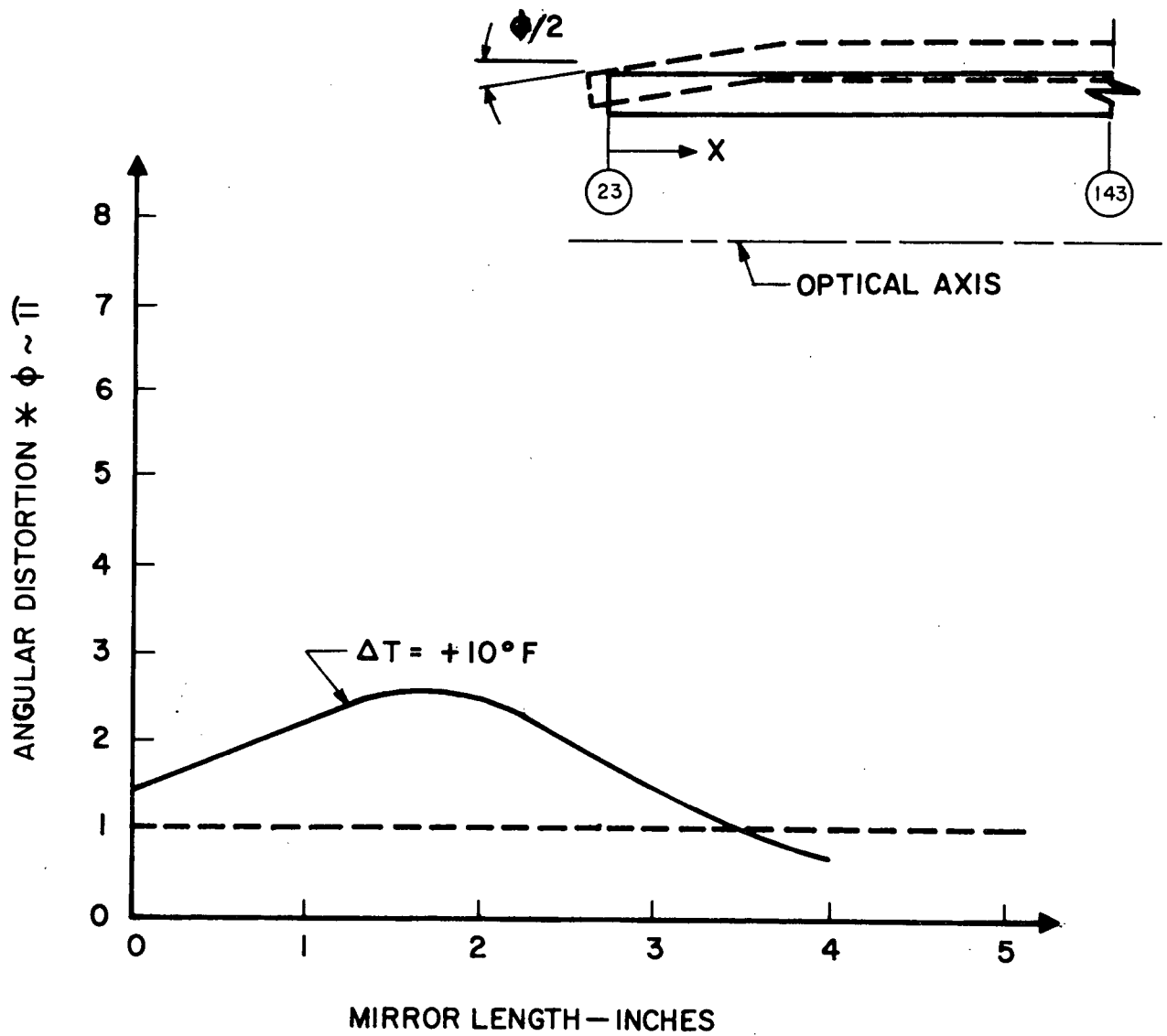
A maximum angular distortion of 1.4 arc seconds was calculated to exist in the mirror wall in the direction parallel to the optical axis approximately 1.0 inch away from each end of the mirror. The distortion dissipated to less than .5 arc seconds within 3.4 inches of the mirror ends. It should be noted that the angular distortion above relates to blur radius, and must be doubled to relate to blur diameter. Therefore, maximum angular distortion relating to blur diameter was 2.8 arc seconds for the  $+10^{\circ}\text{F}$  temperature change case. The results of this analysis are plotted in terms of angular distortion ( $\sim$  blur diameter) vs. mirror station in Figure 5-3.

Note that the angular distortion shown is for a single mirror, thus must be doubled when considering a hyperboloid/paraboloid set. The implication of the calculated mirror wall distortion is that active temperature control of the High Resolution Mirror Assembly may be required. For the thermal expansion coefficient mismatch of  $0.1 \times 10^{-6} \text{ in/in-}^{\circ}\text{F}$  used in this analysis at  $\Delta T$  not exceeding  $2.5^{\circ}\text{F}$  would be required in order to limit the mirror wall distortion to within 1 arc-second. The maximum thermal expansion coefficient mismatch that would hold the mirror wall distortion to within 1 arc-second for a  $\Delta T$  of  $10^{\circ}\text{F}$  is  $0.025 \times 10^{-6} \text{ in/in-}^{\circ}\text{F}$ , a value which may not be achievable.

### 5.3 Mirror Distortion Under Gravity Load

A computer solution (discussed in more detail in Appendix B) of the subject problem was obtained by employing Avco Computer Program #2222, which is a version of the MIT developed SABOR III computer code. The configuration analyzed is defined as a thirty-six inch diameter, twenty-four inch long, hollow circular cylinder with a one-half inch wall thickness constructed from fused silica. The cylinder is supported at both ends by pinned connections around its entire perimeter. The pinned connections lie within a rigid

**FIGURE 5-3**  
**MIRROR WALL THERMAL DISTORTION  $\theta$**   
**VS.**  
**MIRROR LENGTH FOR  $\Delta T = +10^{\circ}\text{F}$**



\*RELATES TO BLUR DIAMETER, ACTUAL WALL DISTORTION IS ONE-HALF ( $\phi/2$ ) THE VALUES PLOTTED

(fixed) plane. The maximum mirror wall radial distortion was found to occur at mid length, its magnitude being  $4.8 \times 10^{-6}$  inches. The maximum mirror wall angular distortion occurred at the mirror ends, its magnitude being 0.27 arc-seconds. It is concluded that, relative to an overall rms mirror resolution requirement of 1 arc-second, earth's gravity field applied laterally to the mirrors during ground focusing has only a minor effect on resolution during operation.

#### 5.4 High Resolution Mirror Dynamic Analysis

The dynamic analysis of the High Resolution Mirror for the lateral launch vibration condition, discussed in detail in Appendix C, was performed to define the natural frequencies and response characteristics (stress vs deflection) of the mirror for various combined circumferential and longitudinal modes of vibration. In computing deflections and stresses, a conservative (higher than expected) transmissability factor of 20 was used. The results support the choice of the mirror configuration from a structural point of view and also serve as a design criterion for the LOXT Optical Bench and its mounting system. (The results are considered to be the fragility levels to be taken into consideration in the LOXT Optical Bench Design).

The vibration environment (reference HEAO Experiment Developer's Handbook) used in this analysis is presented below.

#### Sinusoidal Vibration (all axes)

1.0 to 3.2 Hz	3.0"D.A.
3.2 to 10 Hz	1.5 g
10 to 14 Hz	0.3"D.A.
14 to 50 Hz	3.0 g

#### Random Vibration

20 to 150 Hz	+3db/Oct.
150 to 300 Hz	0.15g <sup>2</sup> /cps
300 to 1000 Hz	-3db/Oct.

1000 to 2000 Hz

-9db/Oct.

10.3g RMS overall

The mirrors were considered to be supported at both ends by pinned connections around the entire perimeter. The pinned connections were confined to a rigid (fixed) plane. The models were then subjected to the following dynamic analysis format.

- a. Mass and stiffness matrices are obtained from MIT SABOR III computer code (Avco Computer Code #2222) for each mirror configuration.
- b. Natural frequencies and mode shapes are obtained from Avco Computer Code #2607 "Frequencies and Mode Shapes of Undamped Structures."
- c. The relative motion of the mirror wall and its supports is determined by the use of the sine and random vibration environments presented above. Avco Computer Code #2921 "Forced Sinusoidal and Random Vibration Program."
- d. The critical mode shape deflection vector  $[\delta]$  from step (b) in this format is normalized with respect to the maximum relative motion obtained from step (c).
- e. The stress resultant matrix  $[B]$  from step (a) in this format is post multiplied by the normalized displacement vector  $[\delta]$  from step (d) to obtain the desired dynamic stress resultants. The dynamic stresses are computed from the stress resultants using the shell relationships.

The lowest natural frequency for the 36 inch diameter, 24 inch long mirror with a 1/2 inch wall thickness (the preferred size and thickness) was determined to be 702 Hz. This value corresponds to a longitudinal mode  $m = 1$  and a circumferential mode  $n = 5$ . The maximum tensile stress calculated in the mirror wall was 725 psi in the hoop (circumferential) direction.

The maximum tensile stresses calculated for all of the mirror configurations considered during the study lie well within the accepted 1000 psi design allowable tensile stress for fused silica

and it is concluded, therefore, that each is adequate in a structural sense.

The natural frequencies, mode values, and tensile stress for each of the fused silica mirror configurations are summarized below.

Configuration #1	Longitudinal Mode	Circumferential Mode	Natural Frequency Hz	Tensile Stress (psi)
36" dia, 24" lg 1/2" thick	1	5	702	725
Configuration #2				
36" dia, 24" lg 1" thick	1	4	1024	561
Configuration #3				
36" dia, 36" lg 3/4" thick	1	4	583	709

### 5.5 Mirror Support Structural Analysis

The mirror support structure (Figure 5-2) consists of a graphite-epoxy cylinder (1.5 in thick) capped at both ends by Invar end plates and supported at the middle by a central Invar support flange which ties directly to the Optical Bench.

#### 5.5.1 Static Analysis

One of the essential requirements of the cylindrical section of the mirror support structure is that it must provide a high degree of rigidity within the mirror assembly in the lg ground environment during alignment and focusing and other static ground tests. The maximum allowable end plate deflection under the condition was established to  $2.5 \times 10^{-5}$  inches (0.23 arc-sec sag in the mirror assembly between the center support ring and the end flanges). A cylindrical section fabricated from graphite epoxy composite material appears to be ideally suited to this application because of the low thermal expansion and high stiffness properties of the material. The other candidate material from a thermal viewpoint was Invar, but graphite epoxy composite has a superior stiffness/weight

ratio in a simple cylindrical configuration. In view of the above, graphite epoxy composite was chosen as the material for the mirror support cylindrical section, and the static and dynamic analysis performed on the mirror support assembly assumes it use.

The 9g sustained acceleration condition during launch (reference HEAO Experiment Developer's Handbook) produces tensile stress less than 100 psi within the graphite epoxy support cylinders, and a tensile stress of 2,240 psi in the Invar end plates.

A temperature change of 30<sup>o</sup>F also produces stresses less than 100 psi within the mirror support structure.

#### 5.5.2 Dynamic Analysis

5.5.2.1 Optical Bench Considered Hardmounted to the Spacecraft - The mirror assembly was considered to be tied directly (hardmounted) to the optical bench, which in turn was considered hardmounted to the spacecraft.

The mirror support structure was analyzed for its first mode frequency in the axial and lateral directions. The mirror assembly is cantilevered off the central support flange for the lateral analysis with one half of the mirror weight reacting through the Invar end plates. The mirrors themselves were assumed to be supported equally between the Invar end plates and central support flange for the axial analysis. The random vibration environment listed in Section 5.4 was then applied to the model. The sinusoidal vibration environment was not considered since the natural frequencies of the support structure were well above the 50 Hz cutoff; thus, maximum stresses would not occur in the region. Dynamic stresses in the graphite epoxy and Invar structure were calculated using a transmissibility factor of 10 at resonance. The results of the analyses are shown in Table 5-1. The lateral mode frequency of the support structure can be seen to be well above that of the mirrors and is at a point in the random vibration environment where inputs are quite low.

The stresses produced in the graphite epoxy support cylinder and the Invar end plates were found to be negligible. The axial mode frequency of the mirror support structure is considerably lower and produces higher stresses in the Invar end plates. These stresses are, however, well below that of the yield strength of Invar, (40,000 psi). The axial stresses in the support cylinder are negligible. The first mode axial frequency of the fused silica mirrors was calculated to be higher than 2000 cps, the upper limit of the random vibration environment, and therefore, behave as rigid bodies with regard to the spring-like support of the Invar end plates.

TABLE 5 - 1

AXIS OF VIBRATION	FIRST MODE (HZ)	DYNAMIC STRESS
LATERAL	1500	GRAPHITE/EPOXY NEGLIGIBLE STRUCTURE
AXIAL (LAUNCH)	110	17,000 PSI INVAR END PLATES

5.5.2.2 Optical Bench Considered Soft Mounted to the Spacecraft - The mirror assembly was considered to be tied directly to the optical bench (hard mounted), which in turn was considered to be soft mounted (vibration isolators) to the spacecraft. The dynamic environments in section 5.4 were applied to combinations of optical bench stiffness and weight and isolator stiffness (see Section 2 of Appendix D) and the resulting environments to the mirror assembly were less severe than for the hard mounted optical bench. As a result of its relatively high natural frequency, the mirror assembly acts as a rigid body within the range of the random and sinusoidal environments applied to the optical bench isolation system (refer to Section 4 of Appendix D).

The need for vibration isolators to the optical bench may evolve from thermal requirements, fragility levels (undetermined at this time) of the High Efficiency Mirror Assembly, or other instrumentation. Thus, the fact that the correct High Resolution Mirror Assembly Design is considered structurally adequate for a hard mounted optical bench design does not imply that the optical bench need not be soft mounted to the spacecraft.

## 5.6 Thermal Analysis

### 5.6.1 Thermal Configuration of Reference Design

The characteristics of the reference design for the High Resolution Mirror Assembly which dominate the thermal configuration may be summarized as:

- a. Ten cylindrical mirrors having relatively low thermal conductance and specular surfaces metallized on both sides.
- b. Outer and inner support cylinders and end plates having high thermal conductance relative to the mirrors.
- c. Principally radiative thermal coupling to the spacecraft.
- d. Direct view to space through the mirror apertures.

Most of the heat flow in the mirror assembly occurs in the graphite epoxy inner support cylinder and Invar end plates. Although these materials have a low conductivity in comparison with most metals, the large cross-sectional areas required for structural purposes result in a high thermal conductance in comparison with that of the fused silica mirrors. The heat flow to space by radiation through the viewing apertures is greatly reduced by providing special protection mounted on the spacecraft end wall; this fact is discussed in Appendix E. The resulting heat flow to space of one to three watts causes a gradient pattern in the mirror assembly directed toward the viewing apertures.

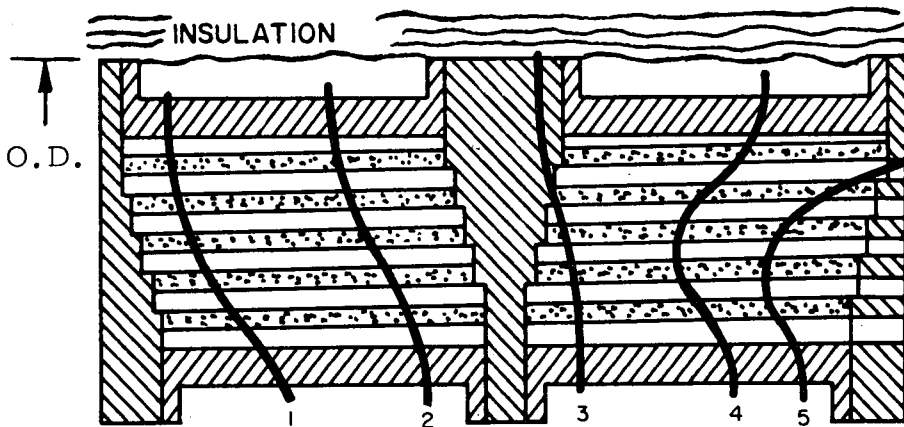
#### 5. 6. 2 Axial and Radial Gradients

A thermal mathematical model of the mirror assembly was formulated in order to determine, in detail, the gradient patterns in the mirror assembly. Figure 5-4 illustrates the gradient patterns of two representative cases for nominal heat flow to space, and with insulation surrounding the outside perimeter of the mirror assembly. Details of the model and other cases considered are contained in Appendix F.

The first illustration depicts the case of passive temperature control, in which the mirror assembly temperature is determined by its radiative coupling to the spacecraft ambient. The isotherms in the figure are in degrees Fahrenheit below the mean spacecraft temperature, which was taken as a reference. The shapes of the isotherms show that the heat flow is almost entirely axial, with a temperature difference of 5<sup>o</sup>F between the inboard and aperture ends of the assembly. This magnitude of temperature gradient represents no problem with respect to the one arc-second design goal. The second illustration shows the cylinders at a constant temperature. The only portion of the gradient pattern remaining is in the immediate vicinity of the apertures, the temperature

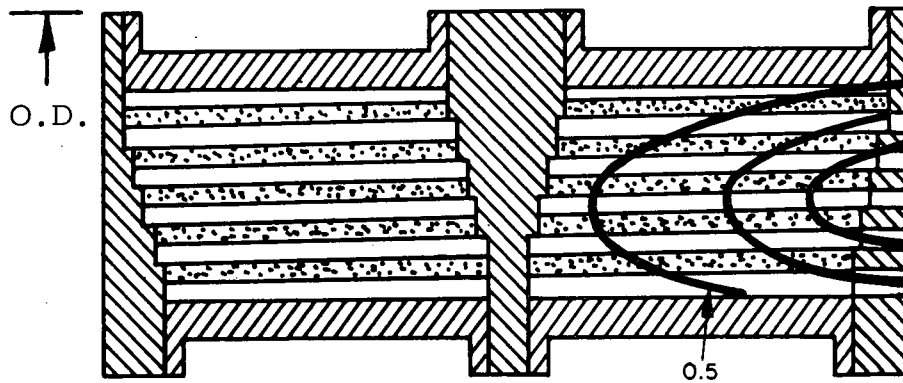
Figure 5-4

Thermal Gradient Patterns In Reference Design  
Isotherms In Degrees Farenheit  
Below Spacecraft Ambient



INSULATED  
MIRROR ASSEMBLY

FOLLOWS  
SPACECRAFT  
AMBIENT



TEMPERATURE-  
CONTROLLED  
MIRROR ASSEMBLY

INDEPENDENT  
OF SPACECRAFT  
AMBIENT

difference being about  $1.5^{\circ}\text{F}$  between the controlled cylinders and the center aperture. This difference could obviously be effectively eliminated, if desired, by providing temperature control on the aperture plates.

It should be noted that this model does not take into account the effect of specularity of the mirror surfaces. This consideration is beyond the scope of a preliminary study, but it may be stated that the gradient patterns calculated will be reduced by specular reflection in the narrow passages between mirrors, and that the assembly would be more uniform in temperature than the cases represented here. The mirrors will be metallized on the back surfaces, as well as on the reflector surface, in order to maximize this effort.

### 5. 6. 3 Circumferential Gradients

The effect of a possible circumferential gradient pattern in the mirror assembly was investigated. Such a gradient pattern might arise because of a temperature difference between the solar and anti-solar sides of the spacecraft immediately adjacent to the assembly. The investigation demonstrated that the circumferential conductance of the mirror assembly is small in comparison to the effective radiative conductance between the outer cylinder and the adjacent spacecraft surface, and that a substantial portion of the temperature difference would appear across the mirror assembly. This fact could result in distortion of the assembly; in fact, a temperature difference of  $10^{\circ}\text{F}$  could cause a "hot-dogging" effect in the assembly equal to one arc-second, which would greatly impact the mirror resolution. It was concluded that multilayer insulation and possibly actual thermal control would be required on the outer circumference of the mirror assembly to attenuate conditions which would lead to circumferential gradients.

#### 5. 6. 4 Temperature Control

The length of the optical bench from mirror assembly support to image plane, referred to as the focal distance, must be matched to the focal length of the mirror assembly within  $\pm 4$  mils for proper focusing conditions at the image plane. The focal length exhibits the coefficient of expansion of fused silica, and will increase by 3.3 mils over the expected ambient temperature range of  $25^{\circ}\text{C}$  (refer to Appendix G). It is clear that a low-expansion optical bench material, such as graphite-epoxy or Invar, will exhibit a change in length over the temperature range that is well within the focusing tolerance. This requirement does not indicate a need for active temperature control of the mirror assembly. One question, unresolved at this point, which could dictate a temperature control requirement is the possible mismatch in coefficient of expansion between fused silica and Invar. As discussed in Section 5.2, unacceptable local mirror distortion may arise at the temperature extremes as a result of such a mismatch in expansion coefficients. Although there is evidence that the mismatch can be minimized, there is no certainty. The solution in such a case, then, would be to restrict the operating temperature range of the mirror assembly by some degree of active temperature control.

#### 5. 7 Fabrication Techniques

In addition to the analysis required to establish that the reference design was structurally adequate, and that the thermally induced distortions were within acceptable limits, it was necessary to investigate fabrication techniques to obtain assurance that the reference design could be built. Meetings were held with a major manufacturer of fused silica, Invar manufacturers, precision optical equipment fabricators, precision machining houses, and

one of the leaders in the use of graphite-epoxy composite material in aerospace hardware.

#### 5.7.1 Fused Silica Mirror Blanks

During preparation of the LOXT Proposal, both Corning Glass Works and Amersil were contacted, and assurance was given that mirror blanks of the size required for LOXT could be obtained. There was no facility available, however, which could produce the required size as a single homogenous boule, i. e. , it would be necessary to fuse together smaller boules to obtain the size required. It was, therefore, necessary during this design study to obtain information on the mechanical, optical, and thermal properties for a boule fused together from smaller pieces and to obtain assurance that the design data being used in this study was correct. A technical conference was held at Corning Glass Works, Canton, N. Y. with several Corning personnel from both the Canton, N. Y. and the Corning N. Y. plants. During this conference the fabrication of fused silica and the fusing process used to join boules together were witnessed. Also observed were several items of raw stock for large optical mirrors in which the fusing process had been used. Data was presented which demonstrated that the fused joints were as strong as the homogenous material itself, and assurance was given that the 1000psi design allowable tensile stress and the  $0.31 \times 10^{-6}$  in/in-<sup>o</sup>F thermal coefficient of expansion used for fused silica in the design study were appropriate for a mirror with fused joints.

Two methods of fabricating mirror blanks of the required size were presented by Corning, both of which appear feasible. One method is to fuse separate 3-5 inch thick boules into a sandwich. Six or seven layers will be required to obtain the length of a LOXT mirror element. The resultant composite boule would then be core drilled

and machined to obtain cylinders of the specified inner and outer diameters. Corning believes that two mirror elements, one larger diameter and one small diameter can be obtained from one boule. The other method utilizes a "slumping" process in which fused silica flat plates of the required thickness are heated and formed over a mandrel. The flat plates would be cut to the proper length for a LOXT mirror element before forming.

Each plate, after forming, would represent a  $120^\circ$  section of the final cylinder. Three sections would then be assembled over an appropriate mandrel and the butt joints fused together by a localized heating process. This latter method has an advantage, in that the fusion planes are axial and could be lined up with the optically dead areas behind the mirror assembly structural webs. The size required for LOXT, however, has never been made by the slumping method, and some amount of development work would be required to verify the process.

During the conference assurance was given that the specification for allowable inclusions on the optical surface planned for inclusion in the procurement specification for the High Resolution Mirrors could be met without difficulty, including the region across circumferential fused joints by selection of the region to be cut during the coring operation.

#### 5.7.2 Mirror Fabrication

As shown in Figure 5-1, each high resolution mirror is held in the assembly by Invar flanges bonded to the end of the mirrors. This mounting technique imposed two requirements on the fabrication of the mirror in addition to the figuring and polishing requirements previously discussed. First, since each mirror is not sufficiently stiff to hold itself round without external support, it is necessary

to use support rings during polishing. Further, it is necessary to install the end flanges before removing the polishing rings, in order that the mirror be externally supported at all times.

Secondly, in order that the Invar flanges be thin in the radial direction, yet sufficiently strong to hold alignment in the dynamic environment, they should be as short as practical in the axial direction. This requirement means that the mirrors have to be cut to the proper length after polishing and after measurement of the focal length. Both of these requirements were discussed at technical conferences with Diffraction Limited, Inc. and Perkin-Elmer, who indicated that both requirements were reasonable; thus, they were incorporated into the reference mirror preliminary design.

### 5.7.3 Machining Tolerances

Meetings were held with Speedring Company and Pioneer Astro Industries, who are representative of the best industrial machining facilities in the country, to determine how close tolerances could be held in absolute diameter, concentricity, roundness, and perpendicularity on machined pieces of the size required for the High Resolution Mirror Assembly. Preliminary drawings of various concepts for mirror end flanges and support structure were reviewed. As a result of this review a concept which obtained axial strength in the mirror support structure by the sandwiching together of individual support flanges, was abandoned because it imposed flatness and perpendicularity requirements which either company would accept only on a best effort basis. Both companies, however, exhibited a good capability for performing precision machining operations.

#### 5. 7. 4 Invar Support Structure

Manufacturers data for low thermal expansion Invar, (Universal Cyclops Unispan LR-35) indicates a thermal expansion coefficient near that of fused silica. Investigation of the properties of Unispan LR-35, however, indicated considerable variability in thermal expansion coefficient from batch to batch, apparently as a result of the heat treat applied and the temperature range over which the data was averaged. In an effort to obtain specific information, a meeting was arranged with Universal Cyclops. Data presented at the meeting indicated that the thermal expansion properties of the material were a strong function of the heat treat procedure; however, since the data covered some 90 pieces of material manufactured over a five year period, heat treated in various ways under different conditions, and generally dilatometer tested at high and low temperatures (not in the region of 70<sup>o</sup>F), it was not possible to determine what heat treat would provide the best material for the LOXT flanges. Universal Cyclops indicated that as a result of our inquiry, along with others they have had in recent weeks regarding the use of Invar mounts to hold precision optical elements, they would run heat treat and dilatometer tests on a number of LR-35 samples and attempt to identify a mix and heat treat that obtained a thermal expansion coefficient near that of fused silica in the 70<sup>o</sup>F region. At the end of this design study the tests were being run, but no data was available. Universal Cyclops did indicate, however, that a thermal coefficient between 0. 21 and 0. 41 x 10<sup>-6</sup> in/in-<sup>o</sup>F used in the design analysis could be obtained.

#### 5. 7. 5 Graphite Epoxy Composite Support Structure

During the design study several meetings were held with the Convair Division of General Dynamics Corporation to obtain

information on the characteristics of graphite-epoxy composite material and to explore the feasibility of fabricating the structural parts of the mirror assembly from this material. This material has been baselined for use for the central support cylinder in the mirror assembly because of its superior stiffness to weight ratio. This material is also considered as a backup for the mirror support flanges and the other structural parts in the event that the low thermal expansion properties claimed for LR-35 Invar are not achieved, or if future fabrication problems develop using Invar.

#### 5.8 Mirror End Flange Design

As shown in Figure 5-1 the design approach adopted in the reference design to hold the fused silica mirrors was to bond end flanges to each mirror which are in turn bolted to support plates. This approach avoided any point loads on the fused silica mirrors. The primary design driver in the end flange design was the thermal expansion mismatch of the fused silica mirror and the material used for flanges. The design philosophy employed was to make the flange thick enough in the region of the bond around the mirror to hold the mirror in position throughout the environmental regime, but no thicker than necessary so as to allow the flange to flex and thereby reduce distortions in the mirrors. Analysis indicated that a flange 0.045" thick provided adequate stiffness, but discussion with precision machining houses indicated that fabricating such a thin flange would be difficult. Analysis was then performed to determine the maximum thickness that would result in acceptable thermal distortions in the mirror.

Uncertainty in the value of the thermal expansion coefficient for the flange material, Unispan LR-35, required a conservative approach to the thermal distortion analysis. A thermal coefficient of expansion for LR-35 of 0.21 to 0.41in/in-<sup>o</sup>F was assumed, and

the resulting analysis indicated that an 0.090 inch thick flange was the practical limit for thermal distortion. As discussed in Section 5.2 a flange of this thickness requires the  $\Delta T$  in the mirror assembly to be held to within  $2.5^{\circ}\text{F}$  if the distortion throughout the mirror is to remain within one arc-second. As discussed in Section 5.7.4 of this report, tests are currently underway to determine more precisely the LR-35 thermal expansion coefficient in the region of  $70^{\circ}\text{F}$ . It is anticipated that these tests will indicate a thermal expansion match to fused silica closer than that assumed in the analysis. A closer match to fused silica would allow a thicker flange, which would ease the fabrication requirements, or would allow a greater  $\Delta T$ , (for the same flange thickness) in the mirror assembly from the temperature at which it was assembled and aligned. This tradeoff remains to be resolved.

#### 5.9 Flange/Mirror Bonding

Preliminary bonding tests were conducted during this design study to the extent that the feasibility of bonding the Invar flanges to the fused silica was established. Both epoxy and eutectic bonds were tested and both exhibited more than adequate glass to metal adherence and shear strength.

The epoxy bond test consisted of bonding a piece of Crown glass, to a piece of Invar. The contact area was approximately one inch square. The epoxy used was Eccobond EP-B-24, which was recommended for this application by Emerson-Cummings. A pull test was performed to determine the force required to separate the bonded parts in shear. Separation occurred at a shear stress of 660 psi.

Another test assessed the feasibility of separating parts bonded together with this type of epoxy. Eccostrip 57 was used. The parts separated with approximately 3 hours immersion.

A test using an eutectic bonding material was conducted. Nickel coated Crown glass was bonded to Invar using Cerrolow 117 which melts at 117<sup>o</sup>F. The shear stress at separation was 537 psi. Further work is required before selecting the bonding material. An eutectic must be chosen with great care, accompanied by thermal analysis of the effects of the melting point. The melting point must be low in order not to distort the mirror in the region around the flanges, thus capturing the mirror in the distorted shape. The melting temperature must also be high enough that the melting point will not be reached in the operational environment. Whether there is a usable temperature range for eutectics remains to be determined.

Epoxy, as a bond, requires evaluation for outgassing, and further testing must be performed to determine the method of application. Also, tests using representative parts must be performed to verify stripping, since scrapping a polished mirror in the event of a bonding error is economically unacceptable.

#### 5.10 Alignment Procedure

The first iteration of the High Resolution Mirror Assembly reference design depended upon machining accuracies to achieve the required alignment of the assembly. A tolerance study, however, made it apparent that several tolerances, particularly in concentricities, were additive. The tolerance stackup across the five concentric optical elements led to tolerance requirements for individual pieces which were not achievable, thus indicating that a design was required which allowed a few mils of axial and lateral adjustment of each mirror element. During the design study several configurations allowing for adjustment during alignment and the accompanying alignment procedure were considered, each iteration improving upon the previous concept.

The final iteration of the reference design is shown in Figure 5-1. The first step in obtaining the required axial position of each mirror is to cut off the ends of the polished mirror as dictated by optical measurement of the focal length of each hyperboloid/paraboloid set. This step fixes the axial location of the mirror, with respect to the center support plate, to within a few mils. After cutting, the mirrors are mounted in the assembly, unbonded in their support flanges, and the few mils of axial adjustment is made as dictated by optical measurements. The end flanges are then bonded to the mirror. The procedure for obtaining lateral alignment is described briefly below.

- a. Within a suitable assembly fixture, the graphite-epoxy composite center cylinder will be attached to the center plate and the main end plates. Next, the two innermost mirror elements (hyperbola and parabola with end flanges attached as previously described) will be attached loosely to the center support plate and to their respective end plates. This pair of mirror elements will then be aligned confocally by lateral adjustment. When they are coaligned the bolts will then be tightened and the center flanges pinned, thus fixing the position of the mirrors.
- b. This procedure then continues with the second innermost set of mirrors and so on, in sequence, to the outermost mirrors. Each set, in turn, will be coaligned and their focus checked with respect to the previously aligned mirrors.
- c. After all mirrors are aligned, the bolts holding the end plates are tightened and then the sandwiched series of end plates are pinned. Pinning allows the assembly to be taken apart at a later time, to clean it for example, and then to be reassembled to the same position.

### 5. 11 Weight and Volume

The estimated weight of the High Resolution Mirror Assembly (reference design) is 1907 lbs. with constituent weights as follows:

	<u>Weight (lbs)</u>
Mirrors (10 elements)	917
Central Support Cylinder	308
Central Support Ring	217
Fore and Aft End Rings	344
Mirror Support Flanges	<u>121</u>
Total	1907

The outer diameter of the mirror assembly is 37.5 inches, not including the diameter of the central support ring which attaches to the optical bench. This diameter (approximately 42 inches) will be determined when its attachment to the optical bench is defined. The overall length of the mirror assembly is 51 inches. Dimensions for constituents parts can be found in Figure 5-1.

### 5. 12 Advantages/Disadvantages of the Reference Design

The primary advantage of the reference design is that the fused silica mirrors will provide the best available polished surface, thus very low x-ray scattering. A secondary, but far from trivial advantage, is that the adjustment features permit machining tolerances within the current capabilities of precision machining houses, and permits alignment to be accomplished using careful, but well understood optical measurement techniques.

The primary disadvantage of this design is that the thin fused silica mirrors will require careful handling during all stages of the HEAO-C hardware program where these mirrors are involved. An additional design problem exists in that the mirrors are not sufficiently rigid to hold themselves round under gravity load, thus they must be externally supported at all times. The design study has taken this into account, however, and suitable methods for holding the mirrors during fabrication and assembly have been

worked out. The strength of glass is always of concern in applications where it must undergo tensile stress. The conventional and conservative 1000 psi design allowable tensile stress for glass was imposed as a design requirement in this study and has been met (709 psi maximum) during exposure to the projected launch environment (the most severe environment to be encountered), including a transmissibility factor of 20 at the resonant frequency of the mirrors.

## 6.0 ALTERNATE DESIGN

### 6.1 Configuration

The overall configuration of the High Resolution Mirror alternate preliminary design is shown in (Figure 6-1). Note that with respect to the overall assembly, a high degree of similarity exists between the reference design and the alternate design. The essential difference is that the alternate design, being all beryllium, does not require bonded end flanges on the mirrors. The analyses and other engineering data that support the selection of this alternate design are presented below.

### 6.2 Stress Analysis

Analysis was performed on the alternate design to determine the stresses and distortions resulting from gravity load, steady state acceleration during launch, and the launch vibration environment. These analyses are described below.

#### 6.2.1 Gravity Load Distortion

The mirror assembly was investigated for maximum deflection under a 1g ground focusing condition. The model for the analysis was a 24 inch long, 36 inch diameter beryllium, circular cylindrical shell fixed at one end and free at the other. Shear deflection was accounted for as well as bending, the combination of which produced a maximum deflection at the free end of  $0.5 \times 10^{-6}$  inches and a slope of 0.1 arc-seconds. It is concluded that, in view of the 1 arc-second resolution requirement that this static deformation is acceptable.

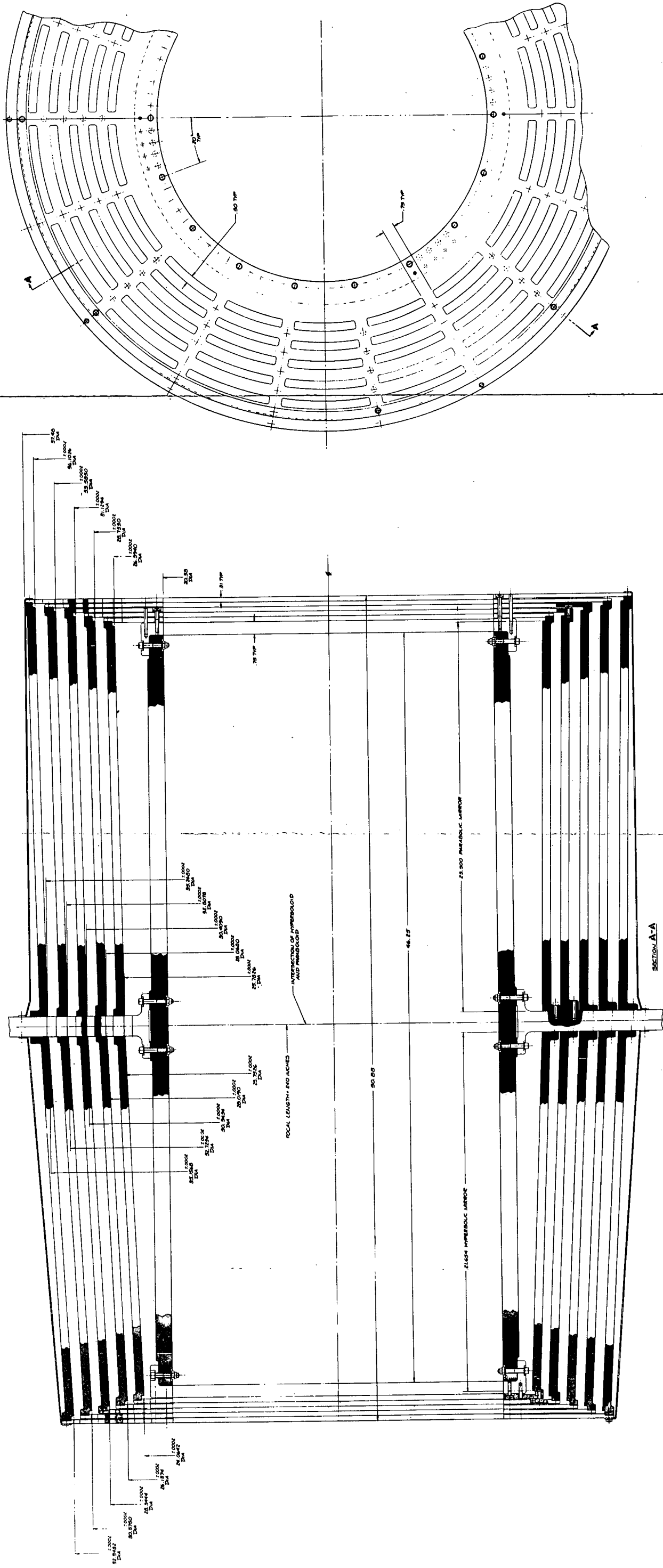


Figure 6-1. LOXT High Resolution Beryllium Mirror Assembly

### 6.2.2 Static Loads Analysis

Application of the 9g steady state launch condition in all axes produced a maximum tensile stress of 15 psi in the mirror and 1850 psi in the mirror support plate. The precision elastic limit for beryllium varies between 2500 psi and 9000 psi, depending upon the alloy and, therefore, this design is considered adequate. The design is discussed in detail in Appendix I.

### 6.2.3 Dynamic Analysis

A dynamic analysis of the High Resolution Mirror Alternate Design for the lateral launch vibration condition was performed to determine the natural frequencies and response characteristics (mirror stress vs. mirror deflection) of the mirror for various combined circular and longitudinal modes of vibration. The results of this analysis support AS&E's choice of the mirror alternate design from a structural point of view.

The mirror configuration analyzed was a 36 inch diameter, 24 inch long beryllium, circular cylindrical shell with a 1/2 inch wall thickness. The inner surface of the beryllium shell was considered to be lined with fused silica of a few microns thickness. The mirror was completely fixed at one end and completely free at the other, that is, as a cantilever beam. Section 5.4 describes the procedure used in this analysis.

The lowest natural frequency for the mirror was determined to be 1058 cps. This value corresponds to a longitudinal mode  $m = 1$  and a circumferential mode  $n = 3$ . The maximum tensile stress calculated in the beryllium mirror wall was 783 psi in the axial direction at the fixed support. This stress lies well below the Precision Elastic Limit (P. E. L. = 2500 psi minimum) of beryllium and thus indicates no microyield during exposure to the vibration environment. The maximum tensile stress calculated in the fused

silica liner was 340 psi. This stress lies well below the 1000 psi minimum long term allowable tensile stress, and therefore, it is concluded that the alternate mirror design configuration is structurally adequate to survive the exposure to the HEAO Spacecraft dynamic launch environment.

#### 6.2.4 Support Structure Analysis

The principal structural support difference between the fused silica mirror reference design and the beryllium mirror alternate design is that the latter is less dependent upon the inner support cylinder for structural rigidity. The glass mirrors, having a stiffness ratio (defined as  $E/p$ ) of 133, were supported by an inner support cylinder of graphite epoxy composite having a stiffness ratio of 450. The stiffer inner cylinder reduced the dynamic stresses in the mirrors to acceptable levels for glass and reduced the focussing error under gravity load. Beryllium has a stiffness ratio of 630, which permitted the central support cylinder to be made of beryllium since its principal function is to tie the ends of the assembly rigidly to the center support plate.

### 6.3 Thermal Analysis

#### 6.3.1 Thermal Configuration of Alternate Design

The two factors which most influence the thermal configuration of the alternate design are the thermal conductivity and thermal expansion coefficient of the beryllium mirror material. Conductivity is approximately one hundred times greater, and expansion coefficient twenty times greater than the corresponding values for fused silica. The effect of the high conductivity is to reduce greatly the magnitudes of temperature gradients, while the effect of the high expansion coefficient is to amplify in importance the distortional effects of those gradients which do exist, and to complicate the relationship between the focal length mirror

assembly and the length of the optical bench.

### 6.3.2 Axial and Radial Temperature Gradients

The magnitude of the axial temperature difference associated with heat flow through the viewing aperture is reduced to a negligible magnitude by the high conductance of the beryllium assembly. The end-to-end temperature difference in the mirror assembly is about  $0.1^{\circ}\text{F}$  for the nominal heat flow of two watts to space. Furthermore, the heat flow and gradient patterns are entirely axial, the direction in which the mirror assembly is least gradient-sensitive. This magnitude of axial temperature difference is insignificant with respect to mirror distortion. It is particularly desirable in this case to insulate the outer periphery of the assembly, both to insure that local effects caused by adjacent items do not upset the symmetry of heat flow, and also to minimize the effects of possible circumferential gradients.

### 6.3.3 Circumferential Gradients

The presence of conditions which would cause circumferential gradients as described in Section 5.6.1 is of concern with the beryllium mirror assembly as well. In this case the higher circumferential conductance tends to increase the total heat flow through the assembly, and even though the side-to-side temperature difference is attenuated, the greater expansion coefficient of the material would cause unacceptably large distortion of the mirror figure. Insulation of the outer circumference is therefore a necessity, as previously stated.

### 6.3.4 Temperature Control

The possibility of an active temperature control requirement applies to the alternate design as well as the reference design.

The principal reason for this requirement is the potential difficulty in maintaining equality of focal distance and mirror focal length. The focal length of a beryllium assembly would change by 1.6 mil per degree Fahrenheit or 70 mils over the expected temperature range. The optical bench temperature and expansion coefficient are greatly constrained by the requirement that the bench length must change by the same amount, within the  $\pm 4$  mil tolerance. Further consideration of the spacecraft temperature control scheme is beyond the scope of this study; suffice it to note that the inter-relationship of control of mirror assembly and optical bench temperature is much stronger for the alternate design than for the reference design. Temperature control of the mirror assembly, if required, would present no significant problem because of the high thermal conductance of the assembly.

#### 6.4 Alignment Procedure

The alignment procedure for the alternate design is the same as that discussed in Section 5.10 for the reference design, except that the steps required to locate the mirrors in their end flanges are not required.

#### 6.5 Weight and Volume

The estimated weight of the High Resolution Mirror Assembly (alternate design) is 1215 lbs., with constituent weights as follows:

	<u>Weight (lbs)</u>
Mirrors (10 elements)	746
Central Support Cylinder	316
Central Support Ring	49
Fore and Aft End Rings	<u>104</u>

Total     1215

The outer diameter of the mirror assembly is 37.5 inches, not including the diameter of the central support ring which attaches to the optical bench. This diameter (approximately 2 inches) will be determined when its attachment to the optical bench is

defined. The overall length of the mirror assembly is 51 inches. Dimension for constituent parts can be found in Figure 6-1.

#### 6.6 Advantages/Disadvantages of Alternate Design

The all beryllium alternate design offers two distinct advantages over the reference design. First, the beryllium mirrors are inherently stronger and less fragile than glass, thus there is less risk that they would be broken during fabrication or subsequent handling. The second advantage is that the mirror assembly, being all of the same material, has the same thermal expansion characteristics among its constituent parts. The only significant disadvantage, and the one which was the overriding factor in choosing the reference design, is that the beryllium mirror would provide a somewhat inferior optical surface.

## 7.0 SPECIFICATION FOR TEST MIRRORS

One of the tasks performed in this design study was the preparation of a procurement specification and associated drawings for two identical test mirrors to be fabricated and tested during Phase B of the LOXT Program. The test mirror specification was to include the design requirements for the inner paraboloid mirror, thus providing the option of using these mirrors in the flight and backup high resolution mirror assemblies, and thereby reducing overall program costs.

These two mirrors will be used to demonstrate the mechanical integrity of the mirror design, evaluate fabrication techniques and surface finish, and establish subcontractor qualifications for fabricating the complete set of mirror elements for the flight mirror assembly. Thus, the test mirror program will establish the validity of the critical areas of the design analysis before entering into the fabrication program required to produce the total complement of flight mirrors.

The specification embodying the requirements discussed above, AS&E Document S144-202, Technical Specification for the Inner Paraboloid of the LOXT High Resolution X-Ray Telescope Assembly is presented in Appendix J.

APPENDIX A

DESIGN PARAMETERS OF PARABOLOID-HYPERBOLOID

TELESCOPES FOR X-RAY ASTRONOMY

/

# Design Parameters of Paraboloid-Hyperboloid Telescopes for X-ray Astronomy

L. P. VanSpeybroeck and R. C. Chase

We have evaluated the principal optical characteristics of paraboloid-hyperboloid x-ray telescopes by a ray-tracing procedure; we find that our results for resolution, focal plane curvature, and finite source distance effects may be approximated in terms of the design parameters by simple empirical formulas.

Giacconi and Rossi<sup>1</sup> first discussed the application of focusing x-ray optics to astronomy. The highest resolution x-ray mirrors presently being used in x-ray astronomy consist of two successive concentric figures of revolution in which the two generating curves are concentric conic sections having a common focal point. These telescopes were first studied systematically by Wolter.<sup>2</sup> Giacconi *et al.*<sup>3</sup> have recently reviewed this subject. Mangus and Underwood<sup>4</sup> have previously discussed some of the design considerations for these telescopes. We have performed a systematic evaluation of the principal properties of x-ray mirrors such as shown in Fig. 1 and called Telescopes of the First Kind by Wolter; in this case the x-rays successively strike a paraboloid and a hyperboloid which are confocal, coaxial, and arranged so that the angular deviations of a ray at the two surfaces are additive. These have a shorter focal length for a given aperture than the other systems considered by Wolter and also have certain structural advantages resulting from the fact that the optical surfaces intersect. We find that our results for resolution, focal plane curvature, effective area, and finite source distance effects can be summarized by simple empirical formulas that should be useful to those considering x-ray telescope experiments.

## Description of the Surface

The equations for a paraboloid and hyperboloid which are coaxial and confocal can be written

$$r_p^2 = P^2 + 2PZ + [4e^2Pd/(e^2 - 1)] \quad (\text{paraboloid}),$$

$$r_h^2 = e^2(d + Z)^2 - Z^2 \quad (\text{hyperboloid}).$$

In the above equations the origin is at the focus for axial rays,  $Z$  is the coordinate along the axis of sym-

metry, and  $r$  is the radius of the surface of  $Z$ . The common focus is at  $Z = [-2e^2d/(e^2 - 1)]$ . There are thus three independent parameters,  $e$ ,  $d$ , and  $P$ , which describe the surfaces. It is useful, however, to consider the surfaces to be determined by three other parameters,  $Z_0$ ,  $\alpha$ , and  $\xi$ , which are more easily visualized, and are defined as follows:  $Z_0$  = the distance from the axial ray focus to the intersection plane of the paraboloid and hyperboloid, this is essentially the focal length and determines the scale of the optics;  $\alpha = \frac{1}{2} \arctan(r_0/Z_0) = \frac{1}{2}(\alpha_p^* + \alpha_h^*)$ , where  $r_0$  is the radius of the surfaces at their intersection and  $\alpha_p^*$ ,  $\alpha_h^*$  are the grazing angles between the two surfaces and the path of an axial ray that strikes at an infinitesimal distance from the intersection. Note that if  $\tan\theta_p^*$  and  $\tan\theta_h^*$  are the slopes of the two surfaces at the intersection,  $\alpha_p^* = \theta_p^*$ ,  $\alpha_h^* = \theta_h^* - 2\theta_p^*$ , and  $\alpha = \frac{1}{2}(\theta_h^* - \theta_p^*)$ ;  $\xi = \alpha_p^*/\alpha_h^*$  = the ratio of the two grazing angles for an axial ray striking near the intersection of the two surfaces.

The asterisk is used in this notation to specify values of the variables at the intersection plane.

The original parameters,  $e$ ,  $d$ , and  $P$  can then be determined as follows:

- (a)  $\theta_p^* = [2\xi/(1 + \xi)](\alpha)$ ,
- (b)  $\theta_h^* = [2(1 + 2\xi)/(1 + \xi)](\alpha)$ ,
- (c)  $P = Z_0 \tan(4\alpha) \tan\theta_p^*$ ,
- (d)  $d = Z_0 \tan(4\alpha) \tan(4\alpha - \theta_h^*)$ ,
- (e)  $e = \cos(4\alpha) [1 + \tan(4\alpha) \tan\theta_h^*]$ .

Two other parameters,  $L_p$  and  $L_h$ , the lengths of the paraboloid and hyperboloid sections, are necessary to define an actual mirror. We have considered  $L_p$  to be a free design parameter but have constrained  $L_h$  to be just long enough so that axial rays striking the front of the paraboloid also strike the back of the hyperboloid. This results in some loss of off-axis rays, which will be discussed below. This constraint results in the following equation for  $L_h$ :

The authors are with American Science and Engineering, Cambridge, Massachusetts 02139.  
 Received 27 May 1971.

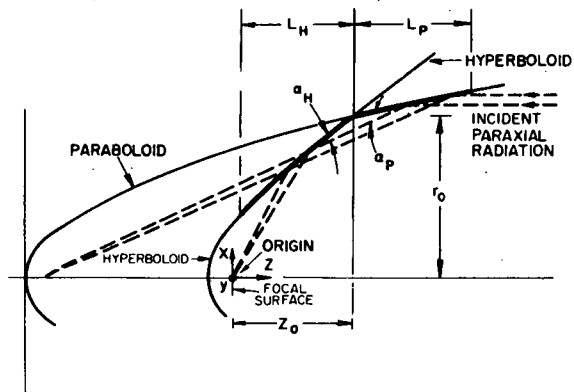


Fig. 1. A representation of the type of paraboloid-hyperboloid telescopes discussed in this paper. The back hyperboloid focus is confocal with the paraboloid focus. The front focus of the hyperboloid is also the focus of the telescope.

$$\frac{L_h}{L_p} = \frac{P}{ed + (e-1)L_p} \approx \frac{\xi}{1 + (\xi L_p/Z_0)} \quad (1)$$

The geometrical properties of a given telescope and source are thus determined by the four free design parameters ( $Z_0$ ,  $\alpha$ ,  $\xi$ ,  $L_p$ ) and the angle  $\theta$  between the incident rays and the optical axis.

### Procedure

Our principal analytical technique has been a Monte Carlo ray-tracing procedure. The input data to the computer programs include a geometrical description of the telescope, the surface material of the reflecting surfaces the wavelength of the incident x-rays, and the location of the point source of x-rays. A random position on the telescope front aperture is chosen, and an incident ray is required to go through this point. The ray is followed until it is reflected onto the focal plane properly, or is lost. The surface reflection efficiency is calculated by the approximate formulas given by Giacconi *et al.*<sup>2</sup> Additional random rays are traced in this way until the desired results are known with sufficient accuracy. The results include the telescope effective area,  $A_{\text{effective}}$ , and rms blur circle radius, for both flat ( $\sigma$ ) and optimally curved ( $\sigma_D$ ) focal surfaces. The formal definitions of these quantities are as follows:

$$A_{\text{effective}} = A(1/N)U_0,$$

$$\sigma^2 = \sigma_x^2 + \sigma_y^2,$$

$$\sigma_x^2 = (U_{xx}/U_0) - (U_x/U_0)^2,$$

and

$$U_0 = \sum_i \epsilon_i^p \epsilon_i^h,$$

$$U_x = \sum_i x_i \epsilon_i^p \epsilon_i^h,$$

$$U_{xx} = \sum_i x_i^2 \epsilon_i^p \epsilon_i^h.$$

The summations include only those rays that reach the focal plane;  $\epsilon_i^p$  and  $\epsilon_i^h$  are the reflection efficiencies for reflection from the paraboloid and hyperboloid, respectively;  $A$  is the geometric area which rays may traverse at the front aperture, and  $N$  is the number of random rays incident on this geometric area;  $x_i$  and  $y_i$  are the coordinates of the point of intersection of a ray with the focal plane. The entries in all the tables and graphs of this paper which were calculated by this Monte Carlo procedure exhibit the random fluctuations characteristic of the method.

### Resolution

A systematic study of many different telescopes reveals that the rms blur circle radius can be described quite accurately by a simple empirical relation,

$$\sigma_D = \frac{(\xi + 1) \tan^2 \theta}{10 \tan \alpha} \left( \frac{L_p}{Z_0} \right) + 4 \tan \theta \tan^2 \alpha, \quad (2)$$

where  $\sigma_D$  is expressed in radians. The coefficient of the second term was fixed at 4.0 (Ref. 5), and the factor of (1/10) is a fit to a selection of points in the region defined below:

$$(1^\circ/2) \leq \alpha \leq (7^\circ/2) \quad 0 \leq \theta \leq 30'$$

$$0.035 \leq (L_p/Z_0) \leq 0.176$$

$$(1/4) \leq \xi \leq 4.$$

Out of 200 points used in the fit, only twenty of the points differ from the formula by more than 20%, and none differs by more than 30%. These deviations may be due to our random procedure or, more likely, to the presence of additional terms in the expansion of  $\sigma_D$ .

The presence of the second term in the formula is due to the fact that Wolter telescopes of this type do not exactly satisfy the Abbe sine rule.<sup>2</sup> We have dis-

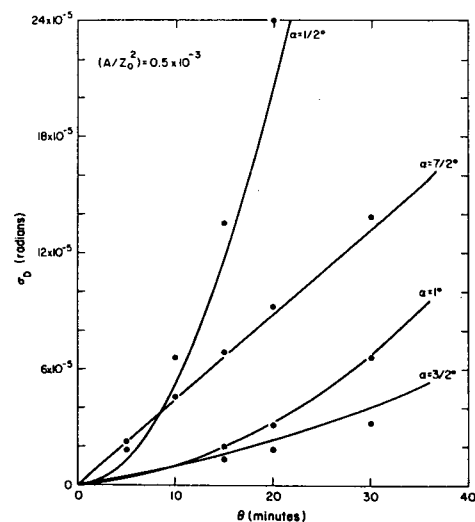


Fig. 2. The rms blur circle radius is given as a function of the incident angle for one value of  $(A/Z_0^2)$  and several values of  $\alpha$ . The solid lines were calculated using Eq. (4) while the points are the results of the Monte Carlo ray-tracing procedure.

covered that this second term disappears for telescopes of the Wolter-Schwarzschild variety.<sup>6</sup> These latter telescopes are similar to the paraboloid-hyperboloid telescopes but exactly satisfy the Abbe sine condition. They will be the subject of a later paper.

The image distribution is quite different for the two cases in which one of the two terms dominates: When the first term dominates, the image distribution in the Gaussian plane is peaked near the center and falls off approximately as  $(1/r)$  to a maximum radius determined by  $L_p$ ; whereas when the second term dominates the image distribution becomes a ring that is unpopulated at the center.

The resolution is seen to be a reasonably slow function of the parameter  $\xi$ ; and there are advantages to the choice  $\xi = 1$ , which approximately maximizes the collecting area for a given total mirror length or polished area, and also maximizes the x-ray reflection efficiencies at short wavelengths for a given diameter to focal length ratio. In the remainder of this paper we usually will set  $\xi = 1$ , and this value may be assumed where no other value is indicated. This also results in  $\theta_p \approx \alpha_p \approx \alpha_h \approx \alpha$ ;  $\theta_h \approx 3\alpha$ .

In stellar x-ray astronomy the most important design parameter usually is the telescope collecting area, and it is useful to reexpress Eq. (2) in terms of the area rather than the segment length. To fix the collecting area, the scale must be chosen by specifying one of the lengths,  $r_0$ ,  $Z_0$ , or  $L_p$ . The geometrical area presented to axial rays is then given by

$$A = (2\pi r_0)(L_p \tan \alpha), \quad (3)$$

and for small  $\alpha$  we can reexpress Eq. (2) as

$$\sigma_D \approx \left( \frac{1}{40\pi} \right) \frac{\tan^2 \theta}{\tan^2 \alpha} \left( \frac{A}{Z_0^2} \right) + 4 \tan \theta \tan^2 \alpha. \quad (4)$$

The rms blur circle radius is given as a function of the incident angle for one value of  $(A/Z_0^2)$  and various values of  $\alpha$  in Fig. 2. The solid lines were calculated using Eq. (4) while the points are the results of the Monte Carlo ray-tracing procedure.

In Figs. 3 and 4 the results of Eq. (4) are plotted as a function of the parameter  $\alpha$  for various values of  $(A/Z_0^2)$  and two fixed incident angles ( $\theta = 5'$ ,  $10'$ ). The curves exhibit an optimum value of  $\alpha$  for a given incident angle, area, and focal length. The optimum value of  $\alpha = \alpha^+$  is given by

$$\tan \alpha^+ = [(3/320\pi) \tan \theta (A/Z_0^2)]^{1/2}. \quad (5)$$

Note that  $\alpha^+$  is fairly insensitive to  $\theta$  and  $(A/Z_0^2)$ . The results of Eq. (5) for typical values of  $\theta$  and  $(A/Z_0^2)$  are plotted in Fig. 5. The optimum value of  $\alpha$  is about one degree for most practical cases.

### Focal Plane Curvature

The optimally curved focal plane can be described in terms of a parameter,  $\delta(r)$ , which is the axial distance of the surface above the normal focal plane at a distance  $r$  off axis. Empirically,

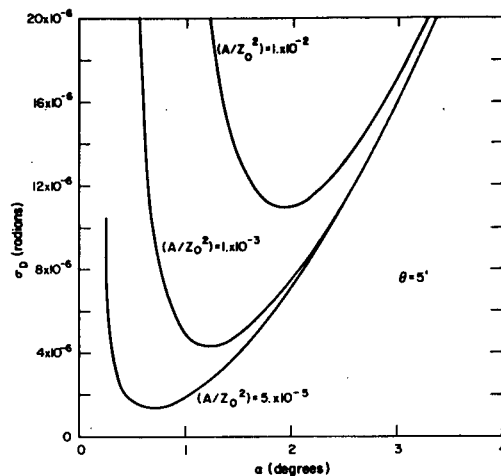


Fig. 3. The rms blue circle radius is given as a function of  $\alpha$  for several values of  $(A/Z_0^2)$ .  $\theta$  is fixed at  $5'$ . The curves were calculated using Eq. (4).

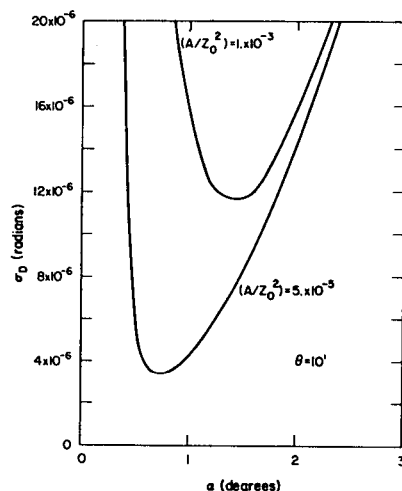


Fig. 4. The rms blur circle radius is given as a function of  $\alpha$  for two values of  $(A/Z_0^2)$ .  $\theta$  is fixed at  $10'$ . The curves were calculated using Eq. (4).

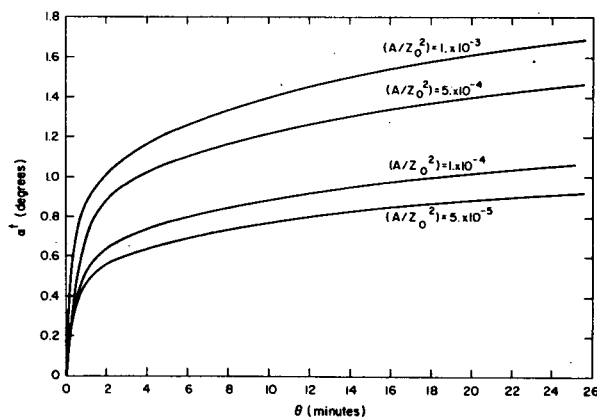


Fig. 5. The optimum value of  $\alpha$  is given as a function of  $\theta$  for several values of  $(A/Z_0^2)$ . The curves were calculated using Eq. (5).

$$\delta = 0.055 (\xi + 1)(r^2 L_p / Z_0^3)(1/\tan \alpha)^2. \quad (6)$$

The accuracy of this formula is roughly the same as that of Eqs. (2) and (4). The effect of using a flat focal plane is to double the first  $(\tan^2 \theta)$  term in Eqs. (2) and (4).

### Collecting Area

Figure 6 is a plot of the calculated effective area of a typical telescope as a function of  $\lambda$  for several values of  $\theta$ . The mirror surface is taken to be a nickel alloy, kanigen, and is similar to one we have flown on several rocket flights. Its descriptive parameters are  $r_0 = 11.43$  cm,  $L_p = 22.86$  cm, and  $Z_0 = 132.08$  cm. The surface reflection efficiency as a function of wavelength and grazing angle has been taken into account using the formalism presented in Ref. (3). The dip at about 14 Å is due to the  $L$  absorption edges of nickel. The effective area of this and similar telescopes can be described very well as the product of three factors,

$$A_{\text{effective}} = (A)[V(\alpha, \theta)][R(\alpha, \lambda)], \quad (7)$$

where  $A$  is the geometric area,  $V(\alpha, \theta)$  is a vignetting factor,  $R(\alpha, \lambda)$  is the surface reflection efficiency for the particular material used, and  $\lambda$  is the wavelength of the x-rays. Our ray-tracing studies show that the vignetting factor is negligibly dependent upon  $(L_p/Z_0)$ . Figure 7 is a plot of  $V(\alpha, \theta)$  vs  $\theta$  and  $\alpha$ ; this result depends upon our technique for choosing the length of the hyperboloid. We find that

$$V(\alpha, \theta) \approx 1 - (2/3)(\theta/\alpha) \quad (\theta < \alpha). \quad (8)$$

### Finite Distance Effects

We have studied the effects of placing the point source of x-rays at a finite distance from the telescope. Tracing rays from this new source location shows that the focal plane is shifted from the normal focal plane approximately as the simple lens law predicts. That is,

$$(1/p) + (1/q) = 1/z_0, \quad (9)$$

where  $p$  and  $q$  are the axial distances from the central plane to the point source and new focal plane, respectively. Figure 8 shows the dependance of  $\sigma_D$  on  $\alpha$ ,  $(L_p/Z_0)$ , and  $(p/Z_0)$ . These results can be approximated by

$$\sigma_D = 4(L_p/Z_0) \tan \alpha (Z_0/p)^2 \quad (10)$$

for on-axis point sources.

There is also a loss of collecting area at finite distances which is primarily due to vignetting. Although there is also some loss in reflection efficiency; the latter effect is less than might be expected because the grazing angles at the two surfaces vary in opposite directions. Empirically we have found that the loss of effective area due to vignetting from finite sources goes approximately as

$$A(P) \approx [1 - (5Z_0/2p)]/[1 + (5Z_0/2p)]. \quad (11)$$

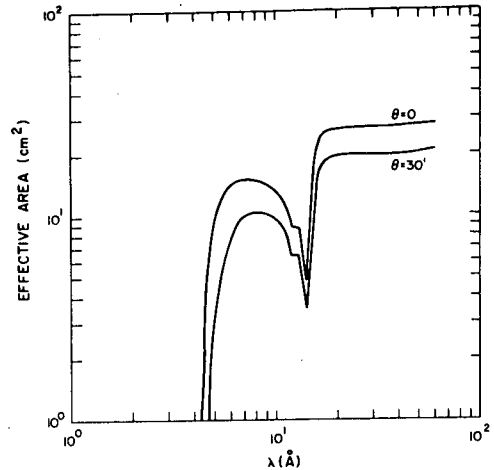


Fig. 6. The effective area of a typical telescope as a function of x-ray wavelength,  $\lambda$ , for two values of  $\theta$ . The mirror surface is made of a nickel alloy, kanigen.

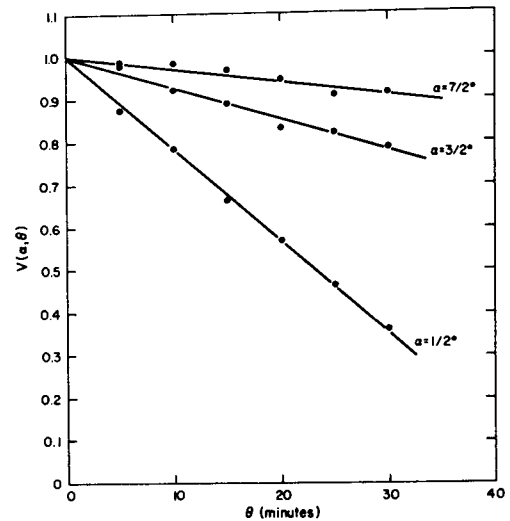


Fig. 7. A plot of the vignetting factor,  $V(\alpha, \theta)$ , as a function of  $\theta$  for several values of  $\alpha$ .

This formula is accurate to about 2%. Note that there is negligible dependence upon either  $\alpha$  or  $L_p$ .

### Nested Surfaces

Equation (2) shows that  $\sigma_D$  increases with  $L_p$ , so that increasing the collecting area by lengthening the mirrors results in a loss of resolution. The collecting area may be increased without a substantial loss of resolution by nesting additional surfaces inside the original surface rather than increasing the mirror length. The tolerances for adding such additional surfaces are determined by the focal plane scale rather than by the wavelength since diffraction limited performance is not expected even from a single surface.

Our method of designing multiple surface telescopes begins with the choice of  $Z_0$ ,  $L_p$ ,  $r_0$ , and  $L_h$  of the largest surface. The minimum wall thickness necessary for

structural rigidity is also fixed. Additional surfaces are then added with smaller values of  $r_0$  but with the same values of  $Z_0$ ,  $L_p$ , and  $L_h$ . These additional surfaces are chosen to be just small enough to pass all axial rays that strike the next larger surface. In practice, the limiting condition is that the back of the hyperboloid should not interfere with rays striking near the intersection plane ( $Z = Z_0$ ) of the next larger surface. Hence, the radii of the inner surfaces are determined at  $Z = Z_0 - L_h$  and not at the central plane where  $Z = Z_0$ . We calculate the parameters describing the paraboloid and hyperboloid of the smaller surfaces by means of an iterative computer program. The choice of  $L_h$  follows the scheme of Eq. (1) only for the largest surface. The focal plane curvature given in Eq. (6) depends upon  $\tan \alpha$  and therefore is different for each mirror of the nested set; the opti-

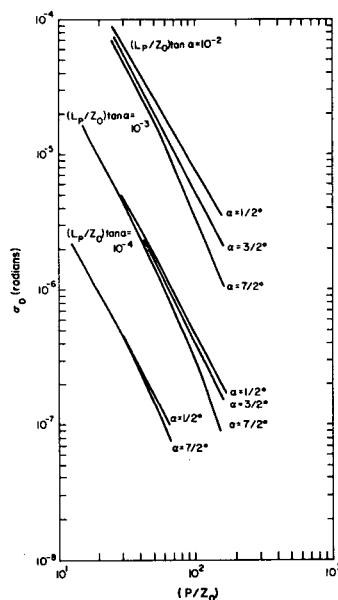


Fig. 8. The rms blur circle radius is given as a function of the finite source distance divided by the focal length. The results are shown for several values of  $(L_p/Z_0)$  and  $\alpha$ .

imum value of  $\delta$  for the assembly will be between the values calculated according to Eq. (6) for the inner and outer mirrors. Our programs determine the optimum focal plane curvature for a nested set of mirrors by minimizing the rms radius of the image distribution obtained when the entire assembly is uniformly illuminated.

Figure 9 is an example of the effect of the parameter  $L_p$  and the number of surfaces upon effective area and resolution. Nine points have been calculated, and the lines have been sketched in to interpolate approximately. Figure 10 is an example of the effect of mirror wall thickness on effective area for a three-surface telescope and a five-surface telescope. The telescope parameters for Figs. 9 and 10 are  $Z_0 = 609.6$  cm,  $r_0^{\max} = 44.75$  cm, and  $L_0 = 55.88$  cm. The advantages of the multiple surface approach are obvious, and the ray-tracing results show that no unexpected consequences of nesting surfaces occur.

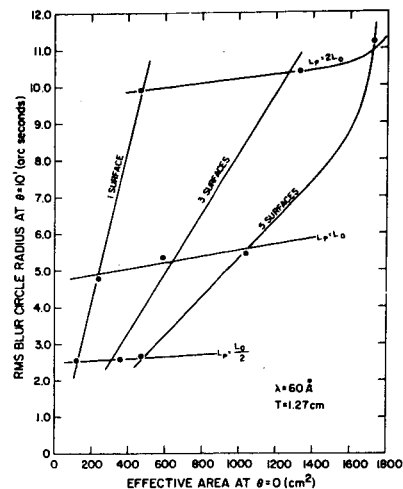


Fig. 9. The rms blur circle radius for a flat focal plane at  $\theta = 10'$  is given as a function of effective area at  $\theta = 0$  for specific telescopes. The effect of  $L_p$  and the number of surfaces are shown. Nine points have been calculated, and the lines have been sketched in to interpolate approximately.

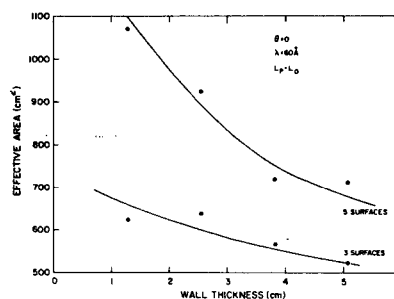


Fig. 10. The telescope effective area is given as a function of the mirror wall thickness for a three-surface telescope and a five-surface telescope.

## Conclusions

The empirical formulas of this paper should be adequate for the preliminary optical design of x-ray telescopes and associated test facilities. Although not demonstrated in this paper, we have found that the ray-tracing techniques used in the present study are useful for determining the properties of particular designs and evaluating the effects of finite tolerances and mechanical deformations upon their performance.

Many people at AS&E have contributed to the development of x-ray telescope technology. The contributions of Ricardo Giacconi and Bruno Rossi, who first suggested these telescopes for astronomical use, G. Vaiana, H. Gursky, W. Reidy, and T. Zehnpfennig have been particularly important. This work has been partially supported by NASA contract NAS8-24385.

## References

1. R. Giacconi and B. Rossi, *J. Geophys. Res.* **65**, 773 (1960).
2. H. Wolter, *Ann. Phys.* **10**, 94 (1952).
3. R. Giacconi, W. P. Reidy, G. S. Vaiana, L. P. VanSpeybroeck, and T. F. Zehnpfennig, *Space Sci. Rev.* **9**, 3 (1969).
4. J. D. Mangus and J. H. Underwood, *Appl. Opt.* **8**, 95 (1969).
5. This term is easily derived for short cone optics and must be present for any two surface mirror with nonzero first surface slope at the intersection of the two surfaces. The focal plane coordinates of an off-axis ray in the  $x$ - $z$  plane, which strikes

near the intersection are given by

$$x_i = -Z_0 \tan\theta \frac{(\cos^2 2\alpha / \cos^4 \alpha) (1 + \cos 2\phi \tan^2 2\alpha)}{1 - \tan\theta \cos\phi \tan 4\alpha}$$
$$y_i = -Z_0 \tan\theta \frac{(\cos^2 2\alpha / \cos^4 \alpha) (\sin 2\phi \tan^2 2\alpha)}{1 - \tan\theta \cos\phi \tan 4\alpha},$$

where  $\phi$  is the azimuthal angle at which the ray strikes the surface. This result does not depend on  $\xi$ .

6. H. Wolter, *Ann. Phys.* **10**, 286 (1952).

7

APPENDIX B

COMPUTER SOLUTION: LOXT HIGH RESOLUTION

MIRROR DISTORTION UNDER GRAVITY LOAD

B-1

COMPUTER SOLUTION: LOXT HIGH RESOLUTION MIRROR  
DISTORTION UNDER GRAVITY LOAD

A computer solution of the subject problem was obtained employing Avco Computer Program #2222, which is a version of the MIT developed SABOR III computer code. The configuration analyzed is defined as a thirty-six inch diameter, twenty-four inch long, hollow circular cylinder with a one-half inch wall thickness constructed from fused silica. The cylinder is supported at both ends by pinned connections around its entire perimeter. The pinned connections lie within a rigid (fixed) plane. The maximum mirror wall radial distortion was found to occur at mid length - its magnitude being  $4.8 \times 10^{-6}$  inches. The maximum mirror wall angular distortion occurred at the mirror ends - its magnitude being 0.27 arc-seconds. The LOXT High Resolution Mirror configuration and the gravity distortions are shown on the attachment in Figure 1 and Table 1 respectively.

The SABOR III computer output describes the mirror surface distortions at any point around the circumference at a particular mirror meridian station in terms of the product of a Fourier coefficient and a simple trigonometric function  $\sin \phi$  or  $\cos \phi$ . Since the output specifies  $K_F$  at discrete points (stations) along the mirror length, it would then seem as though a curve fitting routine could be employed to relate mirror station length  $x$  with the distortion Fourier coefficient  $K_F$  in order that a general equation for the distorted mirror surface could be written. The results of this work then would be incorporated in the ray tracing program in current use at AS&E. Details of the analysis performed are given on the following pages.

Table I

Node No. *	Fourier Coefficients			
	w	v	u	$\beta$
1	0	0	0	$-.013 \times 10^{-4}$
2	$-.025 \times 10^{-4}$	$.074 \times 10^{-5}$	$.042 \times 10^{-6}$	$-.097 \times 10^{-5}$
3	$-.038 \times 10^{-4}$	$.013 \times 10^{-4}$	$.07 \times 10^{-6}$	$-.046 \times 10^{-5}$
4	$-.043 \times 10^{-4}$	$.019 \times 10^{-4}$	$.078 \times 10^{-6}$	$-.019 \times 10^{-5}$
5	$-.046 \times 10^{-4}$	$.022 \times 10^{-4}$	$.064 \times 10^{-6}$	$-.096 \times 10^{-6}$
6	$-.047 \times 10^{-4}$	$.024 \times 10^{-4}$	$.036 \times 10^{-6}$	$-.048 \times 10^{-6}$
7	$-.048 \times 10^{-4}$	$.026 \times 10^{-4}$	0	0

Maximum radial displacement  $w = K_w \cos \phi = 4.8 \times 10^{-6}$  inches

$$\text{@ } x = \frac{l}{2} = 12 \text{ inches (node 7)}$$

Maximum angular rotation  $\beta = K_\beta \cos \phi = .27 \text{ }^\circ \text{ @ } x = 0,$

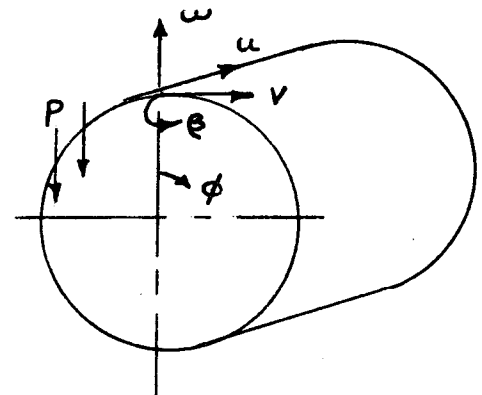
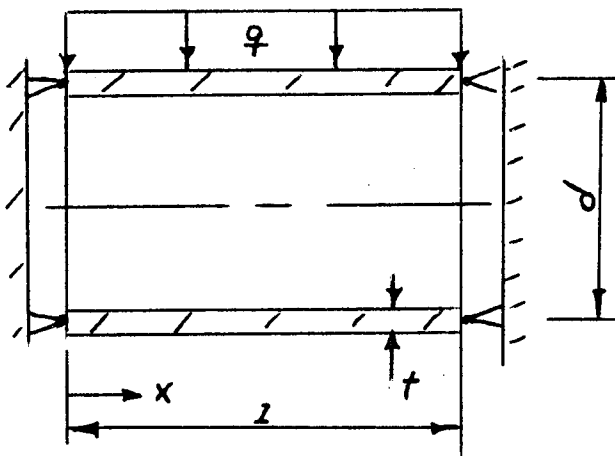
$$l = 0, 24 \text{ inches (nodes 1, 13).}$$

\* Values for only nodes 1-7 are given because of symmetry.

Computer Solution - High Resolution Mirror Distortion Under Gravity Load

The mirror configuration analyzed for a 1 g load condition is shown in Figure 1 below. The configuration represents a cylindrical mirror bonded at each end to the flange of a support plate in such a manner as to allow meridional rotation ( $\beta$ ) of the shell elements at the boundaries ( $x = 0, 1$ ) but no translation ( $w, v, u = 0$ ). The following constants were applied to the configuration analysis:

Material Properties (Fused Silica)	Geometric Properties
$E = 10.5 \times 10^6 \text{ psi}$	$d = 36 \text{ inches}$
$\nu = .14$	$t = 0.5 \text{ inches}$
$\rho = .079 \text{ lbs/inch}^3$	$l = 24 \text{ inches}$



$w, v, u = 0, \beta \neq 0 \quad \text{at } x = 0, 1$

(a)

$q = \rho g t$

$p = \rho t$

(b)

Figure 1

$w, v$  and  $u$  are the respective radial, tangential and axial displacements of any point on the mirror surface.  $\beta$  is the angular displacement of the mirror meridian about the tangent  $v$ . The sign convention is positive as shown in Figure 1 (b).

The mirror was configured to the SABOR III program as shown below in Figure 2.

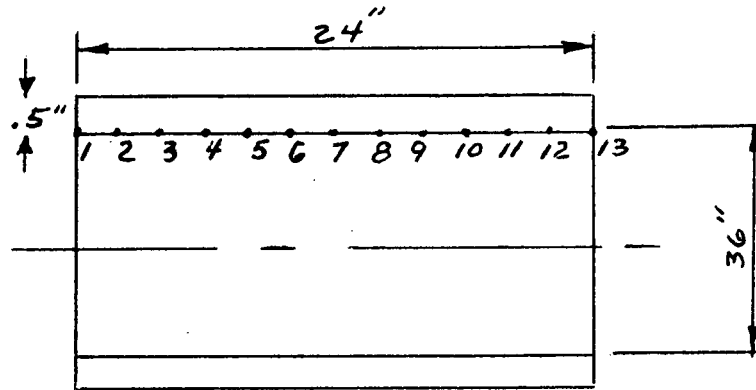


Figure 2

The results of the analysis are given in Table I in the form of Fourier coefficients for each nodal point (1 - 13). The method of converting the values to displacements and rotations is as follows:

$$\text{displacements} \begin{cases} w \text{ (inches)} & = K_w \times \cos \phi \\ v \text{ " } & = K_v \times \sin \phi \\ u \text{ " } & = K_u \times \cos \phi \end{cases}$$

$$\text{rotation} \quad \left\{ \beta \text{ (}\pi\text{)} \right. = K_e \times 2.06 \times 10^5 \times \cos \phi$$

APPENDIX C

LOXT HIGH RESOLUTION MIRROR DYNAMIC ANALYSIS

i

## CONTENTS

- I Results and Conclusions
- II Construction of the Finite Element Model
- III Natural Frequency Analysis for Three Configurations
- IV Stress Analysis Based on Extreme Random Vibration  
Response Deformation
- V References

## LOXT High Resolution Mirror Dynamic Analysis

A finite element dynamic analysis has been performed which determines the frequency and response characteristics of three cylindrical mirror configurations constructed from fused silica.

The three mirror configurations analyzed were as follows:

- Case 1) A 36 inch diameter, 24 inch long hollow circular cylinder with a one half inch wall simply supported at both ends. (Reference Design)
- Case 2) A 36 inch diameter, 24 inch long hollow circular cylinder with a one inch wall fully fixed at both ends.
- Case 3) A 36 inch diameter, 36 inch long hollow circular cylinder with a three quarter inch wall simply supported at both ends.

### I. Results and Conclusions

The minimum natural frequencies associated with these three cases were 702 cps, 1024 cps, and 583 cps respectively. These eigenvalues represent circumferential bending and are characteristic of short shells  $\left( \frac{\text{Length}}{\text{Radius}} \approx 1.0 \right)$ .

When these three configurations were subjected to the HEAO random vibration requirement of Reference (3) the peak shell stresses generated were below 800 psi. The stress level obtained is based on a 3 sigma level of random vibration. The design allowable stress chosen for the fused silica mirror configurations analyzed is 1000 psi (tensile stress). It is therefore concluded that each of the mirror configurations meets the random vibration requirements of Reference (3).

### References

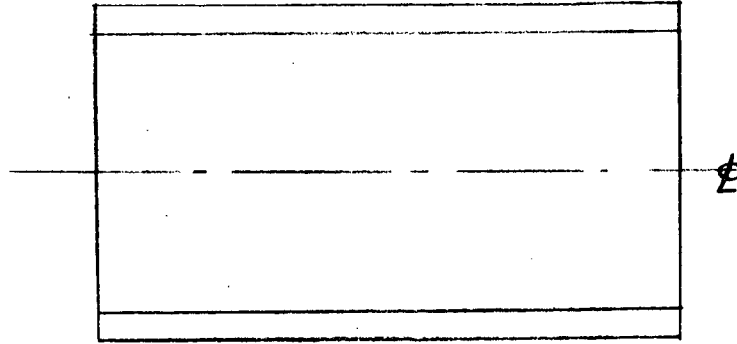
1. "Stresses in Shells" by Wilhelm Flugge, Springer, Verlag, Berlin, 1960.
2. "Static Analysis of Shells of Revolution, Avco Digital Computer Program 2222" (Avco version of M. I. T. Sabor III) by J. J. Baron and J. L. McLean.
3. "HEAO Experiment Developers' Handbook" NASA Document.

PARA. NO.		TITLE:	ANAL. BY	KEP
DWG. NO.			DATE	DEC 71
LOADS ARE			CHKD. BY	

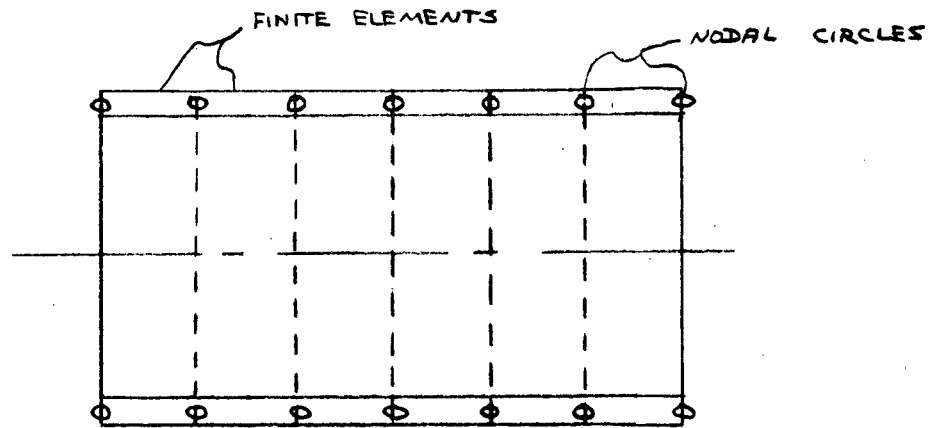
## II CONSTRUCTION OF THE FINITE ELEMENT MODEL.

THE CYLINDRICAL MIRROR SHELL CONSIDERED IS SHOWN IN FIGURE 1.0. THIS REPRESENTS A TYPICAL OUTER MIRROR WHICH WAS SELECTED FOR ITS LOWER NATURAL FREQUENCY AS COMPARED TO THE MORE RIGID SMALLER INNER MIRRORS. THE M.I.T. COMPUTER PROGRAM, SABOR III, WAS EMPLOYED TO ANALYZE THE CYLINDRICAL SHELL. THE BASIC APPROACH OF THE PROGRAM IS TO REPRESENT THE SHELL STRUCTURE BY A FINITE - ELEMENT IDEALIZATION USING THE MATRIX - DISPLACEMENT METHOD. THE CONDITION OF THE SHELL OF REVOLUTION IS REPRESENTED BY THE DIS - PLACEMENTS AT A FINITE NUMBER OF NODAL CIRCLES. THE DISPLACEMENTS AT EACH NODE, NAMELY THE MERIDIONAL DISPLACEMENT  $\tilde{u}$ , THE CIRCUMFERENTIALLY TANGENT DISPLACEMENT  $\tilde{v}$ , THE NORMAL DISPLACEMENT  $\tilde{w}$ , AND THE ROTATION OF THE ELEMENT  $\beta$  IN THE PLANE CONTAINING THE MERIDIAN AND THE AXIS OF ROTATION ARE FUNCTIONS OF THE CIRCUM - FERENTIAL COORDINATE  $\theta$ , AND CAN ALL BE RESOLVED CIRCUMFERENTIALLY INTO FINITE - FOURIER SERIES COMPONENTS. THIS IS SHOWN AS FOLLOWS.

PARA. NO.		TITLE:	ANAL. BY	KEP
DWG. NO.			DATE	JBC 71
LOADS ARE			CHKD. BY	

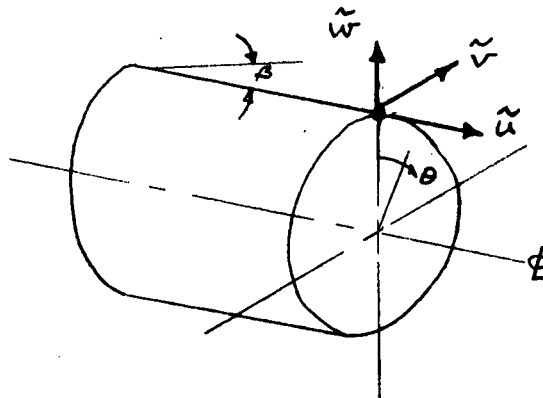


ORIGINAL SHELL



IDEALIZED SHELL

DISPLACEMENT  
COMPONENTS



C-4

PARA. NO.		TITLE:	ANAL. BY	KEP
DWG. NO.			DATE	DEC 71
LOADS ARE			CHKD. BY	

SPECIFICALLY, AT NODE  $p$ ,

$$\tilde{u}_p(\theta) = q_{4p-3}^0 + \sum_{j=1}^m q_{4p-3}^j \cos j\theta$$

$$\tilde{v}_p(\theta) = q_{4p-2}^0 + \sum_{j=1}^m q_{4p-2}^j \sin j\theta \quad (1)$$

$$\tilde{w}_p(\theta) = q_{4p-1}^0 + \sum_{j=1}^m q_{4p-1}^j \cos j\theta$$

$$\beta_p(\theta) = q_{4p}^0 + \sum_{j=1}^m q_{4p}^j \cos j\theta$$

THE COEFFICIENTS  $q$  IN THESE EXPRESSIONS ARE THE GENERALIZED DISPLACEMENTS AT NODE  $p$ . THE SUPERSCRIPIT ON  $q$  IS CALLED THE HARMONIC NUMBER. FOR LINEAR ELASTIC PROBLEMS OF SHELLS OF REVOLUTION, THE GENERALIZED COORDINATES  $q$  FOR DIFFERENT HARMONICS ARE NOT COUPLED.

THE EQUATIONS OF MOTION FOR THE DYNAMIC RESPONSE PROBLEM CAN BE WRITTEN IN THE FORM, FOR THE FREE VIBRATION CASE.

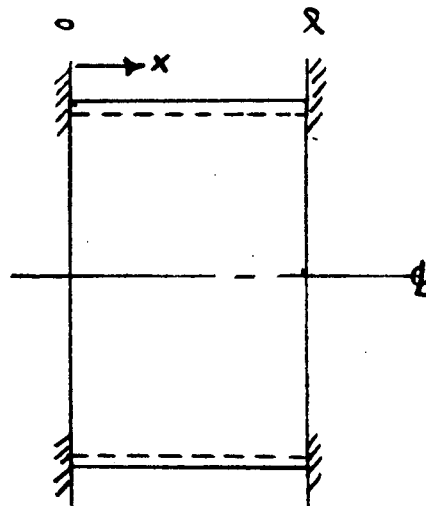
$$[M] \{\ddot{q}\} + [K] \{q\} = 0 \quad (2)$$

HERE FOR EACH HARMONIC  $j$ ,  $[M]$  &  $[K]$  ARE, RESPECTIVELY THE MASS AND STIFFNESS MATRICES. THESE TWO MATRICES DESCRIBE THE STRUCTURAL MODEL FOR ANY HARMONIC  $j$ .

PARA. NO.		TITLE:	ANAL. BY	KEP
DWG. NO.			DATE	DEC 71
LOADS ARE			CHKD. BY	

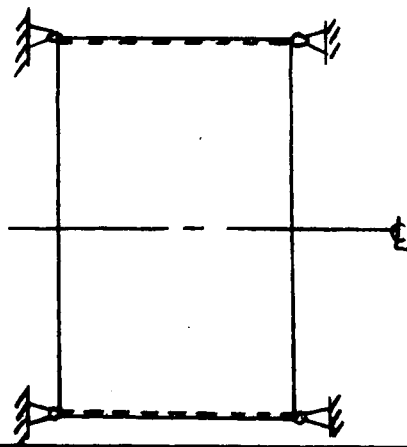
THIS TECHNIQUE OF STRUCTURAL MODEL BUILDING WAS APPLIED TO THE SHELLS SHOWN IN FIGURES 1.0 & 2.0. THREE SPECIFIC THICKNESS VALUES WERE CONSIDERED, ONE, ONE HALF, AND THREE QUARTERS OF AN INCH. THE BOUNDARY CONDITIONS WERE TAKEN AS FULL FIXITY AT BOTH ENDS IN THE ONE INCH THICK CASE AND SIMILAR CONDITIONS IN THE OTHER TWO CASES EXCEPT THAT IN THE LATTER BOTH ENDS WERE ALLOWED TO ROTATE. THIS IS SHOWN BELOW AS.

t = 1.0"



$$\begin{Bmatrix} u \\ v \\ w \\ \rho \end{Bmatrix} = 0 \quad @ x=0, l$$

t = 0.50"  
 $\frac{1}{2}$   
t = 0.75



$$\begin{Bmatrix} u \\ v \\ w \\ M_x \end{Bmatrix} = 0 \quad @ x=0, l$$

PARA. NO.		TITLE:	ANAL. BY	KEP
DWG. NO.			DATE	DEC 71
LOADS ARE			CHKD. BY	

SINCE THERE ARE FOUR DEGREES OF FREEDOM AT EACH NODE IN THE UNRESTRAINED CASE THERE WILL BE 44 D.O.F. IN THE ONE INCH THICK CASE AND 46 D.O.F. IN THE HALF INCH CASE. THIS MEANS THAT FOR EACH CIRCUMFERENTIAL HARMONIC THERE WILL BE MASS AND STIFFNESS MATRICES OF ORDER 44 AND 46 RESPECTIVELY, FOR THE TWO DIFFERENT THICKNESSES. THE DIFFERENCE IN ORDER ARISES AS A RESULT OF THE VARIED END CONDITIONS. DUE TO THEIR LARGE SIZE ONLY A TYPICAL PAIR OF MASS & STIFFNESS MATRICES WILL BE SHOWN HERE. THE COMPLETE MATRICES FOR ALL CASES ANALYZED HAVE BEEN COMPUTED AND ARE AVAILABLE ON REQUEST.

THE TYPICAL CASE SHOWN HERE IS FOR  $t = 1.0$  INCHES AND THE CIRCUMFERENTIAL INDEX  $n = 0$ . THIS INDEX  $n$  IS IDENTICAL TO THE  $j$  USED IN THE SABOR III EQUATIONS & WILL BE USED HENCEFORTH. THE INDEX  $m$  WILL BE TAKEN TO REFER TO THE NUMBER OF LONGITUDINAL HALF WAVES.

THE LONGER 36 INCH SHELL HAS A THICKNESS OF THREE QUARTERS OF AN INCH AND WITH THE THREE INCH SPACING CONSIDERED, AS SHOWN IN FIGURE 2.0, CONTAINS 46 D.O.F. IN THE SUPPORTED CASE.

TYPICAL STRUCTURAL MASS MATRIX

n = 0      t = 1"      l = 24"

$$\begin{Bmatrix} u \\ v \\ w \\ \theta \end{Bmatrix} = 0$$

@ x = 0, l

M(001,001)	3.0604139D-02	(001,005)	7.6510347D-03
(002,002)	3.0604139D-02	(002,006)	7.6510347D-03
(003,003)	3.4101755D-02	(003,007)	5.9022268D-03
(003,008)	-2.8418129D-03		
(004,004)	3.4976159D-03	(004,007)	2.8418129D-03
(004,008)	-1.3116060D-03		
(005,005)	3.0604139D-02	(005,009)	7.6510347D-03
(006,006)	3.0604139D-02	(006,010)	7.6510347D-03
(007,007)	3.4101755D-02	(007,011)	5.9022268D-03
(007,012)	-2.8418129D-03		
(008,008)	3.4976159D-03	(008,011)	2.8418129D-03
(008,012)	-1.3116060D-03		
(009,009)	3.0604139D-02	(009,013)	7.6510347D-03
(010,010)	3.0604139D-02	(010,014)	7.6510347D-03
(011,011)	3.4101755D-02	(011,015)	5.9022268D-03
(011,016)	-2.8418129D-03		
(012,012)	3.4976159D-03	(012,015)	2.8418129D-03
(012,016)	-1.3116060D-03		
(013,013)	3.0604139D-02	(013,017)	7.6510347D-03
(014,014)	3.0604139D-02	(014,018)	7.6510347D-03
(015,015)	3.4101755D-02	(015,019)	5.9022268D-03
(015,020)	-2.8418129D-03		
(016,016)	3.4976159D-03	(016,019)	2.8418129D-03
(016,020)	-1.3116060D-03		
(017,017)	3.0604139D-02	(017,021)	7.6510347D-03
(018,018)	3.0604139D-02	(018,022)	7.6510347D-03
(019,019)	3.4101755D-02	(019,023)	5.9022268D-03
(019,024)	-2.8418129D-03		
(020,020)	3.4976159D-03	(020,023)	2.8418129D-03
(020,024)	-1.3116060D-03		
(021,021)	3.0604139D-02	(021,025)	7.6510347D-03
(022,022)	3.0604139D-02	(022,026)	7.6510347D-03
(023,023)	3.4101755D-02	(023,027)	5.9022268D-03
(023,028)	-2.8418129D-03		
(024,024)	3.4976159D-03	(024,027)	2.8418129D-03
(024,028)	-1.3116060D-03		
(025,025)	3.0604139D-02	(025,029)	7.6510347D-03
(026,026)	3.0604139D-02	(026,030)	7.6510347D-03
(027,027)	3.4101755D-02	(027,031)	5.9022268D-03
(027,032)	-2.8418129D-03		
(028,028)	3.4976159D-03	(028,031)	2.8418129D-03
(028,032)	-1.3116060D-03		
(029,029)	3.0604139D-02	(029,033)	7.6510347D-03
(030,030)	3.0604139D-02	(030,034)	7.6510347D-03
(031,031)	3.4101755D-02	(031,035)	5.9022268D-03
(031,036)	-2.8418129D-03		

M

(032,032)	3.4976159D-03	(032,035)	2.8418129D-03
(032,036)	-1.2116060D-03		
(033,033)	3.0604139D-02	(033,037)	7.6510347D-03
(034,034)	3.0604139D-02	(034,038)	7.6510347D-03
(035,035)	3.4101755D-02	(035,039)	5.9022268D-03
(035,040)	-2.8418129D-03		
(036,036)	3.4976159D-03	(036,039)	2.8418129D-03
(036,040)	-1.2116060D-03		
(037,037)	3.0604139D-02	(037,041)	7.6510347D-03
(038,038)	3.0604139D-02	(038,042)	7.6510347D-03
(039,039)	3.4101755D-02	(039,043)	5.9022268D-03
(039,044)	-2.8418129D-03		
(040,040)	3.4976159D-03	(040,043)	2.8418129D-03
(040,044)	-1.2116060D-03		

(041,041)	3.0604139D-02		
(042,042)	3.0604139D-02		
(043,043)	3.4101755D-02		
(044,044)	3.4976159D-03		

TYPICAL STRUCTURAL STIFFNESS MATRIX

n = 0      t = 1"      l = 24"

$$\begin{Bmatrix} u \\ v \\ w \\ \rho \end{Bmatrix} = 0$$

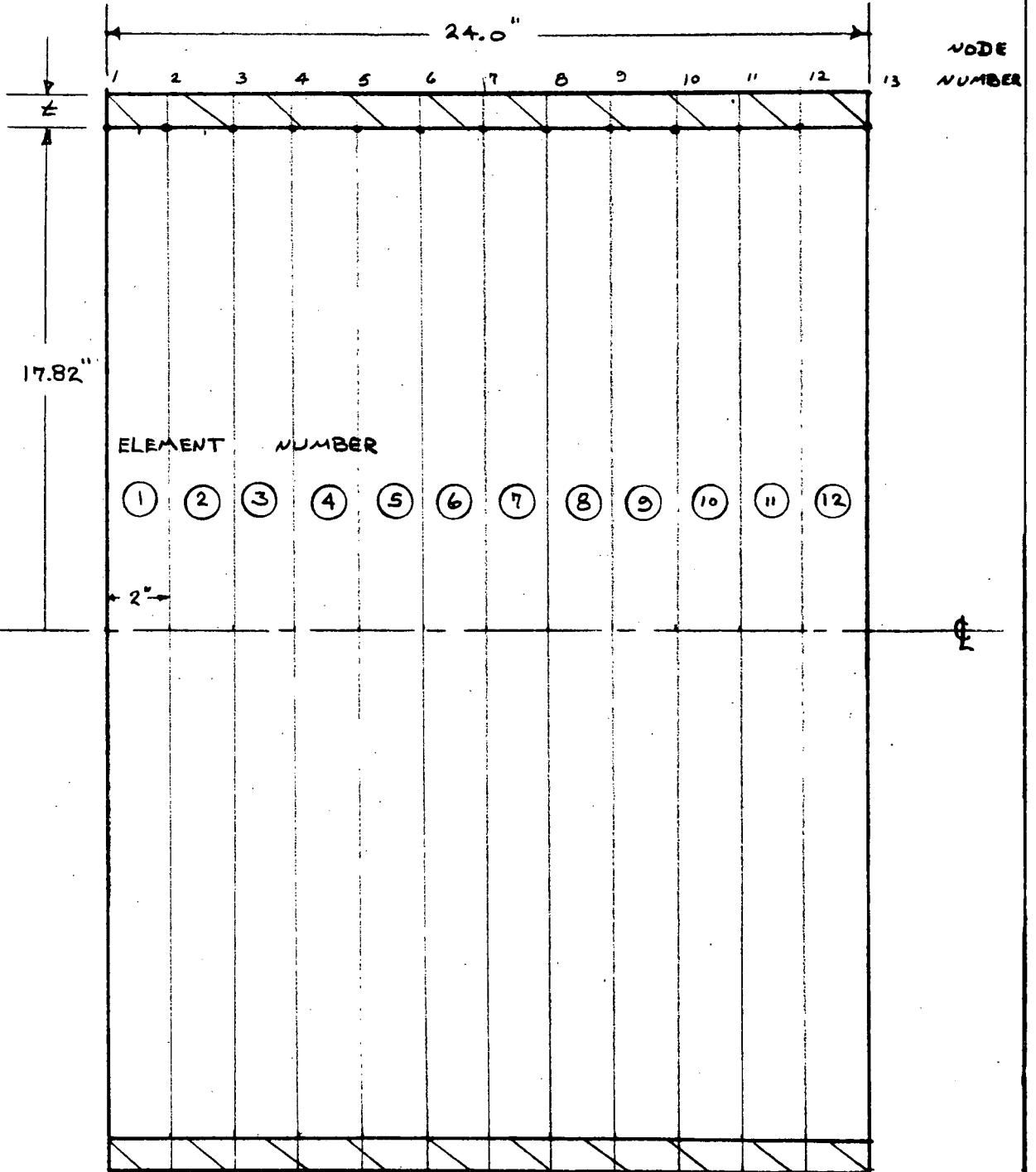
@ x = 0, l

K(001,001)	1.1991501D&09	(001,002)	-3.7252903D-09
(001,004)	-3.1403109D&06	(001,005)	-5.9957507D&08
(001,007)	-4.7104663D&06	(001,008)	1.5701554D&06
(002,002)	5.1617582D&08	(002,006)	-2.5808791D&08
(003,003)	3.0539793D&08	(003,004)	6.7055225D-C8
(003,005)	4.7104663D&06	(003,007)	-1.4892274D&08
(003,008)	1.4942624D&08		
(004,004)	4.0029214D&08	(004,005)	1.5701554D&06
(004,007)	-1.4942624D&08	(004,008)	9.9713394D&07
(005,005)	1.1991501D&09	(005,007)	-3.7252903D-C9
(005,008)	-3.1403109D&06	(005,009)	-5.9957507D&08
(005,011)	-4.7104663D&06	(005,012)	1.5701554D&06
(006,006)	5.1617582D&08	(006,010)	-2.5808791D&08
(007,007)	3.0539793D&08	(007,008)	6.7055225D-C8
(007,009)	4.7104663D&06	(007,011)	-1.4892274D&08
(007,012)	1.4942624D&08		
(008,008)	4.0029214D&08	(008,009)	1.5701554D&06
(008,011)	-1.4942624D&08	(008,012)	9.9713394D&07
(009,009)	1.1991501D&09	(009,011)	-3.7252903D-C9
(009,012)	-3.1403109D&06	(009,013)	-5.9957507D&08
(009,015)	-4.7104663D&06	(009,016)	1.5701554D&06
(010,010)	5.1617582D&08	(010,014)	-2.5808791D&08
(011,011)	3.0539793D&08	(011,012)	6.7055225D-08
(011,013)	4.7104663D&06	(011,015)	-1.4892274D&08
(011,016)	1.4942624D&08		
(012,012)	4.0029214D&08	(012,013)	1.5701554D&06
(012,015)	-1.4942624D&08	(012,016)	9.9713394D&07
(013,013)	1.1991501D&09	(013,015)	-3.7252903D-C9
(013,016)	-3.1403109D&06	(013,017)	-5.9957507D&08
(013,019)	-4.7104663D&06	(013,020)	1.5701554D&06
(014,014)	5.1617582D&08	(014,018)	-2.5808791D&08
(015,015)	3.0539793D&08	(015,016)	6.7055225D-C8
(015,017)	4.7104663D&06	(015,019)	-1.4892274D&08
(015,020)	1.4942624D&08		
(016,016)	4.0029214D&08	(016,017)	1.5701554D&06
(016,019)	-1.4942624D&08	(016,020)	9.9713394D&07
(017,017)	1.1991501D&09	(017,019)	-3.7252903D-09
(017,020)	-3.1403109D&06	(017,021)	-5.9957507D&08
(017,023)	-4.7104663D&06	(017,024)	1.5701554D&06
(018,018)	5.1617582D&08	(018,022)	-2.5808791D&08
(019,019)	3.0539793D&08	(019,020)	6.7055225D-C8
(019,021)	4.7104663D&06	(019,023)	-1.4892274D&08
(019,024)	1.4942624D&08		
(020,020)	4.0029214D&08	(020,021)	1.5701554D&06
(020,023)	-1.4942624D&08	(020,024)	9.9713394D&07
(021,021)	1.1991501D&09	(021,023)	-3.7252903D-09
(021,024)	-3.1403109D&06	(021,025)	-5.9957507D&08
(021,027)	-4.7104663D&06	(021,028)	1.5701554D&06
(022,022)	5.1617582D&08	(022,026)	-2.5808791D&08
(023,023)	3.0539793D&08	(023,024)	6.7055225D-C8
(023,025)	4.7104663D&06	(023,027)	-1.4892274D&08
(023,028)	1.4942624D&08		

K

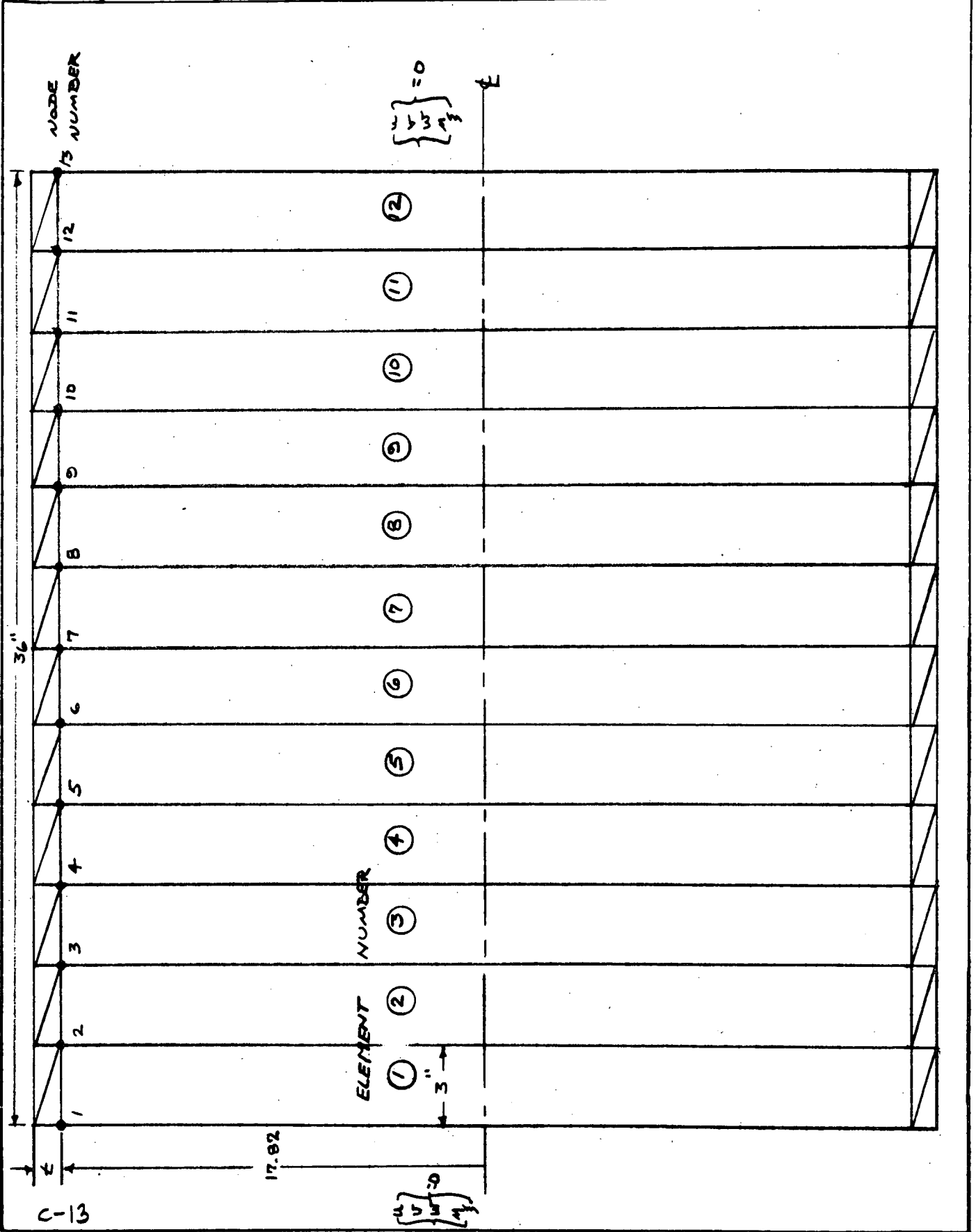
(024,024)	4.00292140&08	(024,025)	1.57015540&06
(024,027)	-1.49426240&08	(024,028)	9.97133940&07
(025,025)	1.19915010&09	(025,027)	-3.72529030-C9
(025,028)	-3.14031090&06	(025,029)	-5.99575070&08
(025,031)	-4.71046630&06	(025,032)	1.57015540&06
(026,026)	5.16175820&08	(026,030)	-2.58087910&08
(027,027)	3.05397930&08	(027,028)	6.70552250-C8
(027,029)	4.71046630&06	(027,031)	-1.48922740&08
(027,032)	1.49426240&08	(028,029)	1.57015540&06
(028,028)	4.00292140&08	(028,032)	9.97133940&07
(028,031)	-1.49426240&08	(029,031)	-3.72529030-C9
(029,029)	1.19915010&09	(029,033)	-5.99575070&08
(029,032)	-3.14031090&06	(029,036)	1.57015540&06
(029,035)	-4.71046630&06	(030,034)	-2.58087910&08
(030,030)	5.16175820&08	(031,032)	6.70552250-C8
(031,031)	3.05397930&08	(031,035)	-1.48922740&08
(031,033)	4.71046630&06	(032,032)	1.57015540&06
(031,036)	1.49426240&08	(032,036)	9.97133940&07
(032,032)	4.00292140&08	(033,035)	-3.72529030-C9
(032,035)	-1.49426240&08	(033,037)	-5.99575070&08
(033,033)	1.19915010&09	(033,040)	1.57015540&06
(033,036)	-3.14031090&06	(034,038)	-2.58087910&08
(033,039)	-4.71046630&06	(035,036)	6.70552250-C8
(034,034)	5.16175820&08	(035,039)	-1.48922740&08
(035,035)	3.05397930&08	(036,037)	1.57015540&06
(035,037)	4.71046630&06	(036,040)	9.97133940&07
(035,040)	1.49426240&08	(037,039)	-3.72529030-C9
(036,036)	4.00292140&08	(037,041)	-5.99575070&08
(036,039)	-1.49426240&08	(037,044)	1.57015540&06
(037,037)	1.19915010&09	(038,042)	-2.58087910&08
(037,040)	-3.14031090&06	(039,040)	6.70552250-C8
(037,042)	-4.71046630&06	(039,043)	-1.48922740&08
(038,038)	5.16175820&08	(039,044)	1.49426240&08
(039,039)	3.05397930&08	(040,040)	4.00292140&08
(039,041)	4.71046630&06	(040,041)	1.57015540&06
(039,044)	1.49426240&08	(040,044)	9.97133940&07
(040,040)	4.00292140&08	(041,043)	-3.72529030-C9
(040,043)	-1.49426240&08	(041,044)	-3.14031090&06
(041,041)	1.19915010&09	(042,042)	5.16175820&08
(041,044)	-3.14031090&06	(043,043)	3.05397930&08
(042,042)	5.16175820&08	(043,044)	6.70552250-C8
(043,043)	3.05397930&08	(044,044)	4.00292140&08
(044,044)	4.00292140&08		

PARA. NO.		TITLE: <b>FIGURE 1.0</b>	ANAL. BY	KEP
DWG. NO.			DATE	NOV 71
LOADS ARE			CHKD. BY	



C-12

PARA. NO.		TITLE: <u>FIGURE 2.0</u>	ANAL. BY	KEP
DWG. NO.			DATE	DEC 71
LOADS ARE			CHKD. BY	



PARA. NO.		TITLE:	ANAL. BY	KEP
DWG. NO.			DATE	DEC 71
LOADS ARE			CHKD. BY	

III NATURAL FREQUENCY ANALYSIS FOR  
THREE CONFIGURATIONS.

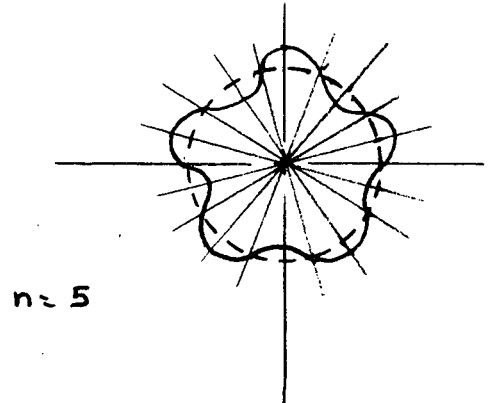
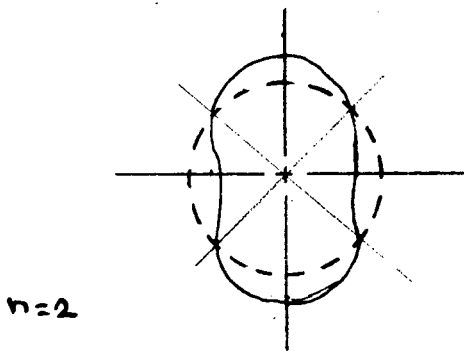
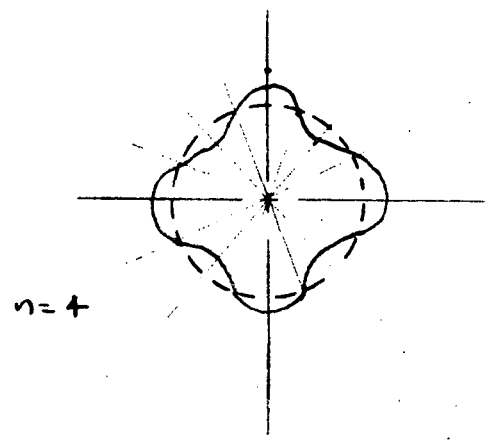
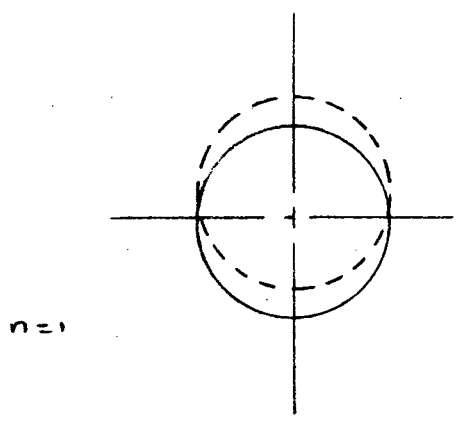
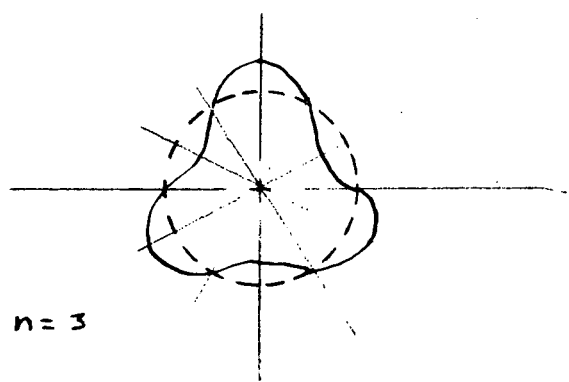
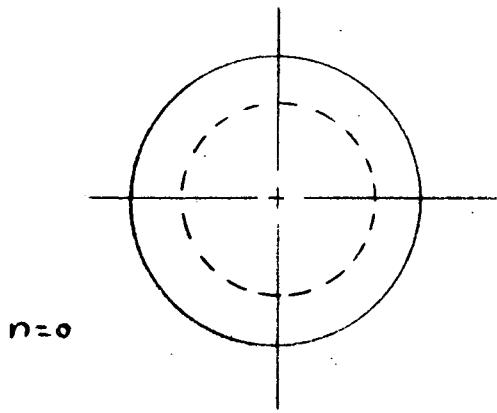
WITH THE EQUATIONS CAST IN THE FORM OF EQUATION (2) FOR EACH VALUE OF THE CIRCUMFERENTIAL INDEX  $n$ , A STANDARD EIGENVALUE ANALYSIS WAS CARRIED OUT. THE SOLUTION WAS PERFORMED ON THE AVO DIGITAL COMPUTER PROGRAM 2607 WHICH USES A MODIFIED HOUSEHOLDER GIVENS ROUTINE TO OBTAIN THE UNDAMPED FREQUENCIES AND MODE SHAPES.

IN DEALING WITH A SHELL STRUCTURE, CONSIDERATION MUST BE GIVEN TO BOTH LONGITUDINAL AND CIRCUMFERENTIAL MODES. THIS IS UNLIKE A BEAM WHICH CONTAINS ONLY LONGITUDINAL BENDING MODES. NO CONSIDERATION IS GIVEN HERE TO AXIAL VIBRATION, WHICH IS A HIGH FREQUENCY CHARACTERISTIC. THEREFORE, ANY SHELL VIBRATION MODE HAS ASSOCIATED WITH IT A LONGITUDINAL MODE INDEX  $m$  AND A CIRCUMFERENTIAL INDEX  $n$ . THE INDEX  $m$  CAN BE THOUGHT OF AS THE BEHAVIOR OF THE SHELL DOWN ITS LENGTH.

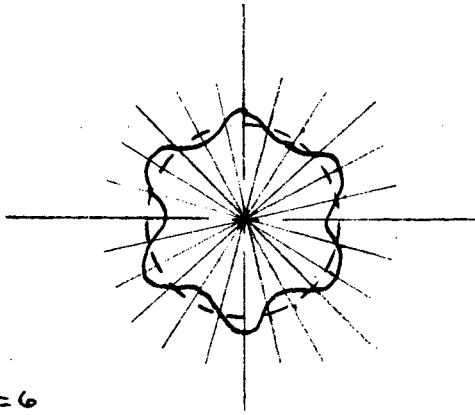
THE MINIMUM NATURAL FREQUENCY FOR THE SHELL OCCURS AT A PARTICULAR VALUE OF THE INDEX  $n$ , AND THE VALUE  $m=1$ . MODES OF CIRCUMFERENTIAL VIBRATION FOR  $n=0 \rightarrow 10$  ARE SHOWN ON THE FOLLOWING PAGES, ALONG WITH THE FIRST THREE MODES OF LONGITUDINAL VIBRATION.

PARA. NO.		TITLE: <i>CIRCUMFERENTIAL NODAL PATTERN</i>	ANAL. BY	KEP
DWG. NO.			DATE	NOV 71
LOADS ARE			CHKD. BY	

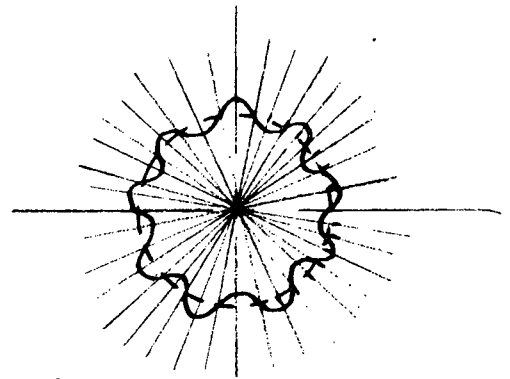
HARMONICS OF CIRCUMFERENTIAL DEFORMATION  
(COSINE EXPANSION)



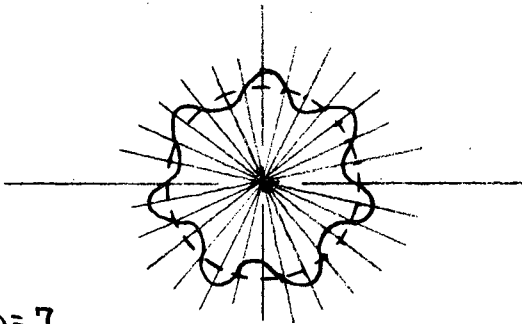
PARA. NO.		TITLE: <i>CIRCUMFERENTIAL NODAL PATTERN</i>	ANAL. BY	KEP
DWG. NO.			DATE	NOV 71
LOADS ARE			CHKD. BY	



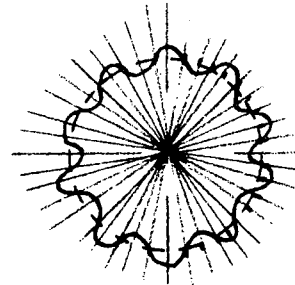
$n=6$



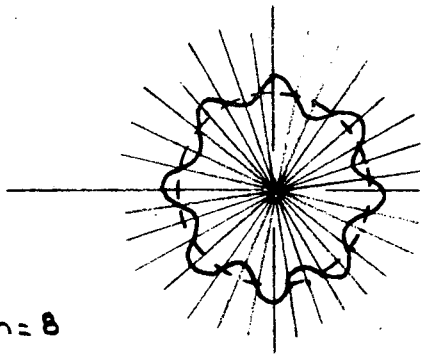
$n=9$



$n=7$



$n=10$

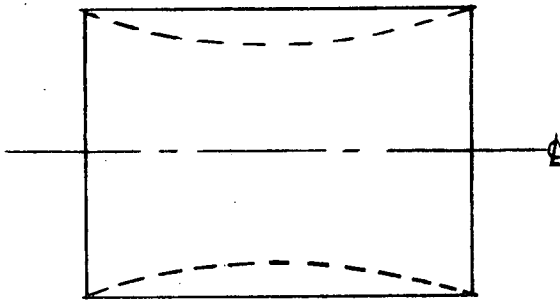


$n=8$

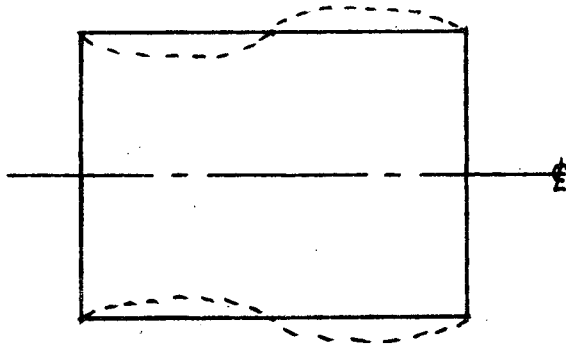
PARA. NO.		TITLE: <i>AXIAL NODAL PATTERN</i>	ANAL. BY	<i>KEP</i>
DWG. NO.			DATE	<i>DEC 71</i>
LOADS ARE			CHKD. BY	

HARMONICS OF LONGITUDINAL DEFORMATION

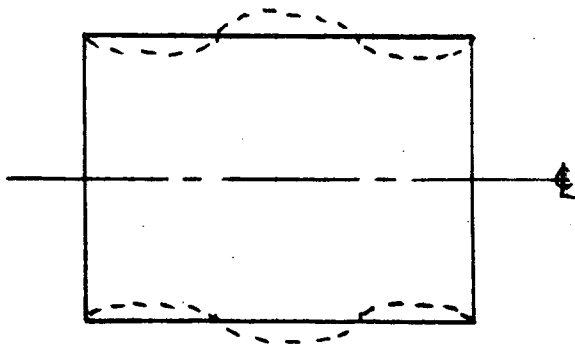
$m = 1$



$m = 2$



$m = 3$



PARA. NO.		TITLE:	ANAL. BY	KEP
DWG. NO.			DATE	DEC 71
LOADS ARE			CHKD. BY	

TABLES OF NATURAL FREQUENCIES FOR EACH OF THE CASES CONSIDERED ARE PRESENTED. THE FUNDAMENTAL (LOWEST) FREQUENCY FOR THE HALF INCH THICK CASE IS 702 CPS ( $m=1, n=5$ ), AND FOR THE ONE INCH THICK CASE IT IS 1024 CPS ( $m=1, n=4$ ). BOTH OF THESE ARE FOR THE 24" LONG CYLINDER. FOR THE 36" LONG  $\frac{3}{4}$ " THICK CONFIGURATION A TABLE OF THE FIRST FOUR NATURAL FREQUENCIES FOR CIRCUMFERENTIAL HARMONICS 0  $\rightarrow$  6 IS PRESENTED. THE FUNDAMENTAL FREQUENCY FOR THIS CASE IS 583 CPS. THIS CORRESPONDS TO THE MODE  $m=1$  AND  $n=4$ .

PARA. NO.		TITLE: <b>EIGENVALUES ~ HZ</b>	ANAL. BY	KEP
DWG. NO.			DATE	DEC 71
LOADS ARE			CHKD. BY	

$\left. \begin{matrix} u_3 \\ u_0 \\ w \\ m_3 \end{matrix} \right\} = 0 \quad @ \quad x=0, l$

$z = 0.50''$        $l = 24''$

(m=1)

n	f <sub>1</sub>	f <sub>2</sub>	f <sub>3</sub>	f <sub>4</sub>
n=0	2041	2060	2175	2490
n=1	1627	1970	2150	2480
n=2	1264	1755	2070	2460
n=3	886	1520	1970	2420
n=4	733	1335	1865	2410
n=5	<u>702</u>	1240	1815	2420
n=6	779	1250	1830	2480
n=7	939	1350	1915	2600
n=8	1155	1520	2065	2750
n=9	1430	1760	2280	2960
n=10	1740	2050	2550	3220

PARA. NO.		TITLE: <b>EIGENVALUES ~HZ</b>	ANAL. BY	KFP
DWG. NO.			DATE	DEC 71
LOADS ARE			CHKD. BY	

	$z = 1.00$ ( $m=1$ )		$\lambda = 24''$	$\left. \begin{matrix} u_3 \\ u_0 \\ w \\ \phi_3 \end{matrix} \right\} = 0$	@ $x=0, \lambda$
		$f_1$	$f_2$	$f_3$	$f_4$
$n=0$		2076	2311	2995	3130
$n=1$		1678	2242	2977	3910
$n=2$		1265	2085	2964	4230
$n=3$		1050	1955	2976	4300
$n=4$		<u>1024</u>	1929	3044	4440
$n=5$		1172	2034	3190	4640
$n=6$		1456	2260	3430	4900
$n=7$		1844	2600	3750	5240
$n=8$		2317	3040	4170	5650
$n=9$		2865	3550	4650	6150
$n=10$		3484	4160	5250	6700

PARA. NO.		TITLE: <b>EIGENVALUES ~ Hz</b>	ANAL. BY	KEP
DWG. NO.			DATE	DEC 71
LOADS ARE			CHKD. BY	

$$\begin{Bmatrix} u \\ v \\ w \\ m \end{Bmatrix} = 0 \quad @ x = 0, l$$

$t = 0.750$   
(m=1)       $l = 36''$

	$f_1$	$f_2$	$f_3$	$f_4$
n=0	1782	2031	2051	2086
n=1	1210	1870	2020	2210
n=2	831	1450	1815	2220
n=3	614	1155	1615	2030
n=4	<u>583</u>	1022	1494	1980
n=5	711	1050	1495	2010
* n=6	946	1220	1620	2130

\* NOTE HARMONIC ANALYSIS TERMINATED  
@ n=6 SINCE FREQUENCIES FOR n > 6  
ARE ON THE INCREASE.

PARA. NO.		TITLE:	ANAL. BY	KEP
DWG. NO.			DATE	DEC 71
LOADS ARE			CHKD. BY	

IV STRESS ANALYSIS BASED ON AN EXTREME DEFORMATION CONFIGURATION, OF RANDOM VIBRATION.

THE STRESS ANALYSIS OF THE CYLINDRICAL SHELL WAS CARRIED OUT USING THE STRESS RESULTANT COEFFICIENT MATRICES GENERATED BY SABOR III. THESE MATRICES ALLOW FOR THE STRAIGHT FORWARD COMPUTATION OF THE STRESS RESULTANTS AT ANY ELEMENT NODE ONCE THE NODAL DISPLACEMENTS ARE KNOWN.

WITH STRESS RESULTANTS KNOWN, THE STRESSES THEMSELVES CAN BE COMPUTED USING THE FOLLOWING RELATIONSHIPS FROM REFERENCE (1). THE STRESS RESULTANT SIGN CONVENTION IS SHOWN ON THE NEXT PAGE AND WILL BE FOLLOWED HENCE FORTH.

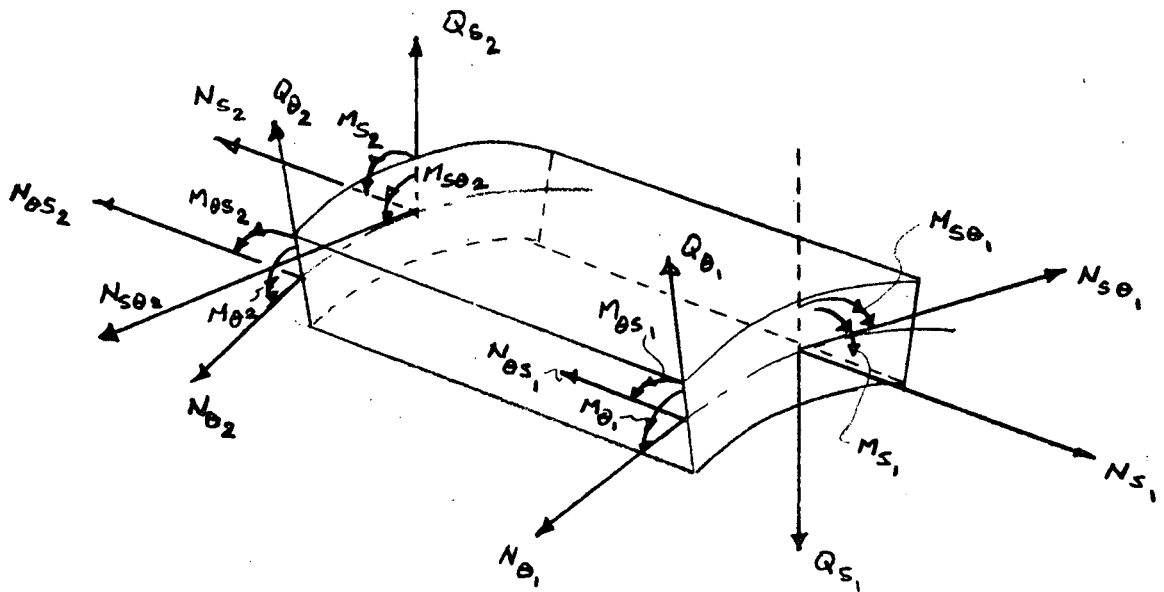
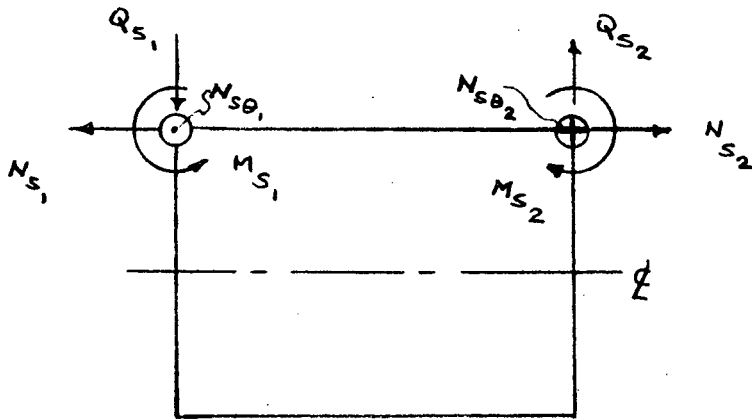
$$\sigma_z = \frac{N_z}{t} + \frac{12 M_z z}{t^3}$$

$$\sigma_\theta = \frac{N_\theta}{t} + \frac{12 M_\theta z}{t^3}$$

$$\gamma_{z\theta} = \frac{N_{z\theta}}{t} + \frac{12 M_{z\theta} z}{t^3}$$

PARA. NO.		TITLE:	ANAL. BY	KEP
DWG. NO.			DATE	NOV 71
LOADS ARE			CHKD. BY	

SHELL STRESS RESULTANTS & SIGN CONVENTION :



COMPUTE @ EACH NODE

$M(S), M(T), M(ST), N(S), N(T), N(ST), Q(S), Q(T)$

PARA. NO.		TITLE:	ANAL. BY	KEP
DWG. NO.			DATE	DEC 71
LOADS ARE			CHKD. BY	

THE STRESS RESULTANT COEFFICIENT MATRICES FOR ANY ELEMENT ARE OF ORDER  $16 \times 8$ , AND WHEN POST MULTIPLIED BY AN ELEMENT DISPLACEMENT VECTOR, OF ORDER  $8 \times 1$ , YIELD THE ELEMENT STRESS RESULTANT COEFFICIENT VECTOR, OF ORDER  $16 \times 1$ . THIS IS INDICATED AS FOLLOWS, FOR ANY HARMONIC  $n$ .

$$\{N\}_n = [B]_n \{s\}_n$$

WHERE :

$\{N\}$  = ELEMENT STRESS RESULTANTS

$[B]$  = ELEMENT STRESS RESULT. COEFF.

$\{s\}$  = ELEMENT DISPLACEMENT FIELD

THIS OPERATION IS CARRIED OUT REPEATEDLY FOR ALL OF THE ELEMENTS OF THE MODEL TO OBTAIN THE STRESS PICTURE BASED ON A NODAL DISPLACEMENT CONFIGURATION.

PARA. NO.		TITLE:	ANAL. BY	KEP
DWG. NO.			DATE	DEC 71
LOADS ARE			CHKD. BY	

FOUR DIFFERENT STRESS CONFIGURATIONS WERE EXAMINED, AND THE RESULTS OBTAINED HEREIN ARE FOR A 3 $\sigma$  STATE OF RANDOM VIBRATION. THE CENTER DEFLECTION VALUE OF NORMAL DISPLACEMENT "W" USED TO SCALE THE MODE SHAPES IN EACH OF THE CASES IS GIVEN AS

CASE	n	$f_n$	$\delta_{1\sigma}$	$\delta_{3\sigma}$
$t = 1''$ $\lambda = 24''$	4	1024 Hz	$3.6 \times 10^{-4}$	$10.8 \times 10^{-4}$
$t = 1/2''$ $\lambda = 24''$	5	702 Hz	$8.01 \times 10^{-4}$	$24.03 \times 10^{-4}$
$t = 1/2''$ $\lambda = 24''$	1	1627 Hz	$1.05 \times 10^{-4}$	$3.15 \times 10^{-4}$
$t = 3/4''$ $\lambda = 36''$	4	583 Hz	$11.32 \times 10^{-4}$	$33.96 \times 10^{-4}$

MODE SHAPES NORMALIZED, SUCH THAT THE CENTER VALUE OF NORMAL DISPLACEMENT IS 1.0", ARE GIVEN ON THE FOLLOWING PAGES FOR THE FIRST THREE CASES.

PARA. NO.		TITLE:	ANAL. BY	KEP
DWG. NO.			DATE	DEC 71
LOADS ARE			CHKD. BY	

$t = 1.0''$       ENDS ARE FIXED       $\begin{Bmatrix} w \\ u \\ v \\ \frac{\partial w}{\partial x} \end{Bmatrix} = 0$   
 $n = 4$  ,  $m = 1$   
 WILL BE THE MINIMUM FREQUENCY  
 CONSIDERED.

	CENTER @ $w_0 = 2.828$ IN.	CENTER @ $w_0 = 1.00$ IN.	
$f_1$	-0.046	-0.016	$u_1$
$f_2$	-0.109	-0.038	$v_1$
$f_3$	0.332	0.117	$w_1$
$f_4$	0.286	0.101	$A_1$
$f_5$	-0.072	-0.025	$u_2$
$f_6$	-0.251	-0.089	$v_2$
$f_7$	1.01	0.357	$w_2$
$f_8$	0.365	0.129	$A_2$
$f_9$	-0.077	-0.027	$u_3$
$f_{10}$	-0.400	-0.141	$v_3$
$f_{11}$	1.720	0.610	$w_3$
$f_{12}$	0.335	0.118	$A_3$
$f_{13}$	-0.064	-0.023	$u_4$
$f_{14}$	-0.528	-0.187	$v_4$
$f_{15}$	2.311	0.817	$w_4$
$f_{16}$	0.249	0.088	$A_4$
$f_{17}$	-0.036	-0.013	$u_5$
$f_{18}$	-0.614	-0.217	$v_5$
$f_{19}$	2.695	0.953	$w_5$
$f_{20}$	0.131	0.046	$A_5$
$f_{21}$	0.0	0.0	$u_6$
$f_{22}$	-0.644	-0.228	$v_6$
$f_{23}$	2.828	1.00	$w_6$
$\vdots$	$\vdots$	$\vdots$	$A_6$

PARA. NO.		TITLE:	ANAL. BY	KEP
DWG. NO.			DATE	DEC 71
LOADS ARE			CHKD. BY	

$t = \frac{1}{2}$ "

ENDS ARE FIXED EXCEPT FOR ROTATION

$$\begin{Bmatrix} u \\ v \\ w \\ M_3 \end{Bmatrix} = 0$$

$n = 5, m = 1$

MINIMUM FREQUENCY CONSIDERED

$f_n = 702$  CPS

(CENTER @  $w_0 = 1.0$  IN.)

$f_i$	$\phi$	FREQUENCY	EDGE
$f_1$	0.466	0.122	$\beta_1$
$f_2$	-0.063	-0.016	$u_1$
$f_3$	-0.157	-0.041	$v_1$
$f_4$	0.922	0.242	$w_1$
$f_5$	0.453	0.119	$\beta_1$
$f_6$	-0.095	-0.025	$u_2$
$f_7$	-0.330	-0.087	$v_2$
$f_8$	1.803	0.473	$w_2$
$f_9$	0.425	0.111	$\beta_2$
$f_{10}$	-0.099	-0.026	$u_3$
$f_{11}$	-0.492	-0.129	$v_3$
$f_{12}$	2.602	0.683	$w_3$
$f_{13}$	0.368	0.096	$\beta_3$
$f_{14}$	-0.099	-0.021	$u_4$
$f_{15}$	-0.623	-0.164	$v_4$
$f_{16}$	3.249	0.855	$w_4$
$f_{17}$	0.272	0.071	$\beta_4$
$f_{18}$	-0.043	-0.011	$u_5$
$f_{19}$	-0.708	-0.186	$v_5$
$f_{20}$	3.669	0.961	$w_5$
$f_{21}$	0.144	0.038	$\beta_5$
$f_{22}$	0.0	0.0	$u_6$
$f_{23}$	-0.737	-0.194	$v_6$
$f_{24}$	3.814	1.0	$w_6$
$f_{25}$	0.0	0.0	$\beta_6$

PARA. NO.		TITLE:	ANAL. BY	KEP
DWG. NO.			DATE	DEC 71
LOADS ARE			CHKD. BY	

$t = \frac{1}{2}''$

ENDS ARE

$$\begin{Bmatrix} u_3 \\ u_0 \\ w_3 \\ m_3 \end{Bmatrix} = 0$$

$n=1, m=1, f_n = 1627 \text{ cps}$

@  $x=0, l$

$\phi_1$

CENTER @

$w_6 = 1.00 \text{ IN.}$

$\{q\} =$	}	$f_1$	-0.478	-0.134	<u><math>\beta_{EDGE}</math></u>
		$f_2$	0.014	0.004	$u_1$
		$f_3$	0.035	0.0098	$v_1$
		$f_4$	-0.942	-0.266	$w_1$
		$f_5$	-0.457	-0.128	$\beta_1$
		$f_6$	0.022	0.006	$u_2$
		$f_7$	0.670	0.188	$v_2$
		$f_8$	-1.806	-0.509	$w_2$
		$f_9$	-0.402	-0.113	$\beta_2$
		$f_{10}$	0.022	0.0062	$u_3$
		$f_{11}$	0.948	0.266	$v_3$
		$f_{12}$	-2.536	-0.715	$w_3$
		$f_{13}$	-0.325	-0.0910	$\beta_3$
		$f_{14}$	0.016	0.0045	$u_4$
		$f_{15}$	1.162	0.325	$v_4$
		$f_{16}$	-3.092	-0.865	$w_4$
		$f_{17}$	-0.228	-0.064	$\beta_4$
		$f_{18}$	0.005	0.0014	$u_5$
		$f_{19}$	1.296	0.365	$v_5$
		$f_{20}$	-3.439	-0.960	$w_5$
		$f_{21}$	-0.117	-0.033	$\beta_5$
		$f_{22}$	-0.007	-0.002	$u_6$
		$f_{23}$	1.341	0.376	$v_6$
		$f_{24}$	-3.557	-1.0	$w_6$
		$f_{25}$	0.0	0.0	$\beta_6$
...	:	:			
...	:	:			

PARA. NO.		TITLE:	ANAL. BY	KEP
DWG. NO.			DATE	DEC 71
LOADS ARE			CHKD. BY	

THE COMPUTATION OF THE SHELL STRESSES AT THE ELEMENT INTERFACES BASED ON THE STRESS RESULTANTS IS CARRIED OUT NEXT. TABLES SHOW THE CONTRIBUTIONS OF BENDING AND MEMBRANE STRESSES, AND PLOTS ARE GIVEN WHICH SHOW THEIR BEHAVIOR DOWN THE LENGTH OF ONE HALF OF THE MIRROR. SINCE THESE STRESSES ARE FOR THE SYMMETRIC  $m = 1$  MODE THE PATTERN IS REPEATED IN THE OTHER HALF OF THE SHELL.

DUE TO THE OSCILLATION OF THE SHELL INWARDS AND OUTWARDS THE SIGNS (TENSION OR COMPRESSION) OF THE STRESSES WILL FLUCTUATE. THEREFORE WHEN READING THE FOLLOWING STRESS PLOTS PEAK ABSOLUTE VALUES MUST BE KEPT IN MIND.

PARA. NO.		TITLE: <u>t = 1.0    N = 4    m = 1</u>	ANAL. BY	
DWG. NO.			DATE	
LOADS ARE			CHKD. BY	

X-in	N <sub>f</sub>	M <sub>f</sub>	M <sub>0</sub>	N <sub>0</sub>	N <sub>f0</sub>	M <sub>f0</sub>
0.0	-115.5	-74.24	-10.	-12.95	-77.2	-.9
2.0	-77.6	-28.0	+1.31	-30.	-95.9	+17.6
4.0	-31.8	-.04	15.8	-.97	-100.2	22.8
6.0	+9.6	+18.7	29.7	+33.1	-94.1	20.9
8.0	53.6	25.05	39.8	52.9	-67.4	15.7
10.0	79.8	29.7	46.5	65.7	-36.2	8.3
12.0	88.79	32.9	49.1	67.6	-2.9	-.26

X-in	σ <sub>f</sub> (MEMBRANE STRESS)	σ <sub>0</sub>	τ <sub>f0</sub>	σ <sub>3</sub> (MEMBRANE + BENDING)	σ <sub>0</sub>	τ <sub>30</sub>
0.0	-115.5	-12.95	-77.2	-561.	-72.95	-82.6
2.0	-77.6	-30	-95.9	-246.	-37.86	-201.5
4.0	-31.8	-9.7	-100.2	-32.0	-104.5	-237.
6.0	+9.6	+33.1	-94.1	+121.6	211.3	-219.5
8.0	53.6	52.9	-67.4	204.0	291.7	-161.6
10.0	79.8	65.7	-36.2	258.0	344.7	-86.0
12.0	88.79	67.6	-2.9	286.	362.2	-6.02



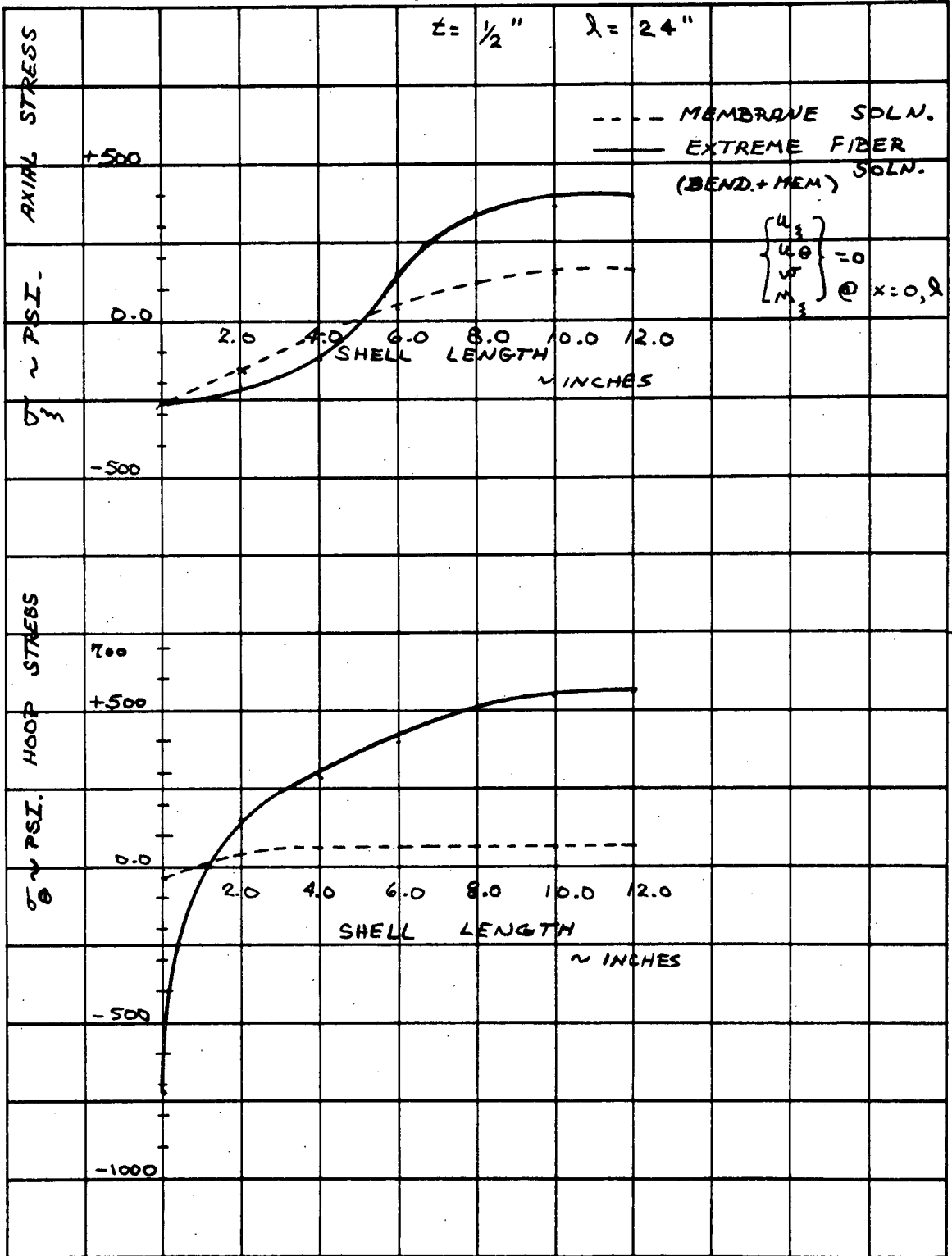
PARA. NO.		TITLE: $t = \frac{1}{2}''$ $n = 5$	ANAL. BY	KEP
DWG. NO.			DATE	DEC 71
LOADS ARE			CHKD. BY	

X IN.	$N_3$	$M_3$	$M_0$	$N_0$	$N_{50}$	$M_{50}$
0.0	- 130	0.0	- 29	- 14.4	- 98.2	7.62
2.0	- 81.5	1.92	+ 4.80	18.5	- 100.	7.38
4.0	- 23.7	3.07	+ 9.71	26.4	- 84.0	6.90
6.0	19.7	4.47	+ 14.0	32.0	- 69.5	5.98
8.0	57.5	9.46	+ 18.15	34.10	- 46.4	4.45
10.0	71.2	8.90	+ 20.2	32.2	- 24	2.40
12.0	79.0	9.85	+ 21.0	31.4	- 2.9	0.0

X IN.	MEMBRANE $\mu$ psi			EXTREME FIBER (MEMBRANE + BENDING) $\mu$ psi		
	$\sigma_3$	$\sigma_0$	$\gamma_{30}$	$\sigma_3$	$\sigma_0$	$\gamma_{30}$
0.0	- 260.	- 28.8	- 196.5	- 260	- 725	- 379.5
2.0	- 163.	+ 37.0	- 200	- 209	152	- 377
4.0	- 47.4	52.8	- 168	- 121.2	286	- 334
6.0	+ 39.4	64.0	- 139	+ 146.4	400	- 282
8.0	115.	68.20	- 92.8	+ 342	503	- 200
10.0	142.4	64.4	- 48	+ 356	549	- 106
12.0	158	62.8	- 5.8	+ 394	567	- 5.8

# STRESS DISTRIBUTION

$n = 5 \quad m = 1 \quad f_n = 702 \text{ Hz}$





PARA. NO.		TITLE: $t = \frac{1}{2}''$ $n = 1$	ANAL. BY	KEP
DWG. NO.			DATE	DEC 71
LOADS ARE			CHKD. BY	

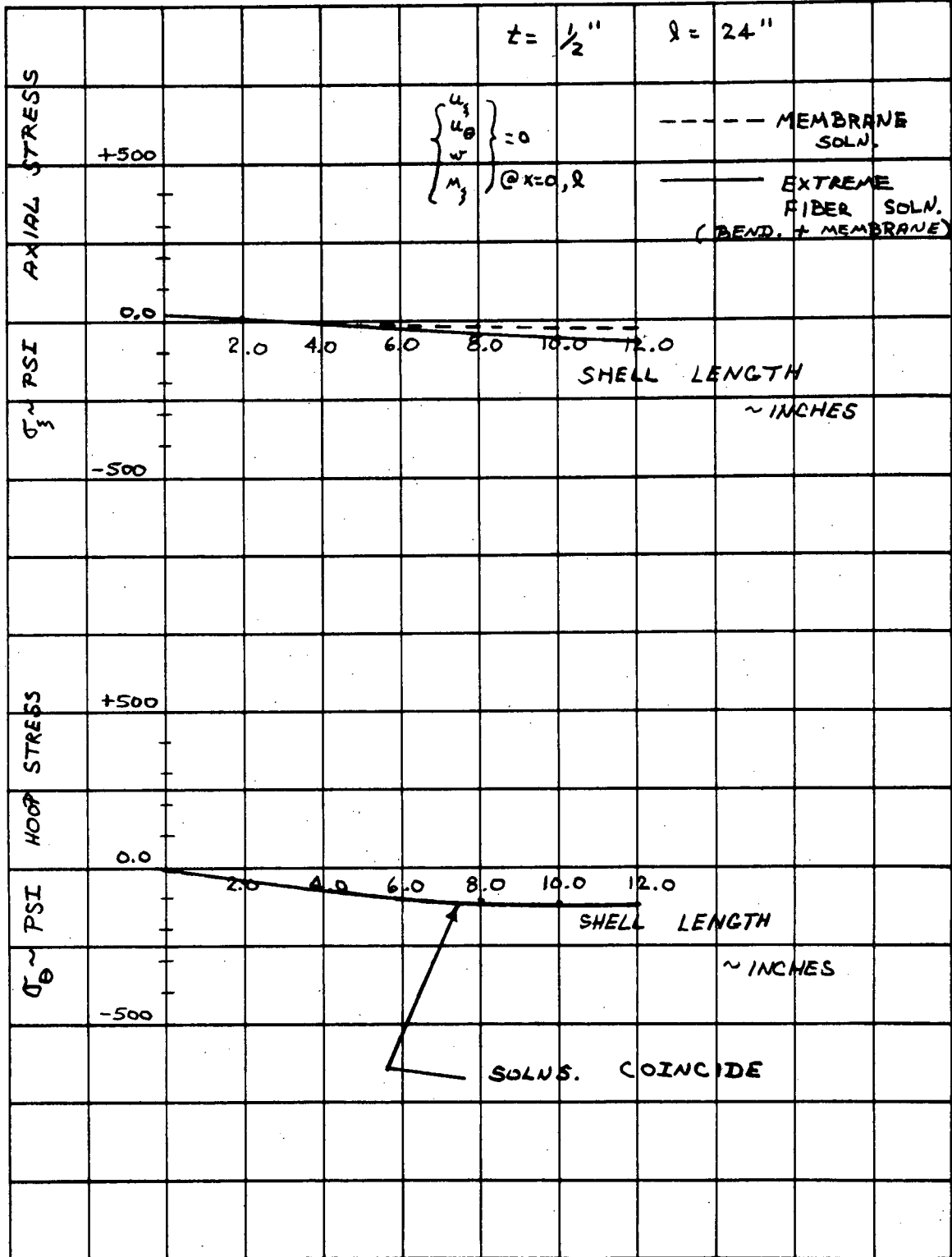
X IN.	$N_{\xi}$	$M_{\xi}$	$M_{\theta}$	$N_{\theta}$	$N_{\xi\theta}$	$M_{\xi\theta}$
0.0	1.86	- 0.120	0.0	0.472	3.87	- 0.218
2.0	1.450	- 0.610	- 0.043	- 23.9	65.9	- 0.066
4.0	- 2.91	- 0.952	- 0.0945	- 29.9	62.7	- 0.041
6.0	- 6.86	- 1.62	- 0.153	- 42.5	+ 23.6	- 0.104
8.0	- 9.40	- 1.67	- 0.151	- 51.5	17.40	- 0.075
10.0	- 10.85	- 1.31	- 0.094	- 56.6	7.25	- 0.047
12.0	- 11.30	- 2.06	- 0.20	- 59.5	0.68	0.0

X IN.	MEMBRANE - psi			EXTREME FIBER (MEMBRANE & BENDING)		
	$\sigma_{\xi}$	$\sigma_{\theta}$	$\tau_{\xi\theta}$	$\sigma_{\xi}$	$\sigma_{\theta}$	$\tau_{\xi\theta}$
0.0	3.72	0.945	7.74	6.60	0.945	12.99
2.0	2.90	- 47.8	131.8	17.55	- 47.9	133.38
4.0	- 2.20	- 59.8	123.4	- 24.8	- 62.10	124.4
6.0	- 17.35	- 85.0	47.20	- 56.25	- 88.67	49.70
8.0	- 18.80	- 103.0	34.80	- 58.80	- 106.62	36.60
10.0	- 21.70	- 113.2	14.50	- 53.2	- 115.46	15.63
12.0	- 22.60	- 119.0	1.36	- 72.10	- 124.0	1.36

C-35

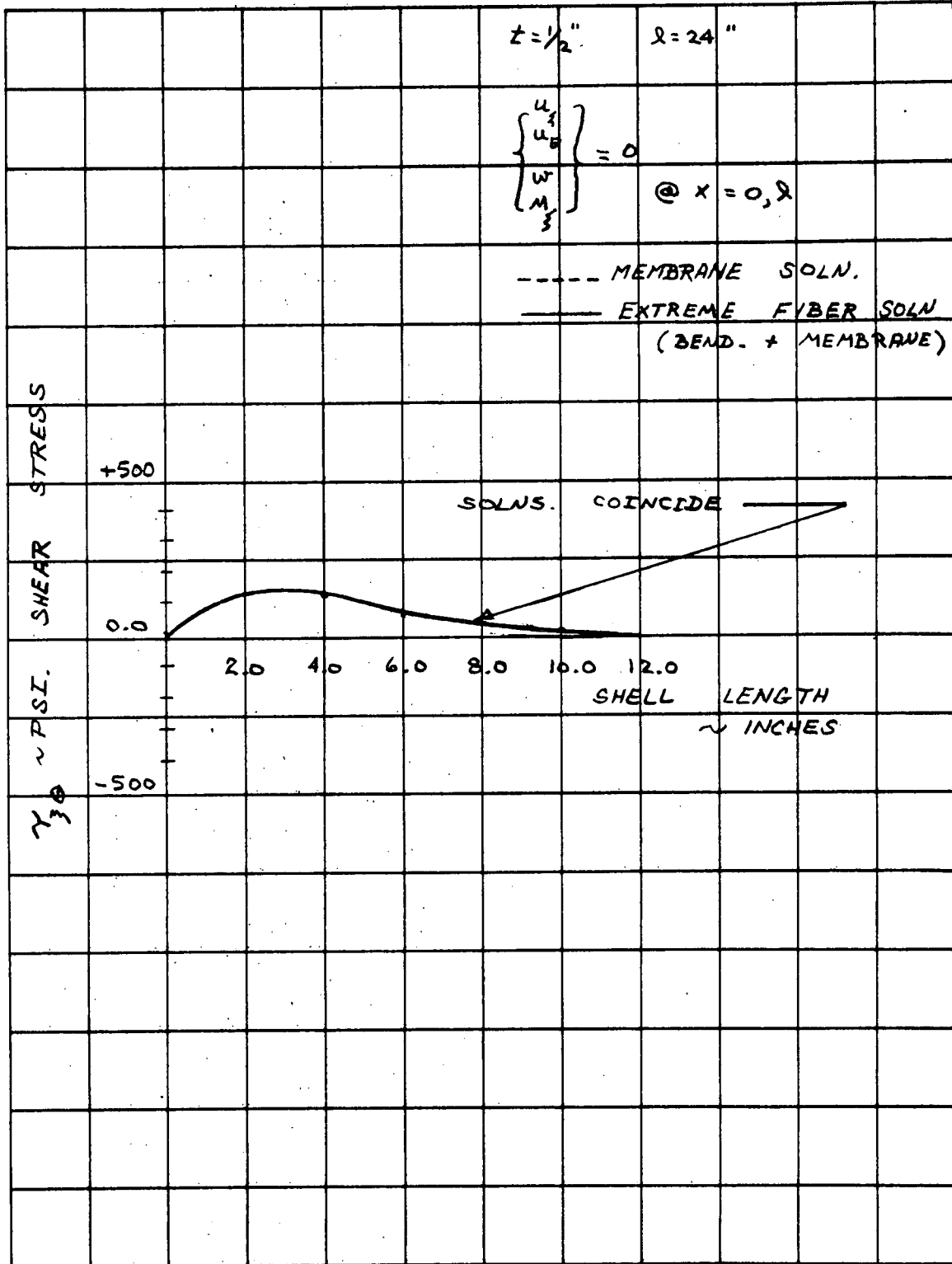
# STRESS DISTRIBUTION

$n = 1 \quad m = 1 \quad f_n = 1627 \text{ Hz}$



# STRESS DISTRIBUTION

$n=1 \quad m=1 \quad f_n = 1627 \text{ Hz}$



PARA. NO.		TITLE: $t = \frac{3}{4}''$ $n = 4$ $R = 36''$	ANAL. BY	KEP
DWG. NO.			DATE	DEC 71
LOADS ARE			CHKD. BY	

X IN.	$N_3$	$M_3$	$M_0$	$N_0$	$N_{30}$	$M_{30}$
0.0	261.9	-4.8	-0.08	28.9	155.5	-17.8
3.0	151.2	-3.8	-13.8	-32.9	157.6	-17.4
6.0	48.6	-7.98	-27.5	-38.4	134.5	-17.1
9.0	-37.4	-14.6	-40.9	-37.5	106.2	-15.4
12.0	-102.5	-20.5	-52.1	-37.4	73.6	-11.8
15.0	-144.0	-24.1	-59.4	-37.3	37.0	-6.4
18.0	-157.7	-25.9	-62.1	-36.1	2.9	0.21

MEMBRANE  $\mu\text{psi}$

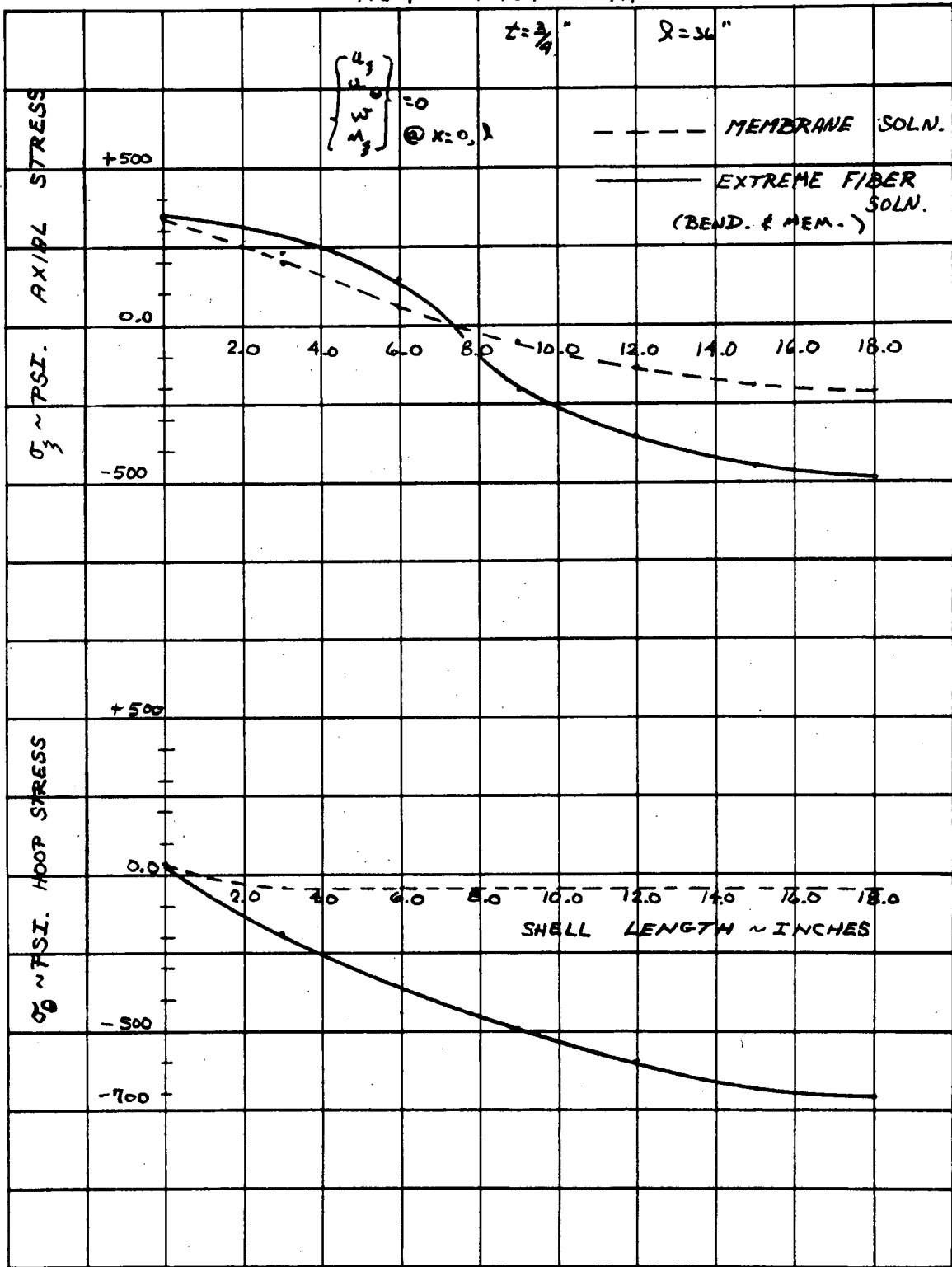
EXTREME FIBER (MEMBRANE + BENDING)

X IN.	$\sigma_3$	$\sigma_0$	$\gamma_{30}$	$\sigma_3$	$\sigma_0$	$\gamma_{30}$
0.0	350.	38.6	208.	355.1	39.4	397
3.0	202.	-44.	211.	242	-191.	396
6.0	65.3	-51.3	180.	150.3	-444.	362
9.0	-50.0	-50.1	141.5	-205.	-486.	305.5
12.0	-136.	-50.	99.0	-354	-605.	224.5
15.0	-192.5	-50.	49.4	-449.5	-684.	117.4
18.0	-211.0	-48.2	3.88	-487.0	-709.	6.12

C-38

### STRESS DISTRIBUTION

$n = 4 \quad m = 1 \quad f_n = 583 \text{ Hz}$



# STRESS DISTRIBUTION

$n = 4$

$m = 1$

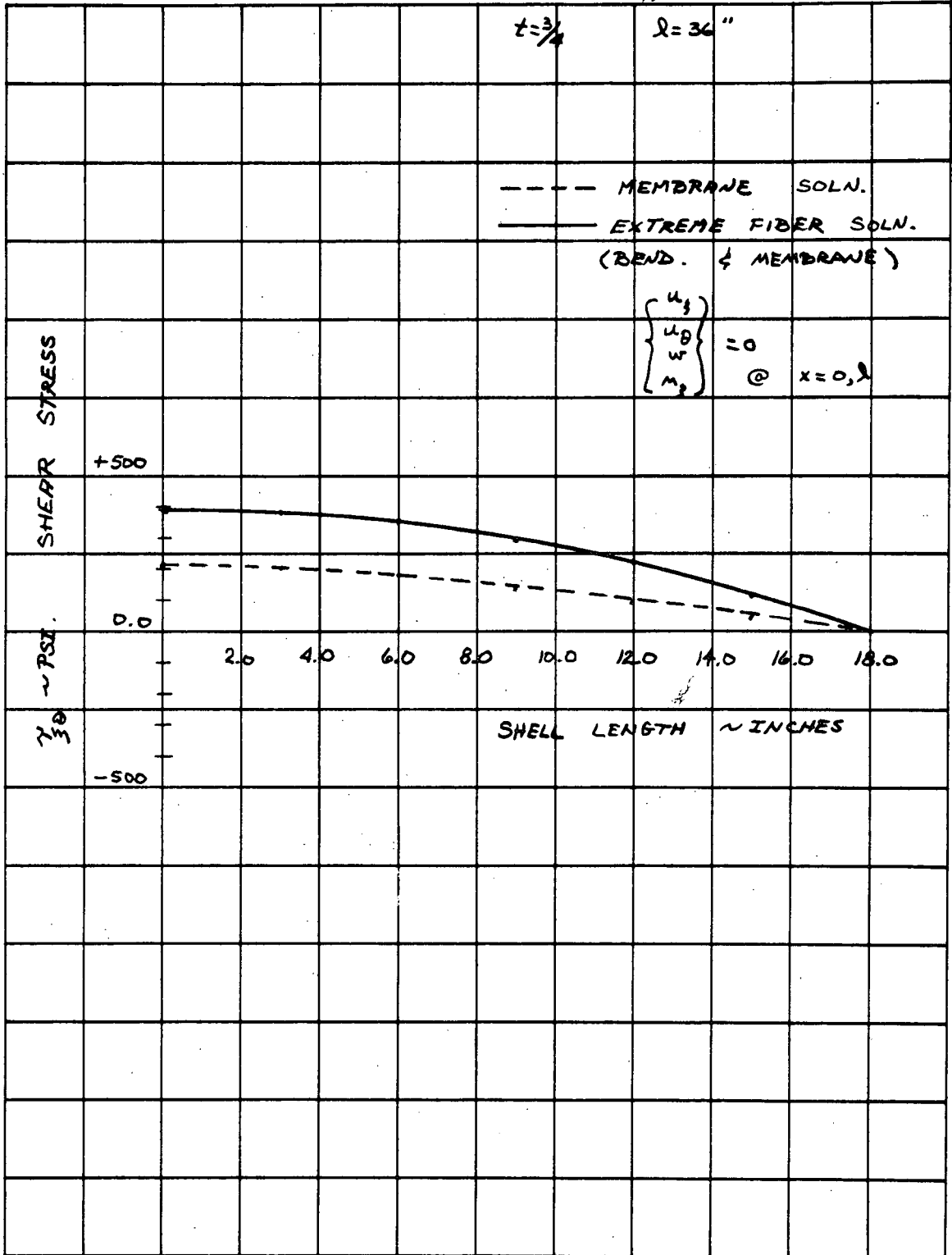
$f_n = 583 \text{ Hz}$

$t = \frac{3}{4}$

$l = 36''$

- - - MEMBRANE SOLN.  
 ——— EXTREME FIBER SOLN.  
 (BEND. & MEMBRANE)

$$\begin{Bmatrix} u_3 \\ u_D \\ w \\ m_2 \end{Bmatrix} = 0 \quad @ \quad x = 0, l$$



APPENDIX D

OPTICAL BENCH ANALYSIS

D-1

## 1.0 INTRODUCTION

The objective of this analysis was to determine conceptually, with as much emphasis on actual design as time allowed, the optimum structural and mounting configuration for the LOXT based on static, dynamic and optical alignment criteria for the telescope and optical bench.

The analysis consists of the following three sections:

- (1) Dynamic Requirements
- (2) Bench Analysis
- (3) Mirror Requirements (LOXT High Resolution Cylindrical)

The section on Dynamic Requirements summarizes the dynamic and static load requirements based on program specifications relating to thrust loading, sinusoidal vibration and random vibration.

The Bench Analysis section discusses three possible optical bench configurations. The structural material considered is graphite epoxy composite, which will minimize thermal dimensional changes because of its extremely low coefficient of thermal expansion.

The three configurations examined were:

- (1) a single 90" diameter tube of various thicknesses
- (2) two 45" diameter tubes of various thicknesses
- (3) a longeron/truss configuration

The section on Mirror Requirements discusses the fragility level of the high resolution mirror assembly as a function of the input power spectral density vibrations.

## 2.0 DYNAMIC REQUIREMENTS

This section deals with the basic dynamic and static requirements as called out below, based on the specifications of the HEAO Experiment Developer's Handbook. The implications of these environments on the design of the single degree of freedom isolated optical bench are presented in order to assess the need of providing a total optical bench vibration isolation system.

The effects of these dynamic and static environments on the non-isolated bench structure, i. e. hard mounted, are discussed in section 3.0.

The vibration environments considered in the analyses are as follows:

### Sinusoidal Vibration

1.0 - 3.2 cps	3.0" D.A.
3.2 - 10 cps	1.5 g's
10 - 14 cps	.3" D.A.
14 - 50 cps	3.0 g's

### Random Vibration

20 - 150 cps	+3db/octave slope
150 - 300 cps	0.15 g <sup>2</sup> /cps
300 - 1000cps	-3db/octave slope
1000 - 2000cps	-9db/octave slope

(10.3 g rms - overall)

These environments are described graphically in Figures 2-1 and 2-2.

With regard to steady-state accelerations, the HEAO Experiment Developer's Handbook calls for 9 g's in all directions for subsystem components, after listing launch loads as 6 g's axial and 1.5 g's lateral with a safety factor of 1.5. It is assumed that the steady-state acceleration for subsystem was specified in this way in order to allow subsystem design flexibility with regard to

FIG. 2-1

SINUSOIDAL INPUT

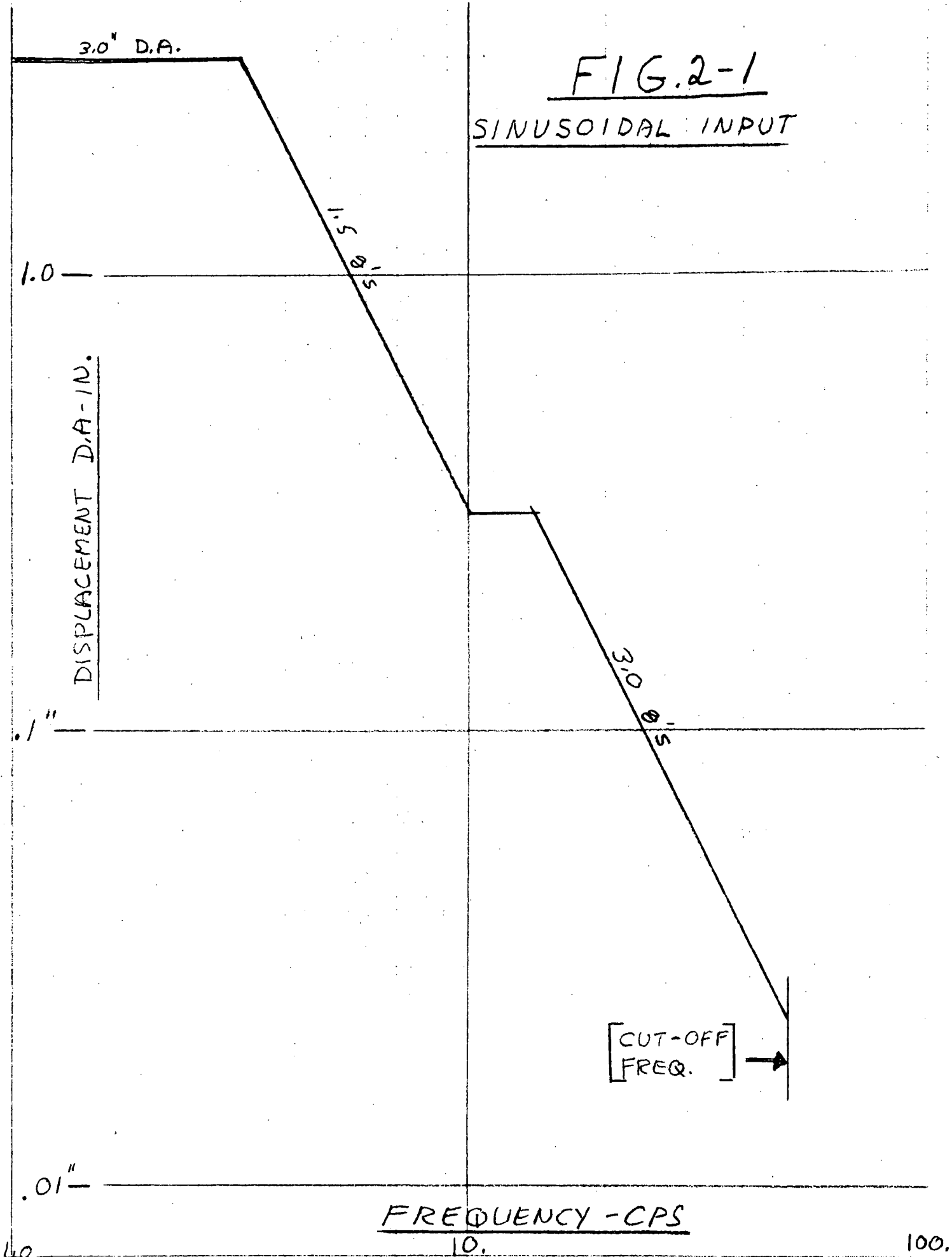
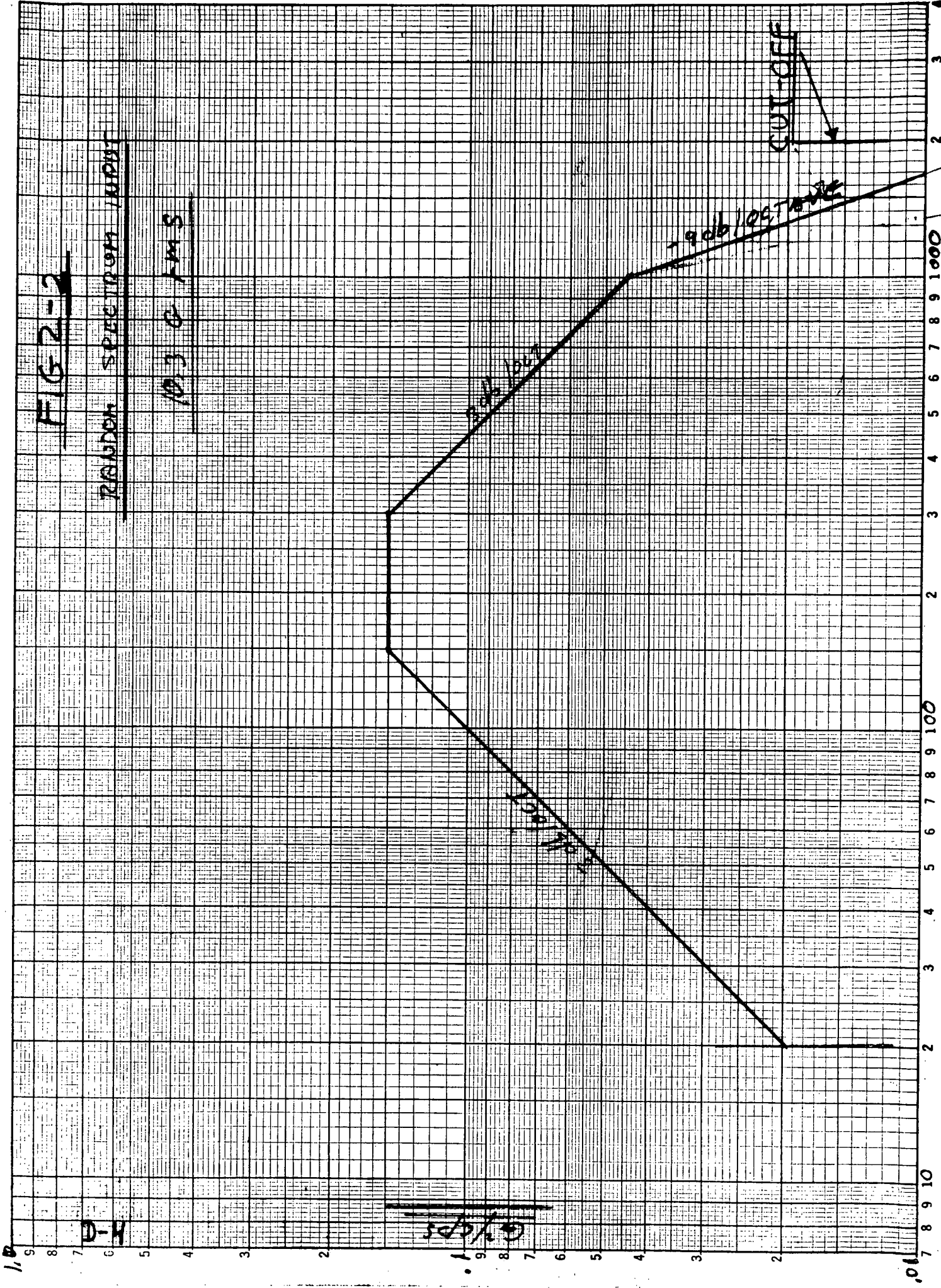


FIG 2-2

RANDOM SPECTRUM INPUT

1000 G RMS



mounting arrangements within the spacecraft. The functional requirements of the LOXT, however, dictate that the optical bench and the High Resolution Mirror be orientated in the spacecraft in a particular way; thus, designing for 9 g, steady-state, lateral acceleration could result in over design. In order to avoid confusion, the studies considered the effects of both 9 g and 2.25 g lateral loads.

The meaning of these inputs can really only be assessed in terms of the natural frequency of a responding system. Section 3.0, the "Bench Analysis" portion of this report, deals with the dynamic responses of a solidly tied down optical bench design, and this portion will be concerned with the general parameters governing the response of a low frequency vibration isolation system should this be required.

For the present, the need for an isolation system will not be considered. This will be evaluated based on

- a) Mirror Fragility Requirements
- b) Resonant Frequency of Support Structure or Bench.

On the assumption of completely rigid body supporting hardware, the input sinusoidal displacement from 1-50 cps will be exactly as noted on the ordinate of Figure 2-1. The motion from a 9 g sustained load will be zero and the displacement resulting from a flat power spectral density of  $.15g^2/cps$  from 20 - (the worst case of Figure 2-2) can be evaluated from:

$$DISPL. RMS = 31.86 \times PSD \times \left( \frac{1}{f_1^3} - \frac{1}{f_2^3} \right)$$

Where

PSD =  $.15g^2/cps$  (flat from 20 to 1500cps)

f1 = 20 cps

f2 = 1500

DISPL. RMS = 0.024 inches

DISPL. PEAK = 0.072 inches (3 SIGMA)

Based on the flat spectrum assumption, these displacements are not particularly severe.

Similarly, the g levels for the sinusoidal inputs are low - 3 g's maximum. The sustained static load, 9 g's and the rms random, 10.3 g's or 30.9 g's, peak over the 20-2000 cps. It should be noted that in the low frequency range, 1-30 cps, hardware tends to be "displacement sensitive" rather than 'g' sensitive. In other words, low g-levels may still have large relative deflections with high associated stresses, or other detrimental effects relating to relative motions. Thus, in considering the performance of a vibration isolation system, the natural frequency becomes very important. The equation of motion for a single degree of freedom linear system is a second order differential equation of the form:

$$M\ddot{X} + C\dot{X} + KX = 0$$

Where

M is the mass of the vibrating body in  $\frac{\text{lb sec}^2}{\text{in}}$

X is the displacement, in inches

C is the damping coefficient, in  $\frac{\text{lb sec}}{\text{in}}$

K is the spring constant in  $\frac{\text{lb}}{\text{in}}$

The natural frequency of the system is simply:

$$f_n = \frac{1}{2} \sqrt{\frac{K}{M}}$$

Where  $f_n$  is the natural frequency in cps.

For a given system mass, selection of a spring constant establishes the system natural frequency and selection of the damping coefficient establishes the maximum resonant amplification. These parameters fix the characteristics of the vibration isolation system.

For purposes of this discussion the resonant amplification has been taken as 4, and the percent of critical damping equivalent to  $C/C_c = 12.5\%$ . This is consistent with some of the more highly damped elastomeric compounds used to fabricate isolators.

Once a resonant frequency for an isolator has been selected, and resonant amplifications determined, response conditions can be calculated and plotted.

Steady state g-loads cause such systems to deflect in a manner which is inversely proportional to the square of the resonant frequency as follows:

$$\delta s = \frac{g \times 386}{(2 \pi f_a)^2}$$

Where:

s is the deflection in inches:

g is the loading, in "g's"

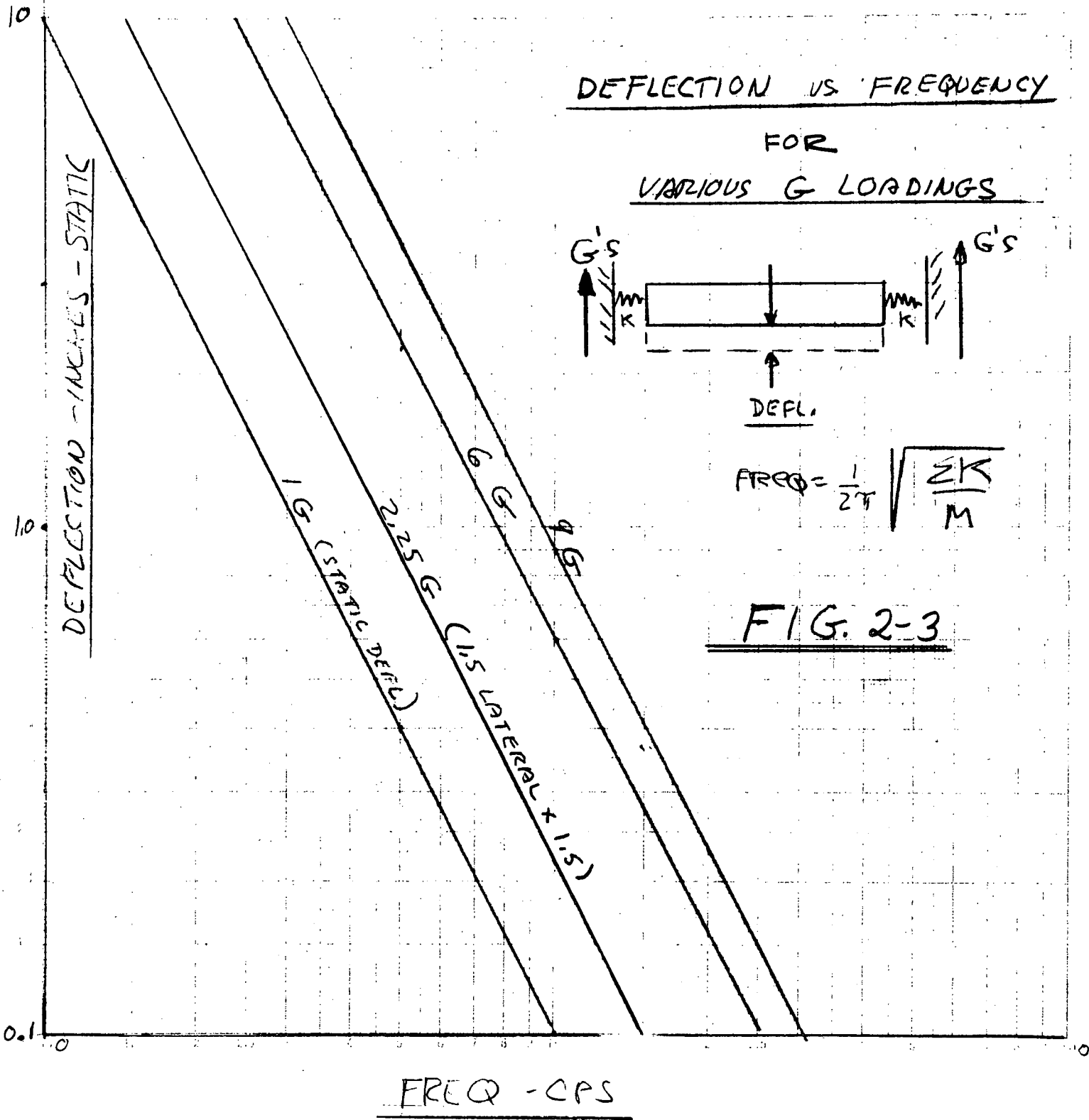
For example, consider just the static deflection of a 10 cps resonant system -

$$\begin{array}{l} g = 1 \\ f_n = 10 \end{array} \quad \delta s = \frac{386}{(2 \pi \times 10)^2} = .097''$$

The same system subjected to 9 g's would deflect 9 times as much, or .88"

What this means in a practical sense is that allowance must be made for this type of motion in all directions; based on 9 g's and whatever the natural frequency of the vibration isolation system that is selected. Plots of deflection vs. natural frequency for various "g" loadings are presented in Figure 2-3.

In similar fashion, the sinusoidal and random vibration inputs to a particular resonant frequency that result in motions (and loads) at resonance which are a function of the damping characteristics, or resonant transmissibility of the system. In general, for pure



viscous damping, the approximate relationship between resonant transmissibility,  $T_r$ , and viscous damping,  $C/C_c$ , is:

$$T_r \cong \frac{1}{2C/C_c}$$

Where  $C/C_c$  is percent of critical damping and  $C_c = 2\sqrt{KM}$

When designing an isolation system, one of the prime considerations is resonant transmissibility or the amplification at the isolator natural frequency. It is obvious that one would not knowingly use a system which would incur large amplitudes during vibration excitation.

Some typical properties are as follows:

#### Metallic Springs

Such springs, without externally applied damping, can evidence resonant amplifications in the order of 10-50:1 and are only used either with external dampers (friction or viscous), or when no excitation at resonance is anticipated.

#### Natural Rubber Compounds

The inherent approximate viscous damping of natural rubber limits resonant amplifications to 7-10:1

#### Neoprene Compounds

These are slightly better than natural rubber, evidencing amplifications in the order of 5-8:1

#### Silicone or 'High Damped' Compounds

These are the "newer generation" of elastomers and can be made to limit resonant amplifications to values of 2-5:1. They also possess excellent temperature vs. modulus characteristics over a very broad range. Silicones, however, do exhibit outgassing and this must be evaluated for the particular compounds used, in the light of the specification requirements.

As a final note, there are other approaches to vibration isolation

which control resonant transmissibilities, such as application of external friction, viscous dampers, the use of air springs, a servo-controlled pneumatic or hydraulic system. All such approaches are costly, large, and present problems in application to three orthogonal axes. As such, these have been deemed inappropriate for LOXT configurations. Should an isolation system be required, initial thinking would be to limit the resonant amplification to a level of 4:1, by using one of the higher damped elastomers, such as silicone, if possible.

Motions based on a resonant transmissibility of 4:1 will now be examined. Obviously, the sinusoidal inputs of Figure 2-1, up to 50 cps, will be multiplied by 4 at resonance, which will result in 4 times the displacement or acceleration at the particular resonant frequency. Figure 2-4 shows a plot of the maximum displacement vs. natural frequency of isolation system (Curve 1) for sinusoidal conditions up to 50 cps.

In a similar fashion, the random input results in an rms/peak displacement above 20 cps, which can be approximately calculated as follows:

$$X_{\text{rms}} = \frac{75.2 \times \text{PSD}}{C/C_c \times f_n^3}$$

Where:

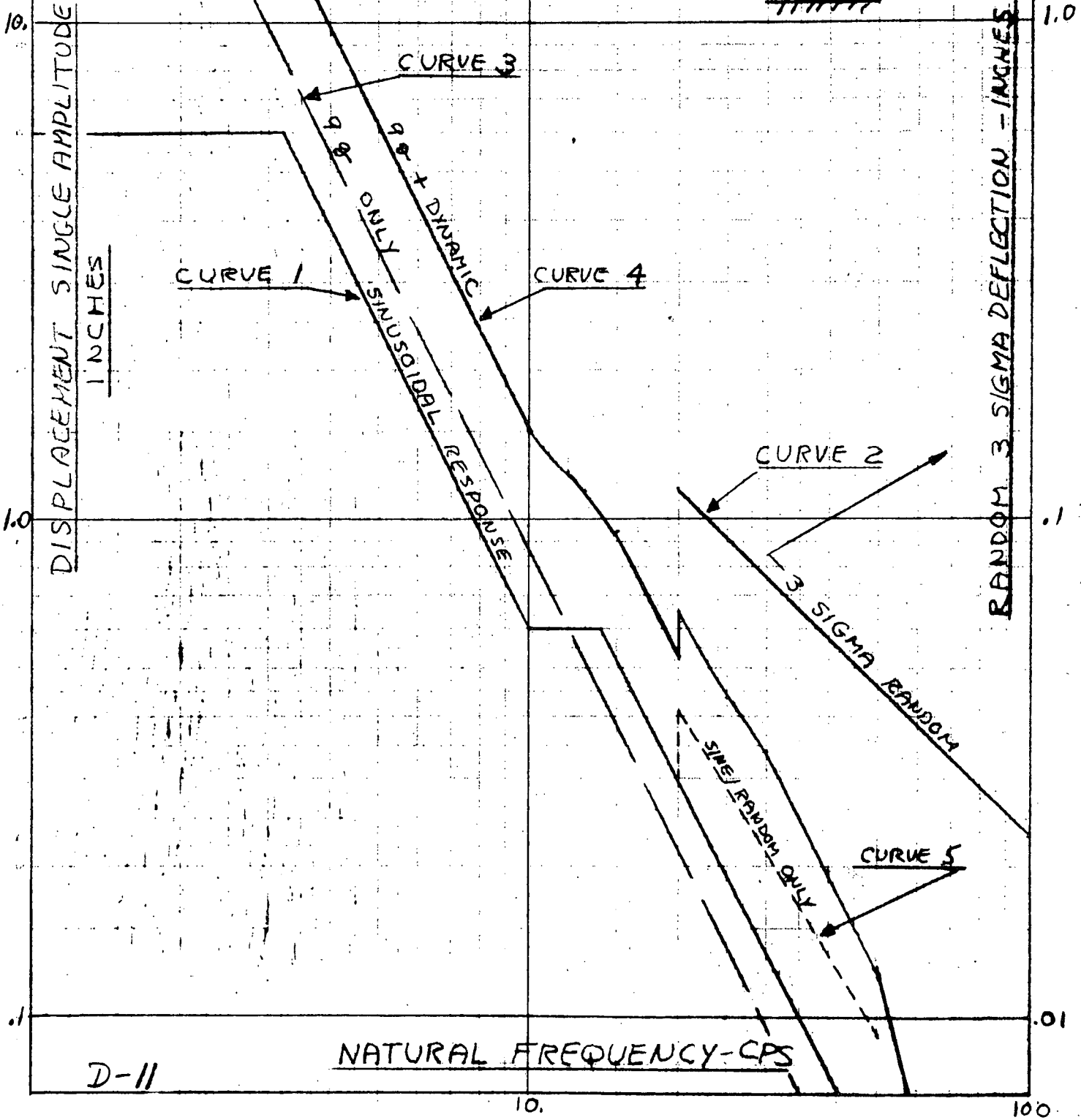
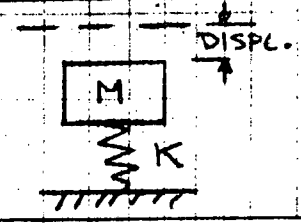
PSD = power spectral density at the particular resonant frequency of the isolation system selected, but assumes a completely flat spectrum at that value of  $g^2/\text{cps}$ . Since the spectrum is shaped sloping upward between 20-150 cps, the answers are only approximate.

Since the displacements thus calculated are random-rms, a good value for expected peaks is 3 sigma or 3x the rms response. Curve 2 of Figure 2-4 is a plot of these 3 sigma responses, from

FIG. 2-4

DISPLACEMENT VS RESONANCE

[ $T_R = 4$ ]  
(9 G THRUST)



20-100 cps, based on the power spectral density levels at corresponding frequencies of Figure 2-2.

Figure 2-4, curve 3, plots the 9g condition of steady-state acceleration, the same as that of Figure 2-3. Figure 2-4a is a repeat of Figure 2-4; but with a 2.25 g sustained loading instead of 9 g's.

It is obvious that if these environments are realistic, and if all three occurred simultaneously, a super position of resulting displacements could occur. Curve 4 of Figures 2-4 and 2-4a superimposes the sinusoidal, random, and 9g steady-state deflections based on  $T_r = 4$ , over the applicable frequency ranges. Curve 5 of Figure 2-4 superimposes only the random and sinusoidal conditions from 20-50cps.

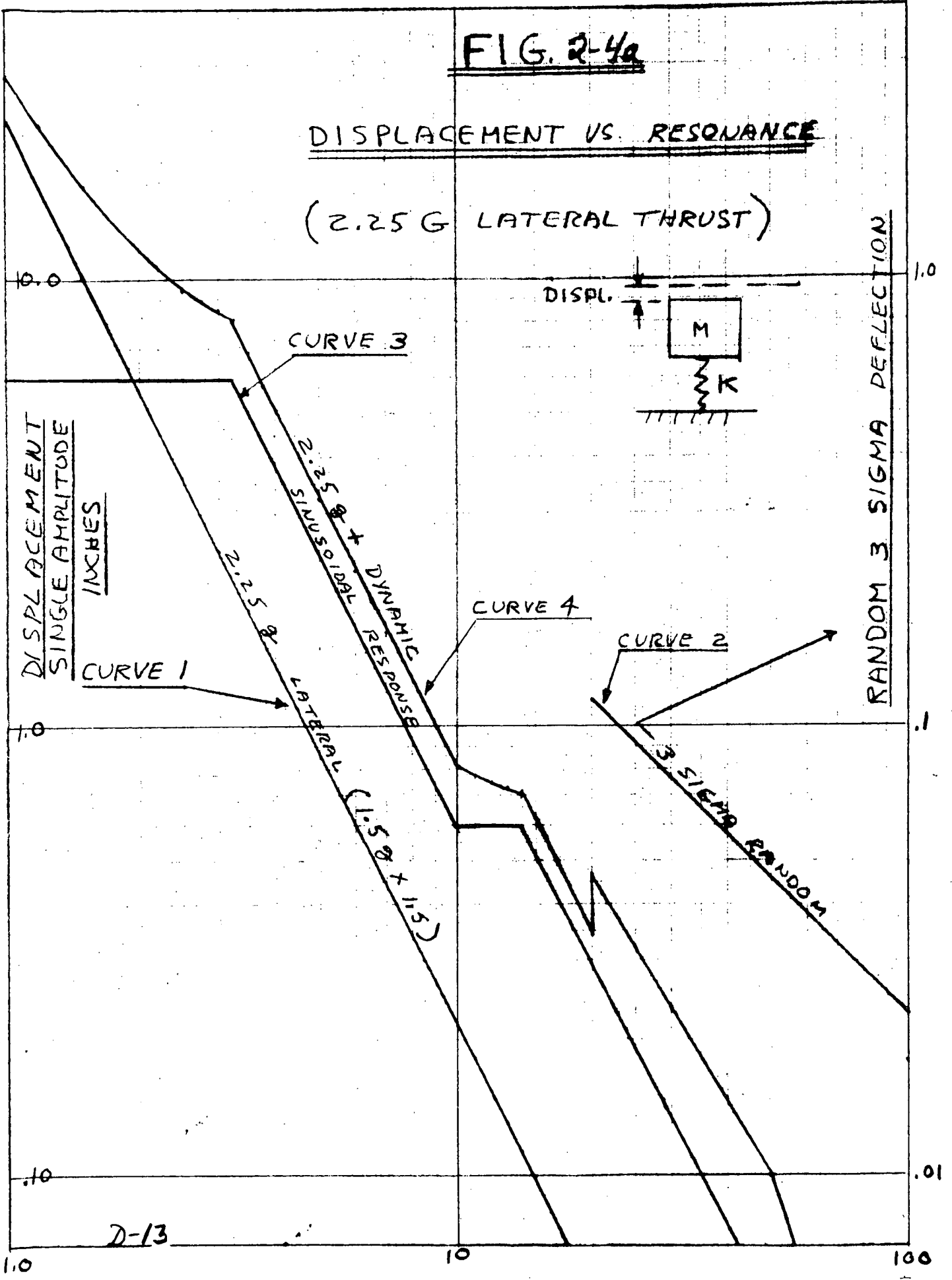
It is apparent that if an isolation system is employed, the characteristics of the launch sequence and trajectory would be vital to the design of the system. For example, if a 10 cps isolation system were employed, a total displacement (single amplitude) at the 9g-plus-sinusoidal loading condition of 1.5 inches would result. (Refer to curve 4 of Figure 4-4). This fact would mean that about 1.5" of relative motion would occur between the spacecraft and the optical bench, assuming this was the structure being vibration isolated. It is probably obvious, however, that the benefits of vibration isolation occur at 1.414 x the resonant frequency and increases with forcing frequency. Resonant conditions occur over a small frequency range, but must be considered to be the "price paid" for the "benefits" received.

A second general consideration is the loading effects, or transmitted loads, resulting from the sustained 9g and 2.25g's and vibratory environments. For these considerations, a total weight

FIG. 2-4a

DISPLACEMENT VS. RESONANCE

(2.25 G LATERAL THRUST)



DISPLACEMENT  
SINGLE AMPLITUDE  
INCHES

RANDOM 3 SIGMA DEFLECTION

D-13

of experiment = 11,000 lbs. will be used. For rigid body solid tie down conditions the maximum loads are as follows:

$$9 \times 11,000 = 99,000 \text{ lbs. static}$$

$$3 \times 11,000 = 33,000 \text{ lbs. sin. vib (s. amp)}$$

$$3 \times 10.3 \times 11,000 = \frac{339,000 \text{ lbs.}}{471,000 \text{ lbs.}} \text{ random-3 sigma}$$

If all of the conditions occurred simultaneously, an instantaneous total loading of 471,000 lbs. could theoretically be exerted. This figure would be divided by the number of tie-down locations between the optical bench and the spacecraft.

A second set of conditions exists if vibration isolators, namely the loads produced by the resonant amplification, (in this case 4.0) of the isolation system. In addition, the required structure of the spacecraft must provide sufficient stiffness at the isolator support points so as not to lower the designed system resonance. If the structure were soft, this resonance lowering would occur. In addition, damping of the isolator would be markedly reduced causing much higher resonant amplifications. A good practice is to have the supporting structure at least 5 times as stiff as the isolator spring, which would only reduce the designed resonant frequency by 9%, which is not significant. Obviously, the stiffer the support structure the better, so that 5:1 should be considered only a minimum.

Figure 2-5 is a plot of total isolation system stiffness vs. resonant frequency for an 11,000 lbs. total weight. A half weight curve for 5500 lbs. has also been included. It should be noted that if 4 isolators were used, the stiffness of each one would only be 1/4 of the value indicated by Figure 2-5, which is one way of achieving a greater than 5:1 ratio between isolator stiffness and structural support stiffness, thus increasing the number of

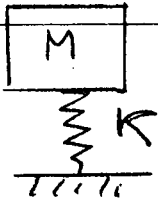
# FIG 2-5

NATURAL FREQUENCY

VS

STIFFNESS

$10^6 \text{ #/in}$



$$K = (2\pi f_n)^2 \frac{W}{g}$$

STIFFNESS -  $K \text{ #/in}$

$100,000 \text{ #/in}$

WEIGHT = 11000 #

WEIGHT = 5500 #

$10,000 \text{ #/in}$

D-15

$f_n$  - SYSTEM NATURAL FREQUENCY - CPS

10.

100

isolators used.

Figure 2-6 is a plot of the loadings that must be reacted by the structure as a consequence of considering various natural frequencies of the isolation system. The plots indicate 2.25 and 9g thrust, sinusoidal vibration, and random vibration loadings that would be produced at resonance, assuming that the isolation system had a resonant transmissibility  $Tr = 4.0$ .

Figure 2-7 presents combined loadings based on the results given in 2-6, both with and without the thrust requirements as a function of resonant frequency.

STRUCTURAL LOADS VS NAT. FREQ

WT = 11,000#

FIG 2-6

REACTED LOAD - TOTAL

160<sup>k</sup>  
140<sup>k</sup>  
120<sup>k</sup>  
100<sup>k</sup>  
80<sup>k</sup>  
60<sup>k</sup>  
40<sup>k</sup>  
20<sup>k</sup>

10 20 30 40 50

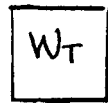
NAT. FREQ - CPS

SINUSOIDAL RESPONSE LOAD

9G THRUST LOAD (ALL AXES)

RANDOM 3 SIGMA LOADS

2.25 G LATERAL THRUST



$T_R = 4$



$\downarrow KX = \text{LOAD}$

NOTE:

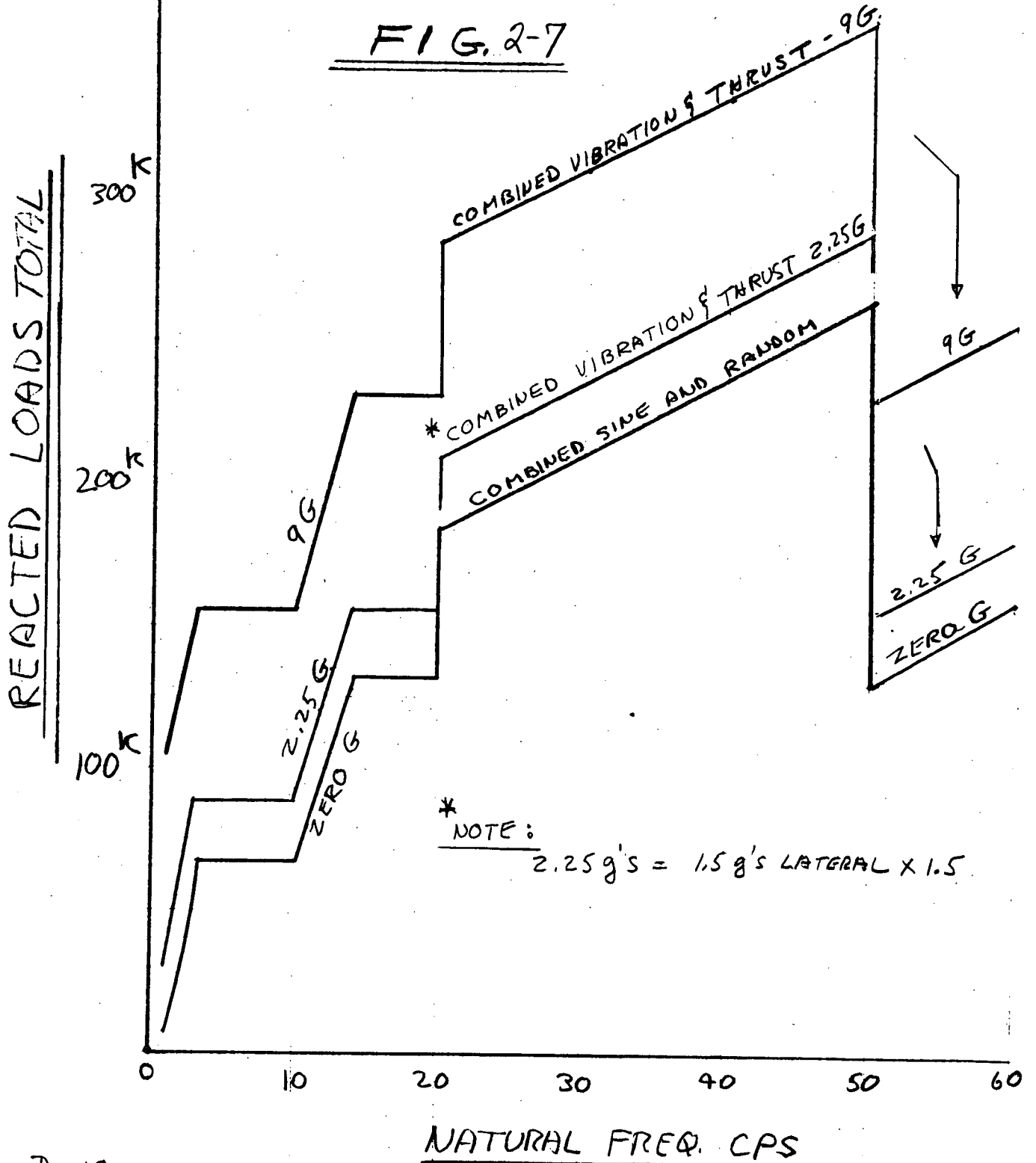
LOADS ARE TOTAL  
MUST BE DIVIDED BY  
NUMBER OF ISOLATORS.

# COMBINED LOADS

(WT = 11000#)

( $T_R = 4$ )

FIG. 2-7



### 3.0 BENCH ANALYSIS

#### 3.1 Basic Design Characteristics

Three possible optical bench configurations were considered in this analysis:

1. a single 90" diameter tube of various thicknesses
2. two 45" diameter tubes of various thicknesses
3. a longeron/truss configuration

The structural material considered was a graphite epoxy composite, because its low coefficient of thermal expansion will minimize thermal distortion of the structure. In this analysis, the properties of graphite epoxy have been taken to be:

- a. modulus of elasticity =  $30 \times 10^6 \text{ lb/in}^2$
- b. density =  $0.07 \text{ lb/in}^3$

Some consideration must be made of these material properties, however, it is a known fact that such materials are anisotropic, that is they possess different properties along different orthogonal axes. Thus, they could exhibit different moduli and varying dynamic response characteristics. Further, many materials, such as elastomers, for example, have dynamic-to-static modulus ratios of greater than one, making resonant frequency calculations subject to some variation.

A 90 inch diameter tube forms the basic structure for the single-tube bench configuration. This size is based on an available space-craft internal diameter of 92 inches, but allowing a minimum 1.0 inches in each direction for dynamic motion and isolation system hardware. The properties of a 90 inch diameter tube with a length of 360 inches are:

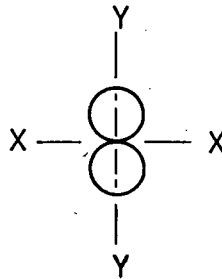
Wall Thickness (inches)	Area (in <sup>2</sup> )	Moment of Inertia (in <sup>4</sup> )	Weight/unit (lb/in) length	Total Weight (lbs)
0.25	70.45	70849	4.93	1775
0.50	140.52	140,520	9.84	3542
1.0	279.46	276,383	19.56	7042
2.0	552.6	534,550	38.68	13900

The ratio of moment of inertia, I, to weight per unit length, w, is:

$$\frac{I}{w} = 14,370 \text{ in}^5/\text{lb}$$

The practical limit of wall thickness is limited to 0.5 inches if a total experiment weight limit of 11,000 lbs. is imposed, since this limit restricts bench structural weight to 3500 lbs.

The properties of a configuration of two, 45 inch diameter tubes joined as shown in the sketch below are as follows (taken about the x-x axis):



Wall Thickness (in)	Area (in <sup>2</sup> )	Moment of Inertia (each tube) (in <sup>4</sup> )	Moment of Inertia (about configuration centroid) (in <sup>4</sup> )	Weight per unit length (lb/in)	Total Weight (lbs)
0.1	14.09	3548	21363	1.96	711
0.25	35.13	8783	53134	4.91	1771
0.5	69.86	17274	105281	9.78	3521
1.0	138.2	33409	206744	19.34	6963

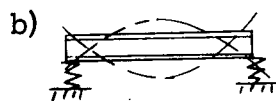
$$\frac{I}{w} = 10,900$$

The normalized stiffness to weight ratio,  $I/w$  is about 14,370 for the single-tube concept and 10,900 for the two-tube approach. Weights are equivalent so that the basic unloaded structural natural frequencies based on uniform stiffness and weight are 1.15 times greater  $[\sqrt{14,370/10,900}]$  for the single tube as compared with the twin tube approach. It is important to note that about the Y-Y axis the stiffness is only 1/3 of that developed about the X-X axis, indicating frequency reductions of 0.57, based on uniform beam concepts.

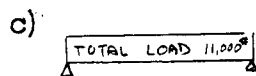
Since it is important to know the resonant frequency characteristics of the structure in order to apply vibration isolators if required and to determine approximate dynamic responses and stresses, a detailed examination of the following configurations will be made for equivalent beam resonant frequencies:



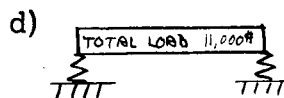
D = 90" TUBE SIMPLY SUPPORTED UNDER ITS OWN UNIFORM LOAD



D = 90" TUBE ELASTICALLY SUPPORTED ON VERY SOFT ISOLATORS UNDER ITS OWN UNIFORM LOAD - THIS APPROACHES THE FREE-FREE CONDITION



D = 90" WITH A TOTAL LOAD OF 11,000# MADE UP OF BEAM WEIGHT + EQUIPMENT (SAME MODE AS (a) ABOVE)



D = 90" WITH A TOTAL LOAD OF 11,000# MADE UP OF BEAM WEIGHT + EQUIPMENT (SAME MODE AS (b) ABOVE)

Before examining resonant frequencies, it is important to recognize that the length-to-diameter ratio of the "beams" is 4:1, which indicates that the beam theory is no longer completely valid. Shear effects as well as potential ring or shell modes should be considered. Ring and shell deflections can be minimized in terms of the effects on basic structural resonances by stiffening locally at load points and by avoiding long unbraced lengths. The general equations for beam frequency ( $f_n$ ) calculations given as standard expressions usually consider  $k_\theta$ , bending only. For approximation purposes, the relationship between  $k_\theta$  (bending) and  $k_s$  (shear) will be examined, and a new overall stiffness,  $\Sigma k$ , determined with which to ratio the natural frequencies to be determined from the expression for beam bending frequencies taken from the Stress and Vibration Handbook (pages 1-15).

$$f_A = \frac{a}{2\pi} \sqrt{\frac{EI}{\mu l^4}}$$

Where:

$a$  is a coefficient = 9.87 for a simply supported beam  
 = 22.4 for a free-free beam

$E$  is the modulus of elasticity, in psi

$I$  is the moment of inertia, in/in<sup>4</sup>

$\mu$  is the beam mass per unit length, in lb sec<sup>2</sup>/in<sup>2</sup>

$l$  is the beam length, in inches.

For a uniform, simply supported beam, the bending stiffness is:

$$K_\theta = \frac{384 EI}{5l^3}$$

and the shear stiffness:

$$K_s = \frac{2AG}{\lambda (l/2)}$$

Where:

A is the cross-sectional area, in in<sup>2</sup>

$\lambda$  is a form factor equal to 2 for a hollow tube

G is the shear modulus, in psi

For the single cylinder configuration:

$$\begin{aligned} A &= 70 \text{ in}^2 & \ell &= 360 \text{ inches} \\ I &= 70,850 \text{ in}^4 & E &= 30 \times 10^6 \text{ psi} \\ G &= 11 \times 10^6 \text{ psi (assumed)} \end{aligned}$$

The results are:

$$\begin{aligned} K_{\theta} &= 3.50 \times 10^6 \\ K_g &= 4.31 \times 10^6 \end{aligned}$$

and the equivalent combined stiffness is:

$$\Sigma K = \frac{K_g K_{\theta}}{K_g + K_{\theta}} = 1.93 \times 10^6$$

Since the  $k_{\theta}$  equivalent that pure bending beam theory would utilize is  $k_{\theta}$ , by obtaining a ratio of the combined stiffness to the bending stiffness and multiplying the various resonances obtained from pure bending deflection stiffness, approximate new resonant frequencies can be obtained which consider shear stiffness  $k_g$  as well as bending, but this is only an approximation. Computer codes exist to consider such parameters accurately. Further, the expression is only good for uniform loading, since  $k_{\theta}$  represents this condition.

In the present case, this ratio, B, is equal to:

$$\beta = \sqrt{\frac{\Sigma K}{K_{\theta}}} = 0.743$$

Considering a 90 inch diameter tube with a 0.25 inch wall thickness for cases (a) and (b), yields the following results:

Case (a) (simply-supported beam):  $f_n = 115.7 \text{ cps}$

Case (b) (free-free beam):  $f_n = 263$  cps

These numbers represent beam modes which consider both shear and bending stiffness. The free-free mode is a limiting case for a stiff beam supported on very soft (low natural frequency) isolators.

For cases (c) and (d), when the beam plus equipment weight = 11,000 lbs., the following results are obtained:

Case (c) (simply supported beam):  $f_n = 46$  cps

Case (d) (free-free beam):  $f_n = 105$  cps

When considering a new thickness the only parameters that change, are  $I$  and  $\mu$  ( $\mu$  + function of  $A$ ), but for a cylinder, it can be shown that the ratio  $I/\mu$  does not change. Therefore, the natural frequencies for the uniformly loaded beam (under its own weight only, cases (a) and (b)) do not change; however, the totally loaded condition of equipment plus bench will indicate lower resonances, since the beam weight increases and the equipment plus beam weight is still limited to 11,000 lbs.

For a 90 inch diameter tube with a 0.5 inch wall thickness, the results for Cases (a) and (b) are:

Case (a) (simply supported beam):  $f_n = 65.4$  cps

Case (b) (free-free beam):  $f_n = 149.2$  cps

Figure 3-1 plots the optical bench moment of inertia vs. the system natural frequency, taking into account the combined bending and shear stiffness. The moment of inertia values for the 90 inch diameter tubes are noted along with resonant frequency values for the unloaded cases. The resonant values for the "twin tube" configuration can be obtained by dividing the frequencies for the single tube by 1.15 in the "stiff axis" and 1.732 in the "soft axis".

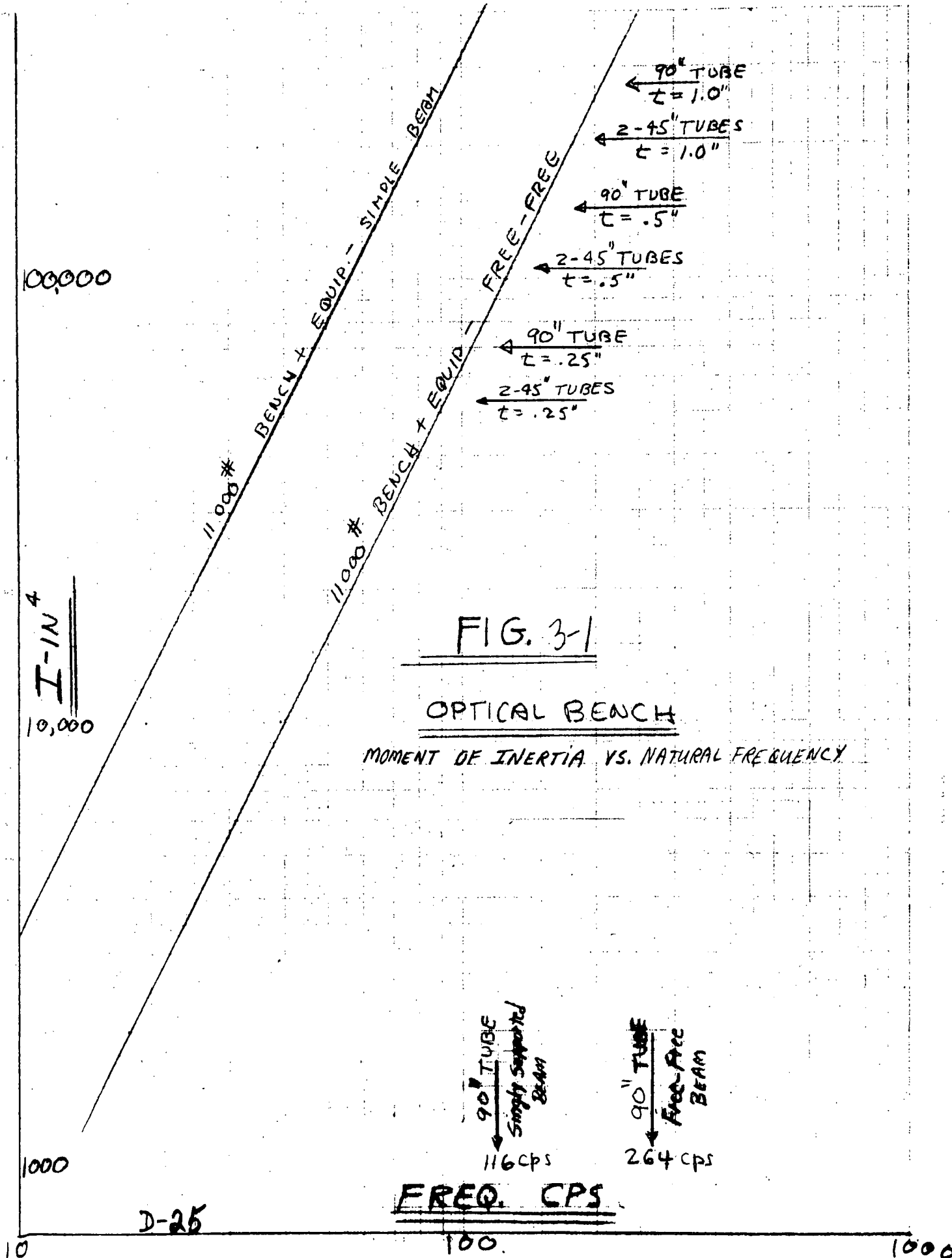


FIG. 3-1

OPTICAL BENCH

MOMENT OF INERTIA VS. NATURAL FREQUENCY

D-25

FREQ. CPS

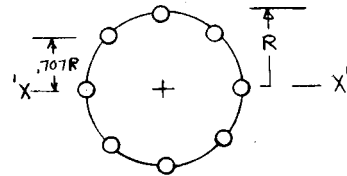
These results indicate that an adequately stiffened single tube 90 inches in diameter is a more superior bench configuration from the standpoint of stiffness than is the twin 45 inch diameter tube configuration. Both, however, have practical disadvantages because of the necessity for access.

A more practical approach to bench construction is a longeron/truss configuration. An expression for the moment of inertia of such a configuration can be derived in the following fashion:

Consider an 8-longeron configuration as shown in the sketch below. If the moment of inertia of each rod about its own axis is neglected, the total moment is:

$$I = 2 [AR^2 + 2(0.707R)^2A]$$

$$= 4 AR^2$$



If a 4-rod configuration were considered, the result would be:

$$I = 2AR^2,$$

and for a 16-rod configuration, it can be shown that:

$$I = 8AR^2$$

Thus, for the general case of N equally spaced circumferential longerons:

$$I = \frac{N}{2} R^2 A$$

The diameter of the rods required to provide a specified moment of inertia is given by the expression:

$$D = \sqrt{\frac{8I}{NR^2}}$$

Where:

D is rod diameter.

The rod diameters required to produce the moment of inertia equivalent to that of a 90 inch diameter, 0.25 inch thick tube

(70,490 in<sup>4</sup>) in 4-, 8- and 16-rod configurations are 4.72 inches, 3.34 inches and 2.36 inches, respectively.

Since the total cross-sectional areas of each configuration are equal, the weights of each are equal. For a graphite-epoxy composite structure, the weight is 1763 lbs, which is identical to the weight of the 90 inch, 0.25 inch thick tube. Stiffeners and braces, have not been included.

The relationships between moment of inertia, rod diameter and number of rods are presented in Figure 3-2. Also noted on the plot are the moment of inertia values for the single and twin-tube configurations considered earlier.

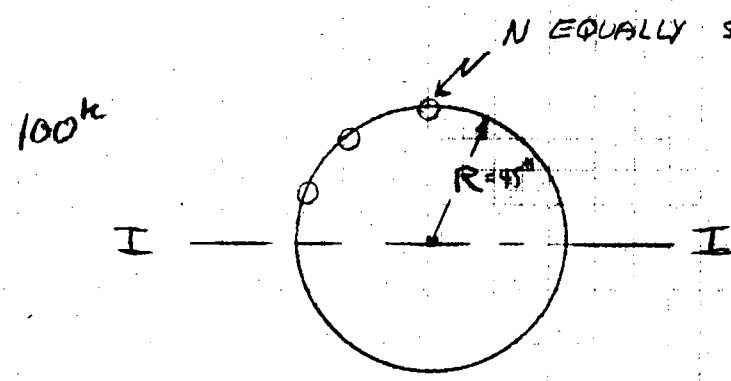
Table 3-1 summarizes the parameters of weight, moment of inertia and natural frequency for the tube configurations of the optical bench.

The resonant frequencies of a longeron type of construction would be identical to these for the loaded case (bench + equipment = 11,000 lbs) for equivalent values of moment of inertia, but in practice would be somewhat lower, since the distributed mass along the length of the beam or bench would have to include frames or bracing members which would act in local shear, but would not contribute to bench longitudinal stiffness.

Figure 3-3 shows a conceptual longeron type of design utilizing 8-3.5" rods. It is important to note that the structural resonance, if vibration isolation of the total bench is considered, must be sufficiently high, with respect to the natural frequency of the mounts, to eliminate undesirable coupled modes which would cause large structural responses. This point has been discussed at greater length in Section 2.0.

MOMENT OF INERTIA VS. ROD DIAMETER  
(SOLID RODS)

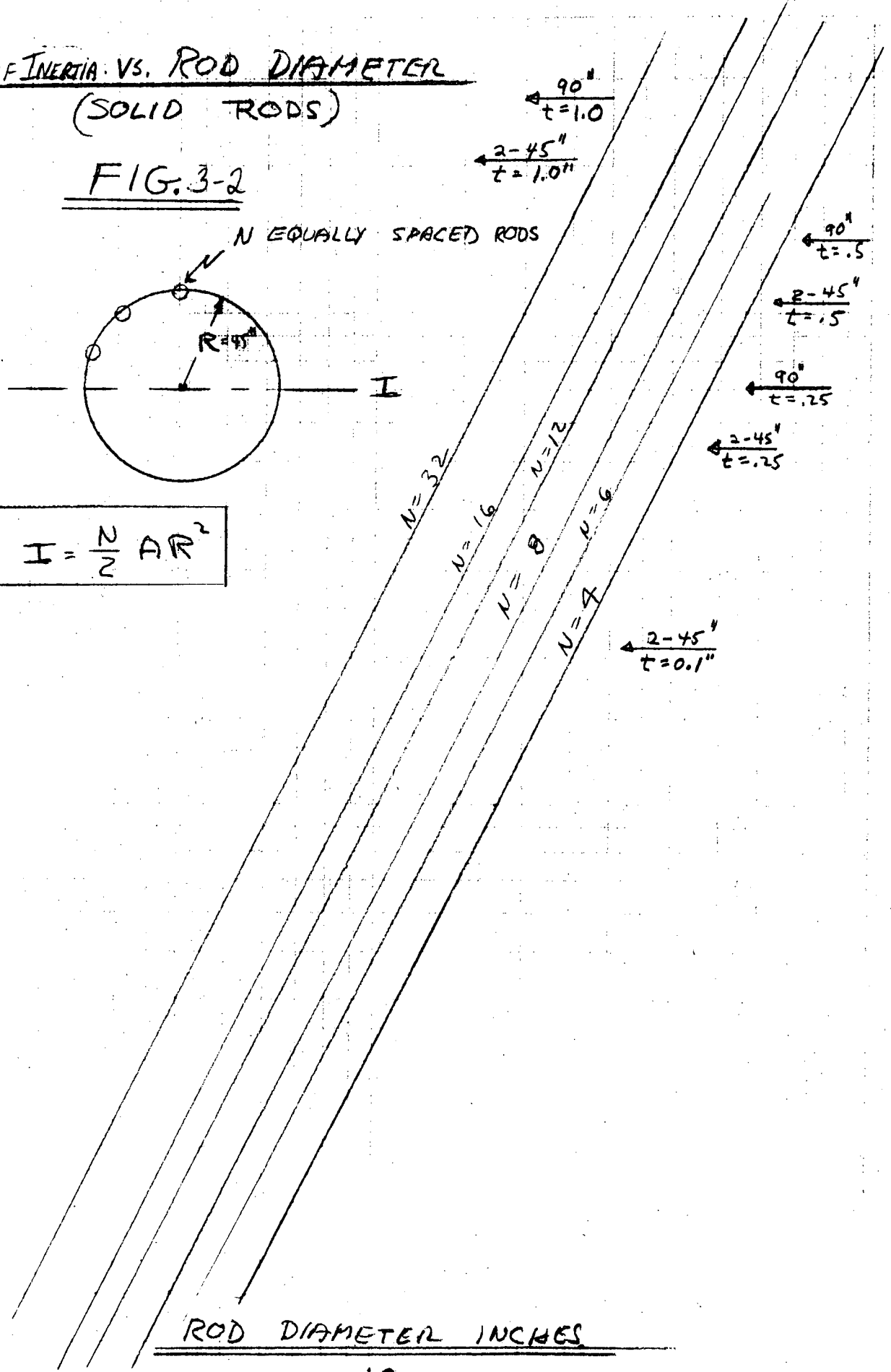
FIG. 3-2



$$I = \frac{N}{2} A R^2$$

I - IN<sup>4</sup>

10000



D-28

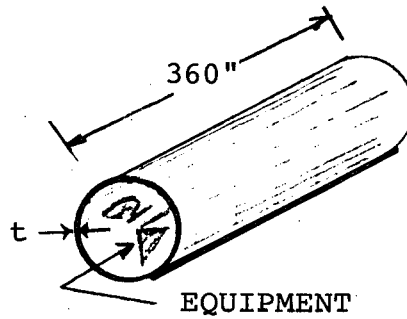
1.0

10.0

One 90" Tube

t inch	$\Sigma W$ lbs.	$\Sigma I$ inches <sup>4</sup>	Natural Frequency (cps)			
			Simple		Free-Free	
			No Load	Load*	No Load	Load*
0.25	1775	70,849	116	47	262	106
0.5	3542	140,520	116	65	262	149
1.0	7042	276,383	116	93	262	210

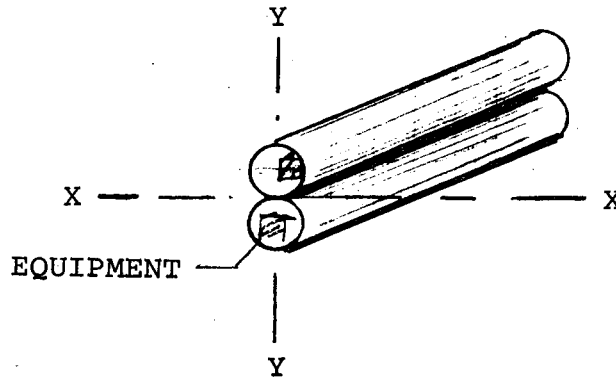
\*Total Load = 11,000 lbs. - Equipment plus Tube



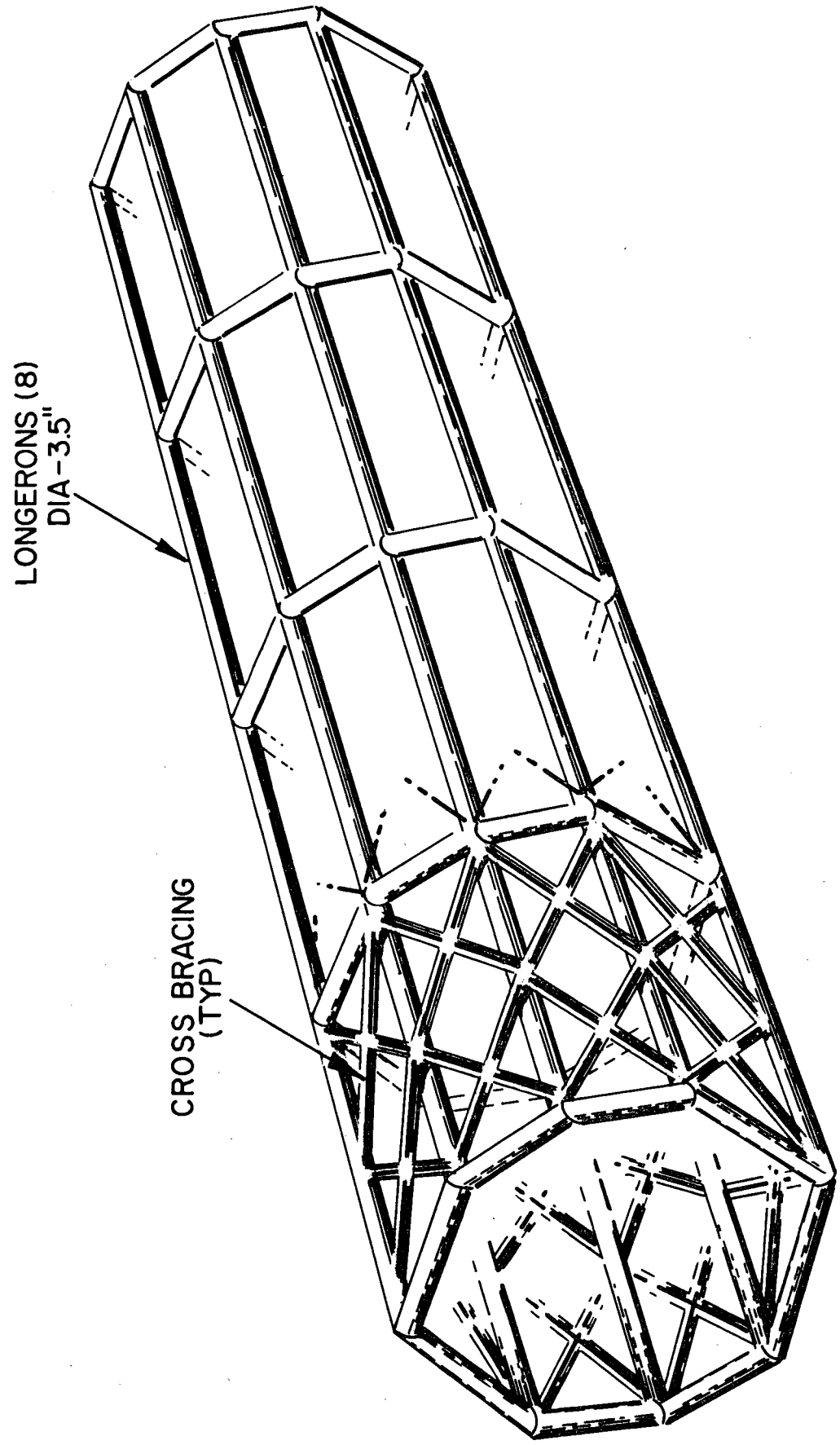
Two 45" Tubes

t inch	$\Sigma W$ lbs.	$\Sigma I$ inches <sup>4</sup>	Natural Frequency (cps)			
			Simple		Free-Free	
			No Load	Load*	No Load	Load*
0.25	1770	53,134	100	40	229	92
0.5	3521	105,281	100	56	229	129
1.0	6963	206,744	100	78	229	185

\*All Values X-X Axis



LENGTH - 360"  
DIAMETER - 90"



OPTICAL BENCH  
(CONCEPT)  
FIG. 3-3

Note that if the structure were simply supported (no end moments); but with rigid or relatively inelastic supports, the lower resonance would apply. As the isolation system resonance got significantly lower than the structural resonance, however, the elastic supports would get softer and the structural resonance would approach the free-free condition. In practice the 50-110 cps range shown here is quite reasonable for this size structure, if it can be achieved.

### 3.2 Bench Structure Stress Analysis

This analysis treats the optical bench as a simply supported structure and considers only direct static and dynamic loads, disregarding isolator effects.

#### 9 G Sustained Load

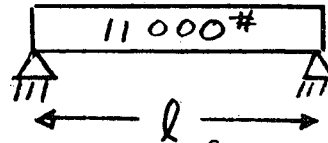
##### Bending

$$M_m = \frac{wl^2}{8} \times 9 \text{ (simply supported - uniform load)}$$

$$w = \frac{11,000}{1} \text{ lb/in}$$

$$l = 360 \text{ inches}$$

$$M_m = \frac{11,000}{360 \times 8} \times 360^2 \times 9 = 4.455 \times 10^6 \text{ in lb (9g's)}$$



Assume  $c = 45 \text{ in}$  (distance to outer fiber)

$I = 77892 \text{ in}^4$  (longeron concept)

$$S = \frac{M_m c}{I} = \frac{4.455 (10^6) (45)}{77892} = 2754 \text{ psi}$$

##### Shear

$$S_u = \frac{V}{A\lambda}$$

$\lambda = (2 - \text{Tubes-Rods etc})$

$A = 77 \text{ in}^2$

$$= 2 \frac{wl}{2} \cdot \frac{1}{A}$$

$$= \frac{11000 \times 360}{360 \times 77} = 143 \text{ psi} \times 9 = \underline{1286 \text{ psi}}$$

### Axial Compression

$$Wt = 9 \times 11,000 = 99000 \text{ lbs}$$

$$A = 77 \text{ in}^2$$

$$Sx = 1286 \text{ psi}$$

### Dynamic Loads

For purposes of calculating dynamic loads (vibration) a natural frequency of 50 cps will be used. This is the lowest frequency of the longeron structure concept.

### Sinusoidal

At 50 cps the sinusoidal input requirement cuts off, but the 3g input level will be used none the less. For an amplification of 10 based on an assumed structural/mechanical damping ratio -  $C/C_c$  = .05 - the maximum unisolated input is:

$$G's \times \text{Ampl.} = 3.0 \times 10 = 30 \text{ g's peak}$$

Although, dynamically, the shape of the elastic deformation - as compared to static or steady-state conditions - is slightly different, it is close enough for approximate calculations. Thus:

$$\text{Bending} - \frac{30}{9} \times 2574 \text{ psi} = \underline{8579 \text{ psi}}$$

$$\text{Shear} - \frac{30}{9} \times 1286 \text{ psi} = \underline{4290 \text{ psi}}$$

### Random Input

At 50 cps the input is  $0.05 \text{ g}^2/\text{cps}$ . Assuming for simplification a single degree of freedom with a flat power spectral density input and an amplification of 10 -

$$\begin{aligned} \text{RMS G's} &= \sqrt{\frac{\pi}{2} \cdot \text{PSD} \cdot f_n \cdot 10} \\ &= \sqrt{\frac{\pi}{2} \times .05 \times 50 \times 10} \end{aligned}$$

RMS G's = 6.267 g's RMS

Peak G's = 18.79 g's peak (3 sigma)

Using the 9g static condition and based on a 3 sigma peak stress:

$$\text{Bending} = \frac{18.79}{9} \times 2574 = \underline{5376.5 \text{ psi}}$$

$$\text{Shear} = \frac{18.79}{9} \times 1286 = \underline{2685 \text{ psi}}$$

### Now Examining Maximum Deflections

#### Bending (Beam)

##### Static - 9G

$$\begin{aligned} \delta_m &= \frac{5}{384} \frac{wl^4}{EI} \times 9 \\ &= \frac{5}{384} \cdot \frac{(11000)}{360} \cdot \frac{360^4}{30 \times 10^6} \cdot \frac{1}{77892} \cdot 9 \\ &= \underline{0.0257 \text{ in}} \end{aligned}$$

#### Shear (Beam)

##### Static 9G

$$\begin{aligned} \delta &= \frac{v_m \lambda l}{GAx2} \times 9 \\ \delta &= \frac{wl \lambda 1 9}{2(11)(10^6)(77)2} \\ &= \frac{11,000(360)(9)}{(11)(10^6)(77)(2)} \\ \delta &= 0.021 \text{ in} \end{aligned}$$

The bending and shear deflections should be added so that the total deflection is:

$$\delta \text{ Total} = 0.0467 \text{ in.}$$

### Sinusoidal Vibration

For a 50 cps resonance, the input is 3G peak, and displacement single amplitude is:

$$X = \frac{\ddot{x}}{\omega^2} = \frac{3 \times 386}{(2\pi 50)^2} = .0117 \text{ in.}$$

And with an amplification of 10 this becomes

$$x = 0.117 \text{ in (single amplitude)}$$

This is equivalent to a single degree of freedom system of 50 cps resonance which has already taken into account the combined bending and shear effects when the frequency was derived.

#### Random Vibration

The previously derived peak response - 18.79 g's @ 50 cps - produces a single-amplitude displacement of:

$$X = \frac{18.79 \times 386}{(2\pi 50)^2} = .073''$$

Based on a single degree of freedom system responding to flat power spectral density input.

The results of the Stress Analysis of the longeron configuration are summarized in Table 3-2. Some points are to be noted:

First, the stresses calculated, although relatively low individually, could be superimposed, depending upon the booster trajectory time relationship between maximum acceleration and maximum vibration conditions. Also, no allowables could be utilized since the ultimate material choice is yet to be made.

Secondly, although a 50 cps bench structure was analyzed, hopefully the resonant frequency will be higher if relatively soft isolators (elastic supports) are applied, which would cause a mode shift toward a free-free structure. In addition, the vibration input at the structural resonant frequency would be attenuated, thus reducing response accelerations and displacements.

TABLE 3-2

## Stress Analysis - Longeron Structure

Configuration: 8 - 3.5 in. diameter rods  
 Moment of Inertia = 77,890 in<sup>4</sup>  
 Weight = 1940 lbs (no braces)  
 Natural Frequencies (cps)

	<u>No Load</u>	<u>Struct. &amp; Load</u>
Simple Support	119	50
Free - Free	262	110

## Stresses (in psi)

9g Static Load	
Bending	2574
Shear	1286
Compression	1286

Sinusoidal Vibration	
Bending	8579
Shear	4290

Random Vibration	
Bending	5377
Shear	2685

## Deflections (in inches)

9g Static Load	
Bending	0.0257
Shear	0.0210

2.25g Static Load	
Bending	0.0064
Shear	0.0052

Sinusoidal Vibration (Single Amplitude)	
	0.117 to 0.155

Random Vibration (3 sigma)	
	0.073 to 0.097

#### 4.0 MIRROR REQUIREMENTS

The crux of the entire optical bench dynamic design to provide safe support for the high resolution mirror assembly. This unit has been assumed to be the most sensitive "component," and conclusions have been based on this premise. The high efficiency mirrors, detectors and other instrumentation have not been considered.

The high resolution mirrors are tentatively considered to be glass with a maximum allowable tensile stress of 1000 psi. The basis of the optical bench structural design and spacecraft tie-in for vibration isolation is the maximum vibration input displacement level to which these mirrors can be subjected without failure. In other words, the adequacy of the bench structure with respect to its resonant frequency and mode shape characteristics, and the need for mirror dynamic protection or vibration isolation, are functions of the mirror natural frequencies and maximum response displacements (stresses).

Appendix C "LOXT High Resolution Mirror Dynamic Analysis" is the basis for a detailed determination of the resonant frequencies, mode shapes, and normalized stresses of the largest diameter, and hence, the most sensitive, mirror. This work is summarized as follows:

1. Develop a finite element model of a shell defined by mass and stiffness matrices using M. I. T. Code SABOR III (IBR 360/75)
2. This must be done for each circumferential harmonic through the 10th mode.
3. The natural frequencies and mode shapes (axial variations) are determined for each harmonic from Avco computer code

2607, which utilizes the mass and stiffness matrices developed in SABOR III.

4. SABOR III, in addition, provides stress resultant coefficient matrices which when multiplied by displacement vectors computes stress resultants.

The basic mirror configuration is shown below in Figure 4-1.

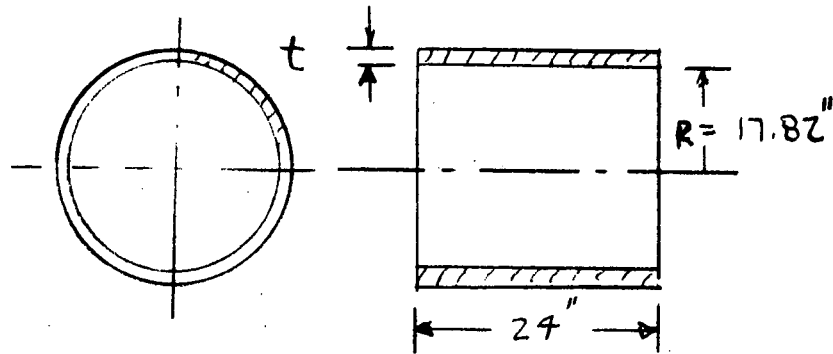


Figure 4-1. Mirror Configuration

The properties of the glass are:

$$E = 10.5 \times 10^6 \text{ psi}$$

$$\rho = 0.079 \text{ lb/in}^3$$

$$\nu = 0.14$$

Two thicknesses were considered,  $t = 1.0$  and  $0.5$  inches.

This mirror is the largest, and therefore is assumed to be the most fragile, of the high resolution cylindrical mirrors. For the case of the  $1.0$  inch thick mirror, the edge restraint conditions were assumed fixed with respect to the transverse beam cross-section plane, for  $t = 1.0$  inch or a completely restrained boundary with respect to the cylinder/shell edge circumference. Figure 4-2a depicts these assumptions. The boundary edge remains circular. For the  $0.5$  inch case, the edge restraint conditions were held in such a manner that the circumference boundary remained circular in the transverse plane, but the edges were allowed to rotate as indicated in Figure 4-2b.

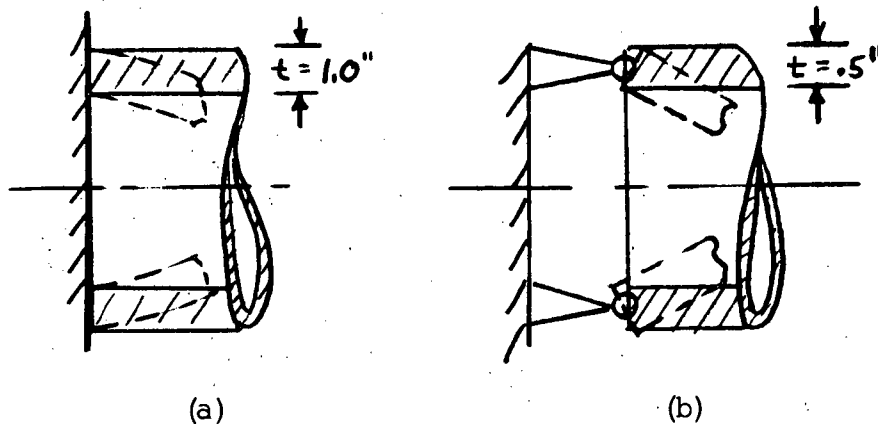


Figure 4-2. Edge Restraints

These assumptions represent two possible boundary parameters, of which (a) is probably the stiffest possible configuration and (b) probably the closest to the current configuration. Time did not permit a complete parametric evaluation.

The major problem area involved relating to the mirror dynamic displacement response at a particular frequency and mode shape given in reference (1) to the input random vibration level. The assumption was made that the lower natural frequencies would incur the highest deflections and therefore the highest stresses, since

- a. Sinusoidal displacements vary inversely to frequency squared for constant G's.
- b. RMS random displacements for a flat power spectral density input to a single degree of freedom system vary inversely as  $f_n^{3/2}$ .

In this case, the lowest natural frequencies are 1024 cps for the  $t = 1.0$  inch case and 702 cps for the  $t = 0.5$  inch case. Thus in both cases, only the random vibration spectrum need be considered since the sinusoidal levels cut-off at 50 cps. The harmonic and mode shapes for the lowest frequencies in each case are presented in Figures 4-3 and 4-4.

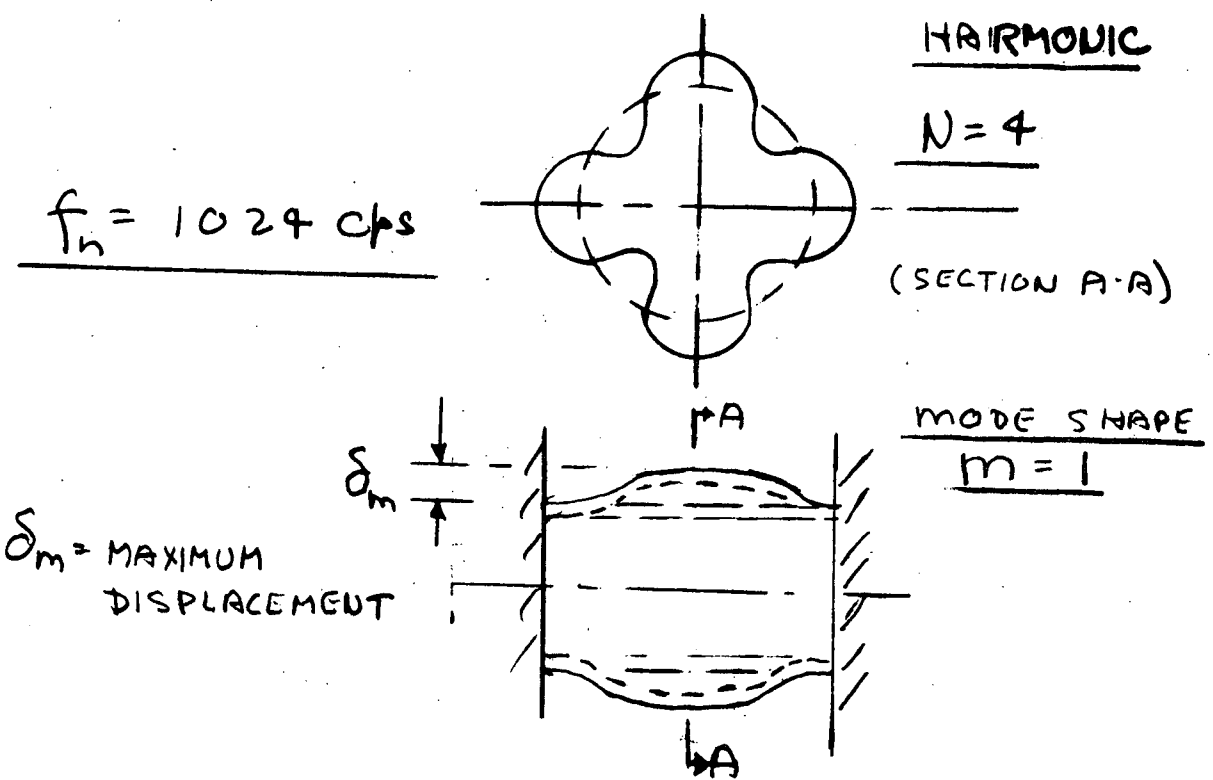


Figure 4-3. Harmonic and Mode Shapes -  $t = 1.0$  inch

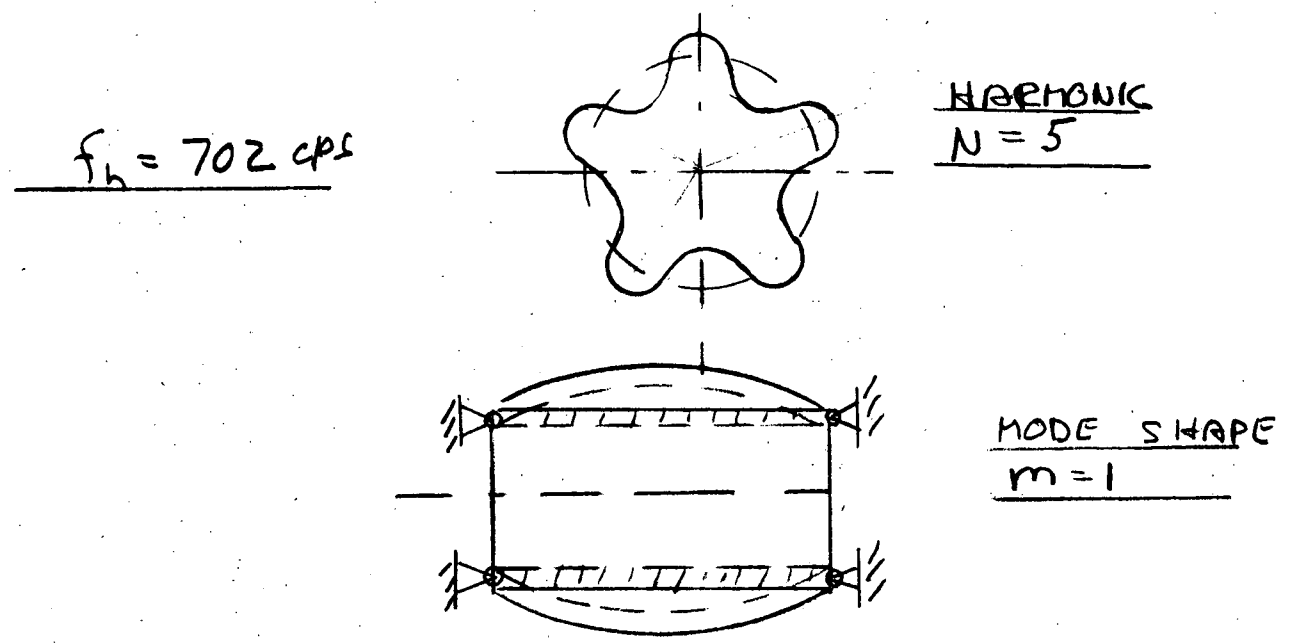


Figure 4-4. Harmonic and Mode Shapes -  $t = 0.5$  inch

In both cases the lowest natural frequency has been called out. Since the frequencies are theoretically not coupled, it becomes a very difficult task to excite anything but the first harmonic ( $N = 1$ ) with any of the existing dynamic computer codes, because the input is usually considered translational at the boundaries.

Although theoretically the harmonics are not coupled, in a practical sense coupling can occur because of a lack of infinite structural rigidity, holding fixture cross coupling, shaker "cross talk," etc., during an actual test or perhaps in the real spacecraft environment. Since the  $N = 4$  harmonic is only 60% in frequency of the  $N = 1$  harmonic, conservative design dictates that it be considered, since as mentioned previously the lowest natural frequency would have the highest associated displacement.

One method of approaching the problem is to assume that the lowest resonance of the mirror responds as a single degree of freedom system with a conservatively high resonant amplification ( $T_R = 20$ ,  $C/C_c = 0.025$ , for example) when subjected to the random power spectral density input requirement. By calculating the 3 sigma peak displacement response of this single degree system, a maximum displacement value can be obtained with which to compute the maximum stress value from the SABOR III stress resultant coefficient matrix.

The procedure for performing this calculation is as follows:

1. Plot the transmissibility curves for  $T_R = 20$  and  $f_n = 1024$  cps and 512 cps. The curve has form given below in Figure 4-5.
2. Square the ordinates of each transmissibility curve, producing curves of the form of Figure 4-6.
3. Multiply the ordinates of Figure 4-6 by the appropriate power spectral density level (Figure 2-2) at each increment of frequency to obtain a  $g^2$ /cps response plot as in Figure 4-7.

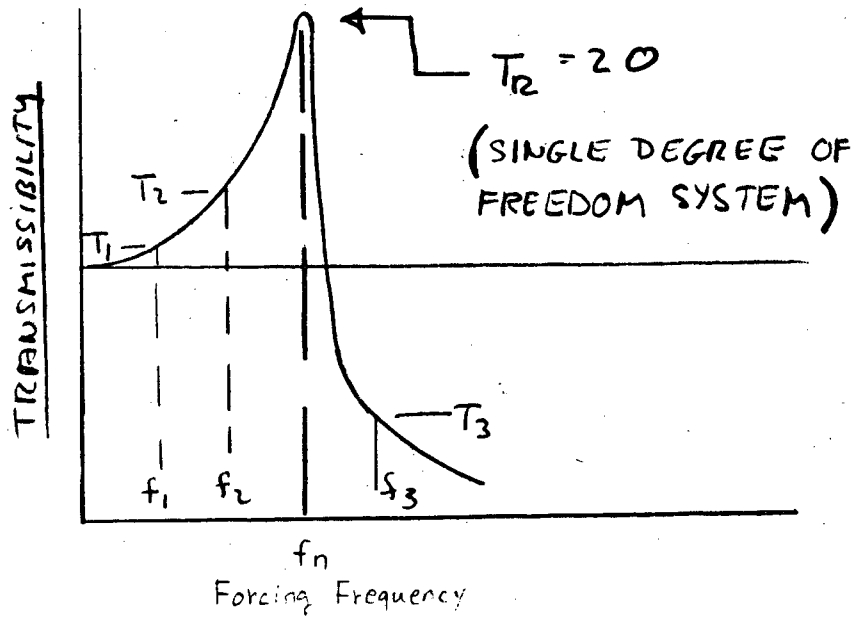


Figure 4-5. Transmissibility Curve

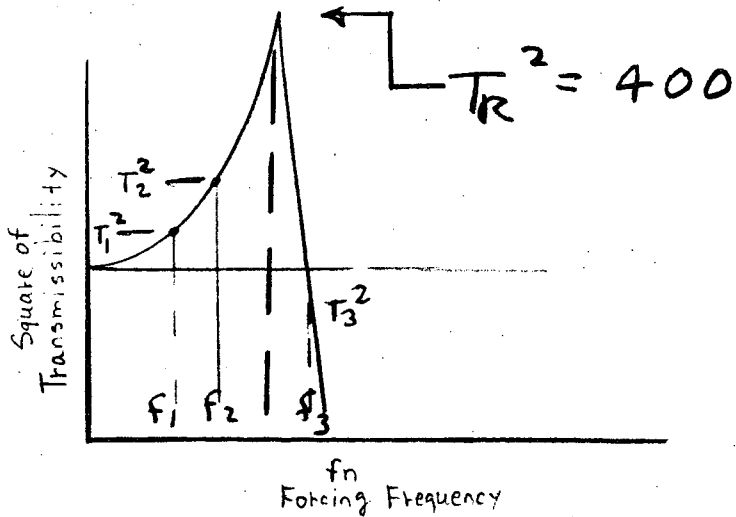


Figure 4-6. Square of Transmissibility

4. Convert the  $g^2/\text{cps} \times T^2$  curve to  $(\text{deflection})^2/\text{cps}$  by multiplying each ordinate by  $g^2/(2\pi f)^4$  or  $\frac{(95.6) g^2/\text{cps}}{f^4}$  at each frequency increment, and plot a new curve of  $S_E$  (inches<sup>2</sup>/cps) vs. frequency as illustrated in Figure 4-8.

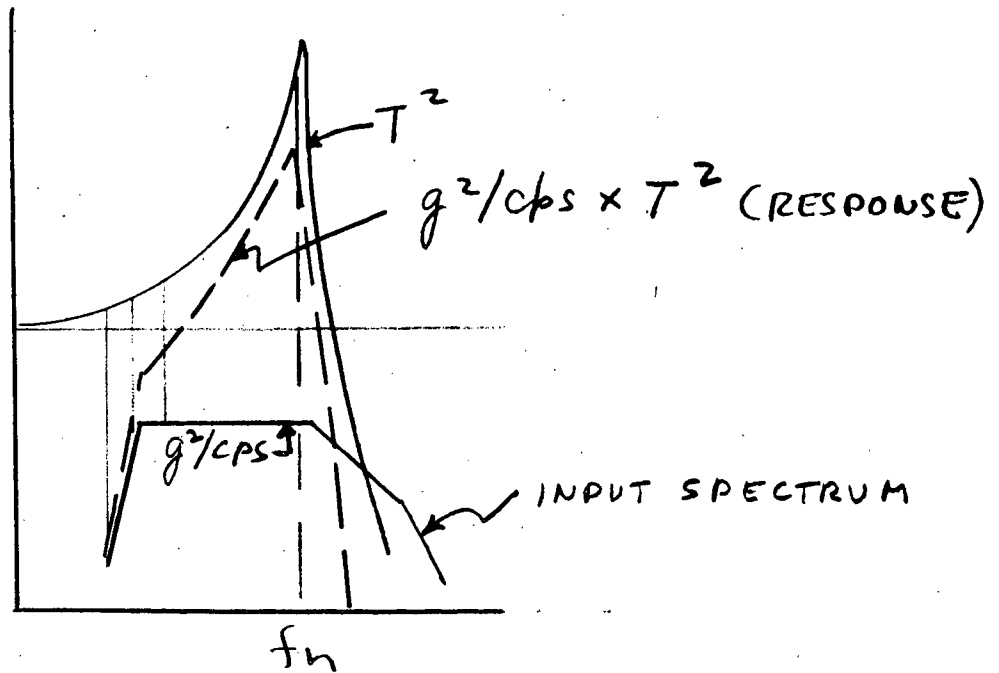


Figure 4-7.  $g^2/\text{cps}$  Response Plot

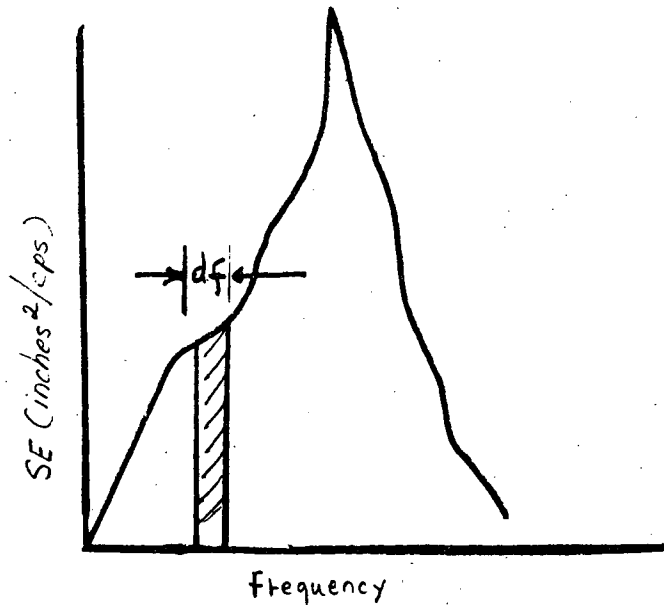


Figure 4-8. Plot of  $(\text{deflection})^2/\text{cps}$  vs. Frequency

5. Integrate the area under the curve of Figure 4-8 to obtain  $(\text{RMS displacement})^2$  and take the square root of this quantity to obtain RMS displacement. Thus:

$$(\text{RMS displacement}) = \sqrt{\int_{f_1}^{f_2} S_E df}$$

This procedure is obviously a tedious one and only as accurate as the number of frequency increments chosen and the accuracy exercised.

In place of the foregoing, Avco computer code 2921 was used to solve for the single degree transmissibility function, and to obtain relative rms displacements. This is a digital computer program which can solve for the sinusoidal or random responses of linear mass spring systems. The general equation is of the form:

$$M\ddot{X} + C\dot{X} + KX = P \sin \omega t$$

and program options permit the calculation of relative displacements. The rms displacements for the 1.0 inch thick mirror are:

		G's (rms) = 38.45
(rms) $\delta_m =$	$3.6 \times 10^{-4}$ inches	$f_n = 1024$ cps
(3 sigma) $\delta_m =$	$10.8 \times 10^{-4}$ inches	$T_R = 20$

and the corresponding values for the 0.5 inch mirror are:

		G's (rms) = 40.23
(rms) $\delta_m =$	$8.01 \times 10^{-4}$ inches	$f_n = 702$ cps
(3 sigma) $\delta_m =$	$24.03 \times 10^{-4}$ inches	$T_R = 20$

The resultant stresses are determined by multiplying the element stress resultant coefficient matrix by the maximum 3 sigma random relative deflection values noted above. The maximum values of interest are noted below in Table 4-1. A complete discussion of the stress matrix is given in Appendix C. It should be noted that the stress values listed are 3 sigma levels, and as such, are quite conservative. In addition, the system resonant amplification was assumed to be 20:1, which is also a conservative premise.

Reference (1) also examines the  $N = 1, m = 1$  case for  $f_n = 1627$ , but the results are lower than those given above. Figures 4-8 and 4-9 plot the stress distribution as a function of half of the

TABLE 4-1

## MAXIMUM STRESS LEVELS

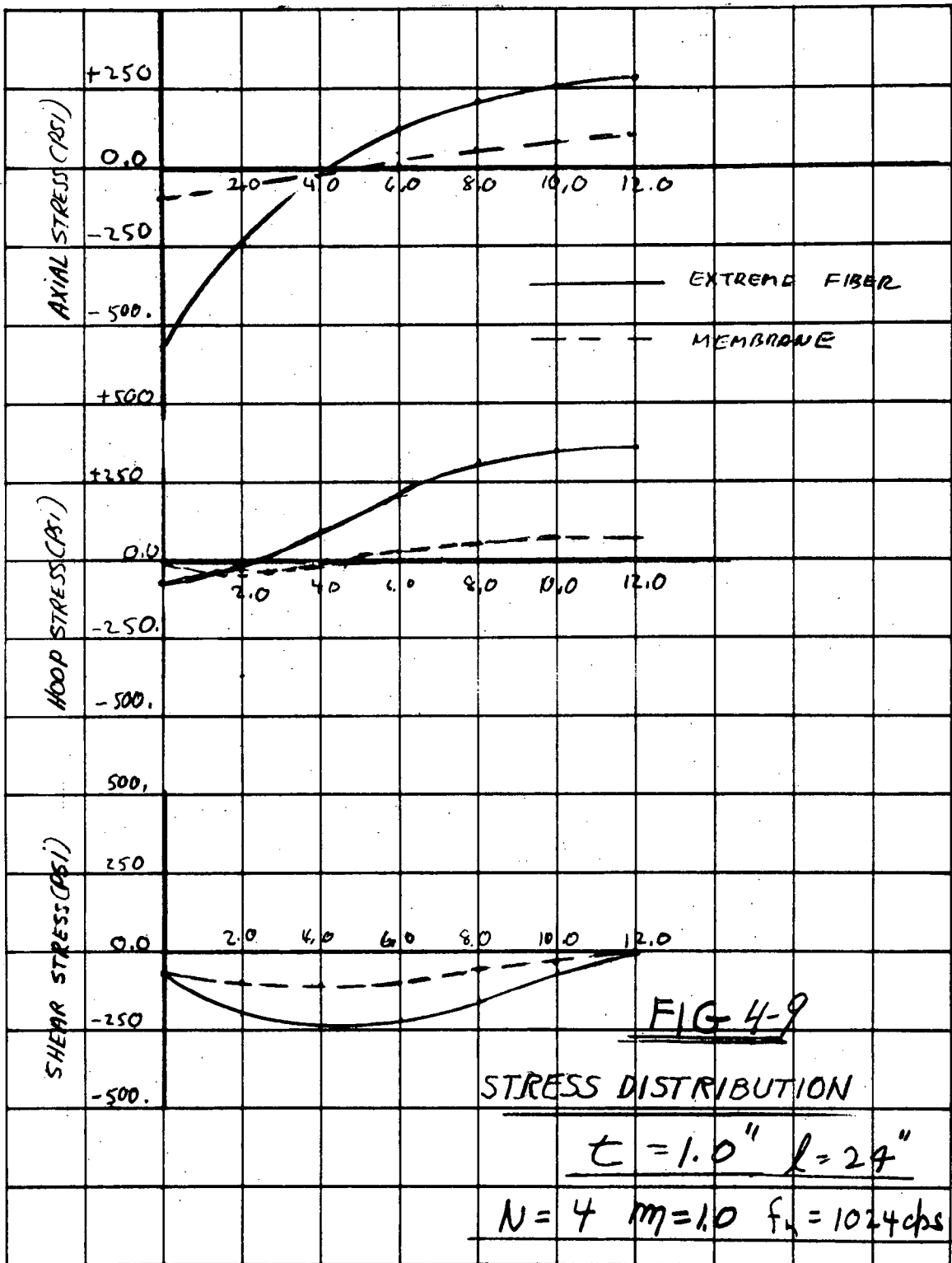
<u>Mode of Stress</u>		<u>t = 1.0 in</u>	<u>t = 0.5 in</u>
$\sigma_{\xi}$	- Axial Membrane	-115.0 psi	-260.0 psi
	Axial Membrane + Bending	-561.0	394.0
$\sigma_{\theta}$	- Hoop Membrane	67.6	68.2
	Hoop Membrane + Bending	362.2	-725.0
$\tau_{\xi\theta}$	Shear Membrane	-100.2	-200.0
	Shear Membrane + Bending	-237.0	-379.5

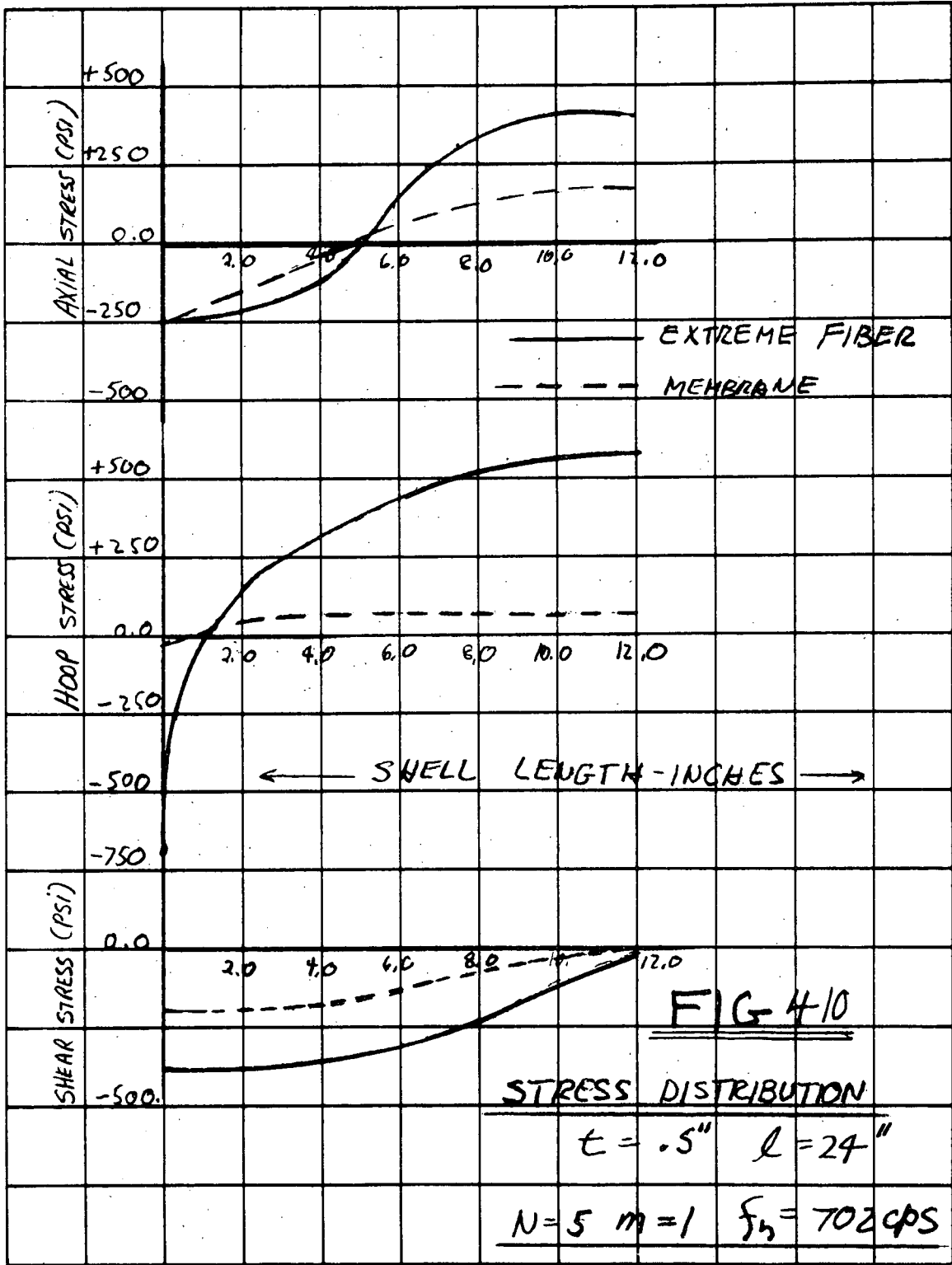
NOTE: t = 1.0", N = 4, m = 1,  $f_n = 1024$  cps  
t = 0.5", N = 5, m = 1,  $f_n = 702$  cps

length of the 24 inch mirror (0 - 12 in.). The stress picture for the other half (12 - 24 in.) would be symmetrical. Negative values indicate compression, while positive values indicate tension, but this fact is academic since vibration motions cause the stresses to alternate between tension and compression.

The results presented in Table 4-1 and Figures 4-9 and 4-10 show the stresses developed in the mirrors to be relatively low. On the basis of these results, it may not be necessary to provide vibration isolation for the entire optical bench in order to protect the mirrors. These results cannot be considered a firm conclusion on the subject of bench mounting, however, as they were derived for the random vibration environment only. Before a final judgement can be made, analyses of the effects of the shock and sinusoidal vibration environments must be carried out. The present analysis continues on the basis of a hard mounted optical bench.

The first mode of the uniformly loaded, simply supported bench based on the longeron design for a system with an 11,000 lb. total weight is about 50 cps (refer to Section 2.0), which would indicate that the mirror, being located at or very near one set of





support points, would see exactly the input spectrum in translation as illustrated in Figure 4-11. In other words, transmissibility between spacecraft and bench in the region of the end supports (at one of which the mirror is mounted is 1:1).

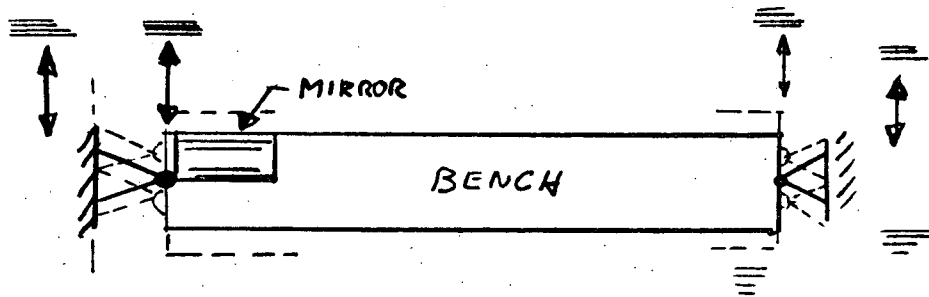


Figure 4-11. Translational Inputs and Responses

This translational input would be strictly a rigid body motion with respect to the mirror, since its lowest resonance as a shell is about 700 cps. This fact means that no relative deflections, and therefore no stresses, would be developed across the mirror. In rotation, however, a slightly different situation is incurred, but with little consequence. The simple support concept allows rotation at the supports; thus the mirror assembly would be subjected to a "pivoting," as illustrated in Figure 4-12, which is the result of the optical bench simply supported mode at 50 cps being excited in translation. Again, 50 cps represents only rigid body motion to the relatively stiff high resolution mirror and therefore no stresses are developed.

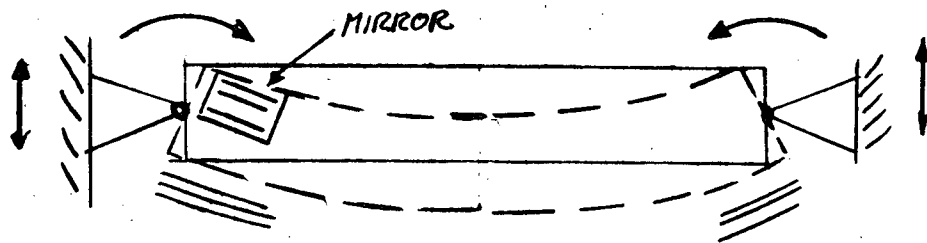


Figure 4-12. Rotational Inputs and Responses

The maximum single-amplitude deflections at the center of the bench length are (from Section 2.0):

Sinusoidal Vibration	0.155 inch
Random Vibration	0.097 inch (3 sigma)
Lateral 2.25 G's	<u>0.012 inch</u> (shear and bending)
	$\Sigma 0.264$ inch

These beam deflections produce pivot angle deflections at the mirrors (as illustrated in Figure 4-13).

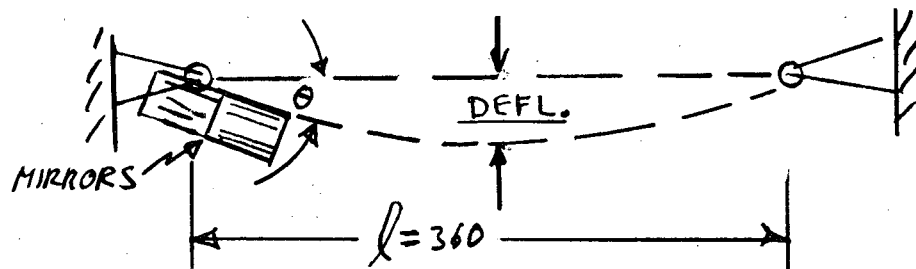


Figure 4-13. Angular Deflections as a Result of Beam Bending

These angular deflections are:

Vibration Only	$\theta = 0.0014$ rads = $0.08^\circ$
Vibration + 2.25 G's	$\theta = 0.000147$ rads = $0.084^\circ$
Vibration + 9 G's	$\theta = 0.000166$ rads = $0.095^\circ$

If the bench resonance were higher than 50 cps, the sinusoidal contribution would be eliminated because of the 50 cps cut-off. The most realistic value of maximum angular deflection would be that resulting from the combination of the random vibratory input plus the 2.25 g lateral loading, a combined value of 0.0006 radians or 0.0346 degrees. This condition would only be evidenced during lift-off or powered flight.

The higher modes of the simply-supported optical bench are:

Mode	1	2	3	4	5
Frequency (cps)	50	200	450	800	1250

These data indicate that at least the fourth mode of the simply supported bench would have to be excited in order to possibly incur mirror shell resonant ( $\approx 700$  cps) responses, which is highly improbable, since it is extremely difficult to excite these higher modes. Also, even if this mode were excited, the amplitudes would be extremely small because the inputs are small, and damping tends to reduce higher frequency resonant responses more than the lower frequency resonant responses.

Should thermal restraint considerations necessitate the incorporation of vibration isolators, a slightly different situation evolves. The isolators, if very soft with respect to the "optical bench," would tend to cause the mode shape of the bench structure to approach the free-free condition as an elastically supported member. This, in turn, would cause the high resolution mirrors to be subjected to translation and rotational inputs at the free-free (upper limit) or elastically supported mode. In this case, the free-free mode first resonant frequency is 110 cps, based on a uniform load distribution of 11,000 lbs. The mode shape allows translation as well as rotation at the ends for vibratory responses as shown in Figure 4-14.

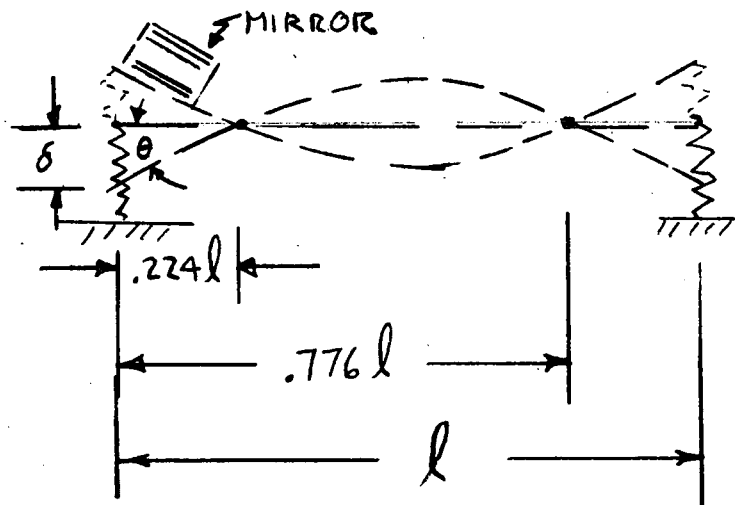


Figure 4-14. Free-Free Mode Shape of Optical Bench

The ideal mirror location would be at a nodal location where only rotation would occur without translation. In reality, the frequency should be somewhat less than 110 cps, because the supports will not be completely soft. Also, the unequal weight distribution will tend to move the nodes toward the support points, assuming the largest portion of weight to be concentrated at the ends near the support points. Again, assuming that the lowest mirror natural frequency is 700 cps, no adverse effects should be incurred by the mirrors either as relative motions or stresses across the mirrors.

At 110 cps the only vibratory input is the random spectrum of Figure 2-2. The maximum end motion based on single-degree-of-freedom considerations, assuming a bench transmissibility of 10 at 110 cps (a conservative approximation) can be calculated from:

$$\delta_{(rms)} = \sqrt{\frac{75.2 \times PSD}{C/C_c \times f_n^3}} = 0.013 \text{ inches}$$

for: PSD = 0.15 g<sup>2</sup>/cps

f<sub>n</sub> = 110 cps

C/C<sub>c</sub> = 0.05

δ (3 sigma) = 0.039 inch (end deflection)

The angular deflection at the ends of the bench (refer to Figure 4-14) is:

$$\theta_{\text{random}} = \frac{\delta}{0.224l} = 0.00048 \text{ radians (3 sigma)}$$

$$= 0.0277 \text{ degrees (3 sigma)}$$

Another parameter of interest is the acceleration resulting at the end of the mirror, which can be expressed as the following (single degree system):

$$\text{RMS } G = \sqrt{\frac{\pi}{2} \times \text{PSD} \times f_n \times T_R}$$

$$\text{RMS G} = \sqrt{\frac{\pi}{2} (0.15)(110)(10)} = 16.1 \text{ g's}$$

$$\text{Peak G's} = 3 \times 16.09 = 48.3 \text{ (3 sigma)}$$

Again, these should act as rigid body motions on the mirror since the major portion of the energy will be concentrated at the first mode of the optical bench.

The higher modes of the uniformly loaded free-free beam are:

Mode	1	2	3	4	5
Frequency (cps)	110	302.5	594	981	1463

Here too, only the third to fourth modes could elastically deform the softest mirror. As in the simply supported case, the deflections, even though the edges are somewhat unrestrained, would be extremely small as a result of the high frequency and damping effects. In all probability it would be extremely difficult to excite the third or fourth mode of such a structure.

Sustained acceleration effects on an elastically supported optical bench would be identical to the simply supported case except that the supports would deflect proportional to stiffness and load. The values of angular deflection are identical to those determined previously for the simply supported case.

#### Summary

On the basis of calculations performed using Avco Computer Codes 2222 (SABOR III), 2607, and 2921, the lowest mirror resonant frequencies and the largest deflection and stress are:

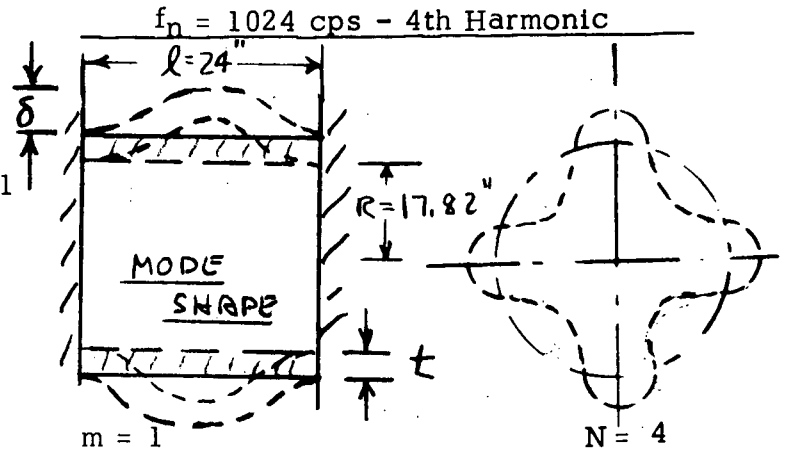
t = 1.0 inch

$\delta_{rms} = 3.6 \times 10^{-4}$

$\delta_{3 \text{ sigma}} = 10.8 \times 10^{-1}$

$G_{rms} = 38.45$

$\sigma_{axial} = -561 \text{ psi}$



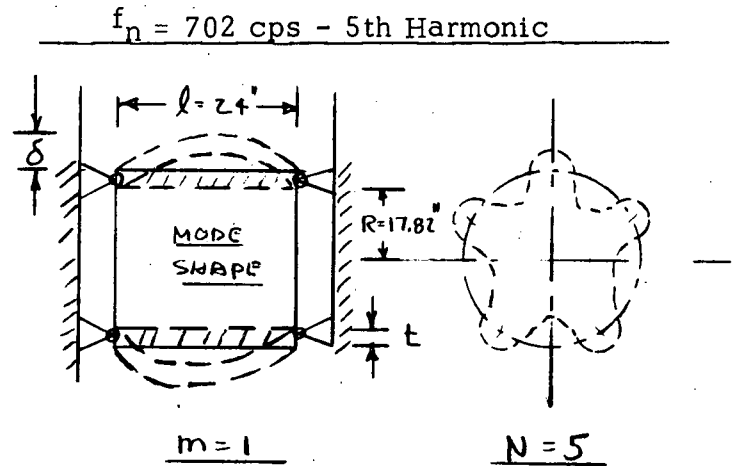
t = 0.5 inch

$\delta_{rms} = 8.01 \times 10^{-4}$

$\delta_{3 \text{ sigma}} = 24.03 \times 10^{-4}$

$G_{rms} = 40.23$

$\sigma_{hoop} = -725 \text{ psi}$



The results of the mirror analyses indicate that the high resolution mirrors can probably survive the vibration environment even without the use of isolation mounting of the optical bench to the spacecraft. Further study will be required, however, before a final commitment to a mounting configuration can be made.

## 5.0 SUMMARY AND RECOMMENDATIONS

The results of the analysis indicate the following:

- a. An "optical bench" configuration of longeron/truss construction is feasible dynamically. Assuming the use of graphite epoxy 3.5 inches diameter and a radius of 45 inches, a natural frequency of 50 - 110 cps is achievable depending upon whether or not isolators are used. Such a "bench" structure would weight approximately 1940 lbs without bracing, based on a total weight of 11,000 lbs including equipment.
- b. It is recommended that at least 4 spacecraft tie-in locations (approximately symmetrical) be provided at each end of the optical bench. If possible, additional mid-span tie-in points would be useful. The two-point hinge tie-down concept at either end of the bench, while perhaps desirable to counteract spacecraft "hot-dogging," is not good practice dynamically and should be avoided.

Any special tie-in hardware which is used should be carefully analyzed or tested for dynamic characteristics.

- c. The high resolution mirrors may not require that the optical bench be vibration isolated from the spacecraft. The highest dynamic stress is 725 psi, based on a 3 sigma random response, which compared to a specified 1000 psi tension allowable, can be considered satisfactory.
- d. The need for vibration isolation may evolve because of thermal requirements, the fragility level of other mirrors, collectors or instrumentation, future dynamic considerations, or design changes. Therefore, preliminary design layouts should allow sufficient space for their possible incorporation.

- e. If vibration isolation mounts are used, dynamic analysis incorporating the effects of response loads and displacements must be considered. In any case, the system natural frequency should not be below 20 - 30 cps, and optical bench response characteristics must be carefully considered together with isolation system performance.
- f. It is recommended that the dynamic characteristics of the flange holding structure at the mirror edges be examined for resonant responses and compared to expected frequencies of the mirror. This recommendation holds true for all mirrors.
- g. It is recommended that all final mirror designs be analyzed for fragility level in a fashion similar to what has been done for the largest high resolution mirror.
- h. It is recommended that the spacecraft tie-in locations be examined for stiffness as well as load bearing capabilities. The spacecraft should be compatible with the final optical bench requirements of load and stiffness as well as thermal considerations.
- i. It is recommended that the final proposed configuration of spacecraft, optical bench, mirror assemblies, and other instrumentation be mathematically modeled and analyzed to determine resonant frequencies, response accelerations and displacements, and worst stress conditions for combined static and dynamic loadings. This analysis would also determine the vibration environment to which internal components (instrumentation, etc.) will be subjected.

APPENDIX E

HEAT FLOW TO SPACE

E-1

## HEAT FLOW TO SPACE

Thermal radiation from the viewing apertures of the mirror assembly to space would be that of a black body of equivalent area and temperature. For the projected aperture of somewhat less than 2 ft<sup>2</sup> and a nominal temperature of 500°R the heat flow to space would be about 60 watts, which obviously would cause unacceptable temperature gradient patterns in the mirror assembly and be wasteful of spacecraft energy. An aluminized plastic membrane is often used as a radiation shield between the apertures and space, and was originally proposed for this application; however, such a membrane absorbs certain X-rays of interest to an undesirable degree, and as a result, a different type of aperture protection is now proposed.

It is proposed that the aperture area of the spacecraft end wall have a radiation shield consisting of a large number of insulated layers or baffles placed between it and space. Each shield would have the aperture pattern cut away so that the narrow field of view for X-rays would be unobscured. The effect on the aperture thermal radiation would be that of a long narrow passageway beyond each aperture slot, and because aperture radiation would be diffuse, most of the radiation would be scattered a large number of times by the diffuse surface formed by the baffles; thus, the net radiation to space would be greatly reduced. This configuration has been called a precollimator.

The effectiveness of such a configuration in reducing heat flow is a function of the geometry of the passageway placed between the source, the aperture, and the sink (space). The baffles will be so configured that the passageway is much larger than its width, for which case attenuations of thermal radiation of the order of 20 times equivalent to that obtained using an aluminized membrane,

is to be expected. Attenuation of a factor of ten has been assumed for purposes of this study, and much of the resulting radiation will come from the spacecraft end wall at the inner ends of the passages. Radiation from the mirror assembly apertures to space is therefore reduced even further, by a factor of two to five.

A sketch of the precollimator configuration is shown in Figure E-1.

# PRECOLLIMATOR CONFIGURATION

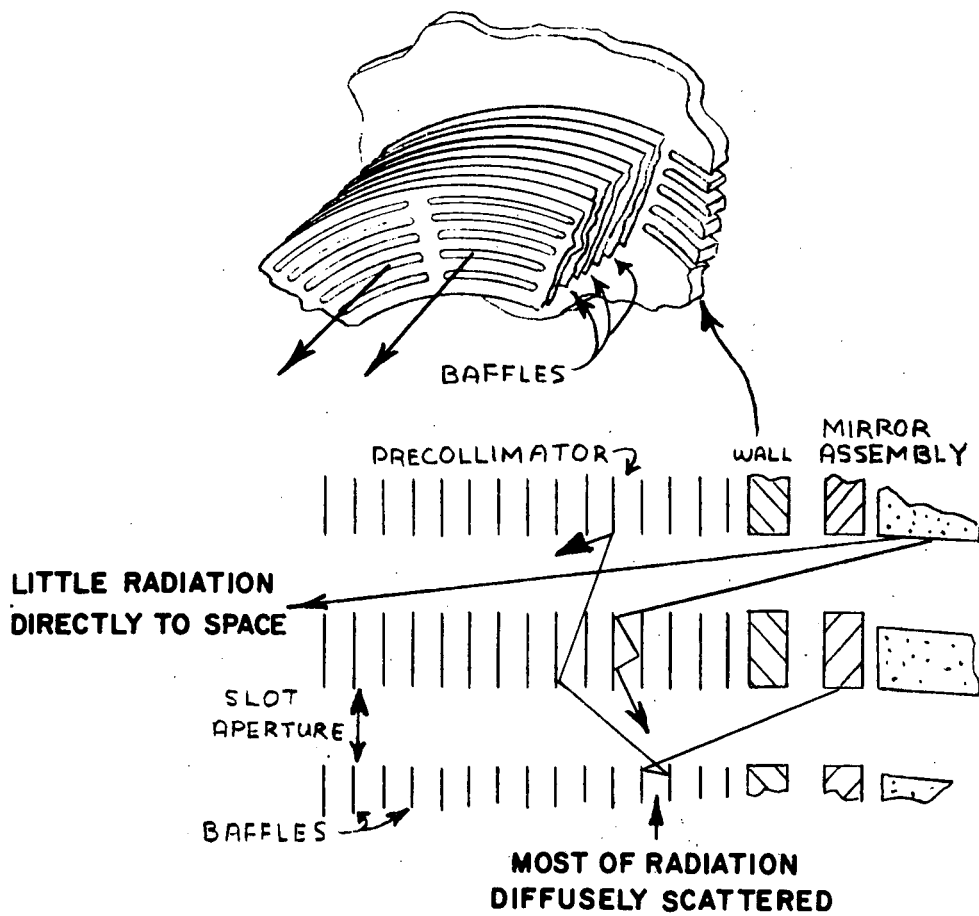


Figure E-1 Precollimator Configuration

APPENDIX F

TEMPERATURE GRADIENT PATTERNS

IN THE

HIGH RESOLUTION MIRROR ASSEMBLY

F-1

## TEMPERATURE GRADIENT PATTERNS IN THE MIRROR ASSEMBLY

Temperature gradient patterns in the mirror assembly were investigated in considerable detail because of the possible effect of thermal distortion on the mirror figure. Two 2-dimensional thermal mathematical models of the mirror assembly were formulated, one describing the assembly in the axial-radial direction (cross-section through the axis) and the other in the circumferential-radial direction (cross-section perpendicular to the axis). Two models were used rather than a single 3-dimensional model in order to provide a sufficient degree of detail with a manageable number of nodes; this action was justifiable because the effects of interest were similarly symmetrical.

In the axial-radial plane the assembly was represented by a model of 80 nodes. Each mirror and support shell were divided into 4 axial sections, with nodes at the centers. The support plates at each end were divided radially into annuli with conduction across the narrow supporting "bridges" carefully represented. The effect of the variable thickness of the end-plate stacks was included, as was the thin ring connection between each mirror and its end plates. Radiative transfer between mirrors and between support shells and mirrors was considered, but the possible effect of specularity of the surfaces was not included (that is, all surfaces were assumed to be diffuse; specularity is expected to improve radiative transfer and thus reduce the gradients calculated). Boundary conditions were modeled in the form of imposed heat loads at the viewing aperture end, and with radiative connections to the interior of the spacecraft, which was assumed to be at constant reference temperature.

Six cases were investigated for the reference design: with and without insulation on the periphery of the assembly and with temperature control on the two support shells, for both metallized mirrors, and completely unmetallized mirrors. In this preliminary study only steady-state solutions were obtained, which is justifiable because the mirror assembly time constant is short in comparison to that of the spacecraft.

Results of the 6 cases are shown in Figures F-1 and F-2 in which isotherms have been interpolated from the numerical results. Several points may be noted, the first of which is that there is little difference between the metallized and unmetallized cases. This is evidence of the fact that most of the heat transfer within the assembly is by conduction; with the small temperature differences present radiation is a minor consideration. The second item of note is that heat flow is almost entirely axial in the insulated cases, while the uninsulated cases show the effects of good radiative conductance between spacecraft and mirror assembly in a skewed heat flow pattern. This fact is of little significance in the reference design, but will be mentioned again in discussing the alternate design. The third point is that temperature control of the shells eliminates most of the gradients by supplying heat directly near the point of loss by radiation. The effect of heat loss to the interior of the spacecraft in the temperature-controlled case is not shown here, but the heat flows involved are significant, and heat sources near the rear apertures would probably be required.

The thermal model was modified to reflect the alternate design and some of the cases repeated for comparison purposes. The results show the shift in emphasis in heat flow patterns resulting from the somewhat simpler configuration and higher conductivity. Axial

ISOTHERMS IN DEGREES FAHRENHEIT - 1.5 WATT HEAT LOSS

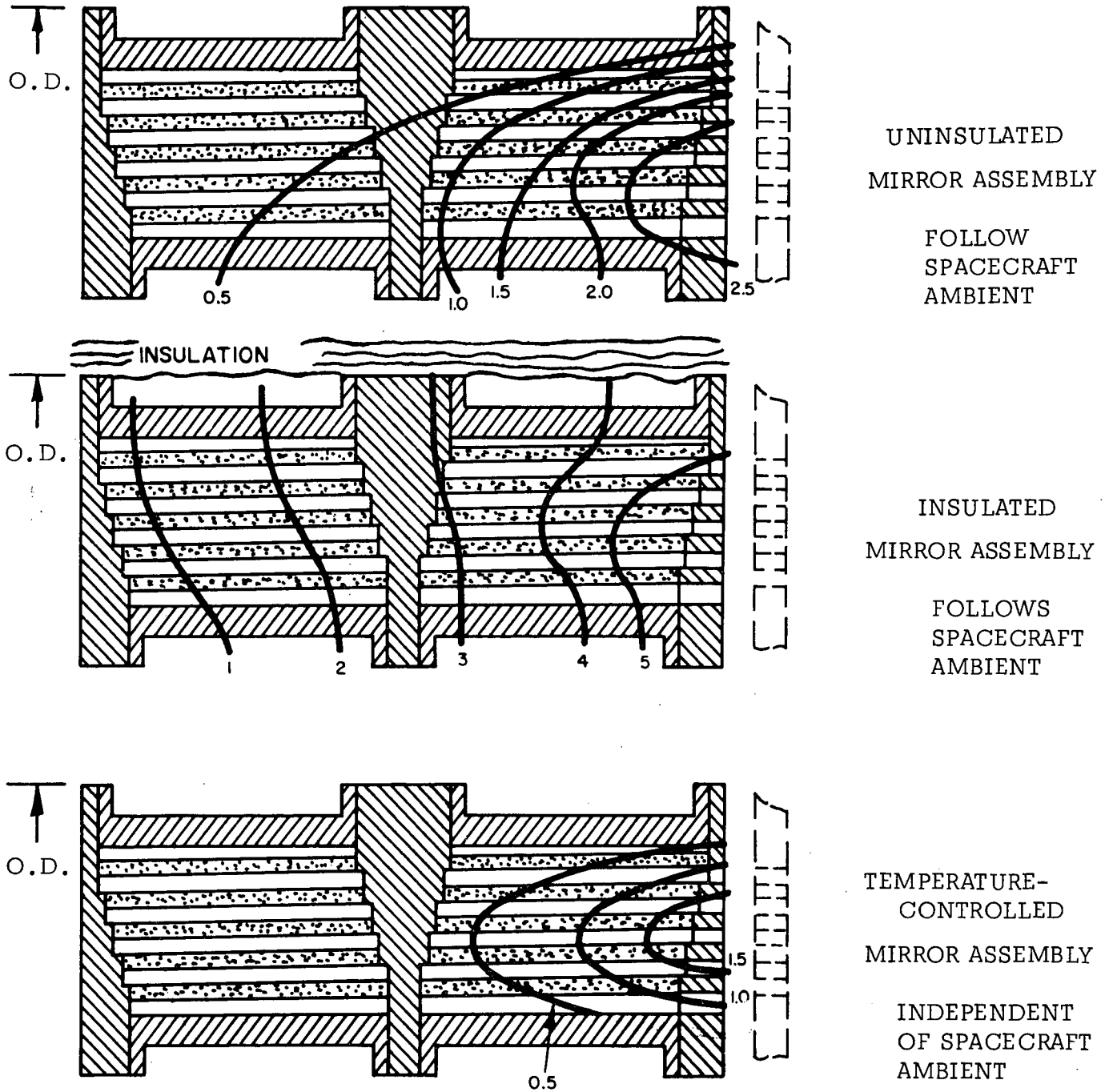


Figure F-1. Temperature Gradient Pattern In Mirror Assembly Metallized Mirrors

ISOTHERMS IN DEGREES FAHRENHEIT - 1.5 WATT HEAT LOSS

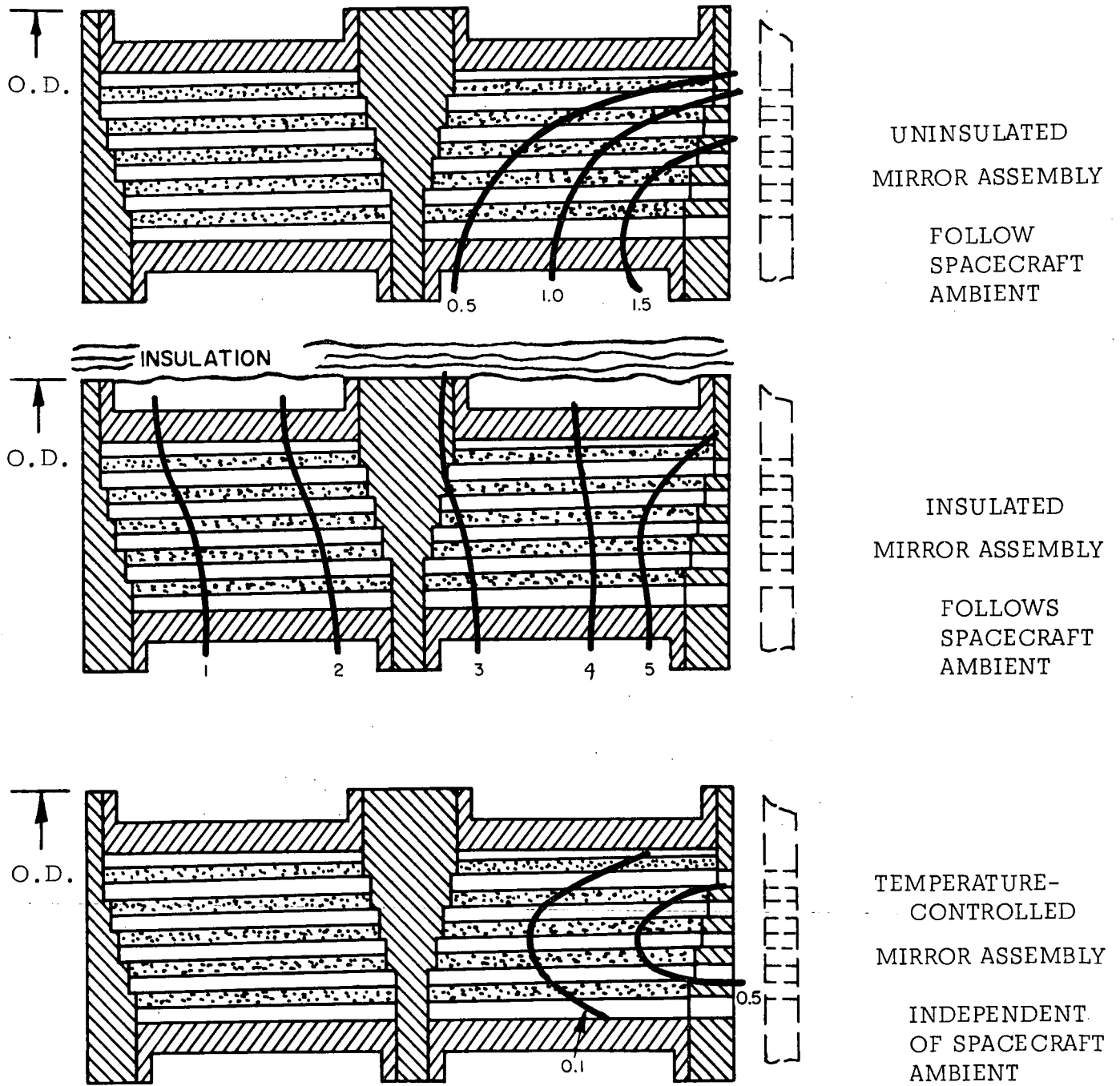


Figure F-2. Temperature Gradient Pattern In Mirror Assembly Unmetallized Mirrors

conductance is increased more than radial conductance because of the increased area-conductivity product even though the support shells are eliminated. This emphasizes axial heat flow even more than in the reference design; axial temperature differences for the nominal case are less than  $0.1^{\circ}\text{C}$ . The higher expansion coefficient of beryllium and its potential for local distortion underscores the need to avoid the type of skewed gradient pattern shown in the figure for uninsulated cases, and makes stronger the case for peripheral insulation. Individual results for these cases are not shown because of the small magnitudes of temperature differences.

The possibility that unequal temperatures of the solar and anti-solar sides of the spacecraft might induce a circumferential gradient pattern in the mirror assembly led to an investigation of this condition. The circumferential thermal model was used to evaluate the effective circumferential conductance across the mirror assembly. For the reference design this is about  $0.3 \text{ watt}/^{\circ}\text{F}$ . The radiative conductance between the assembly and either adjacent spacecraft wall is at least twice this magnitude and the 3 conductances are effectively in series; therefore, at least half the temperature difference across the spacecraft will appear across the mirror assembly. A figure for gross distortion in bending or "hot-dogging" of the mirror assembly due to a uniform z-axis gradient may be calculated using the relationship

$$\theta = \frac{L\alpha\Delta T}{d}$$

where

L = length of assembly

$\alpha$  = coefficient of expansion

$\Delta T$  = temperature difference across assembly

d = diameter of assembly

$\theta$  = angle through which the assembly bends

For the reference design this magnitude is about 0.1 arc-second per degree Fahrenheit, and it is obvious that the resolution of the mirror is significantly affected with even a nominal temperature difference. For a 10<sup>o</sup>F difference, for instance, the bending is of the same magnitude as the desired resolution. It is obvious from this calculation that reduction of circumferential gradients is imperative.

In the case of the alternate design the potential distortion is even greater. The bend angle due to a uniform z-axis gradient is about 1.3 arc-second per degree Fahrenheit, and it is therefore obvious that the greatest care must be taken to insure a symmetrical thermal configuration, including the use of insulation on both inner and outer circumferences of the assembly.

APPENDIX G

AMBIENT TEMPERATURE RANGE

OF THE

HIGH RESOLUTION MIRROR

6-1

## AMBIENT TEMPERATURE RANGE OF HIGH RESOLUTION MIRROR

An operating ambient temperature range of  $25^{\circ}\text{C}$  is considered to be applicable to the High Resolution Mirror Assembly. This figure is based on the detailed analysis performed by the spacecraft contractor for the HEAO-A Spacecraft and includes 3-sigma hot and cold cases for normal and pointing orientations. In fact, the average ranges for several different instruments in the HEAO-A analysis were of the order of  $20^{\circ}\text{C}$ ; an additional  $5^{\circ}\text{C}$  was added to encompass uncertainties in the analysis. (The RSS error given for the analysis is smaller than  $5^{\circ}\text{C}$ .) It is reasonable to assume that the A-mission predictions are applicable to the C-mission because of the physical similarities of the 2 spacecrafts.

It should be noted that an absolute temperature regime is not defined as yet. The choice of spacecraft temperatures can be controlled by control of the optical properties of the Z face, and will depend on the temperature control philosophy selected for the mirror assembly and optical bench. For example, if passive control is chosen, it would be desirable for the mean probable spacecraft ambient to be approximately the mirror fabrication and alignment temperature. An active temperature control method would indicate selection of a lower spacecraft temperature to provide a heat sink for the control system. This choice need not be defined until well into the program.

## APPENDIX H

### RELATIONSHIP BETWEEN MIRROR ASSEMBLY FOCAL LENGTH AND OPTICAL BENCH

Mirror focal length is a characteristic linear dimension of the mirror assembly, and exhibits the coefficient of expansion of the mirror material. The magnitude of change over a given temperature range is expressed by the familiar relationship:

$$\Delta L = L \alpha \Delta T$$

where  $\Delta L$  = change in length over temperature range

$L$  = reference length

$\alpha$  = coefficient of linear expansion

$\Delta T$  = temperature range

For the case of the reference design, using fused silica mirrors having  $\alpha = 0.31 \times 10^{-6} / ^\circ\text{F}$ , the change in the nominal 240 inch focal length is about 75 microinches per  $^\circ\text{F}$ , or 3.3 mils total change in focal length over the expected operating range of  $45^\circ\text{F}$  ( $25^\circ\text{C}$ ). In order to maintain proper focusing conditions at the image plane the optical bench length must equal the focal length within a tolerance of  $\pm 8$  mils for all error sources including thermal expansion of the bench. Arbitrarily assigning half the total tolerance ( $\pm 4$  mils) to thermal expansion for purposes of this discussion, it is obvious

that the optical bench could change in length by 3.2 mils  $\pm$  4 mils or -0.8 mils to +7.2 mils over the operating temperature range. This implies an acceptable coefficient of expansion for the bench material within the range of  $-0.07 \times 10^{-6}/^{\circ}\text{F}$  to  $0.68 \times 10^{-6}/^{\circ}\text{F}$ . (This applies strictly to an isothermal bench, but the distinction is of no consequence for the materials under discussion.)

Graphite-epoxy composite and various formulations of Invar, both of which have been suggested as candidate bench materials, satisfy the requirements; it is equally clear that other common structural materials do not because of higher expansion coefficients.

The reason for investigating these matters in a study of the mirror assembly is to determine whether a requirement for temperature control of the mirror assembly is implied in maintaining focal position. It is clear that no such requirement exists for the reference design, because the total magnitudes of expansion are sufficiently small as to lie well within the acceptable tolerance over the expected range of temperature variation.

The same conclusion may not be applied to the beryllium alternate design. The expansion coefficient of beryllium lies in the range of 6.1 to  $6.5 \times 10^{-6}/^{\circ}\text{F}$ , and the focal length will therefore change by almost 70 mils over the operating temperature range, or about 1.5 mils per  $^{\circ}\text{F}$ . If a passive control scheme is to be used the constraints on the bench are bounded as follows (for the  $\pm$  4 mil tolerance previously assigned) (a) for an exact match in expansion coefficient between bench and mirrors, the average temperature of the bench must be within  $3^{\circ}\text{F}$  of the mirror assembly temperature, (b) for an exact match in temperature, the expansion coefficients must match within about 5%. Because these constraints are quite stringent, active control of the mirror assembly temperature combined with use of a very low-expansion bench may be in order.

APPENDIX I

LOXT HIGH RESOLUTION MIRROR ALTERNATE DESIGN

DYNAMIC ANALYSIS

1-1

CONTENTS

- I. Introduction
- II. General Approach
- III. Summary
- IV. References

## LOXT High Resolution Mirror Alternate Design

### Dynamic Analysis

#### I. Introduction

This analysis was conducted to determine the maximum stresses resulting from application of the HEAO random vibration spectrum (Reference 3) to the alternate design LOXT beryllium cylindrical mirror configuration.

The original effort conducted in References (1) and (2) considered three configurations of fused silica mirrors all of which were supported at both ends but of different thicknesses and restraint conditions.

The current analysis considers a 36" I. D. x .5" thick completely restrained cantilevered beryllium mirror with beryllium end flanges per AS&E drawing SK 502-459. This configuration is shown in Figure 1.

Mass and stiffness matrices, eigenvalues (natural frequencies), maximum displacements and stress levels are the parameters derived in the analysis.

The maximum response values of  $\ddot{X}$  and  $X$  respectively were 38 g's rms and  $3.3 \times 10^{-4}$  inches rms based on linear elastic theory which assumed no coupling of harmonics.

#### II. General Approach

The analytical approach to this problem is identical to that used in Reference (1) except that boundary conditions and material (glass vs. beryllium) are different.

Figure 1 shows the mirror configuration as well as the node and element numbers used for Sabor III modeling. Element 12 was increased in thickness and modulus to account for the added end flange mass and stiffness. The section entitled "Weights, Beryllium End Flanges" details these calculations.

The Sabor III computer program represents the shell by a finite element idealization using the matrix-displacement method. Displacements at each nodal circle are represented as follows: (see Figure 2)

$\bar{u}$  = meridional

$\bar{v}$  = tangential

$\bar{w}$  = normal

$\bar{\rho}$  = rotation (meridian plane)

and mass, stiffness and stress resultant matrices generated.

A more comprehensive discussion of the Sabor III program has already been given in **Section 5.4** and will not be repeated here.

The mass and stiffness matrices produced for the  $N = 0$  to  $N = 5$  (six total) harmonics were input to the 2607 computer program to obtain eigenvalues and phi vectors. Table 1 is a list of the first eight eigenvalues for each harmonic. Actually, since the model has 48 degrees of freedom, there are 48 eigenvalues (resonances) but these have not been reproduced for reasons of brevity.

The lowest resonant frequency, 1058 cps, was determined to be the first eigenvalue ( $m = 1$ ) of the third harmonic,  $N = 3$ . Figures 3 (a-f) show the first several mode shapes ( $m = 1, 2$ , etc.) for each harmonic  $N = 0$  through  $N = 5$ . Figure 3 (d) depicts this third harmonic.

Figure 4 is a composite plot of resonant frequency vs. harmonic number as a function of mode shape ( $m = 1$  through 5) for the first five modes. The modal plots are derived from the phi ( $\phi$ ) vectors of the 2607 eigenvalue solution and are not normalized with respect to each other (i. e.,  $m = 1, 2, 3$ , etc.) and therefore should not be used for amplitude comparison between mode shapes.

Tables 2 and 3 are the applicable restrained mass and stiffness matrices for the  $N = 3$  harmonic. All other harmonic matrices are physically contained in the Sabor III run.

Using the lowest natural frequency, 1058 cps, a 2921 computer program was run for a single degree of freedom system to obtain a random solution for an rms displacement. This response value was .00033" rms or .001" peak (3 sigma). The percent of critical damping used was  $C/C_c = .025$ , corresponding to a resonant amplification of 20:1 which is quite conservative. The input spectrum is shown in Figure 5, and is equivalent to 10.3 g rms, the same spectrum used previously for LOXT analysis.

Since it is not theoretically possible to linearly excite the uncoupled resonant harmonics it was assumed, for conservatism, that all of the energy contained in the spectrum causes only the first mode of the third harmonic (lowest natural frequency) to respond. The 2921 program single degree of freedom displacement was assumed to be the maximum response of this first mode ( $m = 1$ ) of the third harmonic ( $N = 3$ ).

Using the stress resultant matrix generated in the Sabor III program and post multiplying by an element displacement vector (phi vector for the  $m = 1$ ,  $N = 3$  case) normalized to reflect a maximum value of 0.001" peak, stress resultants are determined for all element nodes. Table 4 details these matrices for the minimum frequency case analyzed. Once the stress resultants are known, the actual stresses can be computed; **this procedure has been documented in Appendix C**. Table 5 is a copy of the stress resultant output, with maximum values encircled, while Figure 6 defines these stress resultants pictorially.

The section entitled "Stress Calculations" briefly defines maximum axial, hoop and shear stresses and tabulates (Table 6) stress levels down the length of the shell. Figure 7 plots shear, axial and hoop stresses for both membrane, and membrane plus bending down the length of the cylinder. In all cases bending has been added to either the (+) or (-) value of membrane stress to give the largest value of extreme outside fiber stress. This value has been plotted as plus (+) tension or minus (-) compression based on the convention of the membrane stress, but in actuality all stresses are oscillatory representing equal tension and compression levels.

### III. Summary

The following is a summary of all pertinent results:

#### Alternate Design Configuration

24" x 36" I. D. Beryllium Cantilever - 0.5" thick

Minimum Frequency - 1058 cps (N = 3, m = 1)

3 Sigma Peak Displacement - 0.001"

RMS G - 38.1

#### Maximum Stress Levels - (Outside Fiber - 3 Sigma)

$\sigma_{\xi}$  (Axial) = 783 psi

$\sigma_{\theta}$  (Hoop) = 344 psi

$\tau_{\xi\theta}$  (Shear) = 280 psi

TABLE I

PARA. NO.	TITLE:	ANAL. BY	
DWG. NO.	EIGENVALUES	DATE	
LOADS ARE		CHKD. BY	
( $\omega^2$ ) <u>N=0</u>	(cps) <u><math>f_n</math></u>	( $\omega^2$ ) <u>N=3</u>	(cps) <u><math>f_n</math></u>
4.802223 x 10 <sup>8</sup>	3489	4.420733 x 10 <sup>7</sup>	* 1058.
7.579617 x 10 <sup>8</sup>	4384	2.500183 x 10 <sup>8</sup>	2517.
8.213554 x 10 <sup>8</sup>	4564	6.34577 x 10 <sup>8</sup>	4011.
8.374653 x 10 <sup>8</sup>	4608	1.04081 x 10 <sup>9</sup>	5137.
1.011026 x 10 <sup>9</sup>	5063	1.694566 x 10 <sup>9</sup>	6555.
1.441871 x 10 <sup>9</sup>	6046	2.737505 x 10 <sup>9</sup>	8331.
2.265553 x 10 <sup>9</sup>	7579	3.980981 x 10 <sup>9</sup>	10047.
3.42264 x 10 <sup>9</sup>	9315	4.966142 x 10 <sup>9</sup>	11221.
<u>N=1</u>		<u>N=4</u>	
1.896986 x 10 <sup>8</sup>	2193.	7.126665 x 10 <sup>7</sup>	1344.
6.802878 x 10 <sup>8</sup>	4153.	2.240035 x 10 <sup>8</sup>	2383.
8.855593 x 10 <sup>8</sup>	4739.	5.56843 x 10 <sup>8</sup>	3756.
1.090144 x 10 <sup>9</sup>	5257.	1.018392 x 10 <sup>9</sup>	5081.
1.390109 x 10 <sup>9</sup>	5937.	1.751355 x 10 <sup>9</sup>	6664.
1.695226 x 10 <sup>9</sup>	6556.	2.945949 x 10 <sup>9</sup>	8642.
2.411219 x 10 <sup>9</sup>	7819.	4.815378 x 10 <sup>9</sup>	11049.
3.669276 x 10 <sup>9</sup>	9645.	6.658781 x 10 <sup>9</sup>	12994.
<u>N=2</u>		<u>N=5</u>	
6.083048 x 10 <sup>7</sup>	1241.	9.271641 x 10 <sup>7</sup>	1533.
4.077637 x 10 <sup>8</sup>	3215.	2.897179 x 10 <sup>8</sup>	2707.
7.681933 x 10 <sup>8</sup>	4413.	5.972643 x 10 <sup>8</sup>	3891.
1.088892 x 10 <sup>9</sup>	5255.	1.071411 x 10 <sup>9</sup>	5212.
1.616257 x 10 <sup>9</sup>	6902.	1.858859 x 10 <sup>9</sup>	6865.
2.278293 x 10 <sup>9</sup>	7600.	3.15143 x 10 <sup>9</sup>	8939.
2.971806 x 10 <sup>9</sup>	8680.	5.198698 x 10 <sup>9</sup>	11,481.
4.347459 x 10 <sup>9</sup>	10499.	8.201116 x 10 <sup>9</sup>	14,420.
* LOW VALUE			

# TABLE 2

HARMONIC NO. 1A (ALL HARMONICS EXCEPT N=0)

RESTRAINED MASS MATRIX

1, 1) 6.55964550-C3	( 1, 5) 1.63991140-03
2, 2) 6.55964550-C3	( 2, 6) 1.63991140-03
3, 3) 7.30931920-C3	( 3, 7) 1.26507450-03
4, 4) 7.49673770-C4	( 4, 7) 6.09109940-04
5, 5) 6.55964550-C3	( 5, 9) 1.63991140-03
6, 6) 6.55964550-C3	( 6, 10) 1.63991140-03
7, 7) 7.30931920-C3	( 7, 11) 1.26507450-03
8, 8) 7.49673770-C4	( 8, 11) 6.09109940-04
9, 9) 6.55964550-C3	( 9, 13) 1.63991140-03
10, 10) 6.55964550-C3	( 10, 14) 1.63991140-03
11, 11) 7.30931920-C3	( 11, 15) 1.26507450-03
12, 12) 7.49673770-C4	( 12, 15) 6.09109940-04
13, 13) 6.55964550-C3	( 13, 17) 1.63991140-03
14, 14) 6.55964550-C3	( 14, 18) 1.63991140-03
15, 15) 7.30931920-C3	( 15, 19) 1.26507450-03
16, 16) 7.49673770-C4	( 16, 19) 6.09109940-04
17, 17) 6.55964550-C3	( 17, 21) 1.63991140-03
18, 18) 6.55964550-C3	( 18, 22) 1.63991140-03
19, 19) 7.30931920-C3	( 19, 23) 1.26507450-03
20, 20) 7.49673770-C4	( 20, 23) 6.09109940-04
21, 21) 6.55964550-C3	( 21, 25) 1.63991140-03
22, 22) 6.55964550-C3	( 22, 26) 1.63991140-03
23, 23) 7.30931920-C3	( 23, 27) 1.26507450-03
24, 24) 7.49673770-C4	( 24, 27) 6.09109940-04
25, 25) 6.55964550-C3	( 25, 29) 1.63991140-03
26, 26) 6.55964550-C3	( 26, 30) 1.63991140-03
27, 27) 7.30931920-C3	( 27, 31) 1.26507450-03
28, 28) 7.49673770-C4	( 28, 31) 6.09109940-04
29, 29) 6.55964550-C3	( 29, 33) 1.63991140-03
30, 30) 6.55964550-C3	( 30, 34) 1.63991140-03
31, 31) 7.30931920-C3	( 31, 35) 1.26507450-03
32, 32) 7.49673770-C4	( 32, 35) 6.09109940-04
33, 33) 6.55964550-C3	( 33, 37) 1.63991140-03
34, 34) 6.55964550-C3	( 34, 38) 1.63991140-03
35, 35) 7.30931920-C3	( 35, 39) 1.26507450-03
36, 36) 7.49673770-C4	( 36, 39) 6.09109940-04
37, 37) 6.55964550-C3	( 37, 41) 1.63991140-03
38, 38) 6.55964550-C3	( 38, 42) 1.63991140-03
39, 39) 7.30931920-C3	( 39, 43) 1.26507450-03
40, 40) 7.49673770-C4	( 40, 43) 6.09109940-04
41, 41) 6.55964550-C3	( 41, 45) 1.63991140-03
42, 42) 6.55964550-C3	( 42, 45) 1.63991140-03
43, 43) 7.30931920-C3	( 43, 47) 1.26507450-03
44, 44) 7.49673770-C4	( 44, 47) 6.09109940-04
45, 45) 3.27982270-C3	
46, 46) 3.27982270-C3	
47, 47) 3.65465960-C3	( 47, 48) -1.03080140-03
48, 48) 3.74836880-04	

NOTE: THE NUMBERS OF ABOVE RESTRAINED MASS MATRIX, FOR THE NON-ZERO HARMONIC 1A, ARE NOT MULTIPLIED BY 2.0. FOR EACH RESTRAINT - NP,NDIRCT - THE ROW AND COLUMN GIVEN BY - 4\*(NP-1)ENDIRCT - ARE DELETED FROM THE TOTAL MASS MATRIX AND THE REMAINING ROWS AND COLUMNS ARE RENUMBERED SO THAT NO GAPS IN THE NUMBERING APPEAR.



121-6.6818981D05	9, 131-5.39996930E08
0, 13) 5.1617663D07	( 10, 14)-2.8060266D08
11, 13) 1.0022847D06	( 11, 15)-3.7461386D07
12, 14) 1.4857255D06	( 12, 16) 2.4751085D07
13, 15) 1.24243465D09	( 13, 17)-5.9596963D08
14, 16) 1.6057179D07	( 14, 18)-2.8060266D08
15, 17) 1.8626451D-09	( 15, 19)-3.7461386D07
16, 18) 1.4857255D06	( 16, 20) 2.4751085D07
17, 19) 1.24243465D09	( 17, 21)-5.9596963D08
18, 20) 1.6057179D07	( 18, 22)-2.8060266D08
19, 21) 1.8626451D-09	( 19, 23)-3.7461386D07
20, 22) 1.4857255D06	( 20, 24) 2.4751085D07
21, 23) 1.24243465D09	( 21, 25)-5.9596963D08
22, 24) 1.6057179D07	( 22, 26)-2.8060266D08
23, 25) 1.8626451D-09	( 23, 27)-3.7461386D07
24, 26) 1.4857255D06	( 24, 28) 2.4751085D07
25, 27) 1.24243465D09	( 25, 29)-5.9596963D08
26, 28) 1.6057179D07	( 26, 30)-2.8060266D08
27, 29) 1.8626451D-09	( 27, 31)-3.7461386D07
28, 30) 1.4857255D06	( 28, 32) 2.4751085D07
29, 31) 1.24243465D09	( 29, 33)-5.9596963D08
30, 32) 1.6057179D07	( 30, 34)-2.8060266D08
31, 33) 1.8626451D-09	( 31, 35)-3.7461386D07
32, 34) 1.4857255D06	( 32, 36) 2.4751085D07
33, 35) 1.24243465D09	( 33, 37)-5.9596963D08
34, 36) 1.6057179D07	( 34, 38)-2.8060266D08
35, 37) 1.8626451D-09	( 35, 39)-3.7461386D07
36, 38) 1.4857255D06	( 36, 40) 2.4751085D07
37, 39) 1.24243465D09	( 37, 41)-5.9596963D08
38, 40) 1.6057179D07	( 38, 42)-2.8060266D08
39, 41) 1.8626451D-09	( 39, 43)-3.7461386D07
40, 42) 1.4857255D06	( 40, 44) 2.4751085D07
41, 43) 1.24243465D09	( 41, 45)-8.9395444D09
42, 44) 1.6057179D07	( 42, 46)-4.2104330D09
43, 45) 1.8626451D-09	( 43, 47)-1.2822197D09
44, 46) 1.4857255D06	( 44, 48) 8.3932644D08
45, 47) 1.24243465D09	( 45, 49)-5.0114236D06
46, 48) 1.6057179D07	( 46, 50)-1.2822197D09
47, 49) 1.8626451D-09	( 47, 51)-2.8060266D08
48, 50) 1.4857255D06	( 48, 52) 2.4751085D07
49, 51) 1.24243465D09	( 49, 53)-5.9596963D08
50, 52) 1.6057179D07	( 50, 54)-2.8060266D08
51, 53) 1.8626451D-09	( 51, 55)-3.7461386D07
52, 54) 1.4857255D06	( 52, 56) 2.4751085D07
53, 55) 1.24243465D09	( 53, 57)-5.9596963D08
54, 56) 1.6057179D07	( 54, 58)-2.8060266D08
55, 57) 1.8626451D-09	( 55, 59)-3.7461386D07
56, 58) 1.4857255D06	( 56, 60) 2.4751085D07
57, 59) 1.24243465D09	( 57, 61)-5.9596963D08
58, 60) 1.6057179D07	( 58, 62)-2.8060266D08
59, 61) 1.8626451D-09	( 59, 63)-3.7461386D07
60, 62) 1.4857255D06	( 60, 64) 2.4751085D07
61, 63) 1.24243465D09	( 61, 65)-5.9596963D08
62, 64) 1.6057179D07	( 62, 66)-2.8060266D08
63, 65) 1.8626451D-09	( 63, 67)-3.7461386D07
64, 66) 1.4857255D06	( 64, 68) 2.4751085D07
65, 67) 1.24243465D09	( 65, 69)-5.9596963D08
66, 68) 1.6057179D07	( 66, 70)-2.8060266D08
67, 69) 1.8626451D-09	( 67, 71)-3.7461386D07
68, 70) 1.4857255D06	( 68, 72) 2.4751085D07
69, 71) 1.24243465D09	( 69, 73)-5.9596963D08
70, 72) 1.6057179D07	( 70, 74)-2.8060266D08
71, 73) 1.8626451D-09	( 71, 75)-3.7461386D07
72, 74) 1.4857255D06	( 72, 76) 2.4751085D07
73, 75) 1.24243465D09	( 73, 77)-5.9596963D08
74, 76) 1.6057179D07	( 74, 78)-2.8060266D08
75, 77) 1.8626451D-09	( 75, 79)-3.7461386D07
76, 78) 1.4857255D06	( 76, 80) 2.4751085D07
77, 79) 1.24243465D09	( 77, 81)-5.9596963D08
78, 80) 1.6057179D07	( 78, 82)-2.8060266D08
79, 81) 1.8626451D-09	( 79, 83)-3.7461386D07
80, 82) 1.4857255D06	( 80, 84) 2.4751085D07
81, 83) 1.24243465D09	( 81, 85)-5.9596963D08
82, 84) 1.6057179D07	( 82, 86)-2.8060266D08
83, 85) 1.8626451D-09	( 83, 87)-3.7461386D07
84, 86) 1.4857255D06	( 84, 88) 2.4751085D07
85, 87) 1.24243465D09	( 85, 89)-5.9596963D08
86, 88) 1.6057179D07	( 86, 90)-2.8060266D08
87, 89) 1.8626451D-09	( 87, 91)-3.7461386D07
88, 90) 1.4857255D06	( 88, 92) 2.4751085D07
89, 91) 1.24243465D09	( 89, 93)-5.9596963D08
90, 92) 1.6057179D07	( 90, 94)-2.8060266D08
91, 93) 1.8626451D-09	( 91, 95)-3.7461386D07
92, 94) 1.4857255D06	( 92, 96) 2.4751085D07
93, 95) 1.24243465D09	( 93, 97)-5.9596963D08
94, 96) 1.6057179D07	( 94, 98)-2.8060266D08
95, 97) 1.8626451D-09	( 95, 99)-3.7461386D07
96, 98) 1.4857255D06	( 96, 100) 2.4751085D07
97, 99) 1.24243465D09	( 97, 101)-5.9596963D08
98, 100) 1.6057179D07	( 98, 102)-2.8060266D08
99, 101) 1.8626451D-09	( 99, 103)-3.7461386D07
100, 102) 1.4857255D06	( 100, 104) 2.4751085D07

TABLE 36

INPUT CARDS READ	3/13/72
DATA* A(1,1) -5.9080951D03	3.9730642D05RSL 1 3A*DATA
DATA* A(1,1) -5.9080951D03	2.6273396D04 -6.3895730D05 1 3A*DATA
DATA* A(2,1) -1.0825600D07	8.0645498D05 1.7724285D04 5.9080951D03RSL 1 3A*DATA
DATA* A(3,1) -1.0539057D07	9.1280069D05 1.7724285D04 -5.9080951D03RSL 1 3A*DATA
DATA* A(3,1) -8.0645498D05	-5.5529919D06 -1.4197663D05 -3.9533179D03RSL 1 3A*DATA
DATA* A(4,1) -9.1280069D05	4.9621444D06 -5.5073840D05 -2.5273396D04RSL 1 3A*DATA
DATA* A(4,1) -1.7724285D04	1.4197663D05 -7.2345015D05 -5.8131759D03RSL 1 3A*DATA
DATA* A(5,1) -5.9080951D03	2.6273396D04 -6.3895730D05 -4.3769523D03RSL 1 3A*DATA
DATA* A(5,1) -5.9080951D03	3.9533179D05 6.3131759D05 -8.9730642D05RSL 1 3A*DATA
DATA* A(6,1) -1.0539057D07	9.1280069D05 1.7724285D04 5.9080951D03RSL 1 3A*DATA
DATA* A(6,1) -1.0825600D07	8.0645498D05 1.7724285D04 -5.9080951D03RSL 1 3A*DATA
DATA* A(7,1) -9.1280069D05	4.9621444D06 5.5073840D04 2.5273396D04RSL 1 3A*DATA
DATA* A(7,1) -8.0645498D05	5.5299190D06 1.4197663D05 -3.9533179D03RSL 1 3A*DATA
DATA* A(8,1) -1.7724285D04	5.5073840D05 -6.5246274D05 -6.5395253D03RSL 1 3A*DATA
DATA* A(8,1) -1.7724285D04	1.4197663D05 7.2845015D05 -5.8131759D03RSL 1 3A*DATA
DATA* A(9,1) 0.0	4.1028438D03 3.2248352D04 1.3293214D03RSL 1 3A*DATA
DATA* A(9,1) 0.0	-1.9939821D04 0.0 0.0 RSL 1 3A*DATA
DATA* A(10,1) -3.1903713D05	3.5449570D06 1.1816190D06 0.0 0.0 RSL 1 3A*DATA
DATA* A(10,1) -3.1903713D05	0.0 0.0 0.0 0.0 RSL 1 3A*DATA
DATA* A(11,1) 0.0	-1.1939275D04 0.0 0.0 0.0 RSL 1 3A*DATA
DATA* A(11,1) 0.0	1.1939275D04 0.0 0.0 0.0 RSL 1 3A*DATA
DATA* A(12,1) 0.0	-6.8380730D02 0.0 0.0 0.0 RSL 1 3A*DATA
DATA* A(12,1) 0.0	1.1077678D05 -1.1282820D05 -1.4770239D03RSL 1 3A*DATA
DATA* A(13,1) 0.0	0.0 0.0 -1.1077678D05 -1.3851189D03RSL 1 3A*DATA
DATA* A(13,1) 0.0	-1.9939821D04 -1.3293214D03RSL 1 3A*DATA
DATA* A(14,1) 0.0	4.1028438D03 3.2248352D04 -2.5526423D03RSL 1 3A*DATA
DATA* A(14,1) -3.1903713D05	0.0 0.0 0.0 RSL 1 3A*DATA
DATA* A(15,1) 0.0	3.5449570D06 1.1816190D06 0.0 0.0 RSL 1 3A*DATA
DATA* A(15,1) 0.0	-1.1939275D04 0.0 0.0 0.0 RSL 1 3A*DATA
DATA* A(16,1) 0.0	0.0 0.0 -1.1077678D05 -1.4770239D03RSL 1 3A*DATA
DATA* A(16,1) 0.0	-5.8380730D02 -1.1282820D05 1.4770239D03RSL 1 3A*DATA
DATA* A(17,1) 0.0	7.7875D-2 -1.4325D-1 -1.9574D-1 2.3551D-1 -2.63452D-1 0.999
DATA* A(17,1) 2.6944D-1	2.6123D-1 2.3852D-1 2.836D-1 2.7874D-1 0.999
DATA* A(2,1) 0.0	8.811D-2 2.0533D-1 3.4317D-1 4.9187D-1 6.4447D-1 0.999
DATA* A(7,9504D-1)	9.333D-1 1.0695D0 1.1848D0 1.2821D0 1.363D0 0.999
DATA* A(3,1) 0.0	-2.11D-1 -6.29D-1 -1.0955D0 -1.5725D0 -2.0508D0 0.999
DATA* A(2,5219D)	-2.9731D0 -3.3695D0 -3.7458D0 -4.0109D0 -4.155D0 0.999
DATA* A(4,1) 0.0	-1.786D-1 -2.2735D-1 -2.3692D-1 -2.3927D-1 -2.383D-1 0.999
DATA* A(2,317D-1)	-2.181D-1 -1.9551D-1 -1.5890D-1 -1.0305D-1 -4.715D-2 0.999
DATA* A(5,1) 7.7876D-2	1.4325D-1 1.9574D-1 -2.355D-1 2.634D-1 -2.3087D-1 0.999
DATA* A(2,894D-1)	2.9123D-1 2.896D-1 2.829D-1 2.797D-1 2.7954D-1 0.999
DATA* A(6,1) 8.811D-2	2.0563D-1 3.4317D-1 4.9187D-1 6.4447D-1 0.999
DATA* A(7,9504D-1)	9.363D-1 1.0695D0 1.1848D0 1.282D0 1.3634D0 0.999
DATA* A(1,4551D)	
DATA* A(7,1) -2.110D-1	-6.29D-1 -1.0955D0 -1.5725D0 -2.0508D0 -2.5219D0 0.999
DATA* A(2,973D)	-3.3695D0 -3.7458D0 -4.0109D0 -4.1561D0 -4.2562D0 0.999
DATA* A(8,1) -1.7857D-1	-2.2735D-1 -2.369D-1 -2.3927D-1 -2.3823D-1 0.999
DATA* A(2,3174D-1)	-2.181D-1 -1.9551D-1 -1.5890D-1 -1.0305D-1 -1.0305D-1 0.999
DATA* A(4,7147D-2)	-5.291D-2
DATA* X	2.357D-4
DATA* INPUT /A	16 8
DIMENSIONS OF MATRIX A ARE	16X 8.

A MATRIX  
STRESS RESULTS

B MATRIX  
Φ VECTORS  
DISPLACEMENTS

TABLE 4

16.02.09.30 3/14/72 \*DATA

INPUT CARDS READ  
A: INPUT 70  
R1X D

1. 4.74530690 CO	7.49066670-01	-2.50328660-01	-6.03027900-01	-1.02317110 00	-1.53170240 00	-2.10085970 00	<u>MSI</u>	
2. 83551890 CO	-3.85487300 CO	-4.88046030 00	-7.05251980-02					
3. 1772340 CO	1.91186750 CO	1.48266580 CO	8.39967780 CO	5.48853700 CO	2.99952340 CO	1.00268750 CO	<u>NSI</u>	
4. 64331950 CO	-1.28517110 CO	-1.41753850 CO	-5.45269230-01					
5. 79309510 CO	9.50366890 CO	9.68096330 CO	8.85396500 CO	7.79346790 CO	6.49750260 CO	4.94026640 CO	<u>NSI</u>	
6. 13158420 CO	1.09906910 CO	8.76430000 CO	-9.75715070-01					
7. 629054760 CO	-3.88366400 CO	-1.35593720 CO	2.64344660-01	6.38816710-01	1.04921090 00	1.47959540 00	<u>QSI</u>	
8. 83125110 CO	2.11510710 CO	2.99535970 CO	2.84175410-01					
9. 83342640 CO	3.52615080-01	-1.47782360-01	-4.89899650-01	-9.00557090-01	-1.41627760 00	-2.00025730 00	-2.72888160 00	<u>MSZ</u>
10. 78361830 CO	-4.84087240 CO	-3.21347140 CO	6.06324460-02					
11. 81326850 CO	1.48499870 CO	1.15426220 CO	8.38641240 CO	5.52843750 CO	3.06333010 CO	1.04571910 CO	-3.91171470 00	<u>NSZ</u>
12. 20055370 CO	-1.35433240 CO	-9.05594570 CO	-9.40635700-02					
13. 51234650 CO	9.93251830 CO	9.65929240 CO	8.94541660 CO	7.91897870 CO	6.64212850 CO	5.11586890 CO	3.32456550 CO	<u>NSTZ</u>
14. 32711390 CO	-5.79583870 CO	-2.06318470 CO	8.62073830-01					
15. 27747860 CO	-2.50246520 CO	-2.20434050 CO	-2.58912800 CO	-3.08679520 CO	-3.51283400 CO	-3.91004580 CO	-4.31611380 00	<u>QSZ</u>
16. 64454710 CO	4.28546080 CO	-1.48478530 CO	3.62044120-01					
17. 3213730 CO	-3.72957000-01	-1.59200670-00	-2.84111050 CO	-4.08438040 CO	-5.33168510 CO	-6.56269680 CO	-7.74492520 CO	<u>MTI</u>
18. 83999730 CO	-9.79387230 CO	-1.05073980 CO	-1.07293000 CO					
19. 85604540 CO	1.07696530 CO	5.74360220 CO	-1.54724340 CO	-2.48673550 CO	-3.13849770 CO	-3.74528300 CO	-4.39252990 CO	<u>NTI</u>
20. 03291360 CO	-5.35782400 CO	-4.61581780 CO	-1.86750440 CO					
21. 47922030 CO	-2.68488720 CO	-3.45164690 CO	-3.58182650 CO	-3.61053020 CO	-3.59986480 CO	-3.50899800 CO	-3.31330630 CO	<u>MSTI</u>
22. 97662890 CO	-2.40967480 CO	-1.51133370 CO	-5.36927860-01					
23. 40009350 CO	6.50934540-01	1.21284400-01	4.40702410-01	6.70029280-01	9.17148590-01	1.17567210 CO	1.43619570 CO	<u>QTI</u>
24. 70936050 CO	2.02403160 CO	2.35007320 CO	1.73604180 CO					
25. 9459920 CO	-1.60615680 CO	-2.84421240 CO	-4.08506670 CO	-5.33146580 CO	-6.56275950 CO	-7.74507370 CO	-8.84000040 CO	<u>MTZ</u>
26. 7214330 CO	-1.04586590 CO	-1.08029470 CO	-1.09222440-01					
27. 096910 CO	1.54328020 CO	-1.45151750 CO	-2.39947660 CO	-3.05967610 CO	-3.67852390 CO	-4.33906200 CO	-4.99967650 CO	<u>NTZ</u>
28. 35041230 CO	-4.42733130 CO	-1.86094780 CO	3.03701400 CO					
29. 781730 CO	-3.50813970 CO	-3.61289410 CO	-3.62150520 CO	-3.59381450 CO	-3.48910240 CO	-3.27936840 CO	-2.93188490 CO	<u>MSTZ</u>
30. 3583850 CO	-1.46667410 CO	-5.67269340-01	-6.34182710-01					
31. 1958960 CO	1.451045710 CO	4.57994180-01	6.73921160-01	9.15929220-01	1.17601930 CO	1.43858350 CO	1.70937720 CO	<u>QIZ</u>
32. 01398450 CO	2.30105420 CO	2.14571020 CO	1.77695710 CO					

\* NOTE: T = 0 S = f

# TABLE 5-

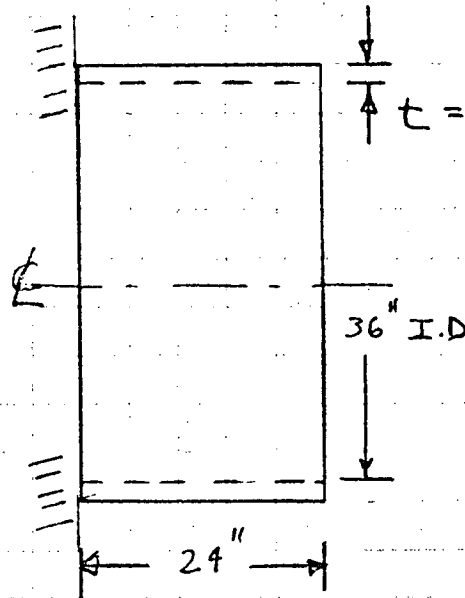
## STRESS RESULTANTS



FIG 1

PARA. NO.		TITLE: <u>CONFIGURATION</u>	ANAL. BY	
DWG. NO.		<u>LOX-T MIRRORS</u>	DATE	
LOADS ARE			CHKD. BY	

P-1

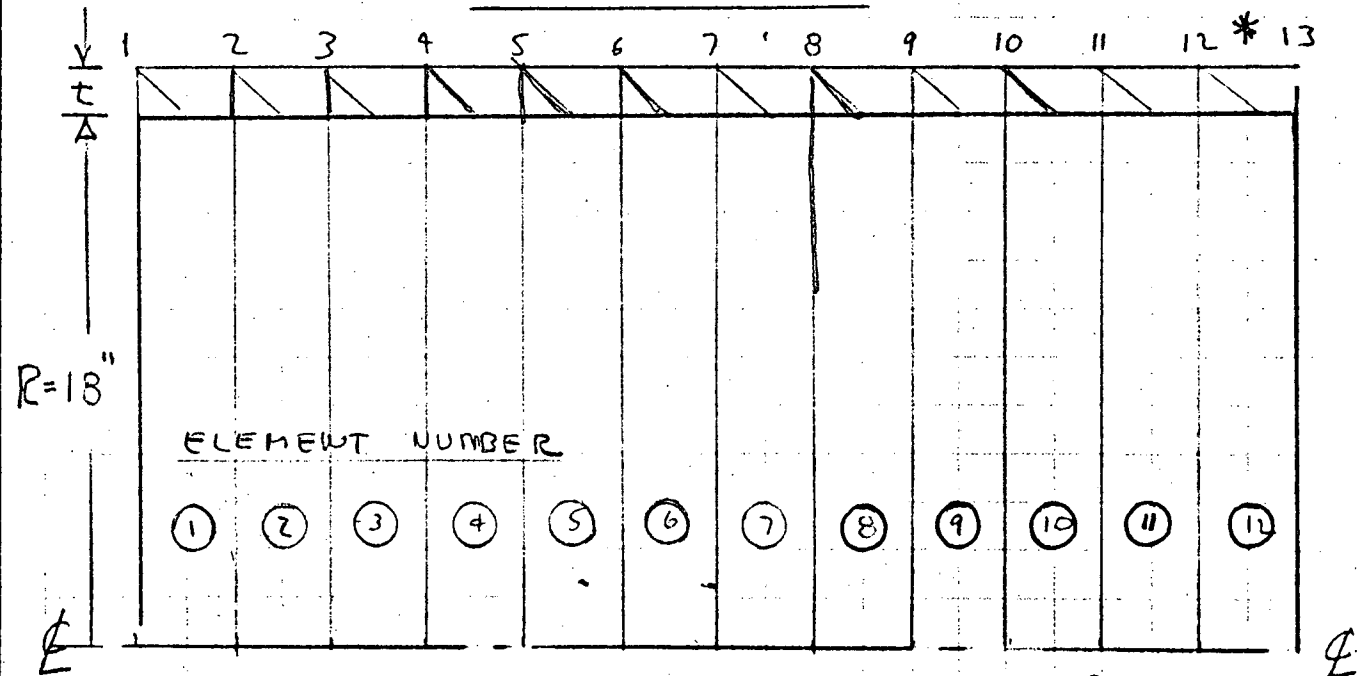


$E = 42.5 \times 10^6$   
 $\nu = .03$

MAT. ~ Be

FIG 1

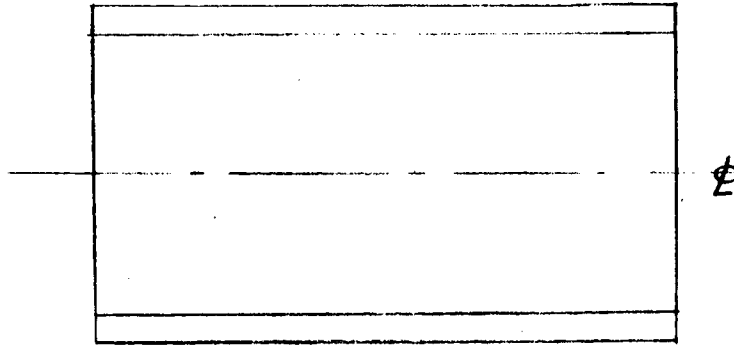
NODE NUMBER



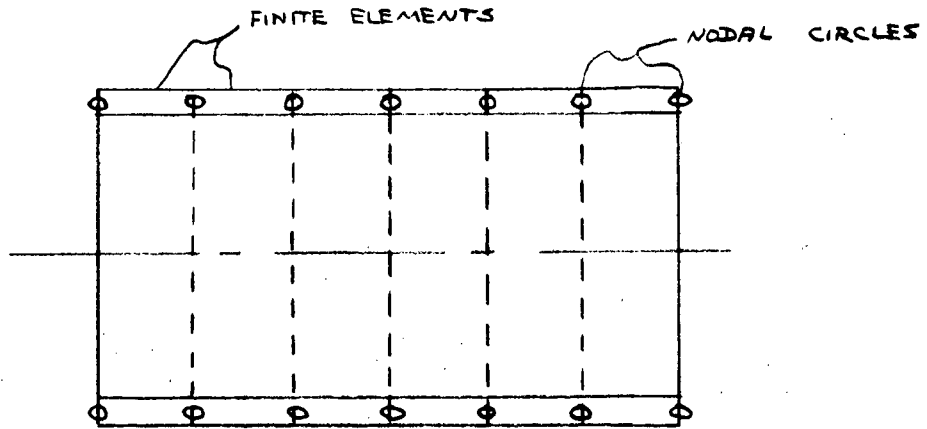
$t = .5$  ELEMENTS 1 - 11       $E = 42.5 \times 10^6$   
\*  $t = .75$  ELEMENT 12      \*  $E = 42.5 \times 10^7$

\* SEE SECTION ON WT. CALCULATION OF BERYLLIUM FLANGES.

PARA. NO.		TITLE:	ANAL. BY	KEP
DWG. NO.			DATE	DEC 71
LOADS ARE			CHKD. BY	

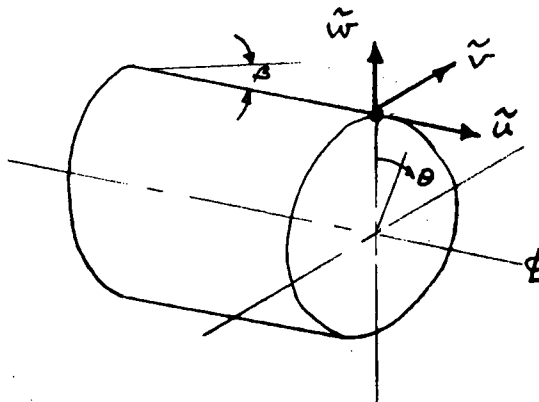


ORIGINAL SHELL



IDEALIZED SHELL

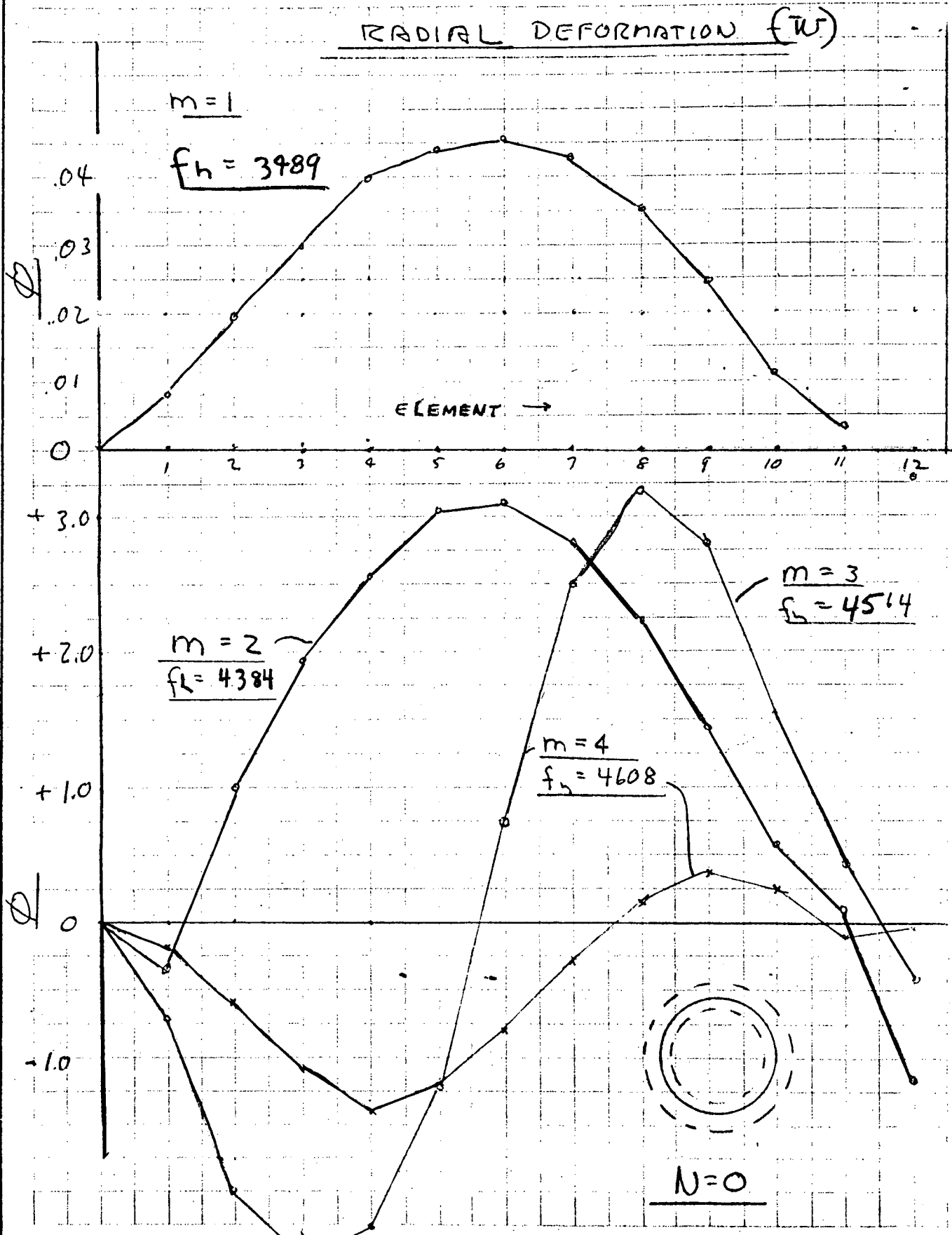
DISPLACEMENT COMPONENTS



9-0408  
1-64

# FIG 3a

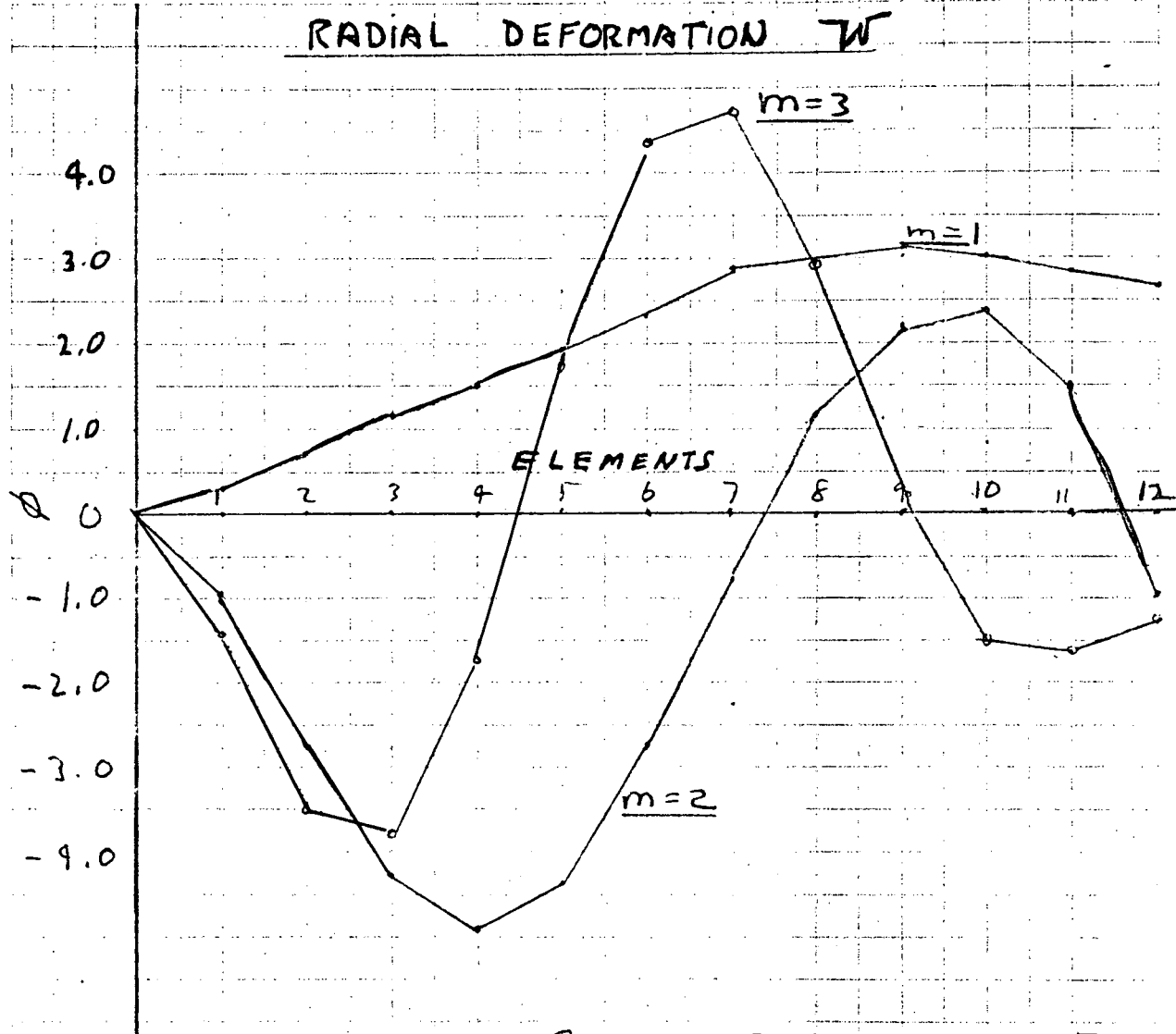
PARA. NO.		TITLE:		ANAL. BY	
DWG. NO.			<u>N=0</u>	DATE	
LOADS ARE				CHKD. BY	



6-0408  
1-84

FIG 3 b

PARA. NO.		TITLE:	<u>N = 1</u>	ANAL. BY	
DWG. NO.				DATE	
LOADS ARE				CHKD. BY	



$m = 1$

$f_n = 2193 \text{ cps}$

$m = 2$

$f_n = 4153$

$m = 3$

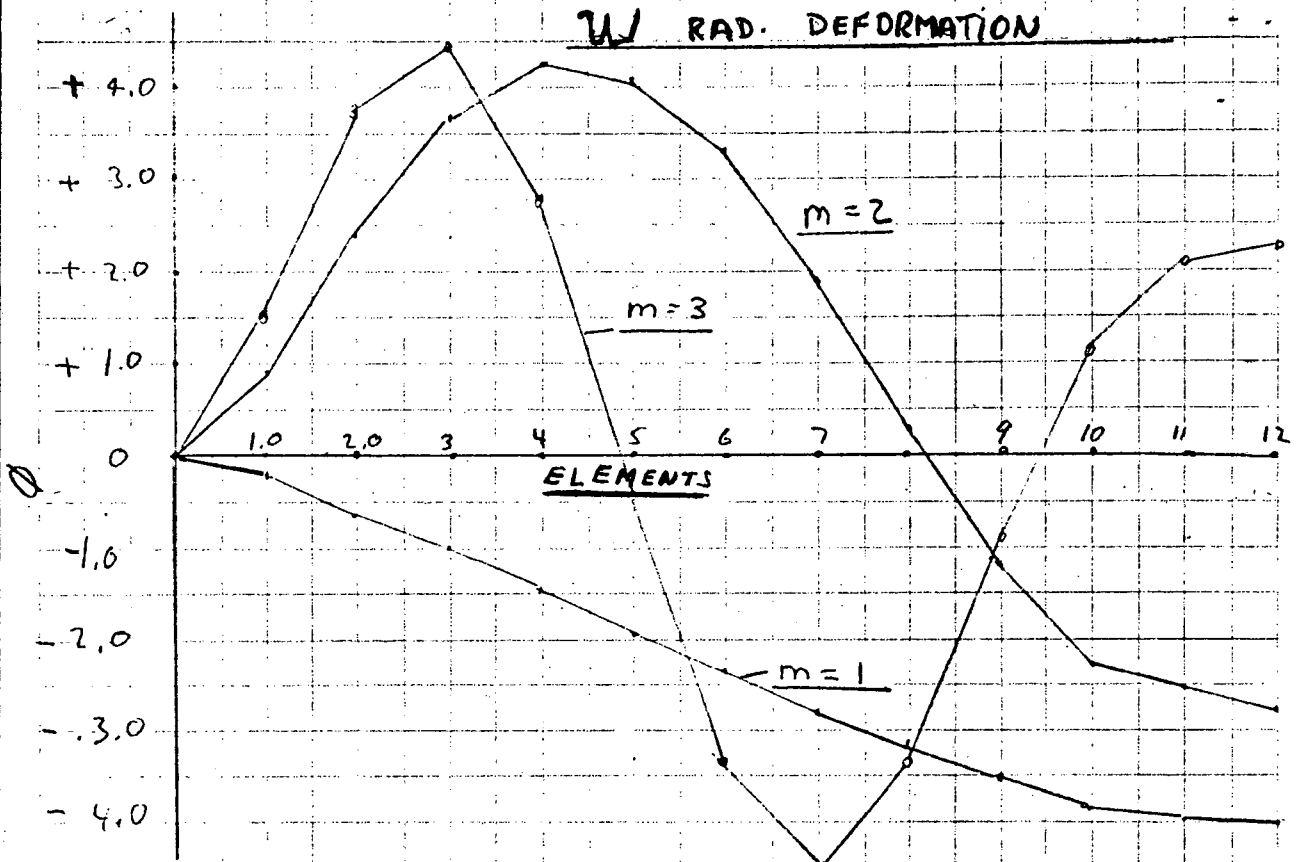
$f_n = 4738$



N = 1

# FIG C

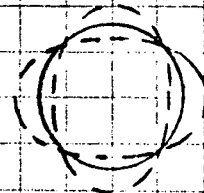
PARA. NO.		TITLE:		ANAL. BY	
DWG. NO.			<u>N = 2</u>	DATE	
LOADS ARE				CHKD. BY	



$m=1 \quad f_n = 1241 \text{ cps}$

$m=2 \quad f_n = 3215 \text{ ''}$

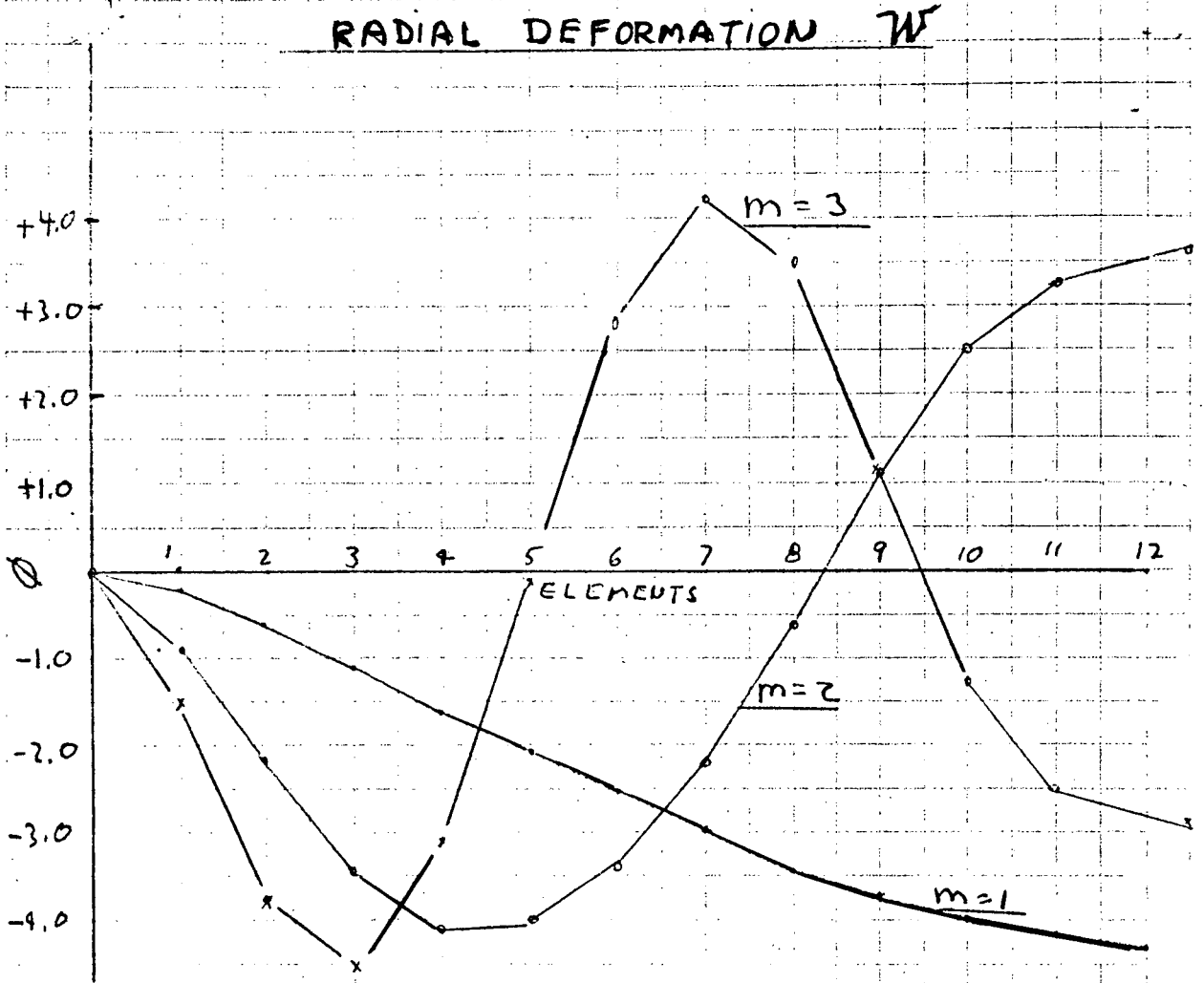
$m=3 \quad f_n = 4413 \text{ ''}$



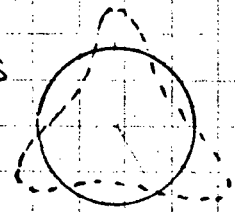
N = 2

# FIG 3 d

PARA. NO.	TITLE:	ANAL. BY
DWG. NO.	<u>N = 3</u>	DATE
LOADS ARE		CHKD. BY



$m=1$        $f_n = 1058$  cps  
 $m=2$        $f_n = 2517$  "  
 $m=3$        $f_n = 4011$  "

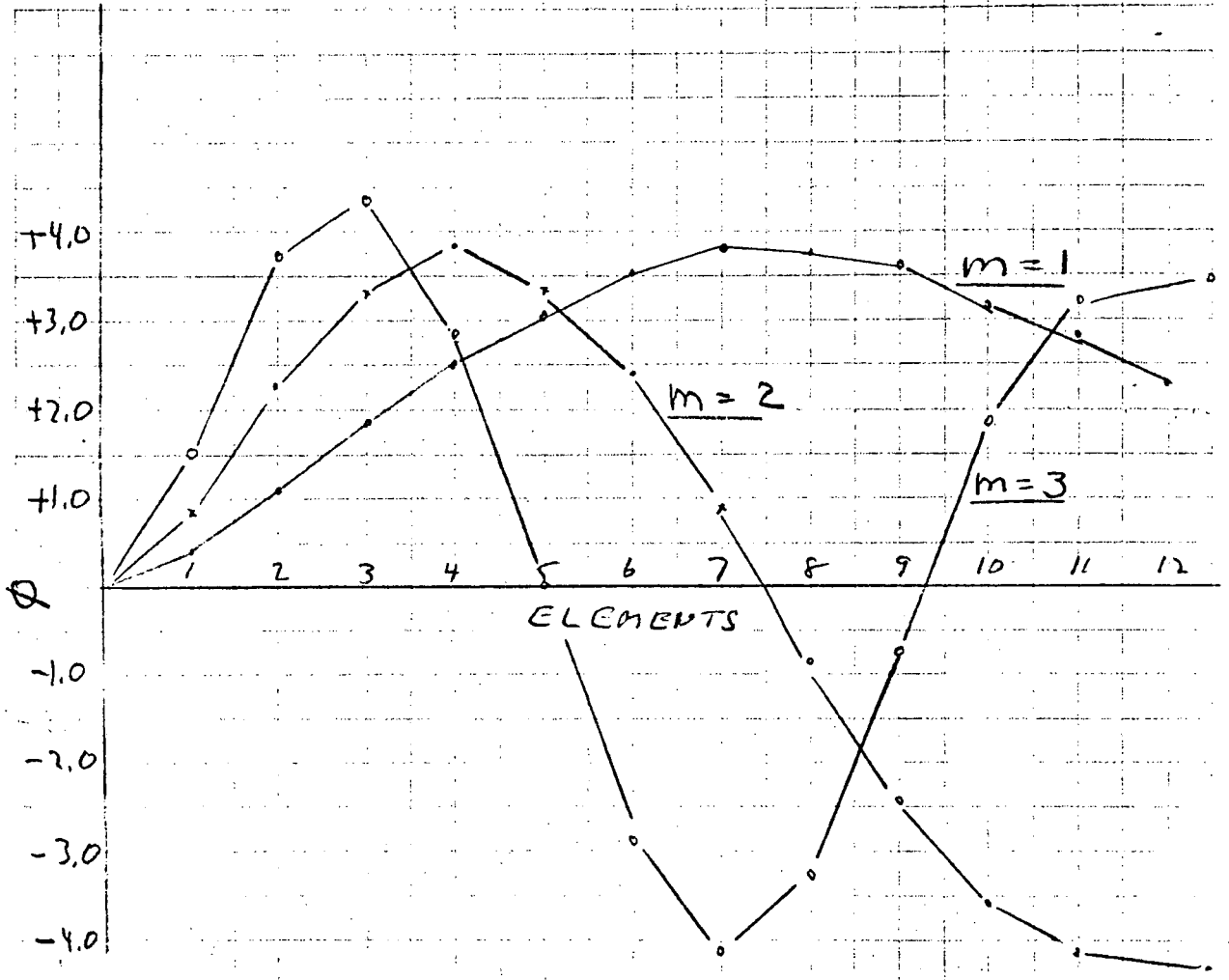


N = 3

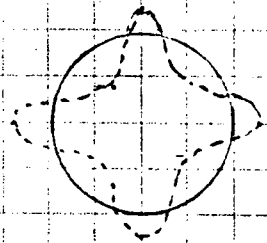
# FIG 3e

PARA. NO.		TITLE:		ANAL. BY	
DWG. NO.			<u>N = 4</u>	DATE	
LOADS ARE				CHKD. BY	

## RADIAL DEFORMATION W



$m=1 \quad f_n = 1344 \text{ cps}$   
 $m=2 \quad f_n = 2383 \text{ ''}$   
 $m=3 \quad f_n = 3758 \text{ ''}$

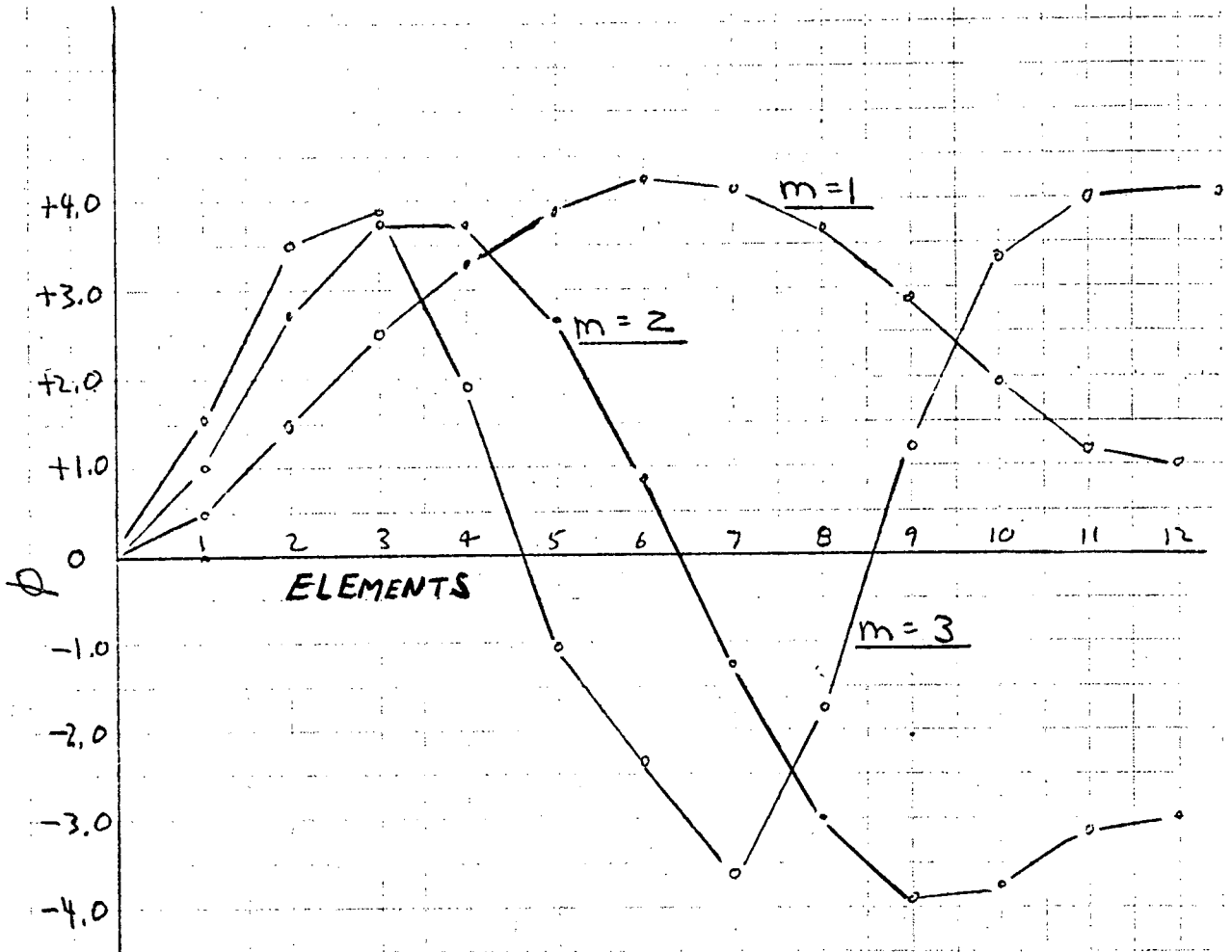


N=4

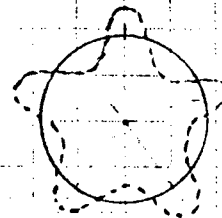
# FIG 3 f

PARA. NO.		TITLE:		ANAL. BY	
DWG. NO.			<u>N = 5</u>	DATE	
LOADS ARE				CHKD. BY	

## RADIAL DEFORMATION $\mu$

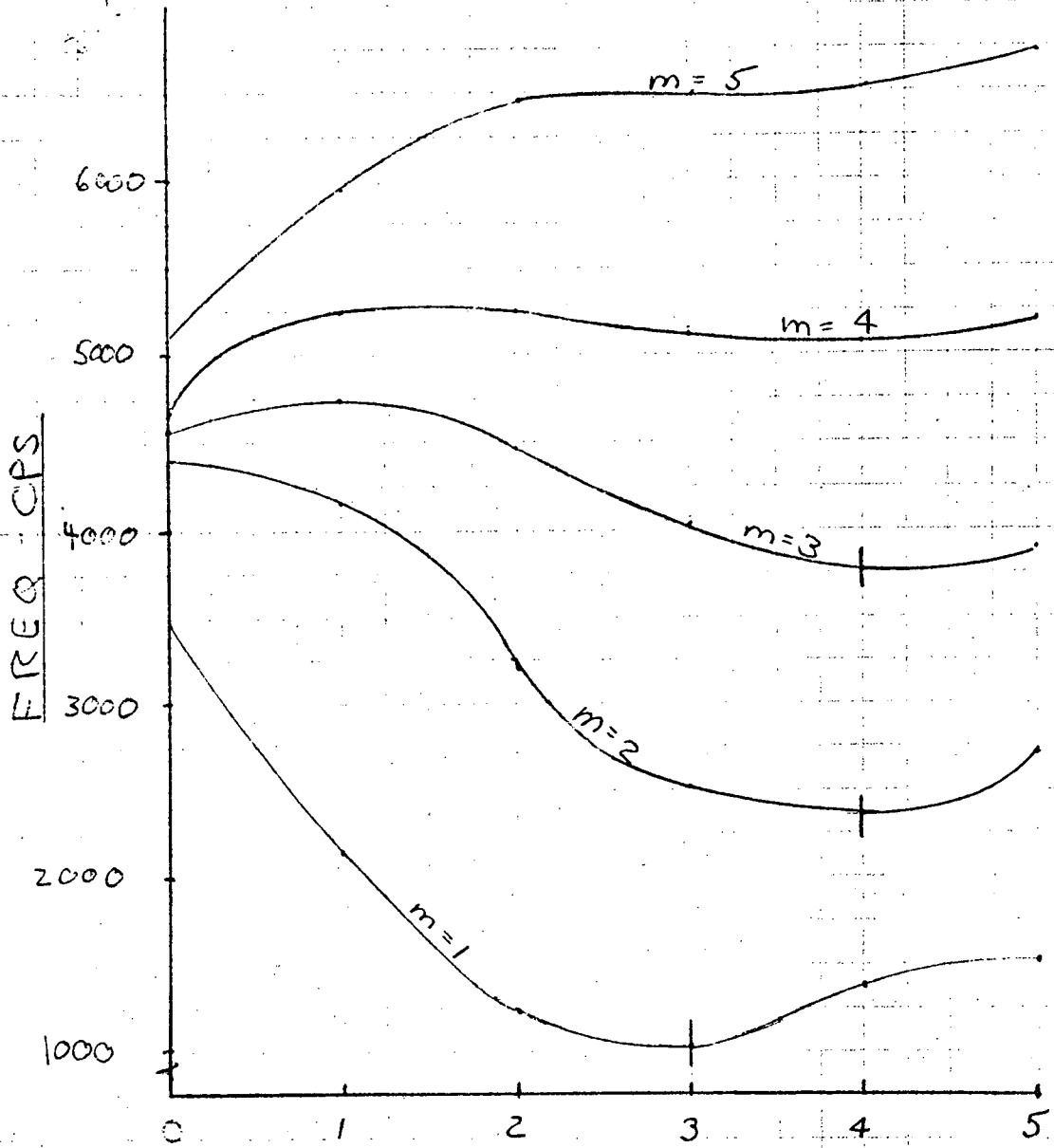


$m=1$        $f_n = 1533 \text{ cps}$   
 $m=2$        $f_n = 2707$   
 $m=3$        $f_n = 3891$



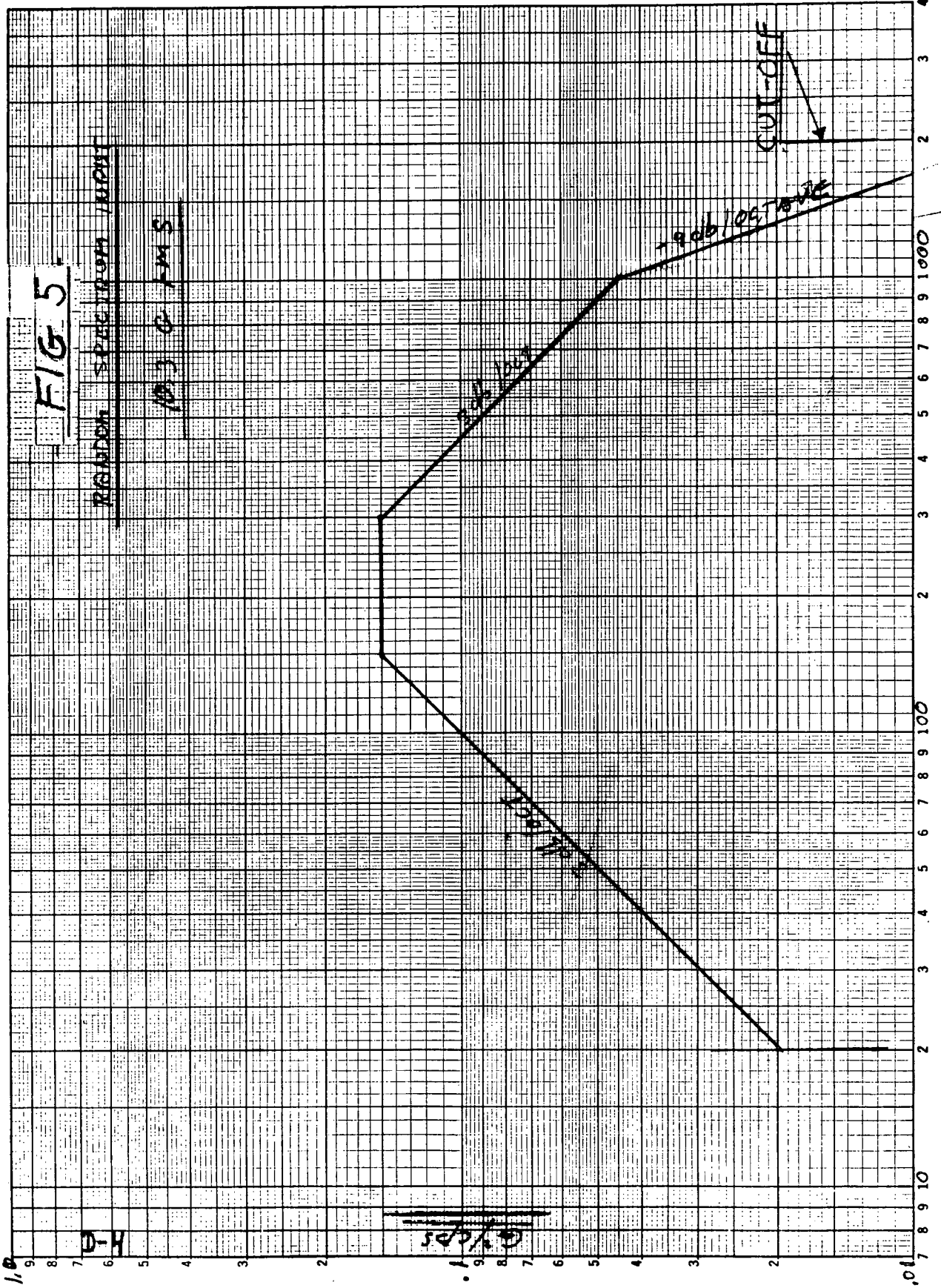
N = 5

PARA. NO.		TITLE: <u>FIG 4</u>	ANAL. BY	
DWG. NO.			DATE	
LOADS ARE			CHKD. BY	



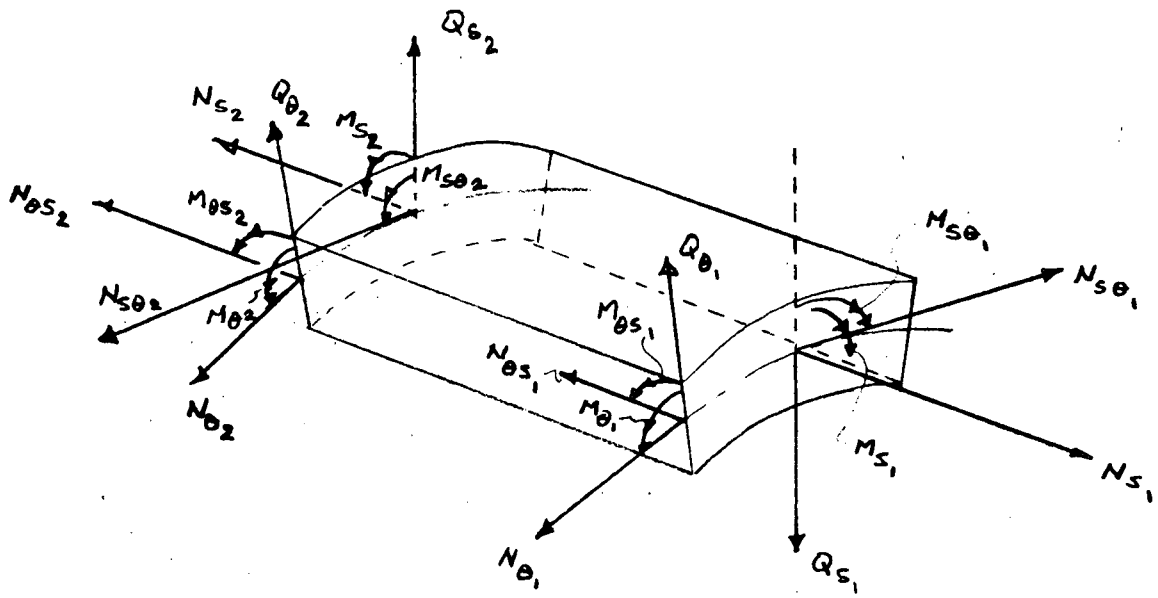
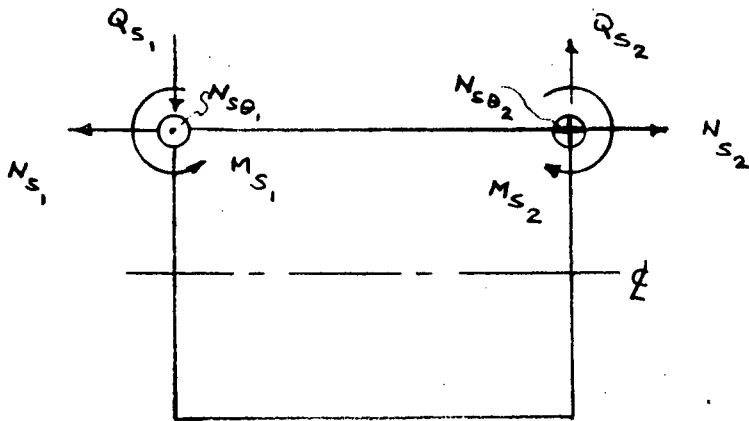
N - HARMONIC

N - VS FREQ FOR 'm' VALUES



PARA. NO.		TITLE:  <b>FIG. 6</b>	ANAL. BY	KEP
DWG. NO.			DATE	NOV 71
LOADS ARE			CHKD. BY	

SHELL STRESS RESULTANTS & SIGN CONVENTION :



COMPUTE @ EACH NODE

$M(S), M(T), M(ST), N(S), N(T), N(ST), Q(S), Q(T)$

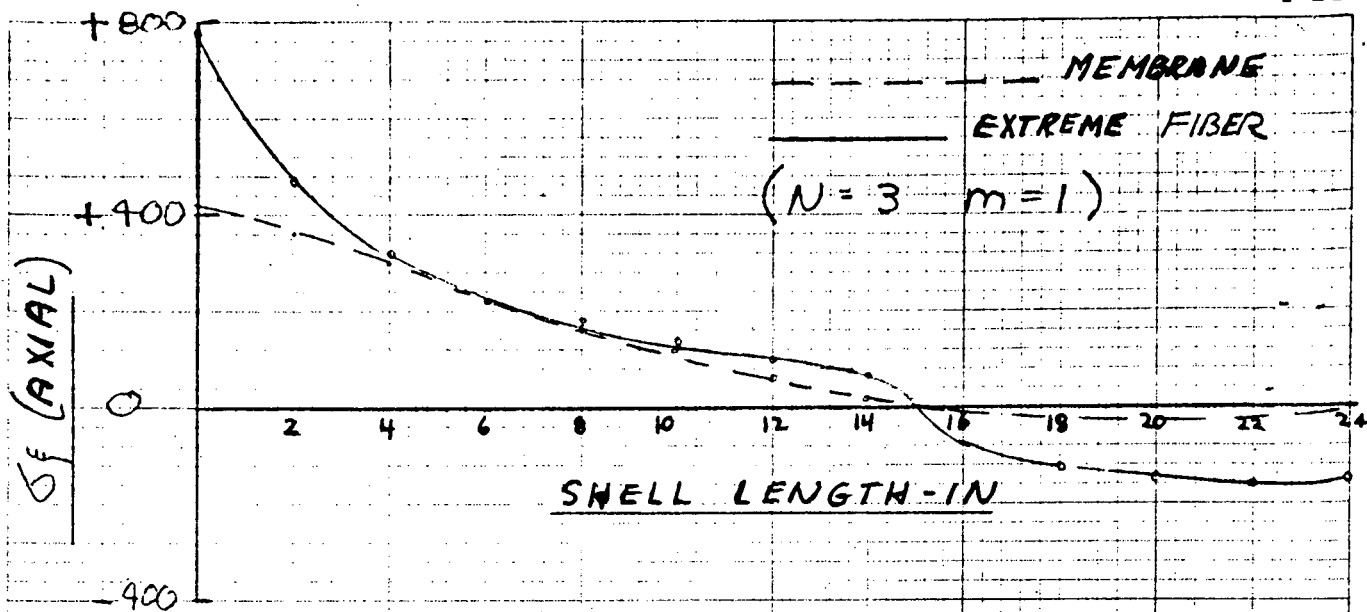
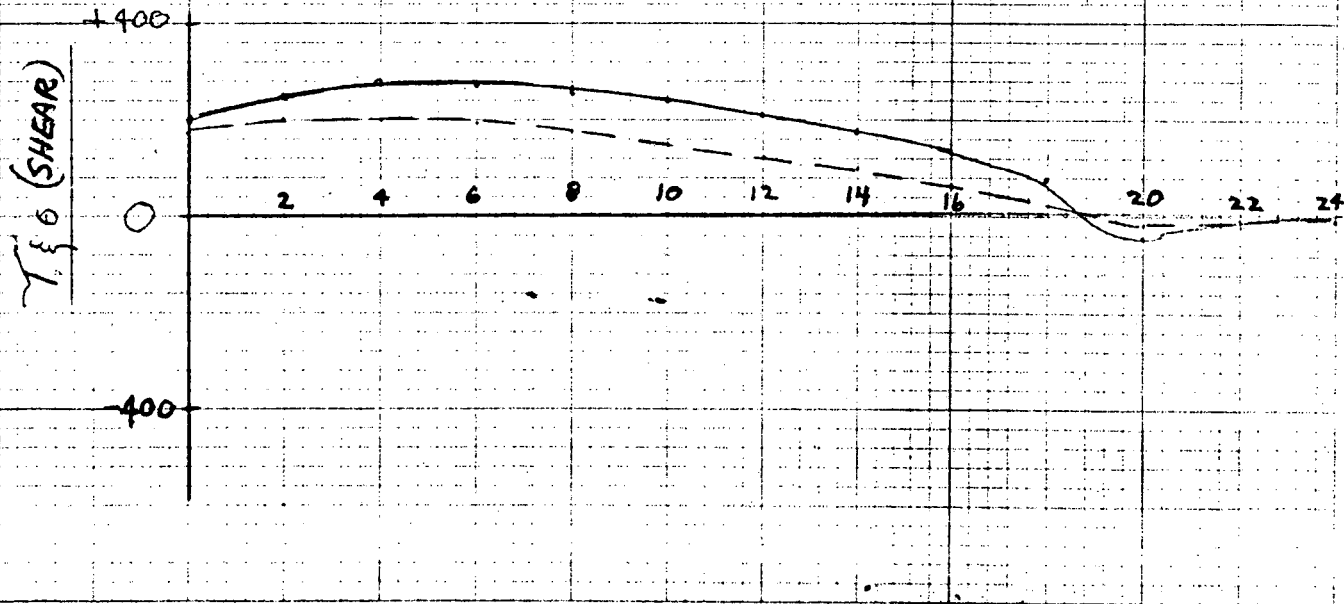
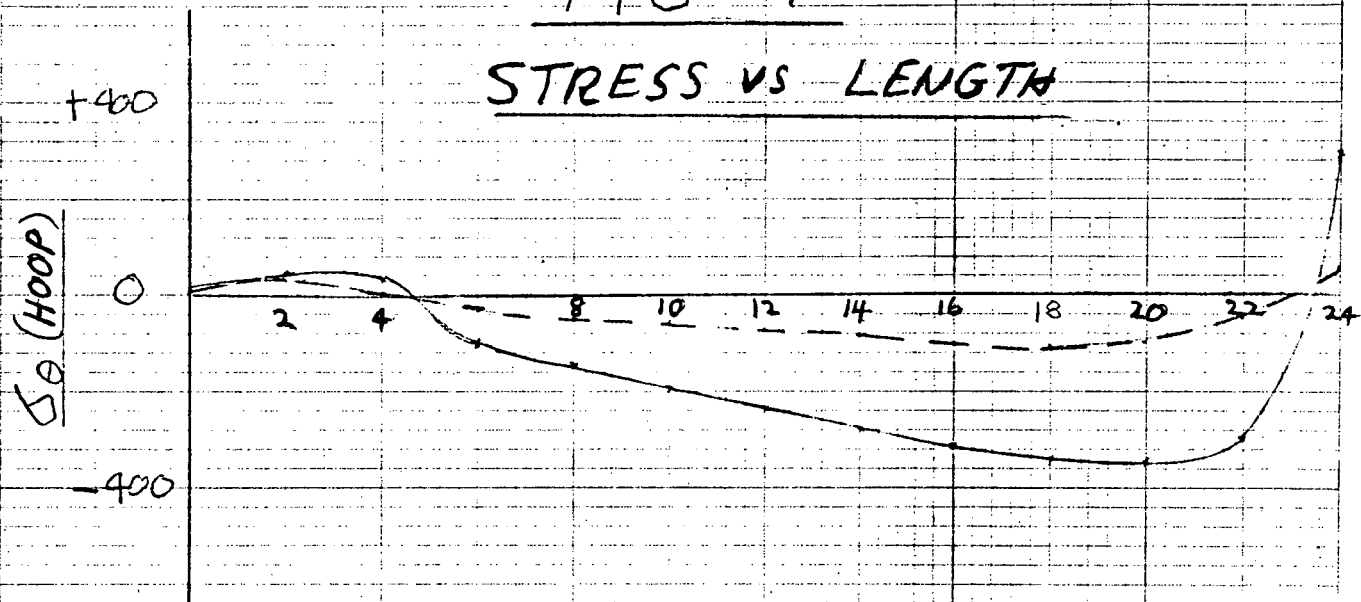


FIG 7  
STRESS VS LENGTH



PARA. NO.		TITLE: <u>WEIGHTS</u>	ANAL. BY	
DWG. NO.		<u>BERY. END FLANGES</u>	DATE	
LOADS ARE			CHKD. BY	

p-1

THE FOLLOWING CALCULATIONS ARE BASED  
ON AM. SC. & ENG DWG SK 502-459

THE INTENT OF THIS SECTION IS TO DERIVE  
THE WEIGHTS OF THE END FLANGES AND TO  
ACCOUNT FOR THESE IN THE SARGOR III  
ANALYSIS.

THERE ARE 6 END FLANGES AS FOLLOWS:

1<sup>ST</sup> FLANGE - (B2)

$$O.D. = 41.4 \quad I.D. = 21.875" \quad t = .25"$$

18 SETS OF 5 SLOTS 4.5" X .5"

$$\Sigma WT = 12.85^{\#}$$

2<sup>ND</sup> FLANGE

$$O.D. = 38.3025" \quad I.D. = 21.875" \quad t = .125"$$

18 SETS OF 5 SLOTS

$$\Sigma WT = 4.8^{\#}$$

3<sup>RD</sup> FLANGE

$$O.D. = 35.725 \quad I.D. = 21.875" \quad t = .125"$$

18 SETS OF 4 SLOTS - 4.35" X .5"

$$\Sigma WT = 3.94^{\#}$$

PARA. NO.		TITLE: <u>WEIGHTS</u>	ANAL. BY	
DWG. NO.		<u>BERYLL. END FLANGES</u>	DATE	
LOADS ARE			CHKD. BY	

p 2

4<sup>th</sup> FLANGEO.D. 33.23" I.D. 21.85"  $\pm 0$   $t = .125"$ 

18 SETS OF 3 SLOTS 4.15" x 5"

 $\Sigma WT = 3.18^{\#}$ 5<sup>th</sup> FLANGEO.D. = 31.83" I.D. = 21.85"  $t = .125"$ 

18 SETS OF 2 SLOTS 4" x .5"

 $\Sigma WT = 2.92^{\#}$ 6<sup>th</sup> FLANGEO.D. = 28.494" I.D. = 21.85"  $t = .125"$ 

18 SLOTS 3.7" x .5"

 $\Sigma WT = 1.92^{\#}$ TOTAL = 29.89<sup>#</sup>

ASSUME PER DWG SK 502-459 THAT THIS WT IS DIVIDED EQUALLY AMONG 6 MIRRORS AND ONE OUTSIDE STRUCTURE. THUS,  $29.89 \div 7 = 4.27^{\#}$

NOW, IN ORDER TO ACCOUNT FOR THIS

PARA. NO.		TITLE: <u>WEIGHTS</u>	ANAL. BY	
DWG. NO.		<u>BERYL. END FLANGES</u>	DATE	
LOADS ARE			CHKD. BY	

P-3

END MASS, ELEMENT 12 WILL BE INCREASED IN THICKNESS.

$$\Delta WT = .785 (O.D.^2 - I.D.^2) \times l \times \rho$$

$$\left\{ \begin{array}{l} O.D. = 37'' + 2 \Delta t \text{ (NEW SECTION)} \\ I.D. = 37'' \text{ (NEW SECTION)} \end{array} \right.$$

$$l = 2'' \text{ LENGTH OF 1 ELEMENT}$$

$$\rho = .067 \text{ \#/cu in}$$

$$\Delta WT = .785 [(37 + 2t)^2 - 37^2] (2) (.067)$$

$$3.94 = .1052 (148t + 4t^2)$$

$$4\Delta t^2 + 148\Delta t - 37.452 = 0$$

$$\underline{\Delta t = .25''}$$

THEREFORE MAKE THICKNESS OF ELEMENT 12 = .75''

ALSO, TO ACCOUNT FOR STIFFNESS OF END FLANGES WITHOUT ADDING UNREALISTIC MASS, E WILL BE INCREASED BY AN ORDER OF MAGNITUDE TO  $42.5 \times 10^7$  #/in<sup>2</sup>

PARA. NO.		TITLE:	ANAL. BY
DWG. NO.		STRESS CALCULATIONS	DATE
LOADS ARE			CHKD. BY

P-1

IN SIMILAR FASHION TO REFERENCE (1) THE TOTAL AXIAL, HOOP AND SHEAR STRESS CAN BE CALCULATED FROM THE SUMMATION OF THE MEMBRANE AND EXTREME FIBER STRESS. THE FOLLOWING RELATIONSHIPS FROM "STRESSES IN SHELLS" BY FLUGGE ARE USED TO CALCULATE MAXIMUM STRESSES FROM THE KNOWN STRESS RESULTANTS

$$\text{(AXIAL)} \quad \sigma_f = \frac{N_f}{t} + \frac{12 M_f z}{t^3} \quad \left(z = \frac{t}{2}\right)$$

$$t = 0.5''$$

$$\text{(HOOP)} \quad \sigma_\theta = \frac{N_\theta}{t} + \frac{12 M_\theta z}{t^3}$$

$$\text{(SHEAR)} \quad \tau_{f\theta} = \frac{N_{f\theta}}{t} + \frac{12 M_{f\theta} z}{t^3}$$

IT SHOULD BE KEPT IN MIND THAT, ALTHOUGH TENSION AND COMPRESSION SIGN CONVENTION HAS BEEN MAINTAINED, ALL STRESSES ARE VIBRATORY IN NATURE. THUS, MAXIMUM VALUES REPRESENT BOTH TENSION AND COMPRESSION REGARDLESS OF SIGN. IN ALL CASES EXTREME FIBER STRESS HAS BEEN ADDED TO EITHER A (+) OR (-) BENDING STRESS TO MAKE A MAXIMUM FOR PLOTTING PURPOSES.

THE FOLLOWING TABULATION INDICATES ALL STRESS VALUES: (SEE FIG 6 FOR PLOTS)

TABLE 6

PARA. NO.		TITLE: <b>STRESS CALCULATIONS</b>	ANAL. BY	
DWG. NO.			DATE	
LOADS ARE			CHKD. BY	

RESULTANTS

p-2

X-IN	N <sub>F</sub>	M <sub>F</sub> (±)	M <sub>θ</sub> (±)	N <sub>θ</sub>	N <sub>Fθ</sub>	M <sub>Fθ</sub> (±)
0	211.8	15.0	0.43	5.86	87.93	.25
2	181.2	4.75	.39	19.77	95.04	2.68
4	148.3	.75	1.59	.57	98.81	3.45
6	114.9	.25	2.84	-15.47	96.06	3.58
8	83.4	.60	4.08	-24.89	88.54	3.61
10	54.9	1.02	5.33	-31.38	77.99	3.59
12	29.9	1.53	6.56	-37.45	64.97	3.51
14	10.0	2.10	7.74	-43.39	49.40	3.31
16	-4.4	2.84	8.84	-50.32	31.32	2.97
18	-12.9	3.85	9.79	-53.57	10.90	2.41
20	-14.2	4.88	10.51	-46.16	-8.76	-1.51
22	-0.55	7.05	10.72	-18.68	-1.97	.54
24	-0.094	6.06	10.93	+30.37	+ .86	.63

STRESSES

	σ <sub>F</sub>	σ <sub>θ</sub>	τ <sub>Fθ</sub>	σ <sub>F</sub>	σ <sub>θ</sub>	τ <sub>Fθ</sub>
0	423.6	11.72	175.96	783.6	22.0	181.96
2	362.4	39.54	190.08	476.4	48.9	254.4
4	296.6	1.14	197.62	314.9	-39.3	280.4
6	229.8	-30.94	192.12	235.8	-99.1	278.0
8	166.8	-49.98	177.08	181.2	-147.9	263.7
10	118.8	-62.76	155.98	143.3	-190.7	242.1
12	59.8	-74.90	129.94	96.5	-232.3	214.2
14	20.0	-86.78	98.80	70.4	-272.5	178.2
16	-8.8	-100.64	62.64	-76.2	-312.8	133.9
18	-25.8	-107.14	21.80	-118.2	-342.1	79.6
20	-28.4	-92.32	-17.52	-145.5	-344.6	-53.8
22	-1.0	-37.36	-1.94	-170.2	-294.6	-14.9
24	.18	+60.74	-1.72	-145.6	+323.0	-16.8

MEMBRANE σ

MEMBRANE + BENDING σ

Comparison Chart of Previous Data

Glass (Both Ends)	N	$f_n$	* $\delta^3$ Sigma	* $\sigma_f$ Psi	$\sigma_e$	$T_f \theta$
t = 1" = 24" clamped	4	1024 cps	$10.8 \times 10^{-4}$	286	362	237
t = .5 = 24" simple	5	702	$24.0 \times 10^{-4}$	394	725	379
t = .5 = 24" clamped	1	1627	$3.15 \times 10^{-4}$	72	124	133
t = .75 = 36" simple	4	583	$33.96 \times 10^{-4}$	487	709	397
<hr/>						
Beryllium (Cantilever)	N	$f_n$	3 Sigma	$\sigma_f$ Psi	$\sigma_e$	$T_f \theta$
t = .5 = 24"	3	1058 cps	$10^{-3}$	787	344	280

\*Note: All stresses are based on 3 Sigma displacements and are a maximum combination of bending and membrane stress (psi).

APPENDIX J

TECHNICAL SPECIFICATION  
For The  
INNER PARABOLOID  
Of The  
LOXT HIGH RESOLUTION X-RAY TELESCOPE ASSEMBLY

i

TECHNICAL SPECIFICATION

TABLE OF CONTENTS

SECTION		PAGE
1.0	SCOPE	2
2.0	APPLICABLE DOCUMENTS	2
2.1	Specifications	2
2.2	Drawings	3
3.0	REQUIREMENTS	3
3.1	Design	3
3.2	Materials	4
3.2.1	Critical Zone	4
3.2.2	Inclusions	4
3.2.3	Anneal	4
3.3	Optical Parameters and Mirror Tolerances	4
3.3.1	Mirror Internal Surface Equation	4
3.3.2	Focal Length	5
3.3.3	Mirror Dimensions	5
3.3.4	Optical Tolerances	5
3.3.5	Surface Finish	9
3.3.6	Fused Silica Cylindrical Mounting Surface	9
3.4	Assembly Tolerances	9
4.0	QUALITY ASSURANCE PROVISIONS	10
4.1	Workmanship	10
4.1.1	Fabrication Environment	10
4.1.2	Fused Silica Surface Grinding	10

TECHNICAL SPECIFICATION

TABLE OF CONTENTS (Cont'd)

SECTION		PAGE
4. 1. 3	Optical Surface Polishing	11
4. 2	Process Control	11
4. 3	Inspection	12
4. 3. 1	Raw Material	12
4. 4	Raw Material Traceability	12
4. 5	Non-Conforming Material	12
4. 6	Tooling Control	13
4. 7	Acceptance Testing	13
5. 0	PREPARATION FOR DELIVERY	14
5. 1	Packaging	14
5. 2	Marking	14
6. 0	NOTES	14
6. 1	Ordering Data	14
6. 2	Specification Revision	14

LIST OF ILLUSTRATION

<u>Figure</u>		<u>Page</u>
1	LOXT Paraboloid Coordinate System	6
2	LOXT Mirror Roundness & Sagittal Depth Tolerance	8

AMERICAN  
SCIENCE  
AND ENGINEERING

REV. LTR.	A									
-----------	---	--	--	--	--	--	--	--	--	--

CODE IDENT. NO. 21802

CONTROL NO.	S144-202
DATE	June 1972
PAGE	2

TECHNICAL SPECIFICATION

1.0 SCOPE

This specification establishes optical requirements for the inner paraboloid of the LOXT High Resolution Telescope Assembly. Tolerances specified herein are typical of those which eventually will be applied to all optical surfaces of the assembly.

2.0 APPLICABLE DOCUMENTS

The following documents of the issue in effect upon receipt of this document form a part of this document to the extent specified herein. In the event of any conflicts between the requirements of this document and the listed documents, the requirements of this document shall govern.

2.1 Specifications

NASA

NPC-200-3

Inspection System Provisions for Suppliers of Space Materials, Parts, Components and Services

MILITARY

MIL-O-13830 (ORD)

Optical Components for Fire Control Instruments; General Specification Governing the Manufacture, Assembly, and Inspection of

Preceding page blank

TECHNICAL SPECIFICATION

2.2 Drawings

American Science and Engineering

SK144-013	LOXT High Resolution Fused Silica Mirror Assembly
SK144-1005, Rev. 5	Inner Paraboloid Test Mirror (Simulated LOXT Flight Configuration)
SK144-1007	End Flange, Support (LOXT High Resolution Test Mirror)
SK144-1008	Center Flange, Support (LOXT High Resolution Test Mirror)
SK144-1009	Fixture, Environmental Test (LOXT High Resolution Test Mirror)
SK144-1010	Transfer Rings (LOXT High Resolution Test Mirror)
SK144-602	Environmental Test Assembly (LOXT High Resolution Test Mirror)

3.0 REQUIREMENTS

3.1 Design

The preliminary design of the LOXT X-Ray High Resolution Mirror Assembly, is shown in AS&E drawing SK144-013. The assembly includes five paraboloids, five hyperboloids, and supporting elements. Each fused silica optical element is supported at both of its ends by Invar flanges. It is anticipated that these flanges will not be present during polishing and also that the mirror material will be extended beyond the design length during polishing, as shown in AS&E drawing SK144-1005. The mirror elements are not sufficiently stiff for polishing without support rings; these rings shall be removable with the permanent Invar flanges and transfer rings in place. The support flanges, AS&E drawings SK144-1007 and SK144-1008, will be supplied by AS&E.

TECHNICAL SPECIFICATION

3.2 Materials

The paraboloid mirror section shall be made from Corning 7940 fused silica. The blank shall contain a maximum of seven (7) fused seals perpendicular to the optical axis.

3.2.1 Critical Zone

The critical zone shall include all material within 1/8 inch of the inside diameter of the finished mirror.

3.2.2 Inclusions

3.2.2.1 Critical Zone

Maximum mean diameter of any inclusion: 0.080 inch. Maximum average number/cubic inch between 0.020 inch and 0.040 inch mean diameter: 1.0. Maximum number between 0.040 inch and 0.080 inch mean diameter: 5.0 (Total).

3.2.2.2 Non Critical Zone

Maximum mean diameter of any inclusion: 0.080 inch. Maximum average number/cubic inch between 0.020 inch and 0.040 inch mean diameter: 1.0. Maximum number/cubic inch between 0.040 inch and 0.080 inch mean diameter: 10.0.

3.2.3 Anneal

Maximum birefringence shall be 10 millimicrons per centimeter of path length.

3.3 Optical Parameters and Mirror Tolerances

3.3.1 Mirror Internal Surface Equation

The equation for the mirror internal surfaces shall be (dimensions in inches)

$$Y^2 + Z^2 = d [2 \{ X + F + 2a (1 + E) \} + d]$$

where: F = 240.0

a = 120.16152016

d = 0.1640561378

E = 6.8333360892 x 10<sup>-4</sup>

TECHNICAL SPECIFICATION

3. 3. 1 Mirror Internal Surface Equation (Cont'd)

This equation is written in the coordinate system as shown in Figure 1. A computer printout of the desired surfaces will be furnished by AS&E. This will include the separation between the mirror surface and a cone, and also the separation between an axial section of the mirror surface and a best fit circle; the latter separation will be given in fringes of visible light at a wavelength of 5461Å and 6328Å.

3. 3. 2 Focal Length

The nominal focal length of the paraboloid will be 480.4873 in. Focal length is defined as the distance from the plane  $x = 0$  (Figure 1) to the center of the focal surface.

3. 3. 3 Mirror Dimensions

The following will be nominal dimensions for the mirror section after polishing and cutting to correct focal length.

- 3. 3. 3. 1 Diameter at front of paraboloid: 25.7487 in.
- 3. 3. 3. 2 Diameter at back of paraboloid: 25.1329 in.
- 3. 3. 3. 3 Length of paraboloid: 23.875 in.

The typical wall thickness for the glass will be approximately 1/2 inch. AS&E drawing SK144-1005, shows the mirror dimensions.

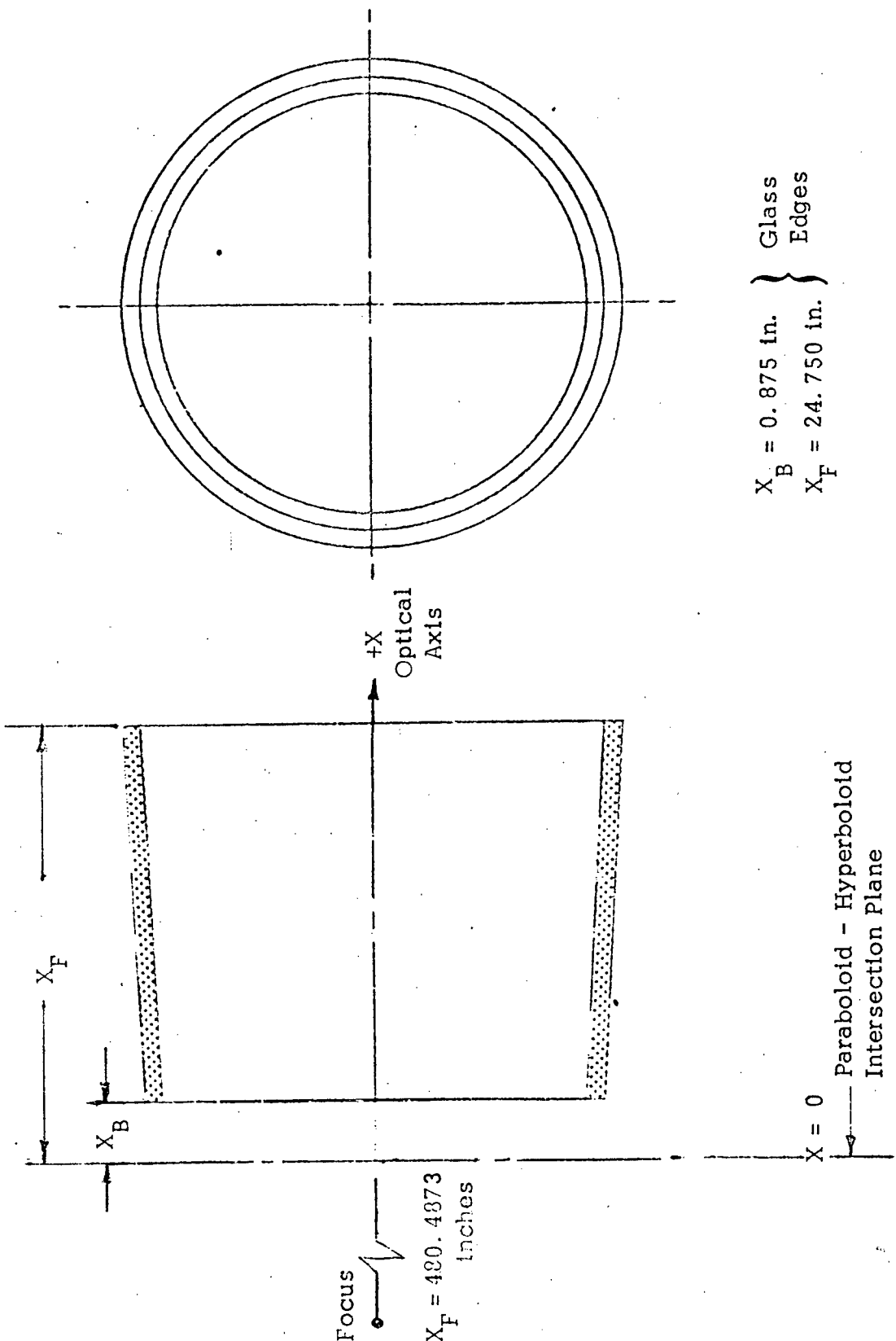
3. 3. 4 Optical Tolerances

All measurements shall be made with the pieces stabilized at a temperature of  $70 \pm 5^\circ\text{F}$ . The following tolerances apply to the paraboloid after polishing and cutting to correct focal length.

3. 3. 4. 1 End Surfaces

The end surfaces will be polished and normal to the axis of symmetry of the optical surface within 1 arc second. Deviation of the surfaces from flatness (waviness) will not exceed five (5) fringes of visible light (5641Å).

TECHNICAL SPECIFICATION



$X_B = 0.875 \text{ in.}$   
 $X_F = 24.750 \text{ in.}$

} Glass  
 } Edges

Paraboloid - Hyperboloid  
 Intersection Plane

Figure 1. LOXT Paraboloid Coordinate System

TECHNICAL SPECIFICATION

3. 3. 4. 2 Out-of-Roundness

Maximum out-of-roundness of the optical surface will be 0.0002 in. T. I. R. = (R max - R min). Roundness will be measured at front and rear for each mirror section. Deviations in the radius will not exceed 25 micro inches per inch of circumference.

3. 3. 4. 3 Forward-Aft Radius Differential

The difference between the forward and aft best fit radii ( $\Delta R$ ) as shown in Figure 2 may differ from the calculated value by no more than 0.00025 inch. \*The difference in the maximum and minimum measured values of  $\Delta R$  around the circumference shall not exceed 0.000050 inch. Owing to the importance of this criterion with respect to obtaining high performance, a total variation of 0.000015 inch shall be the design goal.

3. 3. 4. 4 Sagittal Depth

The allowed variation of sagittal depth, shown as S (x) in Figure 2, from the design curve is plus or minus 5 microinches when measured at a given azimuth angle. The slope shall not deviate from the design slope more than 3 micro-inches per inch of axial length for at least 90 percent of the surface area. The slope deviation for the remaining surface area shall not exceed 6 microinches per inch of axial length. Achievement of this requirement may be demonstrated by multiple-beam interferometry employing high finesse or by another method for which the subcontractor can demonstrate adequate measurement sensitivity. Owing to the importance of this criterion with respect to obtaining high mirror performance a sagittal depth deviation of less than 1.7 microinches per inch shall be the design goal. Sagittal depth shall be measured at a minimum of

\*The tolerance on the absolute value of the diameter is 0.0005 inches. The focal length and final sagittal depth values shall be calculated by AS&E, after the absolute values of the diameters are known. (A new curve will be provided to the subcontractor by American Science and Engineering no later than one (1) week after data is submitted to AS&E so that polishing may be accomplished).

TECHNICAL SPECIFICATION

Total Allowable Variation = .000050 inch  
 Design goal = .000015 inch

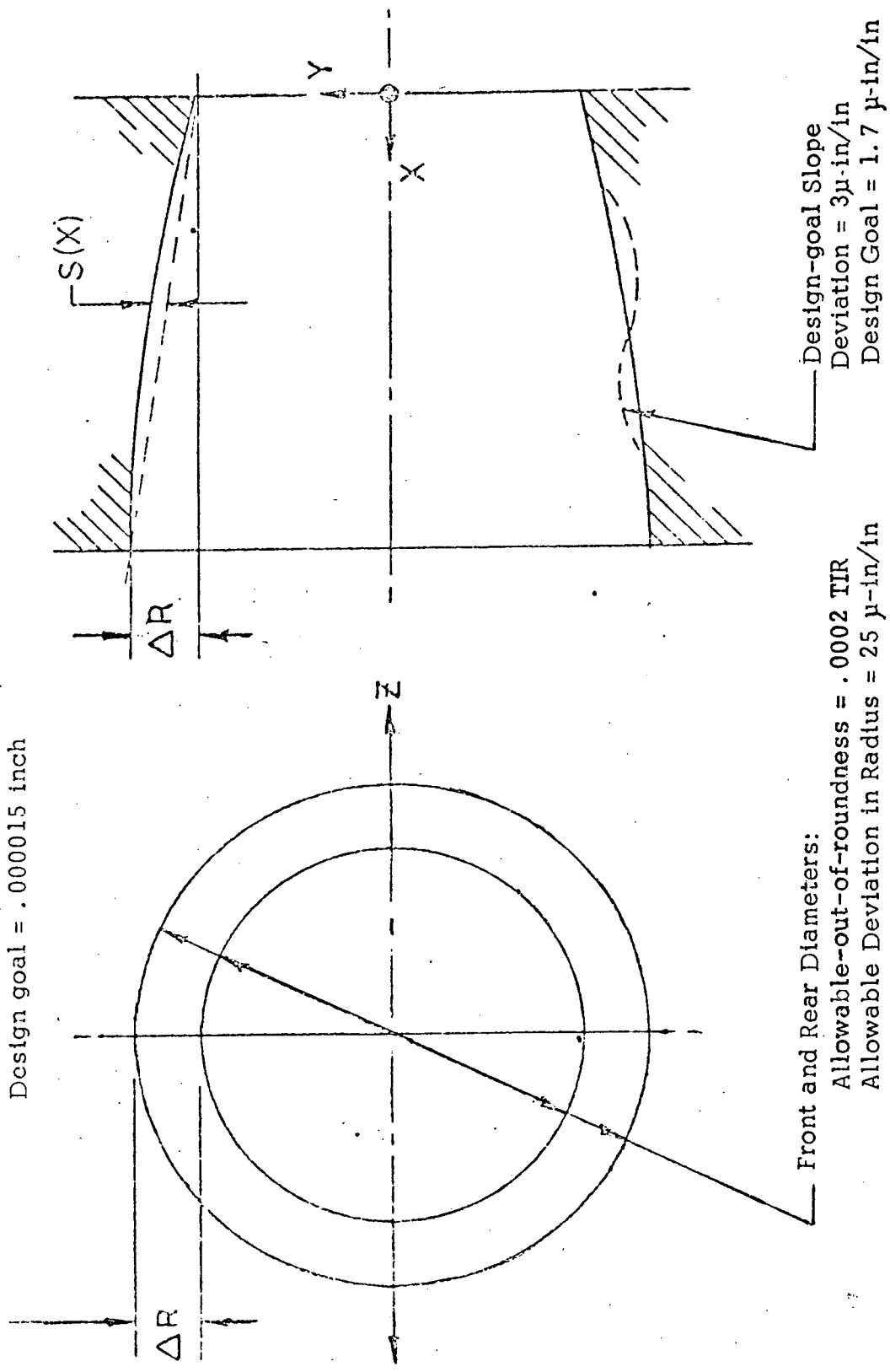


Figure 2. LOXT Mirror Roundness & Sagittal Depth Tolerance

TECHNICAL SPECIFICATION

3. 3. 4. 4 Sagittal Depth (Cont'd)

8 azimuth angles, evenly spaced starting from a reference point selected at random.

3. 3. 5 Surface Finish

Optical surface finish shall be the best obtainable by state-of-the-art optical techniques. Surface finish shall be sampled in a total of 9 places - 5 samples at points approximately equally spaced along one meridian and two samples approximately equally spaced along each of two other meridians located approximately 120 degrees each side of the meridian containing the location of the 5 samples. The optical surface finish acceptance criteria shall be root-mean-square roughness values of  $30\text{\AA}$  or less, with  $20\text{\AA}$  or less as the design goal. Achievement of this requirement shall be demonstrated by multiple beam interferometry employing high finesse.

3. 3. 6 Fused Silica Cylindrical Mounting Surface

The diameter, in inches, of the fused silica cylindrical mounting surface shall be as follows:

Front       $26.6849 \pm 0.0005$  inches

Back       $26.1981 \pm 0.0005$  inches

The center of the cylindrical mounting surface shall, at any section, be within 0.0005 inch of the optical axis of the telescope. Roundness and concentricity tolerances are shown in drawing SK144-1005

3. 4 Assembly Tolerances

The final cutting of the paraboloid shall result in the design focal length plus or minus 0.020 inch.

TECHNICAL SPECIFICATION

4.0 QUALITY ASSURANCE PROVISIONS

The supplier shall institute and maintain an inspection system in conformance with NPC-200-3. Reference to Government or NASA in NPC-200-3 shall be understood to include AS&E.

4.1 Workmanship

The workmanship and fabrication techniques shall be consistant with the best available practice in all unspecified areas. In particular, no sharp edges or corners or fused silica surface scratches which would result in high stress regions will be accepted. (MIL-O-13830, 60/40 is the cosmetic standard).

4.1.1 Fabrication Environment

Environmental conditions during fabrication shall be maintained in keeping with achievement of the specified surface finish and other design requirements.

4.1.2 Fused Silica Surface Grinding

All fused silica surfaces shall be prepared by grinding techniques which avoid subsurface flaws. An acceptable technique for this purpose consists of removing material with successively finer abrasives, the amount being removed with each abrasive being equal or greater than three times the average diameter of the proceeding abrasive particles. The final abrasive average particle diameter shall be less than 0.0005 inches. This shall be followed by polishing to achieve a good surface finish (cosmetic shine) for all surfaces not having an optical function. This procedure shall also be used to prepare the X-ray optical surfaces for final figuring and polishing.

REV. LTR.	A												
-----------	---	--	--	--	--	--	--	--	--	--	--	--	--

CODE IDENT. NO. 21802

CONTROL NO.	S144-202
DATE	June 1972
PAGE	11

TECHNICAL SPECIFICATION

4. 1. 3            Optical Surface Polishing

A low-scatter finishing process, submersible polishing, shall be used during the final polishing stages. In the event that technical problems occur, an alternate method better suited for producing the lowest scatter shall be selected after prior consultation with AS&E.

The fabrication process shall not include any local polishing procedures which, being applied to small areas, could result in slope errors that would be difficult to detect; in particular, the polishing stroke and tools must be of sufficient length in the axial direction so that the design-goal slope tolerance of 1.7 microinches per inch times the particular axial length would result in a vertical height difference that can be detected by the measurement techniques to be used during fabrication of the mirror.

4. 2            Process Control

The subcontractor shall prepare and utilize procedures controlling polishing and other processes where conformance with quality requirements is not readily detectable or measurable by inspection or test of the hardware element. These procedures shall be under subcontractor configuration control and (except for proprietary processes) subject to AS&E approval.

TECHNICAL SPECIFICATION

4.3 Inspection

The subcontractor shall be responsible for the performance of all inspection requirements in accordance with the Statement of Work (SOW 144-202).

4.3.1 Raw Material

4.3.1.1 Fused Silica

Acceptance of the fused silica mirror blank shall be subject to AS&E's approval based upon inspections performed by the supplier and witnessed by AS&E. A certification of compliance by the raw material supplier shall be required.

The raw material shall be inspected in so far as is practical when in the unfinished state. All mechanical dimensions will be confirmed. Birefringence (strain) will be observed by a plane polarimeter. Inspection of the seam, if a seamed piece is provided, will be made by visual techniques (low powered magnifying lenses) and the polarimeter inclusions within the critical zone will be checked by oiling the plate to each end and illuminating the cylinder.

If, after the blank is cored, an over specification inclusion is found the subcontractor shall notify AS&E.

4.4 Raw Material Traceability

The fused silica used in the mirror must be traceable to the raw material batch or lot and the processes involved in its fabrication. Other materials shall be traceable by lot or batch to the manufacturer.

4.5 Non-Conforming Material

The subcontractor shall perform non-conforming material review and maintain disposition records. Use of non-conforming material in any deliverable end item shall require AS&E approval.

REV. LTR.	A																		
-----------	---	--	--	--	--	--	--	--	--	--	--	--	--	--	--	--	--	--	--

CODE IDENT. NO. 21802

CONTROL NO.	S144-202
DATE	June 1972
PAGE	13

TECHNICAL SPECIFICATION

4.6 Tooling Control

All test plates, tooling and fixtures designed for special use on this contract shall be under subcontractor configuration control.

4.7 Acceptance Testing

The subcontractor shall be responsible for performing end-item acceptance tests in accordance with the Statement of Work (SOW 144-202).

TECHNICAL SPECIFICATION

5.0 PREPARATION FOR DELIVERY

5.1 Packaging

The packing shall be equivalent to best commercial practice and shall be sufficient to protect the mirror assembly during shipment.

5.2 Marking

The shipping container shall be marked with the subcontractors name and the part designation.

6.0 NOTES

6.1 Ordering Data

The procurement document should specify the following:

- a. Title, number, and revision letter of this specification
- b. Schedule dates for deliverable data.
- c. Qualification test and/or data (when required)
- d. Schedule dates for design reviews

6.2 Specification Revision

The revised text in this specification is identified by the revision letter in the right margin adjacent to the revised (or new) material.

#### IV References

1. Appendix , "LOXT High Resolution Mirror Dynamic Analysis".
2. Appendix , "LOXT Structural Dynamic Analysis".
3. "HEAO Experiment Developers' Handbook" NASA Document.
4. "Stresses in Shells", W. Flugge, Springer Verlag, New York 1967.

15